Observational Constraints on Global 21-cm Signal from the Epoch of Reionization

A Thesis

Submitted for the Degree of

Doctor of Philosophy

in the Faculty of Science

by

Saurabh Singh

Joint Astronomy Programme
Department of Physics
Indian Institute of Science
Bengaluru – 560 012 (INDIA)

May, 2018

Declaration

I, Saurabh Singh, hereby declare that the work presented in this thesis titled "Observational Constraints on Global 21-cm Signal from the Epoch of Reionization" is entirely original. This work has been carried out by me under the supervision of Prof. Ravi Subrahmanyan (Raman Research Institute), Prof. N. Udaya Shankar (Raman Research Institute), Prof. Shiv Sethi (Raman Research Institute) and Prof. Chanda J. Jog (Indian Institute of Science) at the Department of Astronomy and Astrophysics, Raman Research Institute under the Joint Astronomy Program hosted by the Department of Physics, Indian Institute of Science.

I further declare that the subject matter presented in this thesis has not previously formed the basis for the award of any degree, diploma, membership, associateship or any other similar title of any university or institution.

Department of Physics
Indian Institute of Science
Bangalore-560012
India

Saurabh Singh
Date:

In loving memory of my parents

Acknowledgements

I express my sincere gratitude to Prof. Ravi Subrahmanyan and Prof. N. Uday Shankar; I have immensely learnt from them, right from the fundamentals of radio astronomy to the nuances of experimental cosmology. The "brainstorming" sessions with them over different aspects of the research work have always resulted in a new path to proceed, and have substantially contributed to the work flow in this thesis. Field and observing trips with them to the remotest sites in India has been a memorable part of my PhD, where not only did we get an opportunity to discuss our experiment from a wider perspective, but digressed over anything interesting under sun. I have been fortunate enough to have supervisors who were ready with valuable advice and assistance in academic as well as non-academic matters. I thank Prof. Shiv Sethi, Prof. Rennan Barkana, Dr. Anastasia Fialkov and Dr. Aviad Cohen for the helpful discussions on theoretical aspects of the research. I also thank Prof. Chanda J. Jog for taking care of all the official formalities during PhD and Prof. Sadiq Rangwala for his valuable comments as a member of the advisory committee.

Girish, Vani, Som and Raghu have been an integral part of the SARAS 2 project, and were quick in coming up with ingenious ways to develop the system. Given that Murphy's law (*if anything can go wrong, it will*) has always been on the lookout for us, we have spent countless hours in lab and field fixing the issues and coming with new tests and diagnostics. Working with them has taught me enormously about the development aspects of the radiometers, and has helped me to appreciate and learn the art of sculpting a design. Mayuri and Jishnu, members of the SARAS team, have been excellent colleagues to work with. I would also thank the visiting students in the lab, Santosh, Divya, Kshitij and Souvik, with whom I had an opportunity to work and learn.

I extend my acknowledgement to the staff at Electronics and Mechanical Engineering Group at RRI. They have been extremely adept in getting the system ready, in midst of planned field measurements and observing trips. I also express my gratitude to RRI library, administration and purchase section for their outstanding cooperation in ensuring the timely availability of resources.

Staff at Gauribidanur Field Station, lead by Ashwathappa, can not be thanked enough for their support in electromagnetic characterization of antenna and receiver testings. It is their readiness and enthusiasm in the field trials that facilitated us to iterate over the system design, and achieve a

radiometer capable of performing high-precision night-sky measurements. Gauribidanur Field Station has inevitably become our second home, and has always been welcoming to assist us in our enterprise.

The people we have met during our observing trips, both at Timbaktu Collective and Hanle Observatory, have only enhanced our appreciation towards a completely indigenous way of living. It has been a humbling experience to have spent time in remote parts of India, and witness varied lifestyles and cultures. Siddhartha and Molly at Timbaktu Collective, and G.C. Anupama, Dorje Angchuk, and staff at Hanle Observatory were exceptionally cooperative and were ready with providing any support that we needed during the observations. The logistical support provided by them allowed us to successfully carry out the observations and perform preliminary analysis at the observing sites.

Coursework has been a crucial component in my initiation into astronomy. Being from an engineering background, the initial courses resulted in lot of library hours, trying to make sense of the things. I would particularly thank Biman Nath, who took course on Fundamental of Astrophysics, whose dedication towards the lectures eased my transition into astronomy and astrophysics.

The acknowledgement is never complete without thanking wonderful set of people at RRI who made the entire PhD life a cherished memory. To Janakee, thanks for always being there; I prize the times of late night assignments and the extended talks about the ups and downs of our research work. To Aditi, your non-conventional sense of humor has been very enlivening and has helped me in taking matters less seriously. I thank Vidya and Harini for helping me through the official processes so efficiently. Laxmamma and Hanumanthappa were always there to offer the required, and sometimes increased, intake of tea and coffee that helped me to stare at my laptop screen longer. I would not mind calling my feline companion, Fluffy, as part of the SARAS team if our science community allows us to. She has been a regular member of our meetings, and has given us company during the late night works in the lab, with occasional "treats" from her adventurous hunts.

I will always be indebted to friends from different spheres of my life. To Francis, I find it hard to verbalize my gratitude. You have always been there, fighting all odds, to help me whenever I needed it. I am yet to learn a lot from your unique insights of life. To Anshu, thanks for bearing with me and forcing me to be less robotic. Harsh, your free-spirited nature and philosophical outlook continues to inspire me. Chandan, Himanshu, Rahul, Rishabh, Mugundhan, you all have been great companions at different locations in spacetime.

Coming to my family, I feel deeply grateful to be amidst the most awesome people I have ever met. The unending love and support that I received from my parents is the primary reason that I am able to pursue my interests. Words are powerless to express my gratitude towards them. The incessant chats during the home trips and regular phone calls from Suman, Ashok, Nupur and Shivam have kept me going. They have been a source of immense affection and encouragement throughout my life.

Synopsis

Cosmic Dawn (CD), beginning with first light from the first stars and ultra-faint galaxies, and Epoch of Reionization (EoR), resulting in almost complete reionization of the primordial gas, marks an important period in the cosmic evolution of baryons. There is considerable uncertainty and limited observational constraints on the evolution of thermal and ionization state of the intergalactic medium (IGM) in this period as well as on the nature of the first sources of light that caused the transformation.

One of the most promising probes of these epochs is the rest-frame global 21-cm signal of neutral hydrogen (HI) produced by the intergalactic medium (IGM) prior to the end of the EoR at $z \sim 6$. The intensity of the signal is tied to the star formation history as well as to the ionization and thermal histories of the IGM. Hence, its measurement will bracket astrophysical properties of the first UV and X-ray sources including the ionizing efficiency of first stars and quasars, luminosity and spectra of the first population of black holes, and properties of dark matter particles. At present these properties are poorly understood allowing for a large variety of plausible 21-cm spectra.

Since it is a global signal, high spatial resolution is not needed and a well-calibrated and efficient single-element radiometer can achieve the required sensitivity to detect the signal in a few minutes. However, the detection of the signal is challenging owing to multiple reasons: the signal is predicted to be extremely weak, with maximum amplitude less than a few hundred mK in brightness temperature, smoothly varying over a wide frequency range from about 200 MHz all the way to below 40 MHz, and buried in Galactic and Extragalactic foregrounds of $100 - 10,000$ K.

The SARAS 2 radiometer was purposely designed to detect the global 21-cm signal. SARAS 2 has been designed to have (i) a telescope beam that is frequency independent so that structure in the foreground sky brightness does not result in any spectral shapes in the response, and (ii) a receiver transfer function and internal systematics—both multiplicative and additive—that are spectrally smooth so as to allow a separation of foregrounds and systematics from the predicted global cosmological 21-cm signals.

In this thesis, we describe the radiometer, data modeling for foregrounds and systematics, and derive constraints on EoR from night sky data from SARAS 2 observations. We also discuss alternative means of detecting the global 21-cm signal using interferometers.

Chapter 1: Introduction

In Chapter 1, we begin with an overview of the ionization and thermal history of the Universe emphasizing the physics of dark ages, cosmic dawn and epoch of reionization. We discuss the open questions related to the nature of first sources of radiation, the timings of different processes during CD/EoR and the mechanism of reionization itself. We briefly discuss the major observables for these epochs, namely cosmic microwave background, Lyα emitters and quasars, and the constraints on ionization history placed from them. This is followed by an introduction to 21-cm physics, and its application to the study of CD/EoR. We discuss the theoretical expectations for the spectrum of the global signal, along with its possible variations. We conclude with the challenges in the detection of the signal and ongoing experiments attempting to detect the signal.

Chapter 2: SARAS 2: A Spectral Radiometer for probing Cosmic Dawn and the Epoch of Reionization through detection of the global 21-cm signal

Critical to detecting the 21-cm signal is the manner in which the sky signal is represented through the instrument. It is of utmost importance to design a system whose spectral bandpass and additive spurious signals can be well calibrated and any calibration residual does not mimic the signal. In this chapter, we introduce Shaped Antenna measurement of the background RAdio Spectrum (SARAS), which is an ongoing experiment that aims to detect the global 21-cm signal. Here we present the design philosophy of the SARAS 2 system, followed by a discussion of the SARAS 2 architecture and dedicated algorithms developed for data processing. We discuss its performance and limitations based on laboratory and field measurements. Laboratory tests with the antenna replaced with a variety of terminations, including a network model for the antenna impedance, show that the gain calibration and modeling of internal additive signals leave no residuals with Fourier amplitudes exceeding 2 mK. Thus, even accounting for reflection and radiation efficiency losses in the antenna, the SARAS 2 system is capable of detection of complex 21-cm profiles at the level predicted by currently favoured models for thermal baryon evolution.

Chapter 3: SARAS 2 Observations, Data and Constraints on EoR

This chapter deals with details of the site survey conducted to select a suitable site where SARAS 2 may be deployed, the observations, the methods employed for data modeling and the constraints derived from the data on plausible global 21-cm signals. We begin with the results of the site-survey, which was conducted to characterize the radio frequency environment of the several remote sites in India. This is followed by a description of SARAS 2 observations carried out at Timbaktu Collective, Andhra Pradesh, India. We use 63 hr night time observing of the radio background in the frequency

band 110-200 MHz with the radiometer deployed at the Timbaktu Collective to derive constraints on EoR. We employ Bayesian and frequentist approaches, and reject the theoretically allowed 21-cm signals which are inconsistent with the SARAS 2 data. We have been able to rule out roughly 10% of the theoretically plausible models for the signal, and place limits on the X-ray efficiency of the first sources and the rate of reionization. All the rejected models share the scenario of inefficient heating of the primordial gas by the first population of X-ray sources along with rapid reionization.

Chapter 4: On the detection of Global 21-cm signal from Reionization using interferometers

In this chapter, we look at alternative means of detecting the global 21-cm signal using interferometers. Modeling of receiver noise with mK accuracy and its separation remains a formidable task in experiments aiming to detect the global signal using single-element spectral radiometers. Interferometers do not respond to receiver noise; therefore, we explore the theory of the response of interferometers to global signals. We proceed by first deriving the response to uniform sky of two-element interferometers made of unit dipole and resonant loop antennas, then extend the analysis to interferometers made of 1-D arrays and also consider 2-D aperture antennas. Finally, we describe methods by which the coherence might be enhanced so that the interferometer measurements yield improved sensitivity to the monopole component. We conclude that (a) it is indeed possible to measure the global 21-cm from EoR using interferometers, (b) a practically useful configuration is with omnidirectional antennas as interferometer elements, and (c) that the spatial coherence may be enhanced using, for example, a space beam splitter between the interferometer elements.

Chapter 5: Conclusion

We conclude with the current status of 21-cm cosmology. We discuss the upper limits on the 21-cm power spectrum placed by interferometric experiments worldwide, including results from GMRT, LOFAR, MWA and PAPER. We then summarize the salient features of the SARAS 2 radiometer and its constraints on EoR via observations aimed at detecting the global 21-cm signal. We also describe the constraints on CD/EoR placed by other experiments targeting the the global 21-cm signal. The results from SARAS 2 that rule out a class of CD/EoR scenarios are placed alongside constraints on Gaussian-like absorption features by LEDA and limits on the duration of reionization by EDGES. Finally, we also discuss the recent reported detection of an unexpected signature from cosmic dawn by EDGES and summarize the attempts to find a theoretical explanation for the signature. We then summarize the salient features of SARAS 2 radiometer and its constraints on EoR. We end with an indication of the path forward for SARAS based on the experience gained in this thesis work and the status of the field.

Publications from the Thesis

Refereed Journals

1. **Saurabh Singh**, Ravi Subrahmanyan, N. Udaya Shankar, Mayuri Sathyanarayana Rao, Anastasia Fialkov, Aviad Cohen, Rennan Barkana, B. S. Girish, A. Raghunathan, R. Somashekar and K. S. Srivani, *SARAS 2 constraints on global 21-cm signals from the Epoch of Reionization*, 2018, The Astrophysical Journal, 858, 54

2. **Saurabh Singh**, Ravi Subrahmanyan, N. Udaya Shankar, Mayuri Sathyanarayana Rao, B. S. Girish, A. Raghunathan, R. Somashekar and K. S. Srivani, *SARAS 2: A Spectral Radiometer for probing Cosmic Dawn and the Epoch of Reionization through detection of the global 21 cm signal*, 2018, Experimental Astronomy, 45, 269

3. **Saurabh Singh**, Ravi Subrahmanyan, N. Udaya Shankar, Mayuri Sathyanarayana Rao, Anastasia Fialkov, Aviad Cohen, Rennan Barkana, B. S. Girish, A. Raghunathan, R. Somashekar and K. S. Srivani, *First results on the Epoch of Reionization from First Light with SARAS 2*, 2017, The Astrophysical Journal Letters, 845, L12

4. **Saurabh Singh**, Ravi Subrahmanyan, N. Udaya Shankar and A. Raghunathan, *On the detection of global 21-cm signal from Reionization using interferometers*, 2015, The Astrophysical Journal, 815, 88

Conference Proceedings

1. Ravi Subrahmanyan, Agaram Raghunathan, N. Udaya Shankar, **Saurabh Singh**, Sharath Puthige, Nivedita Mahesh, Mayuri Sathyanarayana Rao, *Wideband Antennas for Precision Spectral Radiometers for Cosmology*, International Conference on Electromagnetics in Advanced Applications (ICEAA), 19-23 Sept. 2016, Cairns, Australia. Page 438 - 41

2. Ravi Subrahmanyan, N. Udaya Shankar, Mayuri Sathyanarayana Rao, **Saurabh Singh**, *Detecting signatures of cosmological recombination and reionization in the cosmic radio background*, IAU General Assembly 2015, 22, 2250805

Contents

List of Figures

List of Tables

Chapter 1

Introduction

Whence all creation had its origin,
he, whether he fashioned it or whether he did not,
he, who surveys it all from highest heaven,
he knows - or maybe even he does not know.
-Nasadiya Sukta, Rig Veda

A paper titled "A Measurement Of Excess Antenna Temperature At 4080 Mc/s" appeared in the Astrophysical Journal Letters in 1965 [124]. The authors reported an excess temperature of 3.5 K in the measurement of effective zenith noise temperature of their radiometer. The paper, according to one of the authors, consisted of "bare-boned account of our measurement —together with a list of possible sources of interference which had been eliminated". The modestly titled paper grabbed the interest of the cosmology community and triggered similar measurements and plausible theoretical explanations for its origins. The most widely explanation hailed it as the first detection of cosmic microwave background radiation (CMB), being predicted more than two decades [34]. 1960s thus heralded an era of observational cosmology with increased interest towards CMB spectral measurements and its predicted spatial anisotropies.

Fast forwarding to present, we have witnessed high precision cosmological observations enabled by innovative design of instruments. Experiments like COBE [87], WMAP [65] and Planck [126] have significantly enhanced our understanding of the evolving Universe. These include, but are not limited to, estimates of cosmological parameters, shape of the matter power spectrum, amplitude of the initial density perturbations, geometry and dynamics of the Universe, properties of neutrinos and details of recombination [157]. However, there are aspects in cosmology which are far from being understood completely. The questions range from the nature of dark matter and dark energy [20], inflationary energy scale [32] to formation of first stars and galaxies in the Universe [19]. The next generation of instruments are being custom designed to enable us to answer these long-standing

questions and deepen our understanding of the Universe. The present thesis addresses questions related to the formation of first stars and galaxies using SARAS 2, a dedicated radiometer for studying the emergence of first sources of radiation, and consequent evolution of the Universe.

1.1 Ionization history of Universe

The ionization state of the Universe has undergone significant evolution from the Big Bang to the present. The Universe was initially a dense, hot soup of plasma where matter and radiation were in thermal equilibrium with each other. When the rate of an interaction fell below the expansion rate of the Universe, the interacting species would decouple from equilibrium. Matter and radiation decoupling took place around 380,000 years after the Big Bang. This is the time when the average energy of the photons, in the tail of their energy distribution, became insufficient to cause ionization of hydrogen atoms, which were formed as a result of electron capture by protons. This was the first change in the ionization state of the Universe and this period is referred to as the epoch of recombination [123]. The photons, after matter-radiation decoupling, free-streamed and constitutes the cosmic microwave background, which we observe today.

The Universe continued to be neutral for a long time since the energy of the CMB photons was insufficient to cause the ionization of atoms. This period is referred to as the dark ages. At this point, collapsed structures had not yet formed from the growth of primordial density perturbations, and the matter and radiation temperatures were falling with time. However, the density perturbations in the matter field, believed to have originated as a result of quantum fluctuations during inflation, were continuously growing. Eventually, the gravitational instability led to collapse of the overdense regions forming the first structures. This was followed by the emergence of first sources of radiation, marking the era of cosmic dawn (CD). The ultraviolet (UV) photons from these sources started ionizing the Universe. Over a period of a few hundred million years after the big bang, the Universe was ionized again. We call this period the epoch of reionization (EoR) [8]. The Universe has continued to be in an ionized state from the EoR to the present.

1.2 Understanding the Dark Ages, Cosmic Dawn and EoR

The dark ages is a term that captures the period between the epoch of recombination and the emergence of the first sources of radiation. Observations of this epoch are extremely useful for constraining fundamental cosmology since structure formation is still in the linear regime. Further, observables are still not contaminated by model dependent astrophysics. Thus observations of this epoch would be extremely useful in recovering basic cosmological parameters, similar to the manner in which the CMB is a probe. The advantage of cosmology from dark ages is that since radiation is decoupled, fluctuations in the matter power spectrum are preserved even at very small angular scales that are not

accessible with CMB since photon diffusion wipes out such fluctuations [52].

Cosmic dawn followed the dark ages and marked the emergence of the first sources of radiation in the Universe [136]. This was the time when astrophysics became important and any observable signature from hereon would hold information on the formation and evolution of the first sources. Cosmic dawn was followed by reionization where the neutral hydrogen fraction started decreasing significantly globally. However, there is no clear demarcation between completion of cosmic dawn and the onset of reionization. It is a continuous period in which the sources form, heat and ionize the intergalactic gas leading to an ionized Universe [82].

1.2.1 A basic picture of reionization

Reionization, and the preceding cosmic dawn, is an exciting intersection between cosmology and astrophysics. Thus any study of CD/EoR is motivated by understanding of the properties of the first stars and galaxies and physics of the intergalactic medium (IGM), since their nature at high redshifts is very poorly constrained by current observations. In Sec. 1.3, we discuss observations that have placed useful constraints on reionization; however these constraints still allow for a large range of plausible astrophysical scenarios.

We now sketch a basic picture of the reionization which is consistent with current observations [81, 93]. The density perturbations, believed to be seeded during the inflationary epoch, grew with time and the resulting gravitational instability caused collapse of overdense regions leading to formation of structures. A fraction of collapsed structures, which we refer to as halos, formed the first sources of electromagnetic radiation. UV photons emitted by ultrafaint galaxies containing the first stars that became these sources ionized the neutral medium around them, creating regions of ionized gas around the sources. However, due to the competing recombination process, the extents of the ionized regions were limited. We call these regions "ionization bubbles". We thus have a scenario where small pockets of the IGM are ionized but the Universe is globally predominantly neutral. This is referred to as the pre-overlap phase.

With time, the ionization bubbles grow, and at the same time more bubbles form due to gravitational collapse of other regions. This eventually leads to overlap between neighboring ionized regions, which significantly increases the mean free path of the ionizing photons. This is an accelerated growth of the ionization where the neutral fraction of hydrogen starts to decrease at a global level and is known as the overlap phase. High density neutral regions are the last to ionize, when ionizing photons from all directions increase the ionization radiation flux. This completes the reionization process [57]. All these processes are shown in Fig. 1.1.

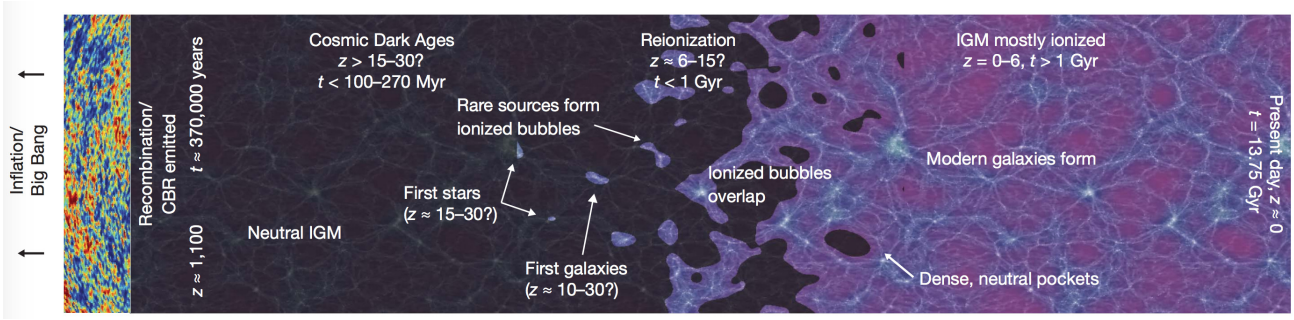

Figure 1.1: The schematic shows the timeline of the evolution of the Universe, with a focus on dark ages, cosmic dawn and reionization [138].

1.2.2 Motivation for studying Cosmic Dawn and EoR

The environment in which the first galaxies formed was significantly different from that of the local Universe. The early IGM was devoid of heavy metals, which get ejected into the medium due to supernovae explosions. Further, the effect and dominance of various feedback processes in the early Universe is also poorly understood [45]. For example, the ionizing radiation from the first stars might suppress hydrogen molecule formation, which is necessary to form stars and thus has implications on structure formation. Consequently the masses, spectral behavior and radiation flux of early sources are assumed to be simply extrapolations from the relations for the local Universe. However, all these relations can have non-trivial redshift dependence [73, 36].

To highlight the uncertain astrophysics, let us consider the formation of halos that can support star formation. The process of gravitational collapse of an overdense region is accompanied by heating of the gas. In order to continue collapsing, a cooling channel is needed that can carry away the heat thus enabling the gas to collapse further. In the local Universe, the most efficient agents of cooling are the metals which cool the gas through radiative transitions. Since the early Universe is devoid of heavy elements, the major channel of cooling would be atomic or molecular [60]. The cooling channel decides the minimum mass of the halo which can enable star formation. More efficient the cooling, lower is the mass threshold, and hence earlier is the star formation. Similarly, for a collapsed halo that is forming stars, the fraction of baryons that go into star formation (star formation efficiency) is equally uncertain. Further, the flux of ionizing photons emitted from the sources and the fraction that may escape the halo, also called the escape fraction, are not known for the early Universe [175].

Thus, assuming a wide range of minimum halo mass for star formation, along with varying star formation efficiency, ionizing flux and escape fraction, we can create scenarios for formation of first sources of radiation that are all theoretically plausible [29].

Another poorly understood aspect of CD/EoR is the timing of different processes. This period is characterized by three major events [134]:

- Formation of first stars and consequent emission of $Ly\alpha$ photons,
- Onset of heating of IGM by X-ray sources, and
- Ionization of neutral hydrogen by UV photons.

All these processes can have substantial overlap in time. Further, the timings of these events depend strongly on the redshift of formation of first sources of radiation, their spectral behavior and on which feedback processes are active and when. Currently, the last phase, reionization, is better constrained observationally, as discussed in Sec. 1.3. However the earlier processes are believed to have occurred at much higher redshifts and hence have very few observational constraints.

The last aspect of CD/EoR is the mechanism of reionization itself. Although different numerical simulations agree on a basic picture for the mechanism, we still have unanswered questions. For example, whether low density regions were ionized first followed by high density regions or vice-versa [107]? Similarly, whether reionization occurred in a single step or was a multi-step process [23, 168]? We also do not know with confidence as to what were the primary sources that caused the reionization; could galaxies reionize the Universe and whether AGNs contributed significantly [94, 83, 117]? Finally, how rapid or gradual was the reionization [13, 26] and how patchy or homogenous was the process over large spatial scales [39, 38]? While the rate of reionization depends on the ionizing flux and escape fraction of ionizing photons, the patchiness depends on the mean-free path for the ionizing photons. E.g., if the reionization occurs primarily via X-ray photons, it would be more uniform throughout compared to the scenario where ionization occurs via UV photons, which is a more plausible scenario.

1.3 Probes of reionization

Given all these uncertainties about a) the nature of first sources of radiation, b) timings of different processes, and c) the mechanism of reionization, there is a strong case for looking at observables that can place constraints on the nature of ionizators or the properties of the IGM [42]. Thus, in this section, we discuss different ways by which we can place observational constraints on CD/EoR.

1.3.1 Quasars (Quasi-stellar objects/QSOs)

Quasars spectra were the first probes of reionization; observations of high redshift quasars established that we reside in a predominantly ionized Universe [59]. Resonant $Ly\alpha$ absorption by neutral hydrogen along the line-of-sight can place upper limits on the neutral fraction of hydrogen. Because

of the large cross-section of interaction, even a small neutral fraction can attenuate the QSO flux to almost zero giving rise to what is called Gunn-Peterson (GP) trough. Quasar surveys at different redshifts show the GP trough at and after $z \sim 6$, as shown in Fig. 1.2 [12, 43]. These observations imply the completion of reionization by $z \sim 6$. GP method can only place upper limits on the neutral fraction since a tiny fraction of neutral hydrogen, of about 10^{-3}, is sufficient to absorb all the flux for wavelengths shorter than $Ly\alpha$ [101].

Another way to constrain the neutral fraction of hydrogen is to look for transmission at $Ly\alpha$, which is seen as spikes in the spectrum and appear due to ionized regions in-between the neutral regions [6]. These are referred to as dark gaps. These gaps get longer with redshift, as expected for increasingly neutral IGM. However, there is also a substantial variation between different lines of sight, pointing to an inhomogeneous reionization process. Numerical simulations then can be employed to get the best match with the observed dark gap distribution and hence compute the resulting neutral fraction [118].

1.3.2 CMB

The CMB temperature and polarization power spectra show the state of the Universe at the epoch of recombination. Additionally, owing to the presence of a quadrupole anisotropy in the ambient CMB, the free electrons generate secondary polarization in the CMB at large angular scales via Thomson scattering [42, 135]. The resulting optical depth also suppresses the temperature anisotropies of CMB at small scales, which is reflected in the temperature power spectrum. The latter is degenerate with the scalar/tensor ratio for the primordial perturbations. However, the polarization power spectrum helps break this degeneracy; this is shown in Fig. 1.3.

The polarization introduced by the free-electrons is also referred to as the "reionization bump", since it shows up at large angular scales as excess power [66]. This enables computation of the optical depth, τ, that can constrain the redshift of reionization, but in a way that is dependent on the ionization history. The latest Planck results place the best estimate of τ at 0.058 ± 0.012 [127]. Since this is an integral measurement, the actual redshift of reionization is model dependent. For the scenario of instant reionization, the transition redshift is $z_{\rm re} = 8.8 \pm 0.9$ [127].

Another EoR imprint on the CMB power spectrum appears at small angular scales. The bulk peculiar velocities of electrons introduce Doppler shifts in scattered CMB photons. Since the peculiar velocities of electrons and the ionization fraction of hydrogen depend on local density fields, the mechanism leads to temperature inhomogeneities at small angular scales [22]. Current upper limits on this imprint, referred to as the kinetic Sunyaev-Zeldovich (kSZ) signal [161], places an upper limit on the duration of reionization. The SPT-SZ survey placed an upper limit on the duration of reionization, $\Delta z < 5.4$ [55].

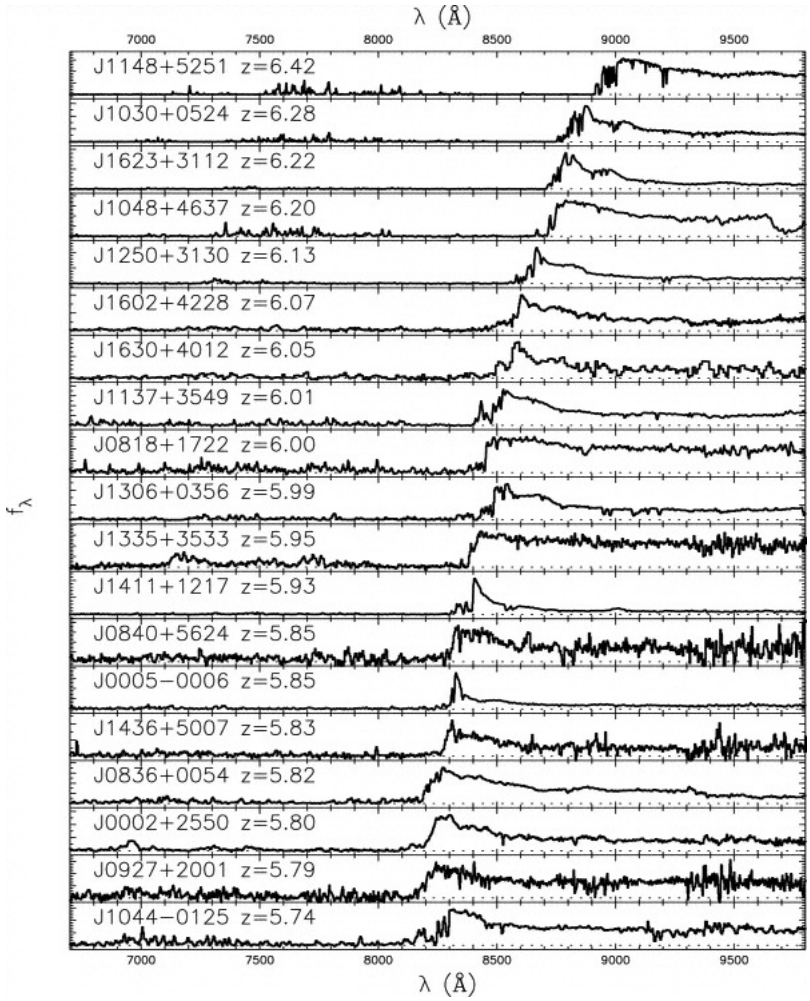

Figure 1.2: The spectra of 19 SDSS quasars between $5.74 < z < 6.42$. Using this sample, evolution of the ionization state of IGM is found to be accelerated at $z > 5.7$. Further, the mean length of dark gaps shows the most dramatic increase at $z \sim 6$. The observations infer the completion of reionization by $z \sim 6$ [43].

The CMB is complement to the other probes since it is sensitive to ionized gas, while most of the other probes, e.g. *Ly*α and quasars, are sensitive to neutral gas.

1.3.3 *Ly*α Galaxies

There are two groups of galaxies whose observations constrain EoR. The first is *Ly*α emitters (LAEs), which have significant emission at *Ly*α wavelength (rest frame wavelength: 1216 $\mathring{A}$). They are generally high star-forming galaxies. The second is Lyman break galaxies (LBG). These galaxies are bright in wavelengths above the Lyman Limit (rest frame wavelength: 912 $\mathring{A}$); however become extremely

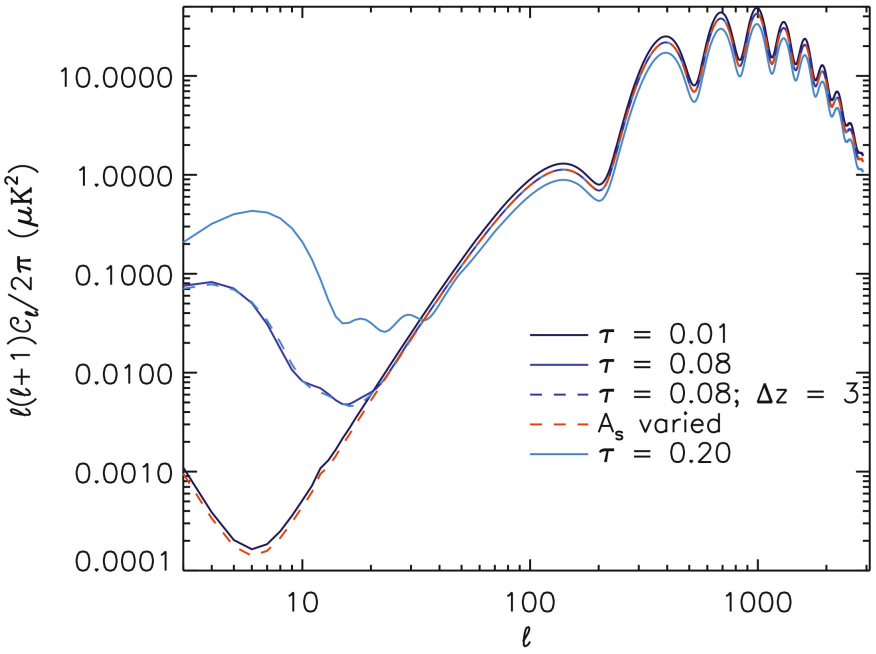

Figure 1.3: Polarization (zero curl) or E-mode power spectrum of CMB. The excess power at low multipoles/large angular scales arise due to Thomson scattering between free electrons and the CMB quadrupole. The power amplitude depends on optical depth as shown by different solid lines. The advantage of polarization power spectrum is that its amplitude and the optical depth are not degenerate. Thus change in the amplitude value, shown by red dotted line, cannot create the low multipole bump [137].

dim or "drop-out" at the Lyman Limit [106].

At redshift $z > 6$, there is a significant reduction in the *Ly*α flux from *Ly*α emitters. There is almost no evolution in the Luminosity Function of LAEs between $z \sim 3$ and $z \sim 5.7$, but a sharp decrease after $z \sim 6$ [85, 68]. This is precisely the redshift where QSO observations indicate the completion of EoR. The suppression of *Ly*α can be explained as caused by the presence of neutral hydrogen in IGM at $z > 6$, where the large optical depth makes the IGM opaque to *Ly*α photons [70].

Another technique is to compute the *Ly*α fraction of Lyman break galaxies, i.e. the fraction of LBGs where spectroscopic observations show *Ly*α emission line with effective width larger than some threshold [35]. This exercise shows an interesting trend as a function of redshift: the *Ly*α fraction first increases at higher redshifts upto $z \sim 6$ and then suddenly drops at $z \sim 7$ [113]. While the increase in the fraction can be attributed to reduced dust and hence enhanced escape of *Ly*α photons, the reduction is consistent with presence of neutral hydrogen in the IGM at $z > 6$ [37].

Both the techniques hint at a global neutral fraction for hydrogen to be $\gtrsim 0.5$ at $z \sim 7$ [69]. In Fig. 1.4, we show the constraints on ionization fraction from all the three probes discussed above.

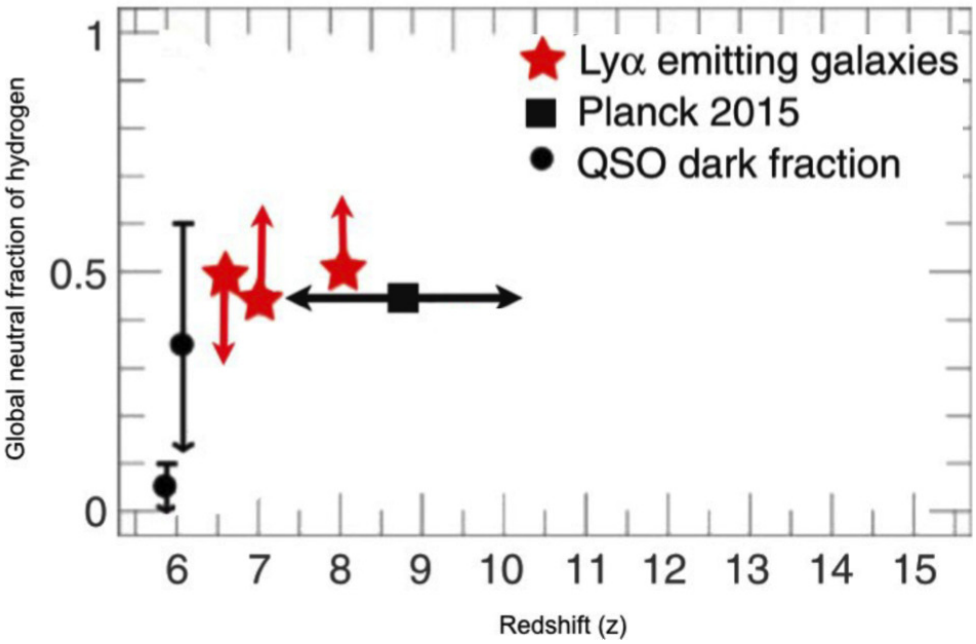

Figure 1.4: Joint constraints on the neutral hydrogen fraction at different redshifts. The circles represent constraints from quasar dark gap fraction in the spectra. The square shows the constraint from CMB optical depth to reionization. The stars represent the constraints from *Ly*α emitting galaxies. The figure is adapted from [35].

1.3.4 21-cm radiation from neutral hydrogen (HI)

Arguably, the 21-cm spin-flip transition of neutral hydrogen is one of the richest probes of CD/EoR and provides a direct probe at each redshift. This is enabled by the fact that the rest frame frequency of this transition is 1420.406 MHz, which is redshifted by a factor of $(1+z)$. Thus measurement at any frequency provides the net strength of this radiation at a corresponding redshift [7]. In comparison, the CMB is a more indirect and integral measurement. Further, since neutral hydrogen is expected at redshifts larger than 6, the 21-cm signal, when measured at each redshift, manifests as a continuous signal from $z \sim 6$ to higher than $z \sim 35$ [132]. Thus the 21-cm measurement allows for a deeper redshift observation compared to the other probes. In the following section, we elaborate on the physics of 21-cm radiation and its importance in probing CD/EoR.

1.4 21-cm Cosmology

The 21-cm line radiation from neutral hydrogen was first predicted by Hendrik van de Hulst in 1944, as originating from the transition between two energy levels in the ground state of hydrogen atom [165]. The two energy levels correspond to the two spin states of the electron and proton, with

parallel spins resulting in higher energy of the system (triplet state) compared to the anti-parallel spin (singlet state). The probability of the spin-flip is very small, given by the spontaneous emission coefficient, A_{21}, 2.85×10^{-15} s^{-1}, which implies a timescale of a million years for a spontaneous spin-flip. However, in astrophysical scenarios, although the density of the gas is low, the number of hydrogen atoms is enormous and we do observe the 21-cm radiation in many regions where neutral hydrogen is present [30].

Moving to higher redshifts, where we expect the IGM to be predominantly neutral, we can predict the strength of the 21-cm radiation depending on the ionization and thermal state of the IGM. We now proceed to elucidate the parameters that determine the specific intensity of the radiation, measured in units of brightness temperature, at different epochs. For this, we make the Rayleigh-Jeans assumption, $h\nu << kT$, and hence we use temperature units (Kelvin) instead of specific intensity $(Wm^{-2}Hz^{-1}s^{-1}sr^{-1})$.

1.4.1 21-cm radiation from Cosmic Dawn and EoR

For radiative transfer considerations, assume a background radiation field with temperature T_R and a foreground source temperature $T_{\rm source}$. Further, let the line of sight optical depth of the source be τ. Putting it all together, the observed temperature $T_{\rm OBS}$ would be [141]:

$$T_{\rm OBS} = T_{\rm source}(1 - {\rm e}^{\tau_\nu}) + {\rm T_R}({\rm e}^{-\tau_\nu}). \tag{1.1}$$

In the high redshift Universe, the background radiation field is the CMB and hence $T_R = T_{\rm CMB}$. The source, which is neutral hydrogen, is characterized by the spin temperature T_S, and in this case the source temperature, $T_{\rm source} = T_S$. We discuss in detail the spin temperature and its dependence on other physical processes in Sec. 1.4.4.

Furlanetto et al. [52] has derived an expression for the optical depth. We use that expression to derive the brightness temperature of the 21-cm radiation as:

$$\delta T_b = 27 x_{\rm HI}(1+\delta)\left(\frac{\Omega_b h^2}{0.023}\right)\left(\frac{0.15}{\Omega_m h^2}\frac{1+z}{10}\right)^{\frac{1}{2}}\left(\frac{T_S - T_{CMB}}{T_S}\right)\left(\frac{H(z)/(1+z)}{dv_\parallel/dr_\parallel}\right) \text{ mK}, \tag{1.2}$$

where $x_{\rm HI}$ is the mean neutral fraction of hydrogen, δ is the overdensity, Ω_m , Ω_b and $H(z)$ are the cosmology parameters denoting the total matter density, baryon density and the Hubble parameter respectively. The last term accounts for the effect of peculiar velocities, where $(dv_\parallel/dr_\parallel)$ is the derivative of the velocity along the line-of-sight.

The brightness temperature varies across redshift, and hence frequency. At the same time, it varies

over spatial scales and hence has a global (aka monopole or sky-averaged signal) [133] as well as a fluctuating component [99]. While the fluctuating component can be measured as the 21-cm power spectrum over different spatial scales and redshifts, the global component can be measured by carrying out an absolute measurement of the sky brightness across different redshifts/frequencies.

1.4.2 21-cm Power Spectrum

The 21-cm power spectrum captures the fluctuations of the physical quantities listed in Eq. 1.2. The fluctuations can originate from variations in a) neutral hydrogen fraction ($x_{\rm HI}$), b) overdensity (δ), c) spin temperature (T_S) and d) velocity gradients [89]. Predictions for the fluctuations and its evolution over redshift can be computed through N-body simulations, semi-numerical simulations or analytic models [90]. Fig. 1.5 shows the power spectrum at different redshifts and spatial scales.

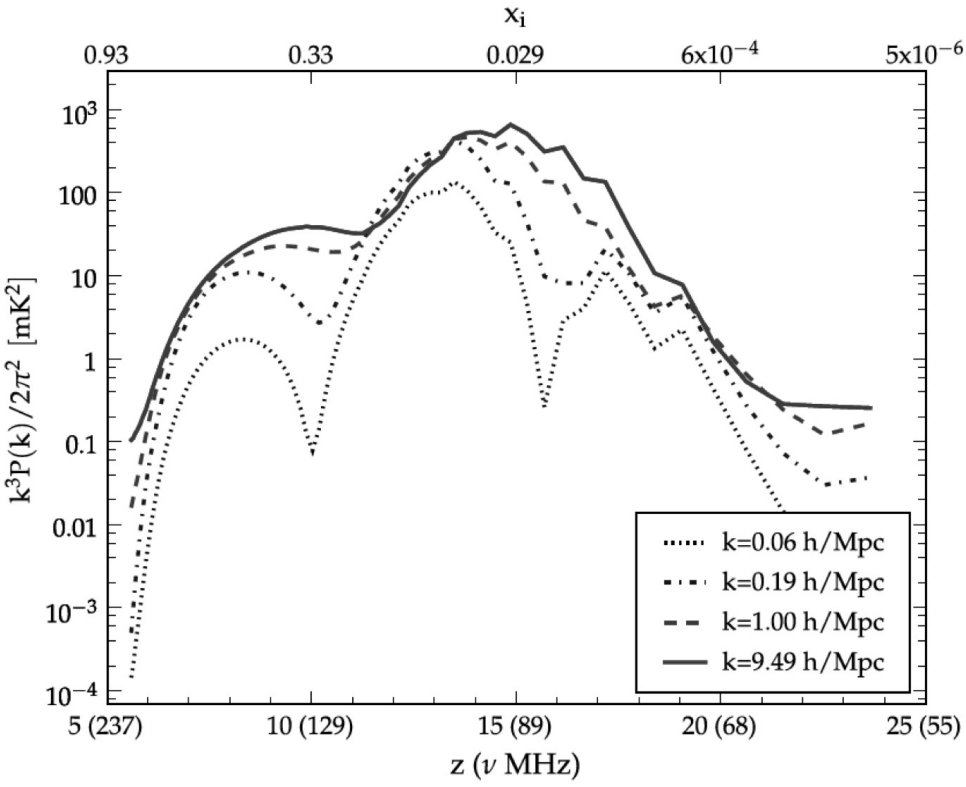

Figure 1.5: Evolution of 21-cm power at different k-modes as a function of redshift. Particularly at low k-modes, we can see the three peaks corresponding to fluctuations dominated by $Ly\alpha$ photons, heating and ionization respectively [142].

1.4.3 Global 21-cm signal

For the monopole component, Eq. 1.2 can be reduced to:

$$\delta T_b \simeq 27 x_{\rm HI} \left(\frac{T_S - T_{CMB}}{T_S}\right) \left(\frac{1+z}{10}\right)^{\frac{1}{2}} \text{ mK}. \tag{1.3}$$

The two quantities that δT_b depends on are a) spin and CMB temperature, and b) neutral hydrogen fraction. The variation in neutral hydrogen fraction dominates the profile in the reionization part of the signal, where there is a progressive reduction in the global neutral hydrogen fraction. Whereas variation in spin temperature is the dominant determinant of the 21-cm profile at high redshifts during dark ages, cosmic dawn and early EoR. Given the dependence of the signal on spin temperature over a wide range of redshifts, we explore the concept of spin temperature and its dependence on the astrophysical parameters.

1.4.4 Spin Temperature

The spin temperature is defined as the ratio of the atoms in the singlet and triplet states given by:

$$\frac{n_1}{n_2} = \frac{g_1}{g_2} \mathrm{e}^{-\frac{\mathrm{E}_{12}}{\mathrm{k_B T_S}}}, \tag{1.4}$$

where n_1 and n_2 are the number densities of hydrogen atoms in the two hyperfine levels, g_1 and g_2 are the statistical weights of the two levels and E_{12} is the energy difference between them.

The spin temperature depends on three factors [134, 52]:

- Temperature of the background radiation field,
- Temperature of the gas, and
- Color temperature of $Ly\alpha$ radiation field.

Its dependence on all three factors is given by the following equation [49]:

$$T_S^{-1} = \frac{T_R^{-1} + x_c T_K^{-1} + x_\alpha T_c^{-1}}{1 + x_c + x_\alpha}, \tag{1.5}$$

where x_c is the coupling constant due to atomic collisions, x_α is the coupling due to scattering of $Ly\alpha$ photons, T_R is the temperature of the background radiation, T_K is the gas temperature and T_c is the color temperature of $Ly\alpha$ radiation field.

As evident from Eq. 1.3, the amplitude of the signal depends on the differential between T_S and T_{CMB}. Thus the signal is expected to be zero whenever the spin temperature is strongly coupled to the background radiation temperature.

At high redshifts in the post-recombination era, where gas densities are relatively high, there are mechanisms through which T_S can couple to gas temperature T_K. Collisional coupling can result in $T_S = T_K$. However, by redshift $z \sim 30$, collisional coupling becomes insufficient. Wouthuysen-Field effect is another way by which T_S couples to T_K at these redshifts [49]. In this case, $Ly\alpha$ photons from the first sources of radiation can excite the electron in the hydrogen atom from one of the hyperfine states to the central 2P hyperfine state. While spontaneously re-emitting the $Ly\alpha$ photon, the electron can come down to either the singlet or triplet ground states and hence has the potential to effect a spin-flip transition.

Detailed analysis shows that $Ly\alpha$ photons can couple the spin temperature to the color temperature of the $Ly\alpha$ radiation in the vicinity of the resonant line. Due to the high optical depth of the line, there is a larger scattering of $Ly\alpha$ photons which causes photons in the vicinity of the $Ly\alpha$ line to be in equilibrium with T_K, hence resulting in $T_C \sim T_K$. Therefore, the Wouthuysen-Field effect can result in $T_S = T_C = T_K$ [134].

1.4.5 The *shape* of the global 21-cm signal

Following Eq. 1.3, we can now make predictions for the brightness temperature of the global signal in different redshift regimes. We also describe different turning points that we expect in the signal spectrum. We study the signal profile in different epochs, and in these different epochs there are different physical processes determining the evolution of the signal with redshift. The detailed physics of the processes are covered in [51, 133]; we provide a brief summary below. A *vanilla* model of the signal is presented in Fig. 1.6.

1.4.5.1 From the Epoch of Recombination through the Dark Ages

During this period, the IGM is mostly neutral. Hence only T_S and redshift decide the amplitude of the signal. To start with, baryonic matter and radiation temperatures are tightly coupled through scattering off the residual free electrons that survive following recombination. Thus $T_S = T_K = T_{CMB}$ and the signal is zero. This scenario breaks down when the proper density of the residual electrons is not sufficient to maintain the coupling between matter and radiation. However T_S continues to be coupled to T_K because of strong collisional coupling.

Thereafter matter, being non-relativistic, cools faster than the CMB in the expanding Universe; while matter cools as $(1+z)^2$, CMB temperature falls off as $(1+z)$. This leads to a negative value for the differential $(T_S - T_{CMB})$ thus giving rise to the first phase of the signal. However, as cosmic time approaches $z \sim 30$, the falling density of the gas results in that the collisional coupling is no longer sufficient to couple T_S to T_K; T_S tends to couple to T_{CMB} instead resulting in the differential $(T_S - T_{CMB})$ going back to zero. This creates the "dark ages" feature of the signal and the first turning

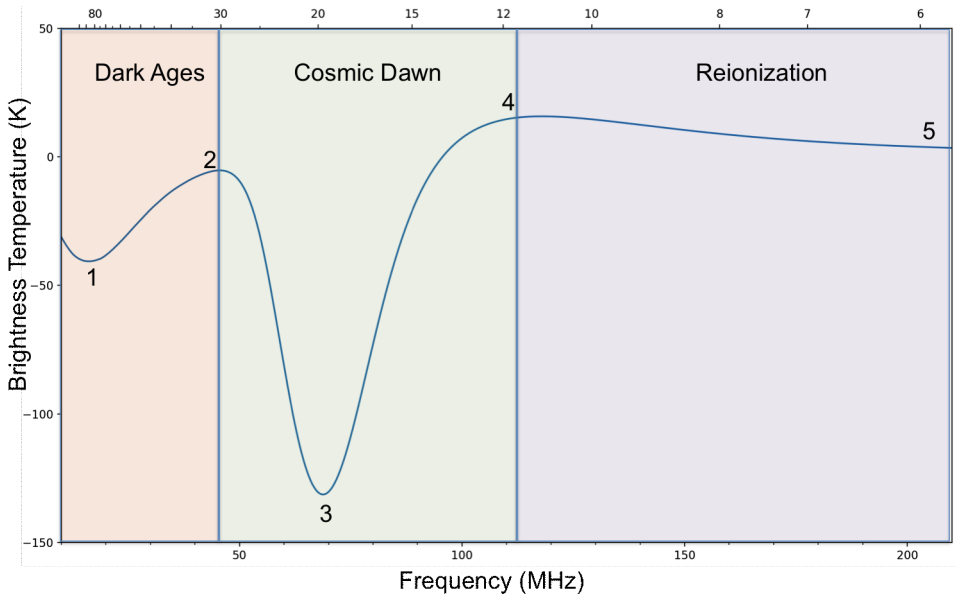

Figure 1.6: A sample global 21-cm signal through dark ages, cosmic dawn and the epoch of reionization. Turning points $1-5$ denote the locations of critical points in the signal. The top x-axis shows the redshift corresponding to the observed frequency shown in the bottom x-axis.

point in the signal. It is perhaps the best understood part of the 21-cm signature since it is completely determined by cosmology and does not have astrophysical uncertainties.

1.4.5.2 Dark Ages to Cosmic Dawn

This is the period when the first sources of radiation are expected to start to form as a result of gravitational collapse. Structure formation leads to emergence of first stars. $Ly\alpha$ photon emission from these stars results in the Wouthuysen-Field effect that couples T_S back to T_K. This causes the second turning point in the 21-cm signal. Since matter has been continually cooling adiabatically, the differential temperature $(T_S - T_{CMB})$ continues to grow more negative and hence the signal has the largest amplitude in this regime. This is referred to as the "absorption trough". Hereafter, T_S is always coupled to T_K through the Wouthuysen-Field effect.

At some time thereafter, heating from X-ray photons from galaxies and quasars becomes effective and starts heating the IGM. This leads to a rise in T_K and hence the magnitude of the differential $(T_S - T_{CMB})$ ceases to grow, causing the third turning point. As the heating continues the gas temperature crosses zero and goes above CMB temperature. $(T_S - T_{CMB})$ is positive in this regime and this is the first instance when the signal would be seen in emission. When $T_K >> T_{CMB}$, the $\left(\frac{T_S - T_{CMB}}{T_S}\right)$ term in Eq. 1.3 approaches unity. Thus the signal amplitude would only depend on $x_{\rm HI}$. This regime is one where the 21-cm signal experiences saturated heating and results in the fourth turning point. However,

if the X-ray sources are inefficient in heating the gas, the IGM temperature may not rise above that of the CMB and the signal may remain in absorption.

1.4.5.3 Cosmic Dawn to reionization

This is the last phase of the signal where the signal profile is primarily determined by the neutral hydrogen fraction, $x_{\rm HI}$, which dominates over the changing effect of fractional temperature differential $\left(\frac{T_S - T_{CMB}}{T_S}\right)$. The signal at this point starts diminishing due to the reduction in the neutral hydrogen fraction and reaches zero at the end of reionization resulting in the fifth turning point. In this period, for saturated heating scenario, there is an upper limit to the maximum positive amplitude reached by the signal. This is clear from Eq. 1.3 where the maximum amplitude of the signal is $8.5\sqrt{(1+z)}$ mK for $x_{\rm HI} = 1$.

In Fig. 1.7, we show the variation of spin temperature and its coupling to gas and CMB temperatures. In Fig. 1.8, we show variations in the global 21-cm signal in selected astrophysical scenarios.

1.5 Reconstructing Astrophysics from global 21-cm

Given the complex astrophysics that determines the spin temperature and global ionization fraction, it is obvious that the amplitude as well as the location of different features in the signal capture important processes in the CD/EoR epochs [54, 53]. While the timeline of different processes, e.g. onset of $Ly\alpha$ coupling or X-ray heating are relatively straightforward to derive from the redshift/frequency of the turning points, the nature of the sources themselves are non-trivial to infer from the signal.

There have been studies attempting the derivation of astrophysical properties from the global signal. E.g. the dark ages signature can be used to compute the background $Ly\alpha$ intensity [95], while the depth of the absorption trough is correlated with the ratio of $Ly\alpha$ intensity and X-ray heating rate [29] as shown in Fig. 1.9. The later part of the signal, towards reionization, traces the mean evolution of neutral hydrogen fraction. Further, it has information about X-ray and ionizing intensities of the sources [29].

It may be noted that it is relatively easier to deduce global properties of the IGM as compared to tracing them back to constrain the properties of the sources themselves. However, for a broadband measurement of the signal, it is possible to constrain parameters like minimum halo mass for star formation, evolution of normalization between bolometric luminosity in X-rays to the star formation rate at high redshifts, etc [96, 47].

1.5.1 Synergy between power spectrum and global 21-cm signal

The 21-cm power spectrum can be independently used to constrain source parameters from reionization. Studies have shown that features in the power spectrum, and the slope of the power spectrum

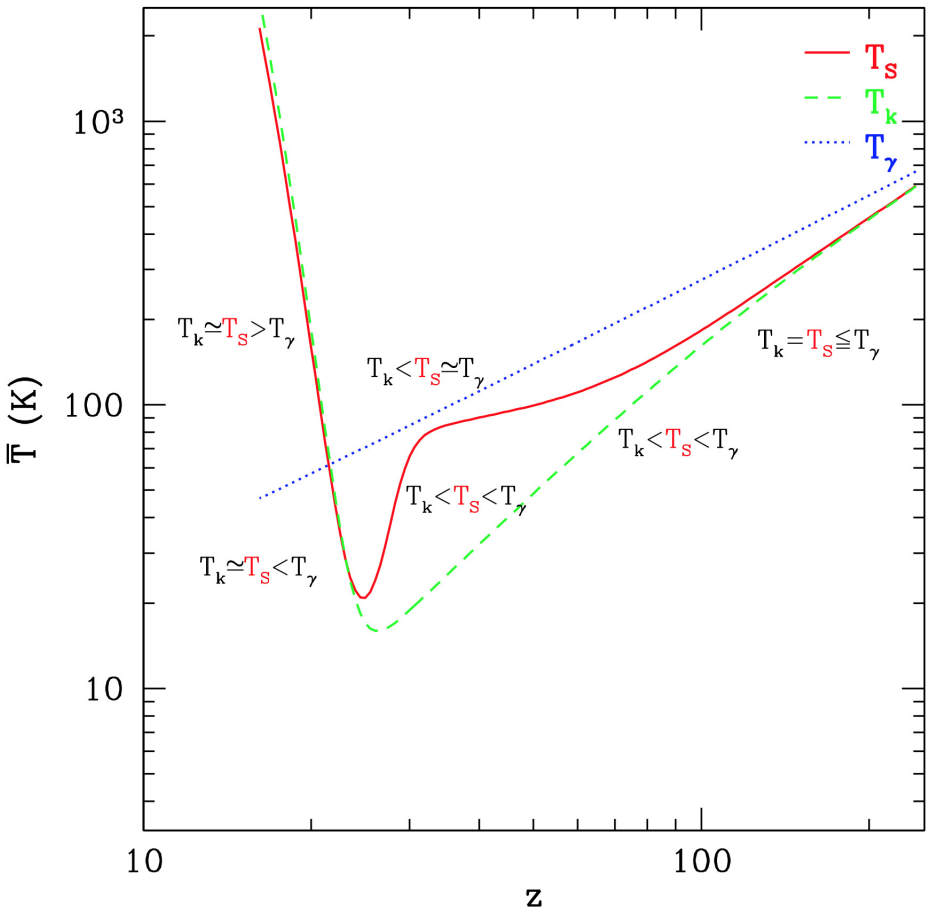

Figure 1.7: The evolution of CMB and gas temperatures over redshifts, along with the coupling of spin temperature to CMB and gas temperatures [91]. T_K is the gas or kinetic temperature, T_S denotes the spin temperature and T_γ represents background radiation field, T_{CMB}.

with respect to redshift, can constrain a variety of astrophysical parameters ranging from redshifts of $Ly\alpha$ and heating transition to determining the X-ray spectra of the sources and mean ionizing fraction of the IGM [28, 89, 99, 17].

However, since the two 21-cm probes, power spectrum and global signal, measure the fluctuations in the brightness temperature field and the absolute sky-averaged brightness temperature respectively, the two can be combined to present a complete picture of CD/EoR. While the fluctuations, measured as the power spectrum, quantifies the inhomogeneities in the temperature, the absolute global signal sets the mean level of the fluctuations thus providing information on whether the fluctuation is in absorption or emission [160]. Further, the global signal gives the zero spatial frequency component of the power spectrum. Thus, a complete information about the temperature field does require a

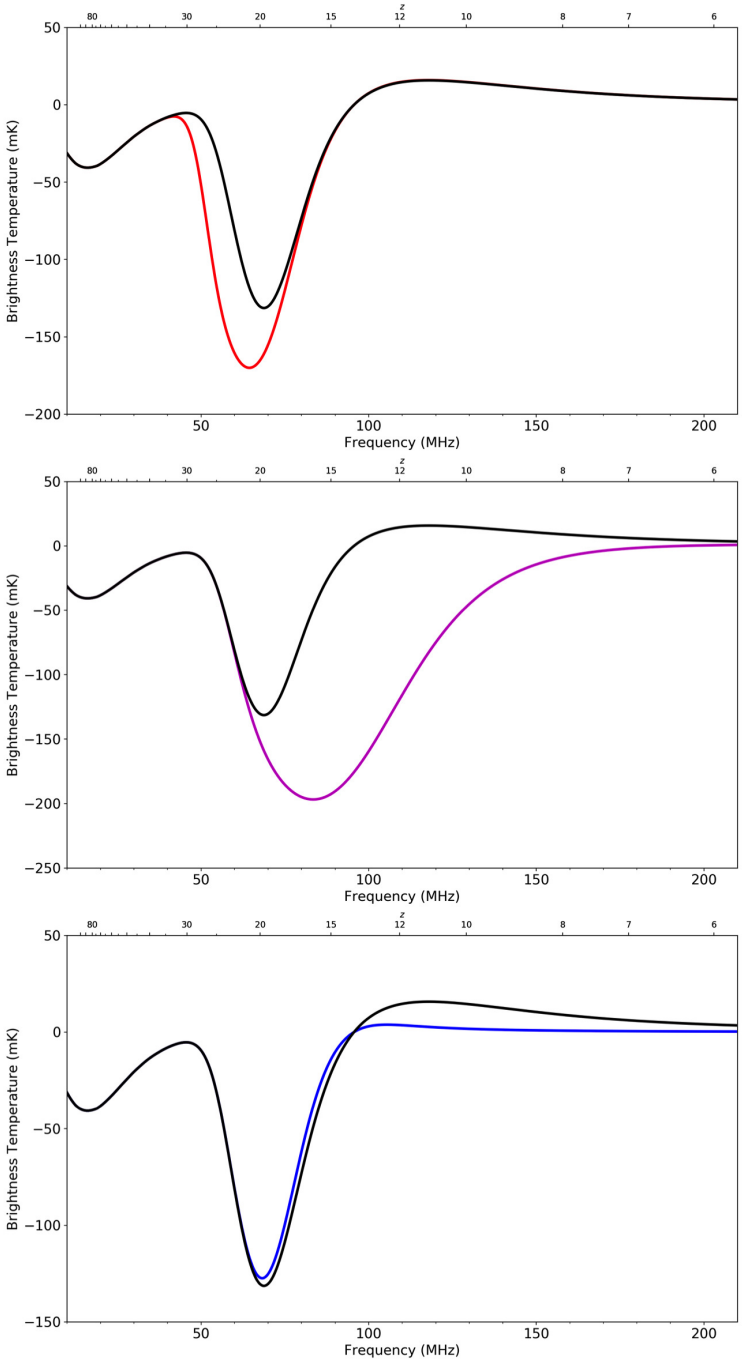

Figure 1.8: Global 21-cm signals representing the effect of $Ly\alpha$ coupling, heating and ionization on the signal profile. The turning points in the signal capture the onset of these physical processes. The signal in black is used as a reference to compare these effects. The top panel has different magnitudes of $Ly\alpha$ coupling; larger the coupling, earlier the signal starts getting more negative (red). The middle panel shows the effect of X-ray heating; weaker the heating, wider is the absorption trough (magenta). The bottom panel shows the effect of ionization; more are the ionizing photons, more rapid is the reionization (blue). All the signals were generated using the publicly available Accelerated Reionization Era Simulations (ARES) code.

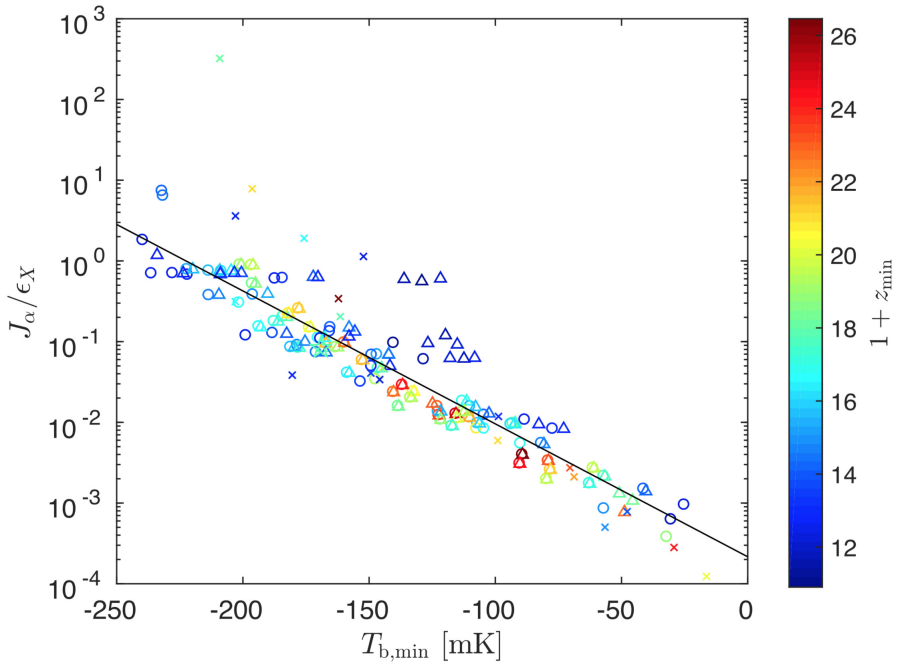

Figure 1.9: An example of deriving astrophysical properties from signal parameters. The x-axis is the amplitude of the absorption trough of the global 21-cm signal, y-axis represents the ratio of *Ly*α intensity and X-ray heating rate. A large amplitude would imply poor X-ray heating and early Wouthuysen-Field effect. Similarly, a small amplitude would point towards strong X-ray heating and late Wouthuysen-Field effect. The color indicates the redshift at which the minima of the absorption trough occurs. Different marker shapes indicate different values of the optical depth to reionization. Figure reproduced from Cohen et al. [29].

measurement of the mean reference level, provided by the global signal, and the fluctuations about it, provided by the power spectrum.

Measurement of the global 21-cm can potentially aid in the joint estimation of astrophysical parameters with the power spectrum. However, a broadband measurement of the signal is essential, spanning over CD and EoR, to add significance to the results [96, 77]. Independent parameter constraints from global 21-cm and power spectrum provide good cross validation. At the same time, the global signal, during EoR, can be employed to derive the ionization fraction and hence compute the optical depth to reionization, τ, with much better precision than Planck [80].

1.6 Experimental efforts

Given the potential in the global 21-cm signal of unraveling the astrophysics of CD/EoR epochs, there have been efforts worldwide to design experiments to detect the signal. Since the signal has

spectral signatures throughout dark ages, cosmic dawn and reionization, experiments are targeting different epochs and hence different frequency bands for the instruments. Currently, there are multiple experiments targeting the global signal as well as the power spectrum measurement. We list the experiments here along with the frequency range of their operation within which the data is being used to constrain CD/EoR.

For power spectrum measurements, there are several interferometric arrays that are planned/observing:

- Low-Frequency Array (LOFAR) [observing phase, 115-180 MHz]
- Murchison Widefield Array (MWA) [observing phase, 80-300 MHz]
- Hydrogen Epoch of Reionization Array (HERA) [commissioning phase, 50-250 MHz]
- Square Kilometer Array (SKA) [design phase, 70-300 MHz]

For global signal measurements, the experiments are listed below.

- Broadband Instrument for Global HydrOgen ReioNisation Signal (BIGHORNS) [70-200 MHz] [154]
- Experiment to Detect the Global EoR Signature (EDGES) [50-200 MHz] [18]
- Large Aperture Experiment to Detect the Dark Ages (LEDA) [40-85 MHz] [131]
- Shaped Antenna measurement of the background Radio Spectrum (SARAS) [40-200 MHz] [151]
- Sonda Cosmológica de las Islas para la Detección de Hidrógeno Neutro (SCI-HI) [40-130 MHz] [170]
- Dark Ages Radio Explorer (DARE) [proposed, 40-120 MHz] [21]

More about the global 21-cm experiments and their instrument designs is discussed in the next chapter, while the current status of the field in terms of the scientific results from these experiments is discussed in Chapter 5.

1.7 Challenges in the detection of global 21-cm signal

From an observational point of view, the challenge is to detect an extremely weak signature, with a maximum expected amplitude a few hundreds of mK, which is dominated by orders of magnitude higher contribution from other unwanted sources. These contaminants include foregrounds, ionospheric effects, radio frequency interference, and the instrumental systematics itself. We briefly describe each of these sources below.

1.7.1 Foregrounds

Foregrounds constitute the dominant component in the frequency range of the expected signal. It represents the contribution from the Galaxy as well as extragalactic sources. Foregrounds are dominated by synchrotron emission from the Galaxy. However, it has contribution from other radiative processes that include free-emission emission, thermal emission etc. [78]. Depending on the frequency and region of the sky, the foreground brightness can vary substantially; nevertheless, they largely have a power law variation across frequency. Fortunately, foregrounds have been shown to be highly correlated in frequency and have smooth spectral shape. They have been modeled by both parametric and non-parametric approaches [24].

Amongst parametric approaches, one method is to employ a physically motivated model that can solve for the required parameters; the modeled parameters may include power law indices for synchrotron radiation, electron temperature for thermal emission, low-frequency absorption turn-over for optically thick medium, etc. [144].

However, another approach is to take advantage of the fact that the foregrounds, in their totality, are smoothly varying functions of frequency. Thus, one can employ functions which have restricted degree of freedom, in that they can fit only to the smooth component of the data, thus ensuring the foreground removal. This can be implemented by low-order polynomials or classes of functions which have smoothness constraints inherent to their formalism [145, 62].

Another method is not to be restricted by spectra-only method, but also take advantage of spatial variations of the foregrounds. In such a case, different lines-of-sight are used to train spectral basis and spatial correlations are used to remove the foregrounds [163].

1.7.2 Ionosphere

The ionosphere can affect the incoming sky signal through refraction and absorption [4]. Both processes are dependent on the electron content in the ionosphere and are time-dependent [74].

Ionosphere has sub-divisions where different processes dominate. While refraction is dominant in the F-layer, lying 200-400 km from Earth's surface, absorption is dominant in the D-layer, lying 60-90 km above Earth's surface [76]. Since the electron density in the D layer is comparatively smaller, it does not contribute to refraction.

The refraction effect can contribute up to 1 K brightness at 85 MHz while the absorption in D-layer can contribute up to 6 K [166]. However, the spectral behavior of both the processes is smooth and tends to vary as ν^{-2}. Therefore, though ionosphere contributes order of magnitude higher power than the signal, its effect can be corrected or modeled. This argument was strengthened by Sokolowski et al. [155], where it was shown that the stochastic error introduced by the chromatic ionospheric

effects tends to zero on average and hence ionosphere should not be an impediment to ground based detection of the global 21-cm signal. However, Datta et al. [31] have pointed out that for experiments at low frequencies that target cosmic dawn and dark ages, ionospheric effects may be the limiting factor in the detection.

1.7.3 Radio Frequency Interference

The frequency range 40-200 MHz is strongly affected by Radio Frequency Interference (RFI). The band contains signals from FM transmitters, TV stations, airport communications, satellites, power-lines, to name a few [111, 112]. RFI can have a variety of spectral characteristics. It can be narrow band (FM, airport communication) or broadband (lightning, power transmission lines) [99]. Depending upon the transmission power and distance to the observation site, it can be strong and of the order of 10,000 K or could be extremely weak and of sub-Kelvin levels. Similarly, their temporal behavior is also varied; it can be transient and with a variety of timescales or be persistent throughout the observation period. The instrument itself, owing to the presence of digital systems and local oscillators, can be a source of RFI; however, proper electromagnetic shielding can suppress the radiation leakage to sub-mK levels [147].

Thus, in order to remove RFI, a thorough test for outliers is needed. Given the temporal and spectral variations of RFI, detection of outliers needs to be performed after smoothing to different frequency bandwidths and time intervals. This can be followed by thresholding methods that can detect outliers at the given time-frequency resolution [110].

1.7.4 Instrument

The instrument is arguably the most critical component in the detection of the global 21-cm signal. It can introduce spectral shapes which can be difficult to model or calibrate. It is to be emphasized here that the total contribution from the instrument might be small compared to foregrounds; however, the spectral shapes introduced by the instrument or the modulation of the foregrounds by the instrument transfer function are more likely to mimic the signal and hence confuse the detection [102, 14].

Different experiments across the globe have adopted different design philosophies for the instrument. The commonality between the approaches lies in an absolute control of spectral features introduced by the instrument, and ways to calibrate/correct/avoid them [79, 97]. The thermal noise levels required to detect most plausible theoretical signals is not the limiting factor. E.g. Sathyanarayana Rao et al. [145] has shown that even 10 minutes integration time is sufficient for an ideal system to reach noise levels so as to make a 95% confidence detection. However, the challenging aspect is to control the internal systematics which can give rise to spectral shapes that can potentially confuse the detection [150].

1.8 Plan of the thesis

The thesis focusses on the experiment SARAS 2 which aims to detect the global 21-cm signal from cosmic dawn and epoch of reionization. In Chapter 2, we lay down the design philosophy for the experiment, describe SARAS 2 system design and tests that evaluate performance. In Chapter 3, we discuss the SARAS 2 night sky observations and the data analysis methods. We then proceed to derive constraints on EoR with the SARAS 2 data. In Chapter 4, we discuss the possibility of using interferometers as an alternate method of detection of the global 21-cm signal. In Chapter 5, we conclude with the current status of scientific results from global 21-cm experiments and discuss pathways for future evolution of the SARAS system that might shed more light on cosmic dawn.

Chapter 2

SARAS 2: A Spectral Radiometer for probing Cosmic Dawn and the Epoch of Reionization through detection of the global 21-cm signal[†]

"New telescopes that push frontiers of technology come with surprises beyond the imagination of its designers and builders."

2.1 Introduction

Radiometers for precision measurement of the 21-cm signals require meticulous design and development. This is owing to the fact that the radiometer modifies the shape of the incident sky signal by a frequency response that manifests as both multiplicative gain and additive components. While the multiplicative gain can be solved for by employing various calibration strategies, additive signals, arising primarily due to multipath propagation of the signals in the system, are challenging to calibrate or model to mK accuracy. If not modeled adequately, the system response can confuse the detection of the signal through its own spurious and residual signatures.

Thus critical to the experiment is a stringent control on spectral signatures from the instrument. Various design and analysis strategies have been evoked to deal with a variety of system architectures [97, 154, 170, 131] and modeling of their response.

Shaped Antenna measurement of the background RAdio Spectrum (SARAS) is a radiometer which aims at detecting the global 21-cm signal from CD and subsequent EoR in the frequency

[†]Based on *Singh, S., Subrahmanyan, R., Shankar, N. U., et al. 2018, Experimental Astronomy, 45, 269*

range of 40 – 200 MHz; this chapter describes the development, architecture and performance tests of the SARAS 2 radiometer. It is a single element spectral radiometer that employs an antenna with a frequency independent beam and a noise source for calibrating the system. It provides a differential measurement between the antenna temperature and a reference load. A splitter is used to divide the signals from the antenna and noise source into two paths and the final spectrum is obtained by cross correlating the signals in these two paths. Further, this measurement is phase switched to cancel additive spurious signals in the system. The signal in the two paths are transmitted to a signal conditioning unit, placed 100 m from the antenna, over optical fibers thereby providing optical isolation. All subsystems are designed with the aim of making the different contributions – additive and multiplicative – to have smoothly varying functional forms that might not confuse with plausible forms of the global EoR signal.

In Sec. 2.2, we provide a brief overview of the SARAS 2 system. In Sec. 2.3-2.5, we discuss different sub-systems of the SARAS 2 system — the antenna, analog signal processor and the digital signal processor — and the underlying design considerations that led to their final adopted configuration. We also discuss the advantages and limitations of the present architecture based on laboratory and field measurements. We describe the custom built software developed to process the output of the radiometer in Sec. 2.6, which includes calibration and flagging, and discuss the rationale behind the algorithms used, most of which were custom developed for SARAS 2. In Sec. 2.7 we evaluate system performance using a set of terminations replacing the antenna. In Sec. 2.8, we compare the architecture of the SARAS 2 system with that of other ongoing experiments to detect the global 21-cm from CD and EoR; Sec. 2.9 presents a summary of the system design and its performance.

2.2 Motivation for SARAS 2

SARAS is a spectral radiometer that aims to detect redshifted 21-cm radiation from CD and EoR. The first version of the instrument, SARAS 1, consisted of a fat-dipole antenna above ferrite-tile absorbers, an analog receiver located at ground level just beneath the antenna, and a digital spectrometer unit 100 m away that measured sky spectra with 1024 frequency channels over the band 87.5–175 MHz [120]. Adopting a hierarchical modeling approach that jointly fits the foregrounds and internal systematics, the sky data was successfully fit with a root-mean-square (RMS) residual of 1.45 K. The maximum fractional systematic error in the modeling was 1.6%. The factors that limited the system from achieving higher sensitivity were Radio Frequency Interference (RFI), multipath propagation between the sky and antenna due to non-ideal absorbers covering the ground, and internal systematics that were dominated by reflections and multipath propagation of system noise within the receiver, which manifested as multi-cycle sinusoids in the spectral response. SARAS 1 provided an improved calibration for the 150 MHz all-sky map of Landecker & Wielebinski [122].

Taking constructive lessons from the SARAS 1 performance, the next version of the experiment, SARAS 2, was designed to have a stronger control over spectral features arising due to internal systematics and to be deployable in remote, radio-quiet sites. The primary consideration in system design was to have a system response, both additive and multiplicative, to be spectrally smooth so as to enable the separation of internal systematics and foregrounds from plausible 21-cm signals.

SARAS 2 described herein was designed to operate over the frequency band 40–200 MHz. The first sub-system in the radiometer is a spherical monopole antenna—consisting of a spherical element above a disc—that acts as the sensor of the electromagnetic field. Beneath the metallic disc of the antenna lies the receiver that splits and amplifies the signals from the antenna, reference and calibration noise source, generates linear combination of these signals and phase switches them before transmitting over optical fibers. 100 m away from the antenna is a signal conditioning unit that re-converts the optical signals back to radio frequency (RF) and filters out frequencies outside the band of interest. Finally, the signals enter a digital spectrometer that digitizes the signal, resolves the data into narrow spectral channels, and cross correlates them to produce the sky spectra. A pictorial representation of SARAS 2 is shown in Fig. 2.1 and a schematic of the entire system is shown in Fig. 2.2. The entire system runs on batteries and can be deployed at remote locations.

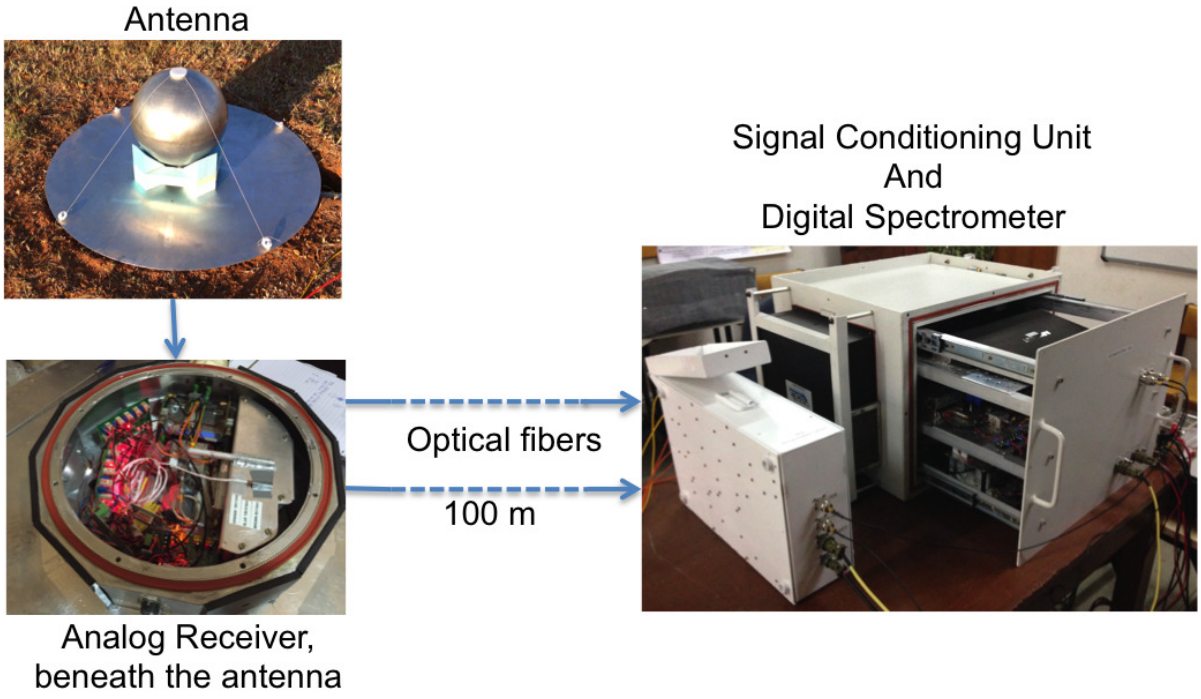

Figure 2.1: SARAS 2 pictorial representation.

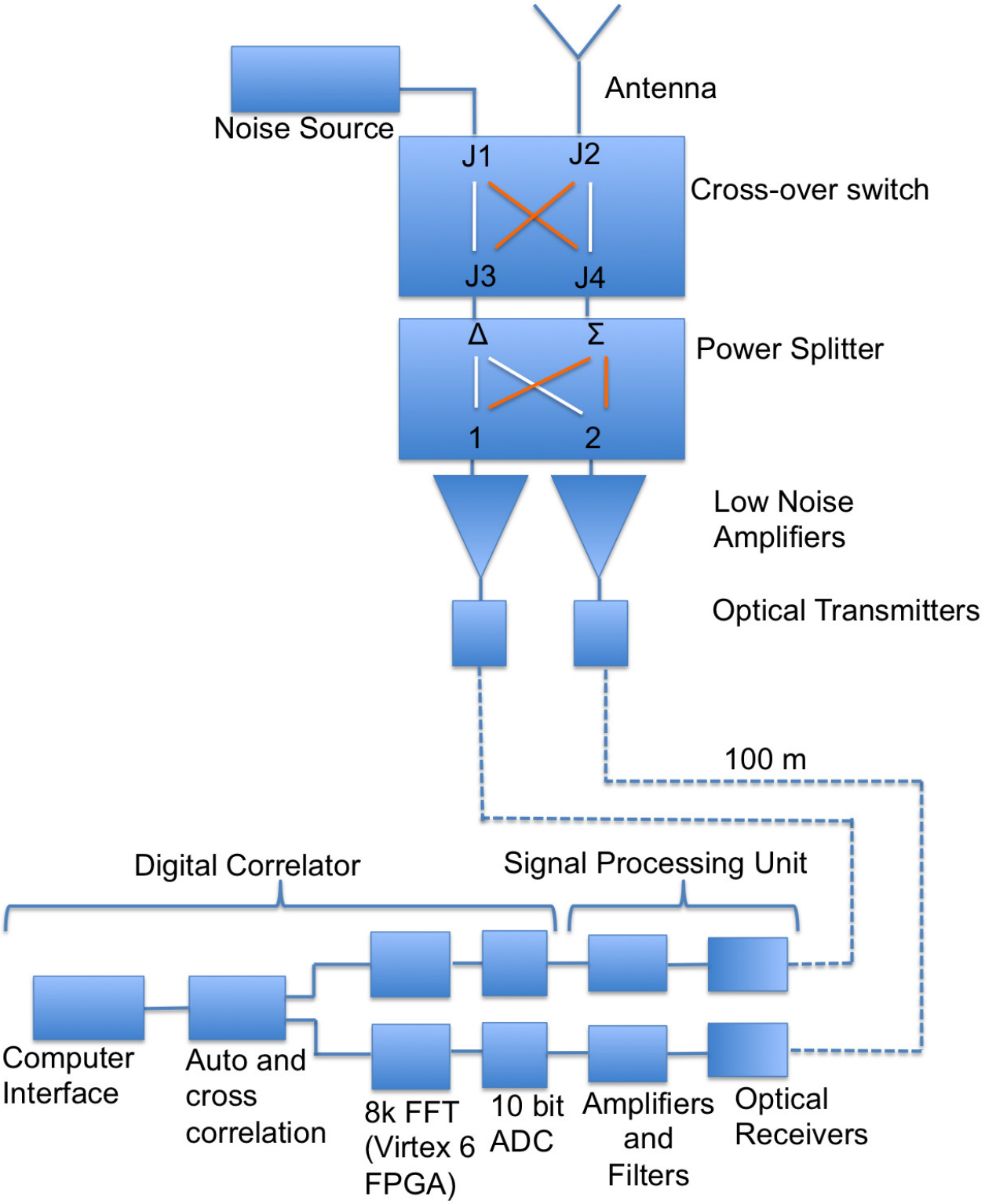

Figure 2.2: Schematic of the SARAS 2 receiver.

First, the total efficiency of the antenna is relatively poorer at lower frequencies. Second, modeling of internal systematics over the entire 40–200 MHz band to describe the frequency dependence of the system results in a large number of degrees of freedom for the model. However, over an octave bandwidth, where the antenna efficiency is relatively higher, the internal systematics may be modeled to the required accuracy by simply assuming many of these parameters to be constant over frequency. For these reasons, SARAS 2 is deemed to be useful for CD/EoR observations in the band 110–200 MHz and this paper presents test of system performance over this restricted band. Night sky measurements to date with SARAS 2 have been able to rule out reionization scenarios where the reionization is rapid and the first X-ray sources have very poor heating efficiency [151, 152].

There are other ongoing experiments for detection of the global 21-cm signal from CD and EoR. We list some below.

1. Experiment to Detect the Global EoR Signature (EDGES) [97]
2. Broadband Instrument for Global HydrOgen ReioNisation Signal (BIGHORNS) [154]
3. Sonda Cosmológica de las Islas para la Detección de Hidrógeno Neutro (SCI-HI) [170]
4. Large Aperture Experiment to Detect the Dark Ages (LEDA) [131]

SARAS, EDGES and BIGHORNS aim at detecting the signal from CD and EoR, where as SCI-HI and LEDA target the low frequency part of the signal corresponding to the expected deep absorption dip from CD. Considering radiometer designs, SARAS 2 uses a short monopole antenna with a frequency independent beam, other experiments employ wideband dipoles or log-spiral antennas that suffer from varying amounts of beam chromaticity. However, due to the choice of antenna, SARAS 2 suffers from low total efficiency as compared with other experiments. Further, the calibration strategy differs across experiments: SARAS 2 utilizes a crosscorrelation spectrometer, where the calibrator is connected to the system through a cross-over switch and power splitter. Other experiments are autocorrelation spectrometers that employ variants of Dicke switching to calibrate the system. The difference between the radiometers and the relative merits and demerits are discussed in detail in Sec. 2.8.

2.3 Antenna

2.3.1 General considerations for EoR experiments

The antenna is one of the critical sub-systems of the entire radiometer. Various antenna properties that affect the data, e.g. the beam pattern, the reflection, radiation and total efficiencies, all vary across the band and require considerable effort and care to measure them to the accuracies required to model

their effects on the data. Thus it is crucial to pay close attention to the design of the antenna and ensure that its characteristics do not limit the detection of the signal. We will discuss the key antenna properties in the following subsections; in particular how they affect the global EoR measurement.

2.3.1.1 Antenna Beam Power Pattern

We denote the sky brightness distribution, weighted by the antenna beam pattern, by $T_W(\nu,t)$; this is a function of frequency ν and for a radiometer pointed towards fixed azimuth and elevation, the spectrum varies with time t as the sky drifts overhead. It may be written as:

$$T_W(\nu,t) = \frac{\int_0^{2\pi}\int_0^{\pi} T_B(\theta,\phi,\nu,t)G(\theta,\phi,\nu)\sin\theta d\theta d\phi}{\int_0^{2\pi}\int_0^{\pi} G(\theta,\phi,\nu)\sin\theta d\theta d\phi}. \tag{2.1}$$

G is the antenna beam power pattern over azimuth, ϕ and elevation θ, and may be a function of frequency ν. T_B is the brightness temperature of the sky towards any azimuth and elevation, which varies over time as the sky drifts. The integral is over 4π steradian accounting for any beam spillover to the ground.

The dominant component of T_B is the Galactic and extra-galactic emission, which we refer to as foregrounds. It arises through various radiative processes and at the frequencies of interest here is dominated by the synchrotron mechanism. Its absolute contribution is about $3-5$ orders of magnitude larger than the predicted 21-cm signal: while the 21-cm signal is expected to be up to a few hundred mK, the foreground can range from a few hundreds to thousands of Kelvin over the band [150].

The foreground in the CD and EoR band has been shown to be a *maximally smooth* function [143], which implies that the foreground spectrum can be represented by polynomials that do not have zero crossings in second and higher order derivatives. Any reference to smoothness in this paper assumes this definition. The foregrounds may be fit to the accuracy needed for 21-cm CD/EoR detection using such polynomials, thus leaving more complex components, including a significant part of more complex EoR signals, as residuals [145].

It may be noted here that the 21-cm signal is also expected to have a smooth component which is inseparable from the foreground. Thus when a maximally smooth function is used to model and subtract the foreground, a part of the 21-cm signal is also inevitably erased. Further, since the total efficiency of the antenna may also result in that only a fraction of the sky signal couples into the receiver, we expect an additional loss in the signal. Thus, we have chosen to aim to design a system in which any additive spurious signals remain below about a mK, allowing for substantial signal loss due to these causes.

If the antenna beam pattern G is frequency dependent, then spatial structure in the foreground

would couple into the spectral domain and result in a non-smooth spectral response to structure in the continuum sky emission, which can be difficult to model to the accuracy needed for 21-cm signal detection. Thus, it is ideal to have an antenna beam pattern that is independent of frequency; in other words, the beam should be achromatic. However, if the beam is a single lobe, without sidelobes, and whose shape only varies smoothly with frequency, the resulting T_W might still be modeled as a maximally smooth function.

It is to be noted here that even though beam is achromatic, refractive effects from ionosphere can introduce chromaticity, which scales as ν^{-2} [4]. The change in the beam size is of the order of a few tens of arc minute over $40-200$ MHz [166]. Since the global 21-cm experiments generally employ antennas with wide beams of a few tens of degrees, the ionospheric refraction would introduce chromaticity at 1% level. However, refraction effect varying as ν^{-2} would only add a smoothly varying power law as a function of frequency [166] and hence the resulting spectrum would continue to be spectrally smooth.

2.3.1.2 Antenna Radiation and Reflection Efficiencies

Radiation Efficiency, denoted by $\eta_r(\nu)$, determines the fraction of beam-weighted sky power, T_W (Eq. 2.1), that couples into the antenna. Depending on the antenna design, $\eta_r(\nu)$ can vary with frequency. The power obtained after being modified by radiation efficiency, T_R, is given by

$$T_R(\nu) = \eta_r(\nu) T_W(\nu). \tag{2.2}$$

In addition, antennas have impedances that vary with frequency and are differently matched to the connecting transmission line across frequency. This is quantified as reflection coefficient. The voltage reflection coefficient of the antenna, Γ_c, determines how much of $T_R(\nu)$ couples to the system [139]. The power T_A that propagates along the transmission line connected to the antenna, which we refer to as the antenna temperature, is given by

$$T_A(\nu) = (1-|\Gamma_c(\nu)|^2) T_R(\nu), \tag{2.3}$$

where T_R is the power available at the antenna terminal [5, Chapter 2]. We term the coupling factor, $(1-|\Gamma_c|^2)$, as the reflection efficiency η_c. Any spectral signature present in Γ_c is clearly imprinted on the sky signal through the reflection efficiency. Therefore, the power or antenna temperature measured by the system in response to the sky brightness is:

$$T_A(\nu) = \eta_r(\nu)(1-|\Gamma_c(\nu)|^2) T_W(\nu). \tag{2.4}$$

The product $\eta_r(\nu)(1-|\Gamma_c(\nu)|^2)$ is termed as total efficiency η_t and hence

$$T_A(\nu) = \eta_t(\nu) T_W(\nu). \tag{2.5}$$

We require η_t to be spectrally maximally smooth in order to avoid any complex distortion arising from the multiplicative transfer function represented by the antenna. Further, as discussed below in Sec. 2.4.3.4, $|\Gamma_c|$ needs to also be spectrally maximally smooth to avoid additive spectral shapes arising from internal systematics.

2.3.1.3 Resistive loss

Antennas, like dipoles, are balanced sensors and often need to be connected to unbalanced transmission lines such as coaxial lines. Most such antenna designs use what is called a balun, or balanced to unbalanced transformer, to provide better match between the antenna impedance and that of the connecting transmission line and thus improve reflection efficiency. The balun also avoids radiation leakage and hence frequency-dependent beam distortions that may arise from unbalanced currents in the connecting cable.

The presence of any such balun almost always results in significant resistive losses that may be complex functions of frequency, particularly over the wide bandwidths needed for CD and EoR detection, and their multiplicative and additive effects on the signal cannot be characterized easily to the required accuracy. Similarly, any loading of antennas to adjust its resonant frequency also leads to resistive losses. All of these result in additive or multiplicative terms in Eq. 2.5 depending upon the origin of the resistive loss [5, Chapter 2]. Thus it is best to avoid antenna designs that might have significant resistive losses and also a balun.

2.3.2 Evolution to the SARAS 2 antenna

Given the considerations in Sec. 2.3.1, we now discuss a variety of classes of antennas that may be suitable for wideband EoR experiments and present here the arguments that led to the adoption of the SARAS 2 antenna configuration.

To avoid coupling of sky spatial structure to spectral domain, we consider the class of frequency independent antennas. These are generally based on self-scaling behavior. If the physical dimensions of the antenna are scaled, then its properties do not change if the operating frequency also scales by the same factor. It has been shown that if the shape of the antenna could be specified entirely by angles, its performance would be frequency independent [140].

Wideband spiral antennas are an example of this class. However, even if the structural bandwidth well exceeds the operating band, the inevitable truncation of structure at both top and bottom causes reflection of currents, leading to frequency dependence in the beam pattern. Further, if the arms of the

spiral are not electrically balanced, the beam would have a squint that rotates with frequency, which would introduce spectral ripples in response to sky structure. Spiral antennas are sensitive to circular polarization.

Linear log-periodic dipoles are the corresponding frequency-independent antennas for linear polarization. They are not strictly frequency independent since their properties in terms of beam pattern and impedance have a periodicity that depends on the logarithm of frequency. This periodicity across the band can result in additional frequency dependent structures in the spectrum, particularly for wide bandwidths that are critical for CD/EoR global signal detection.

Another argument against the above categories is that wideband spirals and log-periodic dipoles are electrically large and hence their reflection efficiency will be a complex function of frequency.

Sidelobes, chromatic beams as well as complex reflection efficiencies may be avoided by using electrically small antennas whose physical dimensions are much smaller than the minimum wavelength of operation. However electrically small antennas are difficult to match to a load due to their low input resistance and high reactance as we move away from its resonance. This results in a low efficiency for short antennas. There is thus a compromise between efficiency and frequency independent performance. An approach is to accept a lower efficiency at long wavelengths since the sky is very bright at long wavelengths and it is adequate to have an efficiency which ensures that sky signal dominates the system temperature.

A short dipole antenna appears to be an attractive choice for CD/EoR detection. However, one of the major concerns of employing dipoles is the use of baluns as discussed in Sec. 2.3.1.3, which leads to a frequency dependent resistive loss that is difficult to characterize. Further, the configuration in which the antenna is used can affect its achromaticity. For example, if the dipole is mounted a certain distance above a conducting plane, there would be multipath propagation of radiation from any sky direction to the dipole - one direct path and a second reflected off the plane. The relative phase would be frequency dependent and hence the beam pattern of the dipole above a reflecting plane would be frequency dependent. A way to avoid this may be to use absorbers below the antenna to suppress the reflected component. Assuming a sky brightness of a few hundred Kelvin, the absorbers would require to have a power reflection coefficient less than -100 dB over the whole band in order to keep any frequency structure in the spectral response below about 1 mK. Absorbers with such specification over 40-200 MHz, implying a bandwidth of 5:1, are impossible with present technology as far as we know. Additionally, any non-smooth frequency characteristics of the absorber would lead to a non-trivial frequency dependent bandshape for the antenna transfer function.

Short monopole antennas are suitable candidate antennas for CD and EoR detection since they do not require baluns, and beam chromaticity due to multipath propagation can be avoided since there is no physical distance between antenna and ground, the latter being part of the antenna. With the

absence of a balun or impedance transformer, we do compromise on the antenna efficiency; however, this is the trade off that may be accepted in order to gain a maximally smooth antenna reflection efficiency and reflection coefficient $|\Gamma_c|$.

The shape of the monopole radiating element also plays a crucial role in determining the spectral shape of reflection efficiency. Any sharp edges or truncation of the structures, like in a discone antenna [159, Chapter 7], will lead to reflection of currents that may interfere to produce complex frequency structure in the impedance characteristics.

We thus choose a sphere-disc type of monopole antenna as the base for the design for SARAS 2, since such an antenna type may be described by a minimum number of parameters. The SARAS 2 antenna consists of two primary elements: a circular aluminium conducting disc on the ground and above that is a sphere that smoothly transforms into a truncated inverted cone as shown in Fig. 3.19. The receiver electronics are mounted beneath the metallic disc, and the vertical coaxial cable connected to the receiver has a central conductor that directly connects to the vertex of the inverted cone and an outer conductor that connects to the disc.

The present antenna design is completely described by six parameters:

1. Radius of the metallic disc
2. Radius of the sphere
3. Radius of the excitation wire
4. Gap at the feeding section
5. Radius of the cone
6. Height of the cone

Simulations show that the radius of the sphere was the primary determinant of the location of resonant frequency. The radius of the metallic disc decides the Q factor, which determines the depth and width of the resonance dip around the resonant frequency. Together they define the reflection efficiency and also its smoothness at frequencies less than the resonance, where the entire operating band lies. The reflection efficiency is also significantly affected by the height of the gap at the feeding section and the radius of the excitation wire. The antenna beam pattern and radiation efficiency are strongly dependent on the dimensions of the disc and sphere.

The optimization of the geometry was carried out through iterative variation of parameters and examining EM performance using the WIPL-D electromagnetic simulation software. Given the requirements of the antenna properties, we varied one parameter at a time and iterated to arrive at the

final configuration. This was later tested and fine-tuned based on field measurements. The simulations and field measurements were carried out for ground conditions with low values of dielectric constant and conductivity.

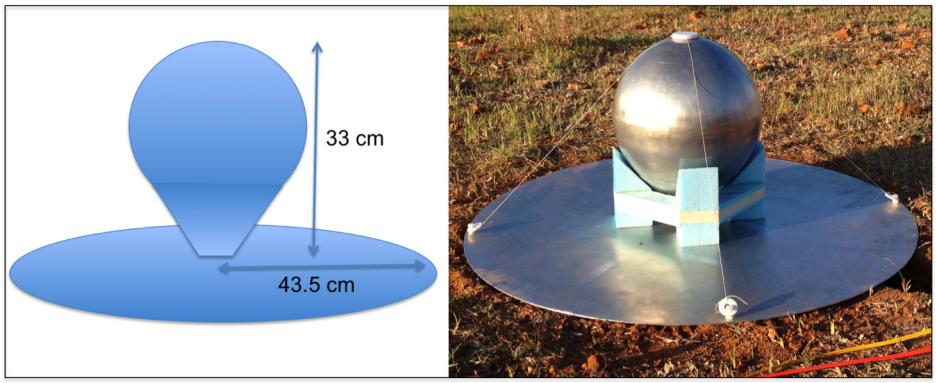

Figure 2.3: SARAS 2 antenna

The height of the spherical radiating element of the antenna was optimized to be 33 cm, and the radius of the disc to be 43.5 cm. The optimization aimed at keeping the resonant frequency outside the band, the reflection efficiency maximally smooth and the beam patterns frequency independent, while also striving to maximize the reflection efficiency at low frequencies. The optimization makes the height of the monopole element less than $\lambda/4$ at the highest frequency, making it electrically short at all operating frequencies. These aspects are discussed further below.

2.3.2.1 Beam Pattern of the SARAS 2 antenna

Field measurements of the radiation pattern were made across the band, and these were compared to those derived from electromagnetic simulations of the antenna.

A half-wave dipole was used as the transmitter for the measurement; this was separately tuned for measurements at different frequencies. It was clamped 8 m above the ground to minimize interactions with the ground, particularly at low frequencies where the wavelength is a few meters. The dipole antenna was kept stationary and the SARAS 2 antenna was moved horizontally over the ground through a set of distances to measure the beam versus elevation angle. The SARAS 2 antenna was used as the receiving element and the power received, after corrections using the Friis equation [5, Chapter 2], was used to compute the beam pattern at different frequencies. The measurement setup is shown in Fig. 2.4 while the simulated and measured beam patterns at different frequencies are shown in Fig. 3.14.

The beam has a maximum response at 30° elevation from horizon and gradually decreases to zero towards horizon and zenith. The beam has a non-directional response along azimuth and a directional

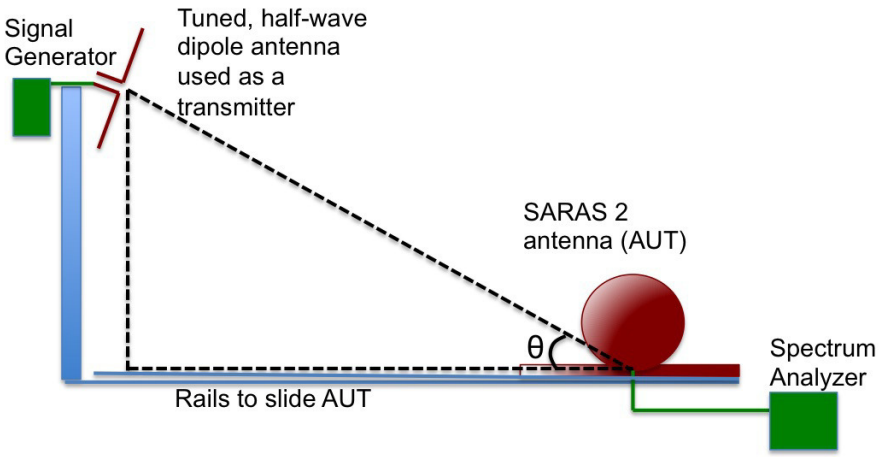

Figure 2.4: The setup for measuring the relative power pattern of the SARAS 2 antenna at different elevation angles θ. AUT refers to Antenna Under Test.

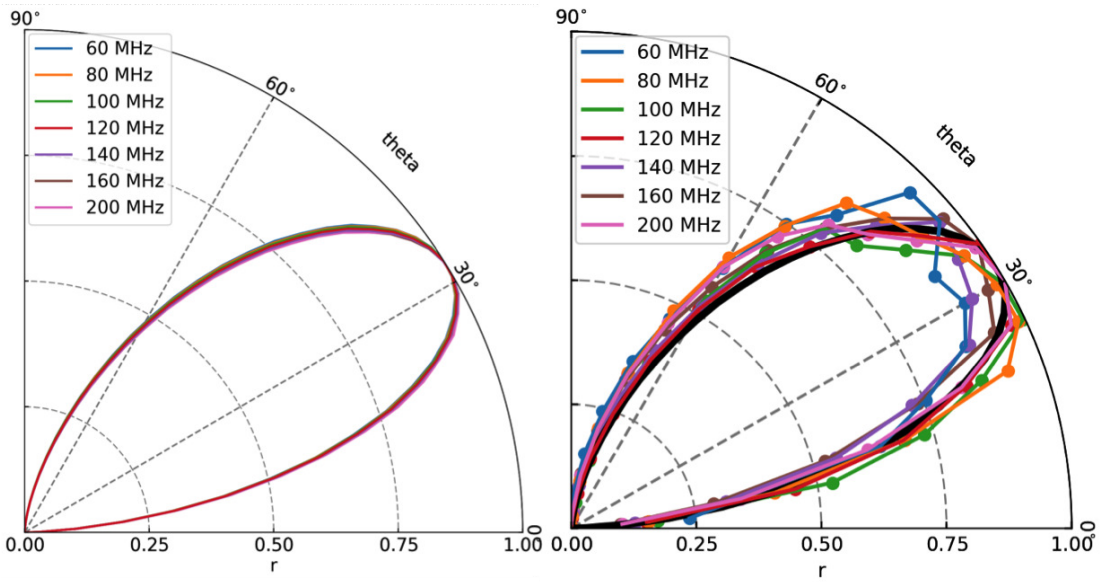

Figure 2.5: The left panel shows the beam pattern at different frequencies as obtained from electromagnetic simulations. The right panel shows the measured beam pattern, which have measurement accuracy of about 10%, together with the mean of the simulations shown overlaid as a solid black line.

pattern along elevation with a half-power beam width of 45°.

The EM simulations indicate a smooth variation of half-power beam width across 40 – 200 MHz, of the order of ~ 2 arc minutes. This is comparable to the chromaticity introduced by ionospheric refraction.

2.3.2.2 Reflection Efficiency

As a primary consideration, antennas with smoothly varying reflection efficiency, and also maximally smooth $|\Gamma_c|$, are preferable. For this reason, we avoid any resonance in the band since that would result in a sharp variation of $|\Gamma_c|$ in the frequency domain at the resonant frequency. The resonant frequency depends on the dimensions of the sphere and that of the metallic disc below. We have made field measurements of the reflection coefficient with different radii for the metallic disc. As shown in Fig. 2.6, the shorter the radius of the disc, the higher is the resonant frequency, and this is favorable in terms of spectral smoothness since the rate of variation of the reflection coefficient in the band would be slower. However, very small dimensions of the disc would lead to reduction in radiation efficiency.

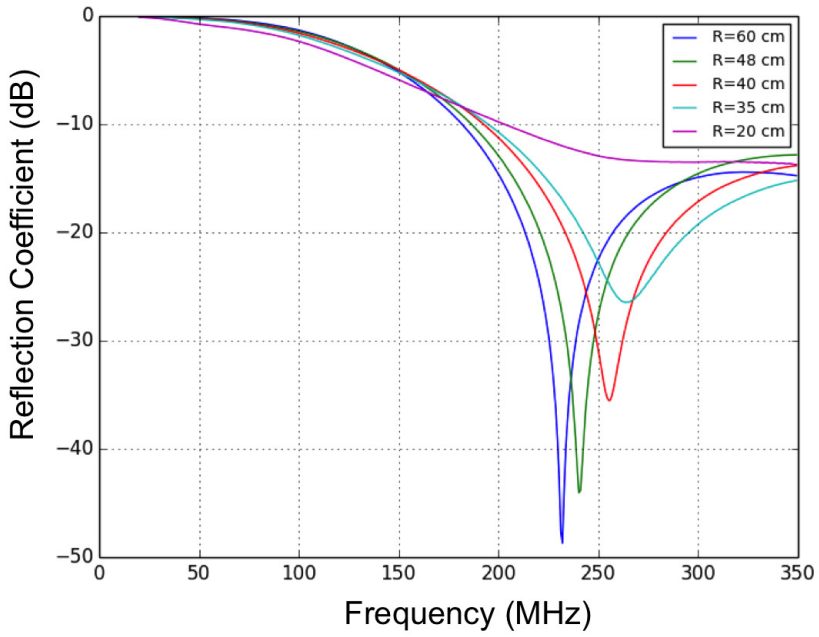

Figure 2.6: Reflection Coefficient versus frequency measured for different disc radii. The height of the radiating element (cone+sphere) from the disc was fixed at 33 cm while the gap at feeding section was kept at 1.3 mm.

We chose the the radius of the disc of the SARAS 2 antenna to be a compromise between sensitivity and spectral smoothness. The disc has radial extent of 0.435 m; thus the antenna operates

well within the first resonance, which lies at 260 MHz. The reflection of currents from the edge of the disc, for the chosen radial extent, can only result in about a half of a sinusoidal ripple in the 40–200 MHz band rendering $|\Gamma_c|$, and hence the reflection efficiency, to be spectrally smooth. This is also confirmed by the measurements as discussed below.

An alternative approach is to separately measure $|\Gamma_c|$, perhaps *in situ*, and use it to model the data. However, that requires a high accuracy measurement, close to 1 part in 10^4, for controlling the systematics to be below a mK (the rationale for this specification is explained below in Sec. 2.4.3.4). Measurement at this accuracy is challenging as the components in the measurement setup itself; *e.g.*, any interconnecting cable between the measuring instrument and antenna, may introduce a spurious shape in the reflection coefficient measurement that is not intrinsic to the antenna. Though such cables may be calibrated as part of measurement process, a change in their warp or a small change in impedance due to temperature change or even switching of connectors to make this measurement may render the calibration solution for the measurement inaccurate.

We made a measurement of the reflection coefficient of the SARAS 2 antenna with extreme care using a rugged field spectrum analyzer, which was placed underground just beneath the antenna and directly connected to the antenna without cables. The calibration setup and measurement was remotely operated to keep the antenna environment stable during the measurement process. Fig. 3.22 shows the measured reflection coefficient, the reflection coefficient expected from electromagnetic simulation, as well as a maximally smooth function fit to the measurement. The fit residuals show no structure above the measurement noise that is about 10^{-4}. Thus $|\Gamma_c|$ has no spectral features to the measured level of accuracy and we discuss below in Sec. 2.4.3.4 the implications for the level of receiver systematics given this upper limit on departures from smoothness in $|\Gamma_c|$.

Based on the considerations discussed above and also the results of the field measurement, we have adopted an approach in which the measurement data is modeled based on assuming a maximally smooth functional form, with free parameters, for $|\Gamma_c|$ and hence η_t.

2.3.2.3 Radiation and Total Efficiency

The antenna radiation efficiency can be measured via various methods, e.g. Wheeler Cap, radiometric, directivity/gain method, using waveguides etc. [67]. Existing methods of efficiency measurement, as described in [128], have large errors. Some methods require precisely controlled environmental conditions and anechoic chambers to carry out the measurements and can be time consuming. It is extremely difficult to adopt these methods for the field measurement of $\eta_r(\nu)$ at the accuracy required for the current experiment, which is 1 part in 10^5. For that reason, we have developed a new method for measuring the total efficiency using the spectral measurements of sky brightness acquired for CD and EoR detection.

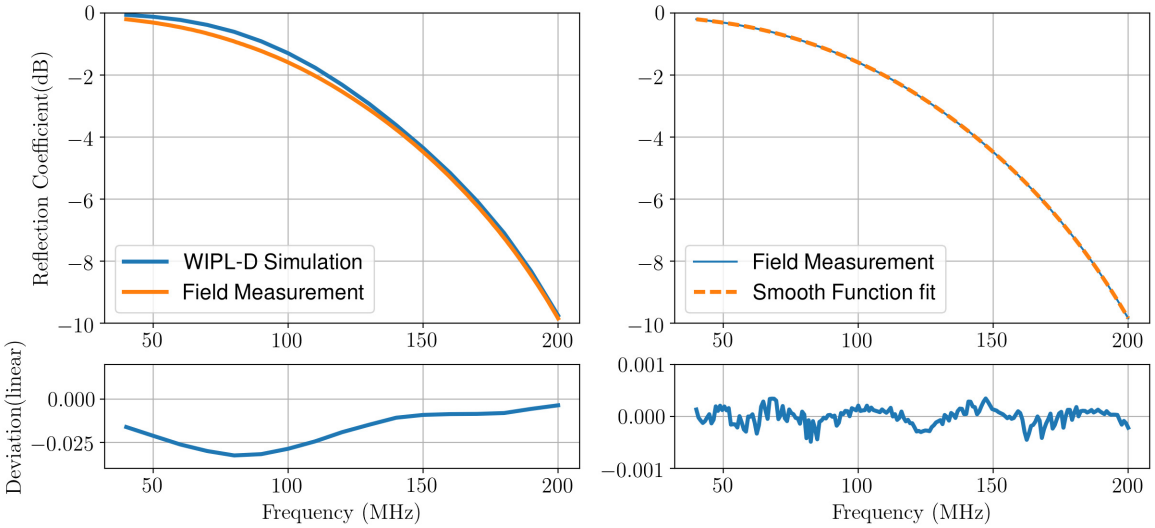

Figure 2.7: The panel on the top left shows the measured reflection coefficient for the SARAS 2 antenna overlaid with that from the electromagnetic simulations. The panel on the top right shows the maximally smooth function fit to the measured reflection coefficient. The lower panels show the deviations in linear units. The maximum deviation between simulations and measurements is 3%, while the maximum deviation between maximally smooth fit and measurements is 0.02%.

We adopt the Global MOdel for the radio Sky Spectrum (GMOSS) [144] as a representation for the sky brightness distribution and compare the absolute sky brightness with measurements made by the spectrometer. The ratio of absolute sky brightness to the foreground estimated from the measurement gives the total efficiency versus frequency. Details of the method are presented in Sec. 3.4. Here, in Fig. 2.8, we present this measured total efficiency.

The total efficiency varies monotonically with frequency consistent with a maximally smooth transfer function for the transformation from the sky spectrum to the measurement data. However, the actual magnitude of the efficiency does indeed decrease fairly sharply to a few per cent at low frequencies. Therefore, as mentioned above, we have restricted the analysis of SARAS 2 data to above 110 MHz, marking the upper end of FM band.

2.4 Analog Signal Processing

The beam-weighted sky signal is coupled into the system with a multiplicative gain, η_t, that is the total efficiency of the antenna. Additionally, the signal further undergoes a multiplicative gain, which we refer to as bandpass, arising from the gains of the devices in the receiver after antenna. The receiver, which follows the antenna in the signal path, is designed with the following considerations:

- The receiver requires a calibration scheme by which the bandpass, which is a multiplicative

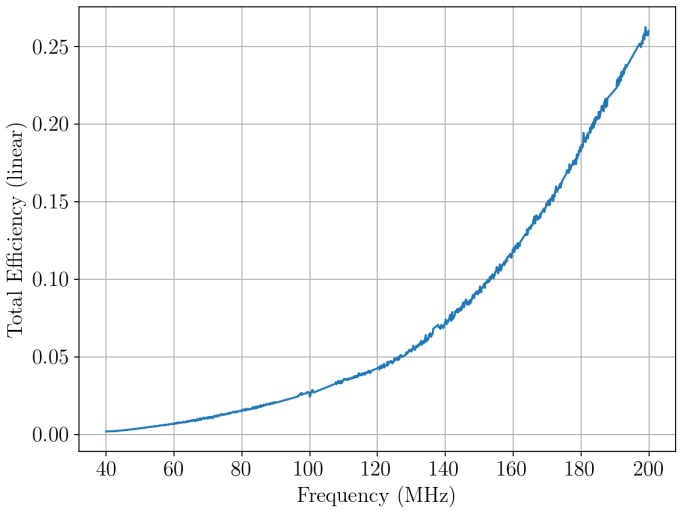

Figure 2.8: Total efficiency versus frequency as derived using the GMOSS model and SARAS 2 measurement data taken during a night.

gain factor for the measurement data, may be flattened.

- Unwanted additive spurious signals, contributed by the receiver, need cancellation or a method by which they do not confuse any CD/EoR detection.

- The receiver chain is designed to distribute the gains and the resulting power levels along the signal path to maintain linearity and low levels of intermodulation products.

2.4.1 Calibration considerations

The antenna signal entering the receiver is modified by the receiver gain. The spectral behavior of system gain is the cumulative product of individual gains of all the modules that the signal passes through. We term the process of correcting the measurement data for frequency dependent multiplicative gain and hence flattening the instrument spectral response as bandpass calibration. At the same time, the arbitrary counts in which measurement data is acquired need to be scaled to be in units of Kelvin of antenna temperature. This is termed as absolute calibration. It is more critical for a global CD/EoR experiment to attain a high precision for bandpass calibration—so that residual errors are within about a mK—compared to getting the absolute temperature scale right. This is so since the latter is simply a scaling factor to the data while an erroneous bandpass calibration can potentially distort the shape of the spectrum. This is a major consideration for the receiver design.

Bandpass calibration, along with calibration for η_t, can be achieved via various means. One way is to have a spectrally flat, broadband signal external to the antenna that traverses the same path as

that of the sky signal. It would then be able to remove the frequency structure imposed by η_t as well as by the system bandpass, given its intrinsic spectral flatness. Such a calibration signal is required to be externally generated by a transmitting system. The difficulty with such an approach is that the problem of bandpass and η_t calibration is not actually solved but simply transferred to the transmitting system!

An alternative approach to generating an external flat-band signal is to deploy a pulse calibration scheme [121]. The method involves generating short duration pulses, with time domain width substantially smaller than the inverse of bandwidth of the receiver, and using the measurement data to compute and correct the bandpass and η_t. The disadvantage of this approach is that in order to attain adequate signal-to-noise for the calibration, the short duration pulses are required to be of high amplitude, which requires a high dynamic range receiver.

The external calibrator source could be an astronomical source like Cas A, the Moon, etc. [150]. Astronomical sources for calibration are routinely used in interferometer measurements [125]. Although astronomical continuum sources may have spectrally smooth emission over the bands of interest here, the spectrum of the Moon may be corrupted by reflected Earthshine, particularly in the FM band [167]. The primary argument against using astronomical sources for CD/EoR radiometer calibration is that the antennas used for such experiments have a small effective collecting area, and even the brightest of point sources would contribute only a few Kelvin in antenna temperature for this class of antennas. Consider, for example, Cas A, which is one of the brightest point sources in the long wavelength radio sky. Its flux at 150 MHz is ~ 8.5 kJy [3, 64]. The antenna temperature due to a point source in the sky is given by [30]:

$$T_A = \frac{A_e S}{2k}, \tag{2.6}$$

where A_e is the effective collecting area of the antenna, S is the flux of the source and k is the Boltzmann constant. The effective area of a monopole antenna at this frequency would be close to 1 m^2 [172]. We infer that even for an extremely strong celestial source like Cas A, T_A is ~ 3 K. Thus, compact strong celestial sources are not suitable candidates for calibration, since the temperature increment when the source comes into the beam would be significantly smaller than the system temperature, which is usually at least a few hundreds of Kelvin.

A more attractive solution to the calibration problem for CD/EoR radiometers is the use of a broadband noise source internal to the system, where there is a better control over the spectral flatness of the signal injected into the signal path. Internal calibration sources may also be switched with small duty cycles and so the calibration may be performed in shorter time intervals thus accounting for shorter period temporal variations in the bandpass. However, since the calibration signal is injected

into the signal path after the sky signal has been coupled into the system through the antenna, the characteristics introduced by the antenna, η_t, cannot be removed by such calibration and hence need to be modeled separately.

Further, there are choices for the way the calibration signal is coupled into the signal path. A widely used scheme is Dicke switching [33] where a switch is used to swap the receiver input between the antenna and the noise source. The spectra obtained in the two switch positions are subtracted to derive a gain solution which is applied to the data [139]. However, the receiver noise related additive signals appearing in the measurement data in the two switch positions may differ due to different impedance characteristics of the antenna and the noise source. Thus the subtraction of the two spectra would create another frequency structure in the calibration solution that can be difficult to model. An alternative strategy is to have a method in which the antenna and noise source are both always connected to the system, and the noise power level of the calibration source is switched between high and low states, so that the nature of internal systematics does not alter in the process of calibration. We explore this approach further in Sec. 2.4.3 below, where we describe the SARAS 2 receiver architecture.

Maintaining linearity in the signal path is important for any of the above calibration schemes to work. As mentioned above, this requires that while power levels are maintained to be considerably above the noise floor of the system so that there is no degradation of signal-to-noise ratio along the signal path, at the same time sufficient headroom is maintained between the operating power and saturation limits.

2.4.2 Considerations related to additive signals from receiver noise

Another parameter which plays an important role in deciding the architecture of the analog receiver is the spectral behavior of the additive signals arising as a result of multi-path propagation of noise from the Low-Noise Amplifiers (LNAs), which propagates in forward and reverse directions. Since the antenna and LNA impedances are not perfectly matched along with their interconnect, a part of the noise from the LNA that travels towards the antenna is reflected back. Interference between this reflected component and the forward propagating receiver noise results in a systematic additive signal in the measurement data [92]. This multi-path propagation of receiver noise voltages and their addition results in a sinusoidal variation for the systematic additive signals versus frequency, which is also modulated by the spectral shape in $|\Gamma_c|$. The period of the sinusoid is governed by the phase difference between the interfering components and hence on the length of the system between the impedance mismatches on the two sides of the LNA. The amplitude of the response depends on absolute value of $|\Gamma_c|$, noise figure of LNAs and the magnitude of correlation between the forward and back-propagating components of LNA noise.

Table 2.1: States of the system

State	Noise Source	Switch Position
OBS0	OFF	0
CAL0	ON	0
OBS1	OFF	1
CAL1	ON	1

Thus, an important criterion in receiver design is to minimize the amplitude and shape the spectral behavior of this additive receiver response to be maximally smooth. It gains importance due to the fact that this internal receiver related component in the measurement data is an additive signal and is often not calibratable. Various system design considerations can make this receiver additive signal spectrally smooth. First, the electrical length of the analog receiver chain can be made so short that the period of the sinusoid is significantly larger than the band of operation. This would ensure that only part of a cycle of the sinusoid appears in the full band and hence appears smooth. Second, as discussed below in Sec. 2.4.3.4, maintaining $|\Gamma_c|$ to be spectrally maximally smooth is an additional way to keep this component devoid of complex spectral features. The amplitude of this additive signal can be further reduced by using LNAs with low noise figure, by making the antenna impedance better matched to that of receiver and thereby lowering the value of $|\Gamma_c|$, and by selecting LNA designs that reduce the correlation between the forward and reverse traveling LNA noise components.

2.4.3 The SARAS 2 receiver

The SARAS 2 receiver uses an internal noise source for generating the calibration signal which is connected to a four-port cross-over switch as shown in Fig. 2.2. When the noise source is in OFF state, this device serves as a reference for the measurement of the sky signal. The antenna is connected to the other input of the switch. The outputs of the switch go to a power splitter module that provides the sum and difference of the two inputs to two paths of the receiver chain. Hereinafter we refer to the two analog signal paths beyond the power splitter as the two arms of the analog receiver. The switch swaps the antenna and reference/calibration signals between the two ports of the power splitter, so that the receiver arm picking up the difference signal alternatingly gets sky minus reference and reference minus sky. For each position of the switch, the noise source is switched on and off with a cadence of about one second. SARAS 2 thus cycles over four system *states* as shown in Table 2.1.

The analog receiver is powered by a Li-Ion battery pack that is mounted with the receiver, in a metallic enclosure, beneath the metallic disc of the antenna. By this we avoid any conductive power lines running external to the antenna, which may result in unwanted coupling between the electromagnetic field in the neighborhood of the antenna and the signal path within the receiver.

Further, such an arrangement is essential to be able to deploy the antenna in remote locations where external power is not available.

2.4.3.1 Signal Flow

We refer to the signal that is coupled to the receiver via the antenna as T_A. We denote the components of the measurement data arising from the noise source in ON and OFF states as $T_{\rm CAL}$ and $T_{\rm REF}$ respectively. $T_{\rm REF}$ is the power from a reference termination—a well matched accurate 50 Ω termination—that will correspond to a noise temperature of value of the ambient temperature, which is approximately $\sim$ 300 K. The two signals, from the antenna and from the reference/calibration, are inputs to the cross-over switch, as shown in Fig. 2.2. When the switch is in position "0", the signal at the input port J1 of the cross-over switch is channeled to output J3. Similarly the signal at input J2 appears at output J4. In position "1" of the switch, the paths are crossed implying that the signal at J1 goes to J4 while that at J2 appears at J3. The two switch positions are denoted in two colors in Fig. 2.2.

The pair of signals are then fed to the pair of input ports of a power splitter—the sum port Σ and difference port Δ—depending on the switch state. The signals undergo a voltage attenuation (g) while passing through the splitter. The signal at the Σ port appears at both outputs of the splitter in phase while the signal at the Δ port appears at the two outputs with a phase difference of 180°.

The signals are transmitted from the receiver to the signal processing unit by RF over fiber: as analog signals modulating the intensity of laser light. Demodulation of the optical signal at the signal processing unit gives back the RF signal. This unit, along with the following digital correlator, are placed about 100 m away from the antenna in an electromagnetically shielded environment to avoid any electromagnetic interference being picked up by the antenna.

The signals in the entire band are low-pass filtered at the signal processing unit such that frequencies above 230 MHz are filtered out. It may be noted here that the amplifiers, attenuators and indeed all components used in the two arms within the signal processing unit do not contribute to any additive signal in the final measurement data, because the arms are optically isolated from each other and hence signals from one arm do not couple to the other. The signals in the pair of receiver arms finally enter the digital spectrometer where they are digitized, Fourier transformed and cross-correlated to produce the measurement data.

The digital stage is shielded by a number of separate methods including gaskets, matching grooves cut into the door and frame, adopting heat pipe based cooling systems etc. The shielding ensures that 100 m away from the digital spectrometer, where the antenna is deployed, any self-generated RFI from the spectrometer is below mK level.

In the SARAS 2 receiver, the sky power, after being modified by the total efficiency, is $\sim$ 300 K

which corresponds to a power of ~ -90 dBm in the band of $40-200$ MHz. The gain at each stage within the receiver arm is chosen such that all devices operate well below saturation and continue to be in linear regime of operation. This criterion becomes more stringent farther in the signal path where power levels progressively increase with each amplifier stage. The gains in the system have been adjusted such that the input power at the last amplifier of the signal processing unit is -52 dBm. This amplifier is chosen to have a 1 dB compression point at +22 dBm; therefore the operating level even at this most critical stage is about 74 dB below saturation.

2.4.3.2 Bandpass Calibration

We now write expressions for the power measured, in temperature units, in different states of the system. Since SARAS 2 is a correlation spectrometer, the mathematical operations performed here are complex operations. The subscripts OBS0, CAL0, OBS1 and CAL1 represent the system states as listed in Table 2.1.

$$T_{\rm OBS0} = G_1 G_2^* g^2 (T_A - T_{\rm REF}) + P_{\rm cor}, \tag{2.7}$$

$$T_{\rm CAL0} = G_1 G_2^* g^2 (T_A - T_{\rm CAL}) + P_{\rm cor}, \tag{2.8}$$

$$T_{\rm OBS1} = -G_1 G_2^* g^2 (T_A - T_{\rm REF}) + P_{\rm cor}, \text{ and} \tag{2.9}$$

$$T_{\rm CAL1} = -G_1 G_2^* g^2 (T_A - T_{\rm CAL}) + P_{\rm cor}, \tag{2.10}$$

where G_1 and G_2 are the gains in the two receiver arms and P_{cor} is the unwanted power appearing in the measurement data due to any spurious coupling of signals between the two arms either within the signal processing unit or at the samplers. P_{cor} would not be expected to change in magnitude or phase in different states and hence subtracting any pair of measurement data would cancel this additive signal. With this aim, we difference the measurements in the two switch states that have the same state of the noise source. We thus get two differential spectra:

$$\begin{aligned} T_{\rm OFF} &= T_{\rm OBS0} - T_{\rm OBS1} \\ &= 2 G_1 G_2^* g^2 (T_A - T_{\rm REF}), \text{ and} \end{aligned} \tag{2.11}$$

$$\begin{aligned} T_{\rm ON} &= T_{\rm CAL0} - T_{\rm CAL1} \\ &= 2 G_1 G_2^* g^2 (T_A - T_{\rm CAL}). \end{aligned} \tag{2.12}$$

We next derive a measure of the system bandpass by differencing the two spectra computed above in Eq. 2.11 and 2.12:

$$\begin{aligned} T_{\mathrm{TEMP}} &= T_{\mathrm{ON}} - T_{\mathrm{OFF}} \\ &= -2G_1 G_2^* g^2 (T_{\mathrm{CAL}} - T_{\mathrm{REF}}). \end{aligned} \tag{2.13}$$

This complex spectrum represents the system bandpass, which we we use to calibrate the measurement data for the bandpass. The term $(T_{\mathrm{CAL}} - T_{\mathrm{REF}})$ represents the *step* change in the noise temperature from the reference port when the noise source is switched on, and is the excess power above the OFF state. This step in power is also referred to as the Excess Noise Ratio (ENR) of the noise source; we call this T_{STEP}.

We divide Eq. 2.11, which represents the measurement data with calibration source off, by Eq. 2.13, which represents the bandpass calibration, to flatten the system bandpass:

$$\frac{T_{\mathrm{OFF}}}{T_{\mathrm{TEMP}}} = -\frac{(T_A - T_{\mathrm{REF}})}{T_{\mathrm{STEP}}}. \tag{2.14}$$

This calibration, being a complex division, also results in the sky data being in the real component of the complex calibrated spectrum and yields the differential measurement:

$$T_A - T_{\mathrm{REF}} = -\frac{T_{\mathrm{OFF}}}{T_{\mathrm{TEMP}}} T_{\mathrm{STEP}}. \tag{2.15}$$

This signal processing cancels any internal additive systematics originating in the signal processing unit and digital signal processor, as shown in the process of differencing spectra through Eq. 2.7 - 2.12, and also performs a complex bandpass calibration of the measurement data, as shown in Eq. 2.15. We finally get a differential measurement of the antenna temperature T_A with reference to the termination T_{REF}. The only unknown is the power step corresponding to the difference in the noise source in ON state compared to OFF state, T_{STEP}. We discuss the method adopted to derive the value of T_{STEP} next.

2.4.3.3 Absolute Calibration

Absolute calibration for the measurement data is provided by determining the scaling factor for the data from the arbitrary counts in which data is acquired to units of Kelvin. T_{STEP} is used in Eq. 2.15 above to convert the calibrated spectra from arbitrary units to units of Kelvin.

In order to measure this temperature step for the calibration, we make a laboratory measurement using the receiver. The antenna is replaced with an accurate 50 Ω termination. Temperature probes are firmly fixed on the outer conductor of this termination and another on the reference termination.

We now immerse the termination that is in place of the antenna, along with its temperature probe, into hot water in a thermally insulated dewar and let it cool slowly over time. The temperatures of the terminations are logged by the probes. At the same time, the bandpass calibrated power is recorded by the receiver system. We repeat this exercise by immersing the termination that is in place of the antenna in ice water and let this bath heat slowly over time to ambient temperature.

We denote the true physical temperatures of the termination and reference loads by T_A and $T_{\rm REF}$, while their respective temperatures as measured by the probes are denoted by T_{a_m} and T_{r_m}. Considering the reference load, its true temperature $T_{\rm REF}$ would always be somewhat higher than the measured T_{r_m} since the measurement from the probe is on the outer conductor of the probe which would be cooler than the actual temperature. Thus, we may write that

$$T_{\rm REF} = T_{r_m} + k_1, \tag{2.16}$$

where k_1 is always positive. Similarly, for the termination that replaces the antenna, we have

$$T_A = T_{a_m} + k_2, \tag{2.17}$$

where k_2 can both be positive or negative. When the termination is immersed in hot water, T_{a_m} would overestimate the true temperature of the termination whereas when immersed in ice water bath, it would be lower than T_A. Both these effects are due to the fact that there is thermal resistance between the outer metallic bodies of the terminations, where the temperature probes are fastened, and the source of electrical noise is at the core of the electrical resistance within the terminations. Hence the probe measurement either leads or lags depending on whether the termination is placed in an environment that is above or below the ambient temperature respectively.

Thus, from the experiments with hot and cold water baths we have two sets of physical temperature measurements for the LHS of Eq. 2.15 and corresponding ratios $T_{\rm OFF}/T_{\rm TEMP}$ from corresponding measurement data. A plot of the difference of the two temperature probes versus the corresponding ratios from the measurement data is expected to result in a straight line, with the slope of the line yielding $T_{\rm STEP}$ in accordance with Eq. 2.15. We also solve this data for offsets k_1 and k_2 in the straight line model to account for the difference between the measured and true temperatures in each of the temperature probes.

We thus plot the probe measurements versus the system measurements and model each of the hot and cold bath experimental data as straight lines, constraining the slopes to be same, but allowing for different intercepts. The common slope gives an estimate of $T_{\rm STEP}$ of value 446 K with 1% accuracy. We note here that the absolute calibration provides a scaling factor which converts arbitrary

counts to units of Kelvin without affecting the spectral shape of the 21-cm signal. Hence the absolute temperature of the signal would be accurate to within 1% with the current method. We show the data and their model fits in Fig. 2.9.

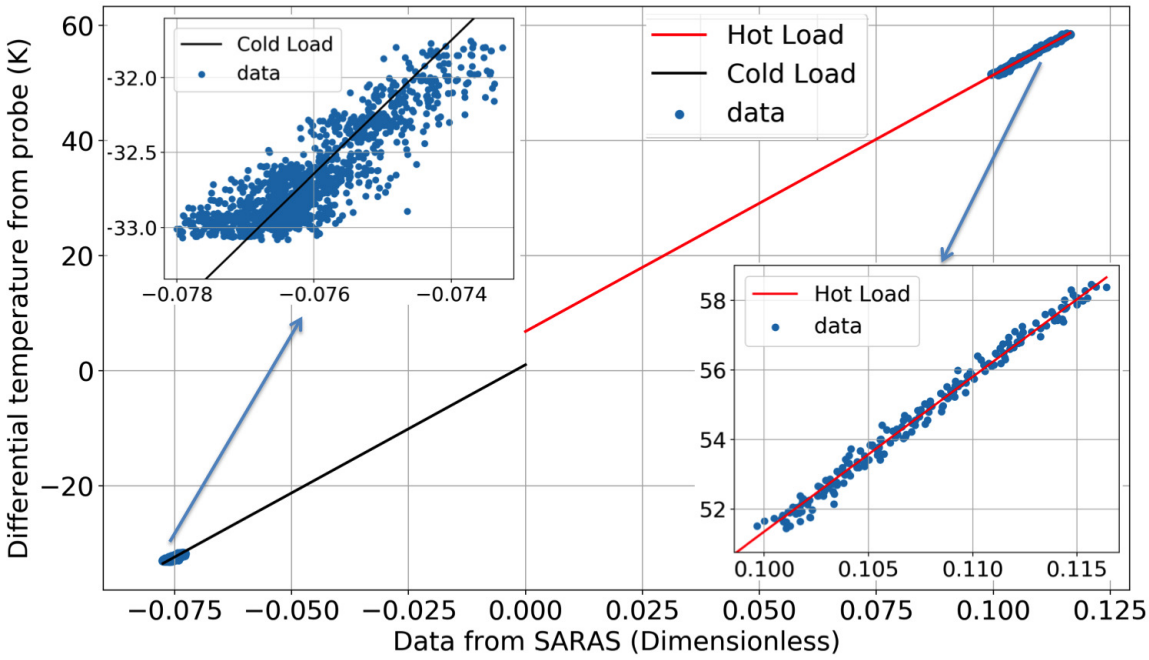

Figure 2.9: Fit that yields the Absolute Calibration Scale factor T_{STEP}.

2.4.3.4 The measurement equation

There are three sources of signals within the system:

- sky and ground radiation entering through the antenna, resulting in an antenna temperature T_A,
- signal from the reference termination T_{REF}, which becomes the calibration signal T_{CAL} when the calibration source is on, and
- signals corresponding to receiver noise from the LNAs, corresponding to the receiver noise temperatures T_{N_1} and T_{N_2} that are the noise figures of the LNAs.

Since the antenna and the LNA's have impedances at their ports that are not perfectly matched to the interconnects, all of the above signals propagating along interconnects get partially reflected at their terminals. All these signals thus suffer multipath propagation with differential delays from their respective sources to the digital signal processor and interfere to produce frequency dependent shapes. However, owing to the correlation spectrometer scheme adopted, a significant part of receiver

signal arriving at the correlator from the two arms is uncorrelated and does not result in any response. It is when the receiver noise signal from an LNA in one receiver arm propagates to the antenna and reflects back into the other receiver arm that we have a correlated receiver response in the measurement data. Thus the amplitude of receiver related component in the measurement is reduced relative to that in autocorrelation spectrometers. The formalism and derivation of additive signals arising due to impedance mismatch in correlation spectrometers, for the SARAS 1 system, is in [120]. The configuration in SARAS 2 is somewhat different from that in SARAS 1 and we provide below generalized expressions for the calibrated measurement data, with multi-order reflections, without pedagogical derivation.

$$T_{\rm meas} = \left[\left(\frac{C_1}{C_2}\right)T_A - T_{\rm REF} + \left(\frac{C_{n1}}{C_2}\right)T_{\rm N_1} + \left(\frac{C_{n2}}{C_2}\right)T_{\rm N_2}\right], \quad \text{where} \tag{2.18}$$

$$C_1 = \left[\sum_{l=0}^{\infty}|\gamma^{2l}|\sum_{m=0}^{\infty}\Re(\gamma^m e^{im\phi})\right], \tag{2.19}$$

$$C_2 = \left[1-|\psi|^2\left(\sum_{l=0}^{\infty}\gamma^l e^{i(l+1)\phi}\right)\left(\sum_{m=0}^{\infty}\gamma^m e^{i(m+1)\phi}\right)^*\right] + \left[2i\Im\left\{\psi\left(\sum_{n=0}^{\infty}\gamma^n e^{i(n+1)\phi}\right)\right\}\right], \tag{2.20}$$

$$C_{n1} = f_1\chi^* + f_1^2|\chi|^2, \text{ and} \tag{2.21}$$

$$C_{n2} = f_2\chi + f_2^2|\chi|^2. \tag{2.22}$$

The expansions for γ, ψ and χ are:

$$\gamma = (\Gamma_1+\Gamma_2)\Gamma_a g^2, \tag{2.23}$$

$$\psi = (\Gamma_1-\Gamma_2)\Gamma_a g^2, \text{ and} \tag{2.24}$$

$$\chi = g^2\Gamma_a e^{i\phi}\sum_{l=0}^{\infty}\gamma^l e^{il\phi}. \tag{2.25}$$

The term C_1 in the RHS of Eq. 2.18 represents the antenna signal and its associated reflections at the LNA, and C_2 refers to the signal from the reference termination and its reflections at the LNA and the antenna terminal. For each of these components, the terms in Eq. 2.19 and 2.20 correspond to the response due to direct propagation of the signals along the two receiver arms, propagation along the two arms with multiple internal reflections but with equal delays in both arms, and lastly propagation along the two arms and arriving at the digital signal processor with unequal delays.

The last two terms in Eq. 2.18 represent the response to receiver noise signals that arise from

the interference of forward and reverse propagating noise from the individual LNAs that arrive at the digital signal processor along the two arms. Γ_1 and Γ_2 are the reflection coefficients at the inputs of the LNAs, and f_1 and f_2 are the respective correlation coefficients between the forward and reverse traveling components of receiver noise voltages of the two LNAs. Φ is the phase difference between the forward and reflected signals, which depends on the phase difference due to the length of the system as well as the additional phase shift introduced by reflection Γ_c.

In ideal conditions, where the antenna and LNAs are perfectly matched with the rest of the system, only the direct path would exist resulting in C_1 and C_2 to be unity and C_{n1} and C_{n2} to be zero. In such a case, T_{meas} would simply be $T_A - T_{\mathrm{REF}}$ as given in Eq. 2.15.

In order to minimize spectral variations in these terms, we have miniaturized the overall physical length of the system to reduce the impact of the phase terms that result in sinusoidal responses in frequency. The total path length was reduced so that the period of the ripple increased and hence the observing band has only a fraction of a sinusoid, thereby maintaining smoothness in responses to the above sources of signals in the system. Through the choice of broadband LNAs, we expect a minimal variation of Γ_1 and Γ_2 across the band of operation. The correlation coefficients f_1 and f_2 were measured separately using the method described in [120]. They are found to be $\sim 10\%$ for the LNAs in SARAS 2.

Using these values, the amplitude of receiver response is estimated to be 10 K, which is multiplied by $|\Gamma_c|$. Since $|\Gamma_c|$ is shown to be maximally smooth to at least 1 part in 10^4 (Sec. 2.3.2.2), any deviation of receiver response from smoothness would at most be at the sub-mK level.

We further remark that our estimates for Γ_1, Γ_2, Γ_c etc. provide the mechanism to decide on the number of higher orders in Eq. 2.19 – 2.22 that require to be included in the modeling so that the contribution from unaccounted reflections drops below a mK. We expand on this while analyzing test data acquired using accurate terminations in Sec. 2.7.

2.5 Digital Signal Processing

The digital correlator is the last signal processing section of SARAS 2. This computes the auto-correlation spectra of the signals in the two arms of the receiver and the crosscorrelation spectrum between the two arms. The autocorrelation spectrum is a real-valued function of frequency whereas the crosscorrelation spectrum is a complex-valued function.

The first module in the correlator is an Analog-to-Digital Converter (ADC) that digitizes the two analog signals into 10-bit digital levels with a sampling frequency of 500 MHz. The signals are then windowed using a four-term Blackman-Nuttall window [108] and channelized using an 8K FFT algorithm implemented on a Virtex-6 FPGA. The 8K FFT gives 8K-point complex output, which has Hermitian symmetry. Thus, we have 4K complex spectral estimates across the band. Since the

noise equivalent bandwidth of the Fourier Transform of the Blackman-Nuttall window is 1.98 [108], the total number of independent channels at the output of the FFT is very close to half of the 4K spectral measurements. Thus the sampling, windowing and Fourier transformation of the time-domain voltage waveforms results in 2048 independent complex numbers, corresponding to complex-valued samples of voltages in a 2048-point filter bank spanning the 0–250 MHz band, in each of the two signal paths. This provides an effective frequency resolution of 122 kHz. These complex outputs of the Fourier transforms from the two arms are used to generate the crosscorrelation spectrum as well as autocorrelation spectra for each of the two receiver arms separately [156]. These spectra are streamed by the FPGA in the form of data packets to a computer. The data, acquired through User Datagram Protocol (UDP), is then processed to construct the spectra with high fidelity. The spectra are written and stored on the hard disk of the acquisition PC in MIRIAD file format [146]. While the crosscorrelation spectrum is used in the data analysis, the autocorrelation spectra are useful for estimating the spectral power in each analog arm and also serve as a good system diagnostic tool.

For the sensitivity requirements of the present experiment, we now derive tolerances on various aspects of the design and performance of the digital system.

2.5.1 Tolerance on the clock jitter

Jitter in the sampling clock leads to uncertainty in the sampled amplitude of the input signal [2]. The uncertainty increases with increase in the frequency of the input signal. This results in a deterioration of the Signal-to-Noise ratio (SNR) in the ADC, which is given by [105]:

$$\mathrm{SNR}_{\mathrm{jitter}}(\text{in dBc units}) = -20\log_{10}(2\pi f_{\mathrm{in}} t_{\mathrm{jitter}}), \tag{2.26}$$

where f_{in} is the input frequency of the signal and t_{jitter} is the clock jitter.

The SNR of the ADC is also limited by thermal noise and other spectral components, including harmonics of the input signal [72]. This is quantified as the Signal-to-Noise-and-Distortion (SINAD), which is the ratio of the RMS signal amplitude to the mean value of the root-sum-square of noise and all other spectral components. Thus $\mathrm{SNR}_{\mathrm{jitter}}$ should be below the SINAD of the ADC so as to avoid any deterioration in total SNR. For the ADC selected for SARAS 2, which is a 10-bit sampler, the SINAD is 48.7 dB. From Eq. 2.26, we infer that t_{jitter} should be less than 2.9 ps considering operation at the highest frequency of 250 MHz. The actual jitter in the sampling clock, derived from the SARAS 2 synthesizer, is 1.8 fs, which is well within the tolerance derived above.

2.5.2 Tolerance on the clock drift

The sampling frequency of the clock might drift over time and this can lead to inaccuracy in the bandpass calibration. To estimate the tolerance on clock stability, we examine the maximum slope in

the total system bandpass.

The bandshape is found to have a variation of 0.8 dB with two cycles of ripples over the band of $40-200$ MHz. Assuming a maximum correlated response of 300 K, including RFI, foregrounds and system contribution, it would result in an overall ripple of peak-to-peak amplitude 60 K. We may model this variation as a sinusoid in frequency domain, given by $T = 30\sin(2\pi\tau\nu)$, where $\tau = 1/80$ MHz^{-1}. For a frequency shift of $d\nu$, we estimate the change in the measured temperature to be $\frac{dT}{d\nu} = 2\pi \times 30\tau\cos(2\pi\tau\nu)$. For the experiment, it is desirable to have $dT \leq 1$ mK. This would result in a maximum allowed frequency shift to be less than 424 Hz. Given that the sampling frequency is 500 MHz, we infer that the tolerance on the fractional frequency stability is 8.5×10^{-7}.

SARAS 2 uses a rubidium oscillator as the primary frequency standard for deriving the sampling clock. There is also an option for GPS disciplining built in for long term stability. The SARAS 2 sampling clock, disciplined by a rubidium oscillator, has a fractional frequency stability of 10^{-10}; therefore the design fulfills the required tolerance on the clock stability.

2.5.3 RFI leakage

A fraction of the power in any frequency channel leaks into neighboring channels in any filter-bank spectrometer. This is of particular concern when there is RFI and its leakage into neighboring channels results in corruption and hence loss of a large number of channels on either side of the frequency of interference. Although the RFI in the central channel might be detected using algorithms discussed below in Sec. 2.6, their contamination over the spectrum is difficult to estimate at the levels necessary for this experiment.

SARAS 2 uses a Blackman-Nuttall windowing of the time sequences to suppress the spillover of signals in any frequency channel into adjacent channels. This leads to loss in spectral resolution and also sensitivity by a factor of two; however, the windowing results in modifying the point spread function defining the spectral channels so that sidelobes in the spectral domain are substantially suppressed.

We have measured the suppression factor to be better than 10^8 in power. Thus even if an RFI in a channel is as strong as 10^5 K, its contribution in the rest of the independent channels would still be at a mK level. This threshold on tolerable interference sets thresholds for the RFI rejection algorithm in that spectra with RFI exceeding this threshold are completely rejected. Second, the threshold suggests that the observing site needs to be one in which there is no continuous RFI exceeding 10^5 K.

2.5.4 RFI headroom

The gains in the amplifiers of the receiver arms are set so that there is sufficient headroom for RFI and the system continues to operate in the linear regime while experiencing tolerable RFI. At the end

of the receiver arm, the input power at the ADC is such that it does not exceed its full scale. This ensures that the signal is not clipped in digital domain even if the total power increases appreciably due to presence of a strong RFI. The SARAS 2 ADC clips if a sinusoid signal input to the device has a power exceeding -2 dBm. The SARAS 2 system presents what is almost always a Gaussian random noise voltage to the ADC, whose power is set be nominally at a much lower total power of -28 dBm, which is 30 dB higher than the noise floor of the ADC but is also sufficiently below the clipping level. At this level, the probability of any random sample to be close to the clip level is vanishingly small. This reduces the effective number of bits available for the digitization of the signal; however provides enough headroom for strong RFI. Typically during observing at radio quiet sites, it is very unlikely that RFI increases the total power by even a few dB and, therefore, SARAS 2 is guaranteed to operate without non-linear effects of saturation due to the spectrometer and yield useful data during most of the observing duration.

2.6 Algorithms: Calibration and RFI rejection

In this section we describe the data processing steps that are used off-line on the measurement data acquired. These processing steps primarily cater to the calibration of the data, rejection of RFI, and computing noise estimates for each frequency channel. These noise estimates differ across the spectrum due to differing number of samples rejected due to RFI and their propagation through the different processing steps.

The cadence in each system state (Table 2.1) is 1 s. In each state a set of 16 spectral records are acquired, each with integration time of 1/16 s. We refer to the set of 16 spectral records as a frame. Each spectral record consists of a complex crosscorrelation spectrum, representing the crosscorrelation between the signals in the two arms of the correlation spectrometer, and their autocorrelation spectra, representing the power spectra corresponding to the signals in each arm.

In the following subsections, we describe the off-line processing steps for data reduction, calibration and RFI rejection (flagging of channels affected by interference). RFI can be of a range of strengths, either narrowband or broadband, and their temporal variations can differ greatly from being transient to persistent over the period of observing. While some RFI are clearly visible in a single spectral record, some may be weak and only detectable after averaging spectra over time and frequency to reduce noise. We follow a hierarchical approach to detect and reject data corrupted by RFI, targeting the relatively stronger RFI in the pre-processing stage and progressively aim to reject weaker lines in the post-calibration processing steps.

2.6.1 Pre-Processing

The first processing step performs a median filter [61] separately on crosscorrelation and autocorrelation spectra of each record of the 16-record frame, where one record has an integration time of (1/16)-s. The median filter is performed using a moving spectral window of width 2 MHz spanning over 17 independent frequency channels. At this pre-processing stage, a threshold of 2σ—twice the standard deviation—is adopted. This removes strong RFI from the data that stand out in the (1/16)-s integration spectra.

Processing each 1-s frame separately, the unflagged spectral points at each frequency are averaged across the 16 records in the frame, separately for the crosscorrelation as well as the two autocorrelation spectra. A maximum of 16 unflagged points are averaged at each frequency channel, and if the number of points available for averaging is less than 4 at any frequency, we flag that frequency channel in the averaged spectrum corresponding to that time frame. Corresponding to each of these time frames, we also compute and record the standard deviation, $\sigma(\nu)$, at each frequency channel by computing the standard deviation from the unflagged points for that frequency channel, and also record the effective integration time for each averaged spectral measurement.

2.6.2 Calibration

At the end of the pre-processing, for each system state, we have three averaged spectra, namely one crosscorrelation and two autocorrelations of the signals in the two arms of the receiver. We follow the method described in Sec. 2.4.3.2 to calibrate the bandpass. We use the value of $T_{\rm STEP}$ as derived in Sec. 2.4.3.3 for absolute calibration. We perform complex operations on the crosscorrelation spectra, yielding a complex calibrated spectrum in which the sky is expected wholly in the real component.

The calibrated spectra are derived from

$$\begin{aligned} T_{\rm SPEC}(\nu) &= \frac{T_{\rm OFF}(\nu)}{(T_{\rm ON}(\nu) - T_{\rm OFF}(\nu))} T_{\rm STEP} \\ &= \frac{T_{\rm OFF}(\nu)}{T_{\rm TEMP}(\nu)} T_{\rm STEP}. \end{aligned} \tag{2.27}$$

For each frequency channel, we also have associated estimates for RMS uncertainty σ for $T_{\rm OFF}$ and $T_{\rm ON}$. We propagate these by computing the resulting uncertainty in $T_{\rm SPEC}$ using the following expression:

$$\sigma_{\rm SPEC} = |T_{\rm SPEC}| \sqrt{\left(\frac{\sigma_{\rm OFF}}{|{\rm T_{OFF}}|}\right)^2 + \left(\frac{\sigma_{\rm TEMP}}{|{\rm T_{TEMP}}|}\right)^2 + 2\left(\frac{\sigma_{\rm OFF}}{|T_{\rm OFF}|}\right)\left(\frac{\sigma_{\rm TEMP}}{|T_{\rm TEMP}|}\right)\sigma_{(T_{\rm OFF},T_{\rm TEMP})}}, \tag{2.28}$$

where $\sigma_{\rm OFF}$ and $\sigma_{\rm TEMP}$ are the standard deviations computed from the pre-processing step and $\sigma_{(T_{\rm OFF},T_{\rm TEMP})}$ is the covariance between the two spectra. This last term is non-zero because the noise in $T_{\rm OFF}$ and that in $T_{\rm TEMP}$ are correlated since the latter is the difference between $T_{\rm ON}$ and $T_{\rm OFF}$. The larger is the calibration signal, the lesser this covariance and hence the smaller will be the relative importance of the third term under the square root in the above expression.

2.6.3 RFI detection/rejection post calibration

We now discuss the methods developed, and their underlying rationale, in flagging RFI on the calibrated spectra. There are various algorithms in the literature to detect outliers in a Gaussian noise-like signal [109]. We choose median filtering as the preferred approach, with a threshold of 3σ for classifying any point as RFI in the post-calibration rejection of RFI, σ being the standard deviation in the data.

2.6.3.1 RFI detection in 1D individual time frames

The first and critical step towards the detection of RFI in any spectrum is the modeling and subtraction of the best estimate for the true spectral shape, so that outliers may be recognized and rejected without introducing any systematic biases. We then use median filtering as an outlier rejection algorithm on the residuals, which rejects high amplitude excursions on both positive and negative sides with equal probabilities.The concern is that if a strong RFI is present that locally biases the estimate of the true spectral power, median filtering of deviations might result in biased outcomes. If RFI results in a positive bias in the estimate of the true spectral level locally, the high amplitude noise points that are positive will be preferentially flagged in that spectral region. This would result in systematic local biases in the spectra when averaged after such asymmetric clipping. Thus in the process of estimating for the true spectral shape, the algorithm design is required to ensure that any bias introduced would be at sub mK levels.

To make an estimate for the true spectral shape—which we call the baseline—we first divide the frequency band of $40-240$ MHz into two sub-bands. We fit each sub-band with a 12-th order polynomial. The sub-band and the order of polynomial is high enough to represent foregrounds and systematics, whose expected shapes we have estimates of from modeling of the system, and 21-cm signal, for which we have predictions in the literature [29], to mK accuracy.

We denote the fit by $y_{\rm fit}$ and the data by $y_{\rm data}$. There are two norms we adopt for optimization of the fit to the data: the L_1 norm or Least Absolute Deviations minimizes $|y_{\rm data}-y_{\rm fit}|$, where as the L_2 norm or Ordinary Least Squares minimizes $|y_{\rm data}-y_{\rm fit}|^2$. The L_2 norm is the best linear unbiased estimator of the coefficients in a fit [25]. In the first pass of the RFI detection we adopt the L_1 norm since it is less sensitive to outliers as compared to the L_2 norm [103]. The residuals, obtained as the

difference between data and fit, are tested for outliers using median filtering. We repeat the process after rejecting the RFI detected in the first step, again using L_1 fit, to improve the estimate of the true baseline and also progressively improve upon RFI rejection.

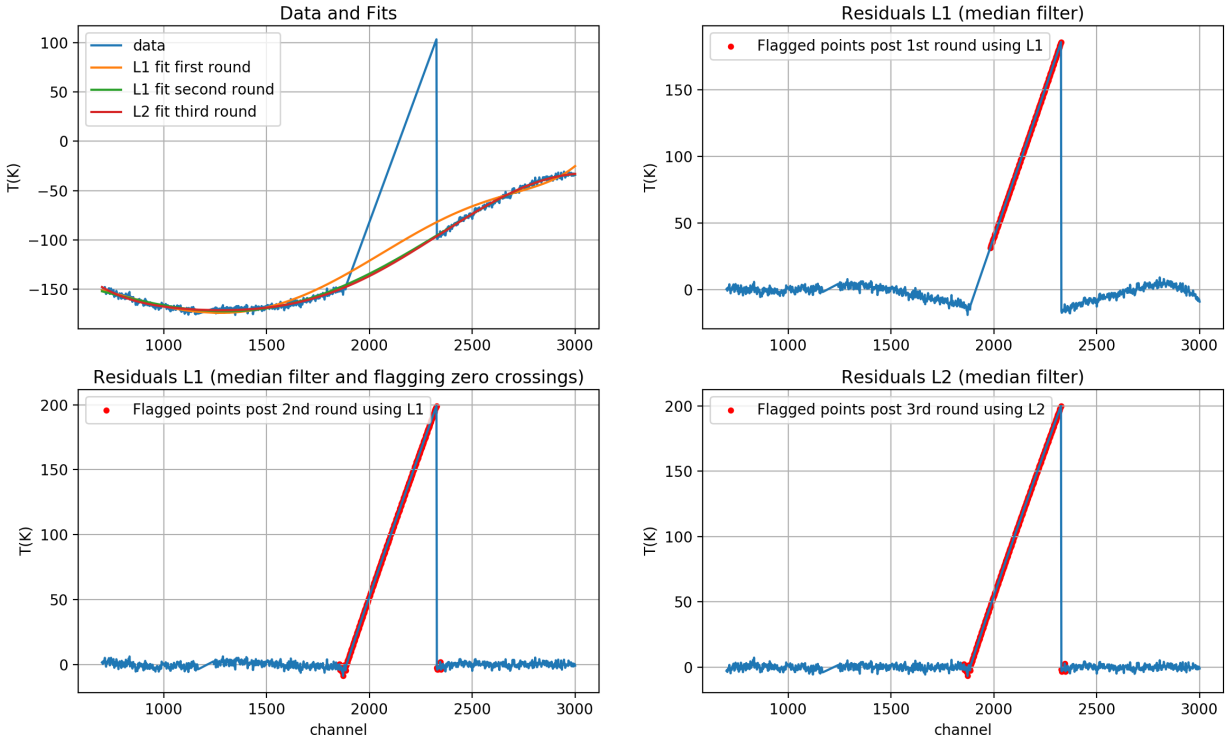

Figure 2.10: Demonstration of the RFI rejection discussed in Sec. 2.6.3.1. The top left panel shows the mock spectrum that has an added artifact representing a block of RFI with linearly varying strength. The RFI detection is done in a sequential manner, as discussed in the text, and this panel shows the baseline fits at the different stages overlaid on the mock spectrum; obviously the bias in the baseline fit reduces progressively in successive stages. The upper right panel shows the residual after the first fit; the data detected as RFI at each stage is shown in red. There is a clear structure in the residuals due to the bias in the baseline fit at this first stage. The bias is substantially reduced when the fit is revised after rejection of RFI based in the first iteration; this is shown in bottom left panel. A median filter is applied on the residuals and in the final third iteration an L_2 norm based fit for a baseline is performed; the bottom right panel shows the resulting residuals. At this last stage, the entire triangular artifact is seen to be rejected.

RFI often appears in clusters and there is often relatively weaker RFI close to stronger RFI. If RFI is strongly clustered, the bias in the baseline fit can be severe, and such circumstances require a different method. To illustrate this case, consider a particularly adverse case where RFI is low in strength at one edge of an RFI cluster and progressively increases in strength towards the other end of the RFI cluster. In such a scenario, even after the two RFI rejection iterations using L_1 minimizations

to fit for baselines, the low level RFI lying at the *wings* of the cluster might still survive. This is shown in Fig. 2.10. In order to detect such low-lying RFI at the edge of an RFI cluster, we have adopted an additional data rejection step in the difference data: on each side of any rejected channel we also reject all the points along the frequency spectrum till two zero crossings of the data residual values are encountered. This additional rejection step does inevitably cause loss of good spectral data; however, it does succeed in rejecting low levels of RFI in channels close to relatively stronger RFI.

Following two such iterations of RFI rejection based on fitting to baselines using the L_1 norm, we finally perform RFI rejection using the L_2 minimization for estimation of the baseline followed by median filtering of residuals. Finally, as a test of the total quality of each spectrum, we compute the variance for each of the difference spectra and reject all those spectra that are outliers in their variance. This detection of poor quality spectra is also done via a median filtering of the variance estimates.

We have carried out simulations with mock data which demonstrate that for the adopted threshold of 3σ, if the offset in baselines as a result of RFI is within 20 mK at the final stage, the bias after outlier detection will be ~ 1 mK. The order of the fitting polynomial and the three step process have been chosen to satisfy this tolerance.

We find that for data acquired with SARAS 2 in reasonably radio quiet sites in Ladakh in the Himalayas and in sites in South India, this process successfully rejects almost all of the obvious isolated RFI in the spectrum.

2.6.3.2 Rejection of data in 2D Time-Frequency domain

Following the detection of RFI in the 1D individual spectra separately and sequentially, we next move to 2D time-frequency domain to detect lower levels of RFI. The strength of RFI might be lower than the median filtering threshold used on the 1D spectra, but may be detected with that confidence when the data is averaged in 2D time-frequency space. We follow a "matched filter approach" for this. Since RFI might be spread over a time-frequency region, we progressively average the data over this 2D domain to detect lower levels of RFI as they cross the 3σ median filter threshold when the averaging enhances the amplitude of the RFI relative to the noise.

We begin once again with subtracting a baseline from each spectrum, using a fit that is an estimate of the foreground, systematics and any 21-cm signal. We divide the total spectrum in three overlapping sub-bands and separately fit each segment with 10-th order polynomials. We construct a single residual spectrum using the three residual segments, avoiding using the edges of each segment where the fits sometimes diverge from the data.

This is done for all the spectra in the dataset yielding a 2D image of residuals over the entire time-frequency domain of the dataset. The next step of the processing is a median filtering of the entire dataset in 2D time-frequency to detect outliers. We then average the data both in time and

frequency using moving windows of different widths, which progressively grow with each iteration, and perform a two-dimensional median filtering following each averaging. The maximum averaging window length currently used is 1 MHz in frequency, assuming that CD/EoR signal has greater width.

In the 2D time-frequency domain detection of RFI, we avoid having a uniform threshold in temperature units for RFI detection using median filters, since different data points have different associated uncertainties. This is because in the pre-processing, as well as successive iterations of RFI rejection described above, time-frequency data points are rejected and then the data is averaged and, therefore, different time-frequency data points have different effective integration times. For every point, we examine its absolute value against its own uncertainty σ and if the absolute value is larger than 3σ, we reject the point as RFI.

We also examine the integrated powers in each of the spectra using the corresponding polynomial fits, and reject spectra that have integrated powers that are 3σ outliers. Such outliers result from wideband RFI, like lightning, that raise the overall power in the spectrum.

2.7 Performance Measures of SARAS 2

Performance tests have been conducted in the laboratory to examine for spurious signals in the SARAS 2 receiver system and to evaluate whether the modeling of the system performance as described above (Eq. 2.18) is accurate at the mK level. We replace the antenna with accurate reference loads or terminations with different reflection coefficients, Γ_c, acquire measurement data and construct a model to search for unaccounted spectral structure.

We use three types of terminations with a range of complexity in their Γ_c:

- Accurate 50 Ω termination: This is the most ideal case where $|\Gamma_c|$ is close to 0. Thus we have minimum reflections resulting in minimum additive signals arising from multipath propagation of receiver noise, reference noise and signal from the termination.

- Accurate Open and Short loads: Open and short terminations are completely mismatched with the receiver, with $|\Gamma_c|$ of 1 and -1 respectively. All internal reflections of signals from receiver noise and reference are maximized, and in this case there is almost no signal from the termination itself.

- Resistor-Inductor-Capacitor based network (RLC): To have a frequency behavior in $|\Gamma_c|$ similar to that of the antenna, we choose values of the resistor, capacitor and inductor so that the network resonates at 260 MHz, same as that of the SARAS 2 antenna, and the shape of Γ_c is similar to that of the antenna. Thus all signals that reflect off this termination and suffer multipath propagation appear in the measurement data with systematic shapes that have the imprint of the frequency dependence of $|\Gamma_c|$.

With each of these terminations in turn we acquired data for 10 hours in the laboratory and processed the measurement sets using the algorithms discussed in Sec. 2.6. The final set of spectra, after processing with the RFI rejection algorithms, were averaged in time to derive a single spectrum. We discuss below the modeling of these data, and the method of examining the residuals for the presence of spurious signals. The RMS noise in the residuals of the spectrum, after data modeling and without any spectral averaging, is in the range 15–20 mK.

2.7.1 Examining measurement data for spurious signals

We analyze the residuals seeking to detect two forms of spurious signals: sinusoids and Gaussian shaped structures. Sinusoidal spurious signals are spread out in the spectral domain but appear as spikes in its Fourier domain while the Gaussian shaped spurious signals have a compact base in both the spectral and in its Fourier domain.

2.7.1.1 Sinusoidal spurious signals

Any sinusoid in the residual spectra would stand out as a spike in its Fourier domain. Thus, to detect the presence of sinusoidal spurious signals, we perform Fourier transformation of the residuals to get a spectrum of Fourier amplitudes at different Fourier modes. These amplitudes of the Fourier transform, where the input is zero mean Gaussian noise, follows a Rayleigh distribution [116, Chapter 6]. Thus, if any sinusoidal spurious signals exist in the residual that are detectable given the measurement noise, we would expect an outlier in the Rayleigh distributed amplitudes.

We compute the cumulative distribution function for the amplitudes of the Fourier modes and inspect if the fraction of amplitudes above 2, 3 and 4 σ are within the expectations for a Rayleigh distribution, assuming that the residuals are Gaussian random noise. Further, since the real and imaginary components of the Fourier transform are expected to have Gaussian distributions if the spectra are Gaussian random noise, the 2D distribution of real versus imaginary of the components in the Fourier transform would be expected to have a symmetric distribution. To quantify this, we test for the uniform distribution of phase of the Fourier transform using Chi-Square test [58]. Any significant deviation from uniform distribution would imply the presence of coherent structure in the residuals. This is a second test for departure from Gaussianity in the Fourier domain.

2.7.1.2 Gaussian spurious signals

We adopt a matched filtering approach to examine if the residuals contain Gaussian shaped structures. Gaussian functions, with a range of widths σ are centered at a range of frequencies ν_0 within the band. The 1σ width is iteratively varied from $1-20$ MHz in different trials. We convolve the residuals with these Gaussian windows of various widths and positions. At any location and for any width, if the summation over the product of the Gaussian window with the residual significantly exceeds the

expectation from convolution of same window with a mock data that is Gaussian random noise, we may infer the presence of a Gaussian structure of width σ at the frequency ν_0.

2.7.2 Modeling internal systematics

We use the model based on the analysis of signal propagation in the SARAS 2 system, as given by the measurement equation in Eq. 2.18, to fit to the data. As discussed in Sec. 2.4.3.4, we include higher order reflections that are expected to result in structure above mK in the model. Since contributions from orders higher than three are at sub-mK levels, we restrict to third order reflections ($\{l,m,n\} = 3$ in Eq. 2.18). For reasons explained in Sec. 2.2, we restrict our analysis to the band $110 - 200$ MHz.

The model fit to the calibrated measurement data, using the measurement equation, was done using the Nelder-Mead optimization [104]. Further, to avoid solutions that are unphysical, we appropriately constrain the parameters to be within expected ranges and also use multiple iterations of the Basinhopping algorithm [171] to get parameters that are meaningful and acceptable given the hardware configuration and measured characteristics of the system components.

We finally compute the difference between the spectrum and the fitted model to get the residuals. We then carry out the tests discussed above in Sec. 2.7.1 for examining for sinusoidal or Gaussian shaped spurious structures in the residuals.

2.7.2.1 Results from the 50 Ω termination data

The measured spectra, along with the residuals, for the case of modeling of measurement data from 50 Ω termination are shown in Fig 2.11. After averaging the data over the entire 10 hours, the RMS noise in the residual is 15 mK.

We further test for the presence of underlying sinusoids and Gaussian structures with the methods discussed above in Sec. 2.7.1. We do not find any sinusoidal structures in the data down to a sensitivity of ~ 1 mK. This level is considerably lower than the reported RMS noise of 15 mK since in the Fourier domain, sensitivity to any Fourier mode is enhanced by a factor that is of order the square root of half the number of independent channels. We also show the real and imaginary parts of the Fourier transform and the distribution of these Fourier amplitudes in Fig. 2.12. The sensitivity of the test for Gaussian structures varies with the width of the Gaussians for which the test is done. The upper limits on amplitudes of Gaussian-type spurious signals range from $1 - 10$ mK for widths of 25 MHz to 1 MHz respectively. At the reported sensitivities, all the results are consistent with the measurement data being Gaussian random noise.

2.7.2.2 Results from the Open/Short termination data

Whereas in the case of a termination that is an electrical short we expect the reflected voltage to be phase shifted by 180°, there is no phase change on reflection from an electrical open termination. The

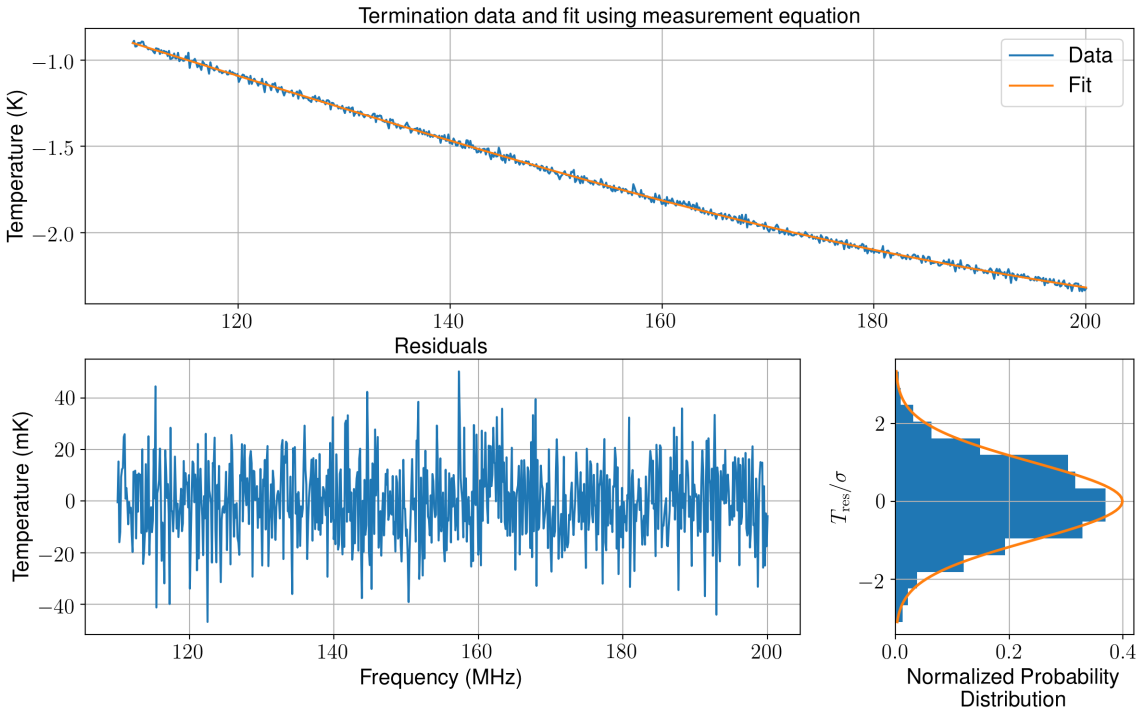

Figure 2.11: The top panel shows the measurement data for the case of termination of the receiver with a 50 Ω load. The bottom left panel is the residual after subtracting the best fit model. The bottom right panel shows the distribution of the residuals overlaid with a Gaussian distribution of the same mean and standard deviation as that of the residuals.

two spectra, obtained using open and short terminations, are similar except for this 180° phase shift in the reflected components. Therefore, we show the results of modeling and analysis for systematics only for the case of the open termination.

For both the open and short terminations, there is no source of signals at the terminations. The spectrum contains multi-order reflections from only the reference and receiver noise $T_{\rm REF}$. We model the data using the measurement equation Eq. 2.18, setting $T_A = 0$. The residuals, after subtracting the best-fit model, are shown in Fig. 2.13. The residuals appear consistent with Gaussian random noise, with an RMS of $\sim$ 15 mK.

Similar to tests for the 50 Ω termination, we carried out tests for presence of sinusoids and Gaussian structures in the data for the open termination. The real and imaginary part of the Fourier Transform and the distribution of Fourier amplitudes are shown in Fig. 2.14. We do not see any evidence for sinusoids and Gaussian spurious structures at the same sensitivity levels as reported in Sec. 2.7.2.1 for the case of the 50 Ω termination.

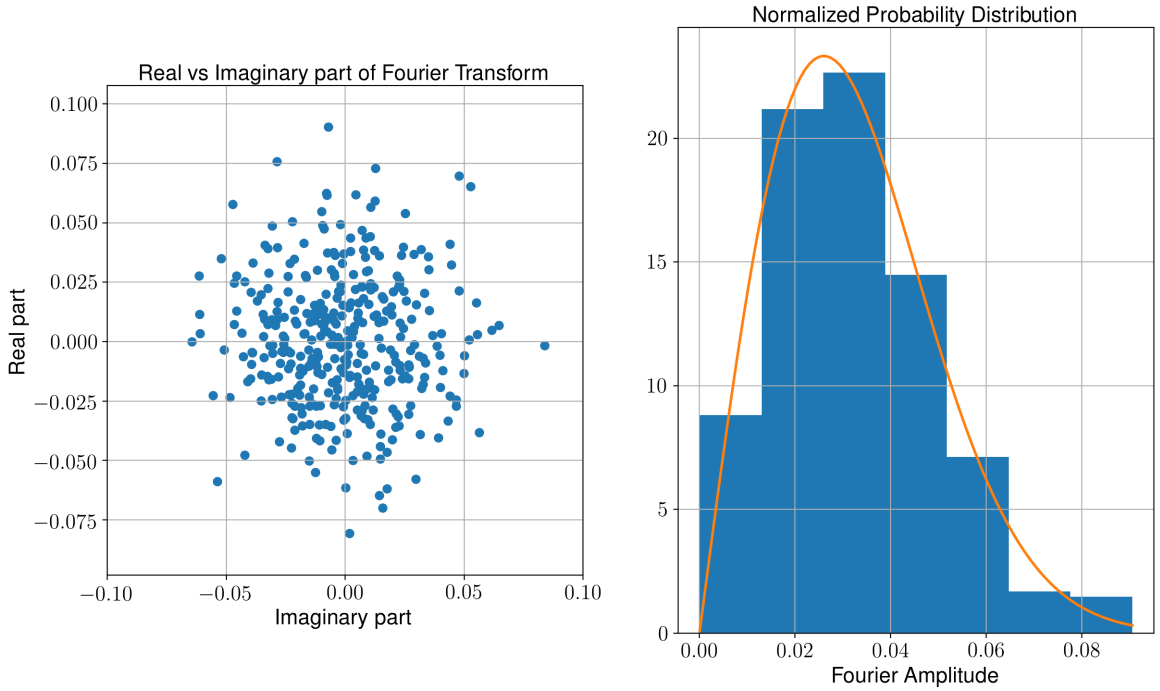

Figure 2.12: The left panel shows real versus imaginary components of the Fourier transforms of the residuals. The right panel shows the distribution of amplitudes of the Fourier transform overlaid with a Rayleigh distribution of amplitudes. The Fourier transform is carried out on normalized residuals; i.e., data residuals are first divided by the corresponding RMS uncertainties and hence the standard deviations of the normalized residuals is unity. Both these plots are consistent with a residual containing Gaussian noise and there is no evidence for spurious signals.

2.7.2.3 Results from the RLC termination data

To model the measurement data in the case of the RLC termination, we use the complete measurement equation (Eq. 2.18) taking into account the spectral shape of Γ_c, coupling of T_A into the system as well as multi-order reflections due to the receiver noise and also a T_A equivalent to the resistance in the RLC network. We show the residuals to the model fit and its Fourier components in Fig. 2.15 and 2.16 respectively. The RMS noise of the residuals, after removing the best fit model from the data, is 20 mK. This is higher than 15 mK RMS noise obtained in the other terminations. This is primarily due to more RFI flagging in case of RLC termination compared to better electromagnetically shielded 50 Ω and Open/Short terminations.

From the Fourier analysis, we do not find any outliers that may be evidence for sinusoids in the residual data above the measurement noise, which is ~ 2 mK. Similarly, with the matched filter tests using different Gaussian functions, we conclude that there are no Gaussian artifacts at a level of $2-15$ mK for widths in the range 25 MHz to 1 MHz respectively.

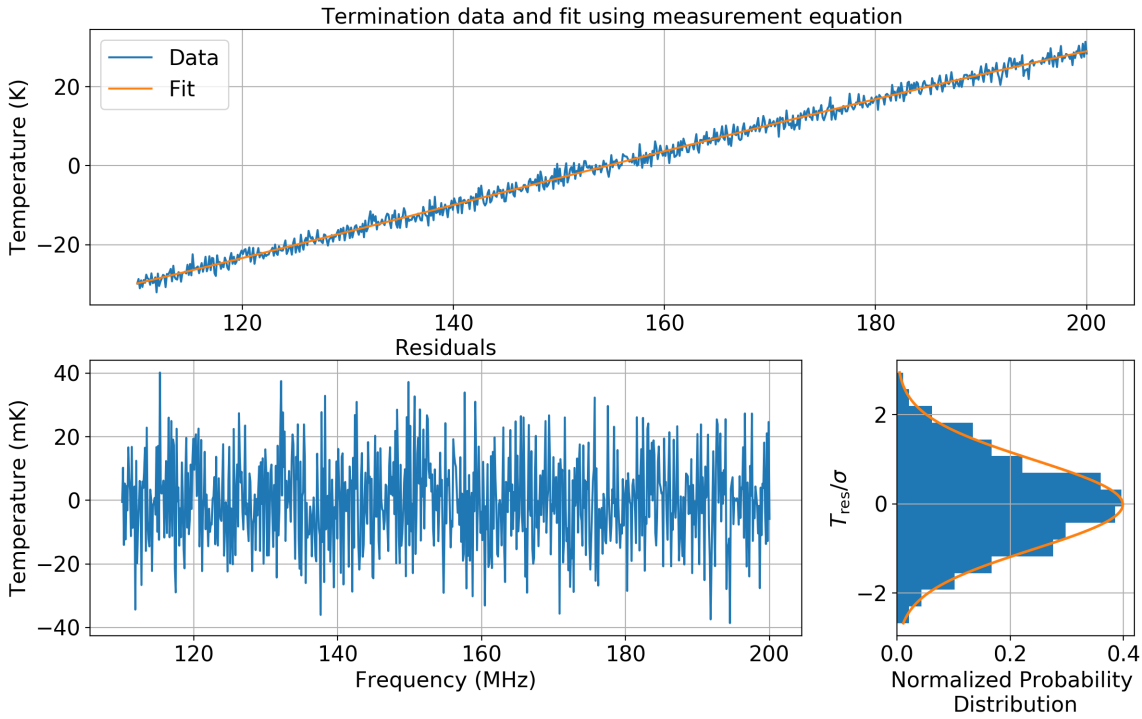

Figure 2.13: The top panel shows the spectrum for the case of an open termination, after removal of the common additive component that is in measurement data acquired in both the open and short terminations. The residuals, including noise, in the data has been amplified by a factor of 100 for better representation (only for the top panel). The bottom left panel is the residual after removing the best fit model. The bottom right panel shows the histogram of residuals overlaid with a Gaussian of same mean and standard deviation as that of the residuals.

2.7.3 Modeling using maximally smooth functions

Modeling using the measurement equation is challenging when the number of parameters necessary to describe the data increases, and as the complexity of $|\Gamma_c|$ increases. This is the case when an RLC termination replaces the antenna, with a reflection coefficient that varies across frequency, and would be the case when the antenna is connected to the system and the antenna temperature includes sky and ground radiation. The large number of parameters in the modeling, if left free and without being determined by field or laboratory measurements, would give the model considerable freedom. There may also be degeneracy between parameters describing the model for the system and foregrounds, and confusion arising from degeneracy between parameters describing the system, foreground and 21-cm global CD/EoR signal. This results in increased uncertainty in the derived parameters for the CD/EoR signal.

A better approach may be to use a model description for the system, and perhaps foregrounds

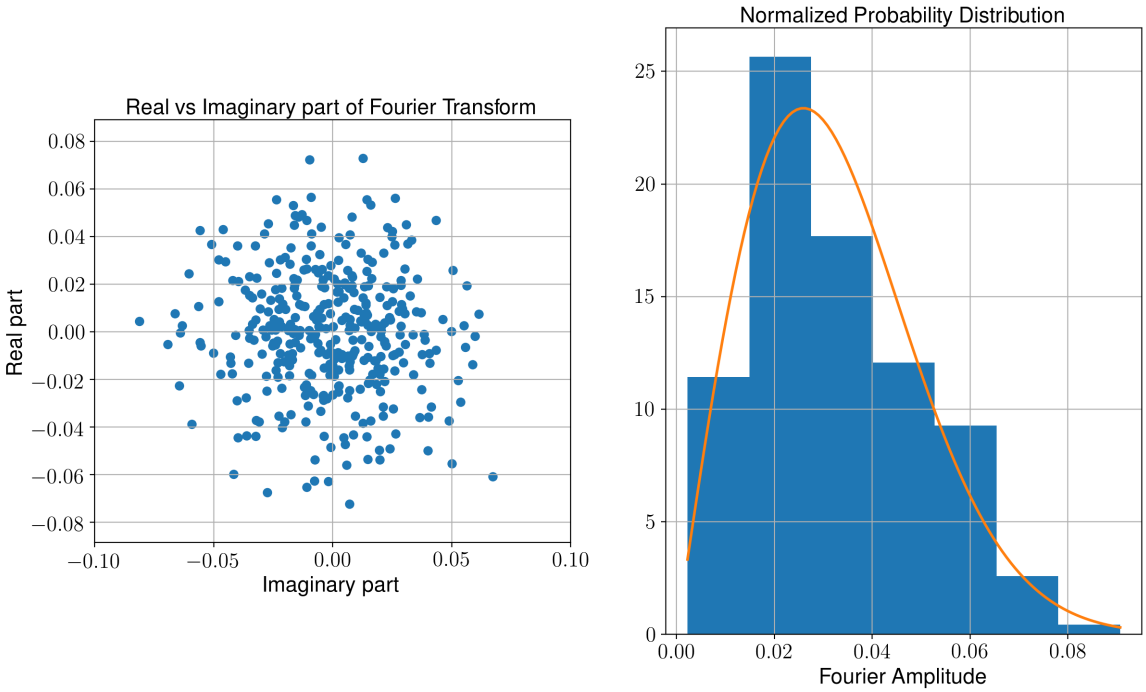

Figure 2.14: The left panel shows the 2D distribution of real versus imaginary components of the values of the Fourier transform for residuals of the data obtained in the case of the open termination. The right panel shows the distribution of amplitudes of the Fourier transform overlaid with a Rayleigh distribution function. The Fourier transform is carried out on normalized residuals; i.e., data residuals are first divided by the corresponding RMS uncertainties and hence the standard deviations of the normalized residuals is unity.

as well, that is less likely to subsume a substantial part of the 21-cm signal. We may thus try to approximate the calibrated measurement data with a maximally smooth function [143], or a variant of that which allows minimum freedom to fit out complex cosmological signals while having the necessary freedom to fit out the systematics and foregrounds. The motivation for modeling the data using a maximally smooth function is to have a limited freedom in the model such that it causes minimum loss of 21-cm signal, preserving its higher order structures, while being able to model the foreground with mK accuracy [145].

Following this alternative approach, we fit each dataset corresponding to 50 Ω, Open/Short and RLC terminations with maximally smooth functions. Since there are higher order reflections of receiver and antenna signals that contribute above a mK, we allow for a maximum of one inflection point in the band. With this approach, the residuals from different terminations reach the same noise levels as the residuals resulting from the fit to the data using the measurement equation in Sec. 2.7.2.1, 2.7.2.2 and 2.7.2.3. We show here, as an example in Fig. 2.17, the maximally smooth function fit and

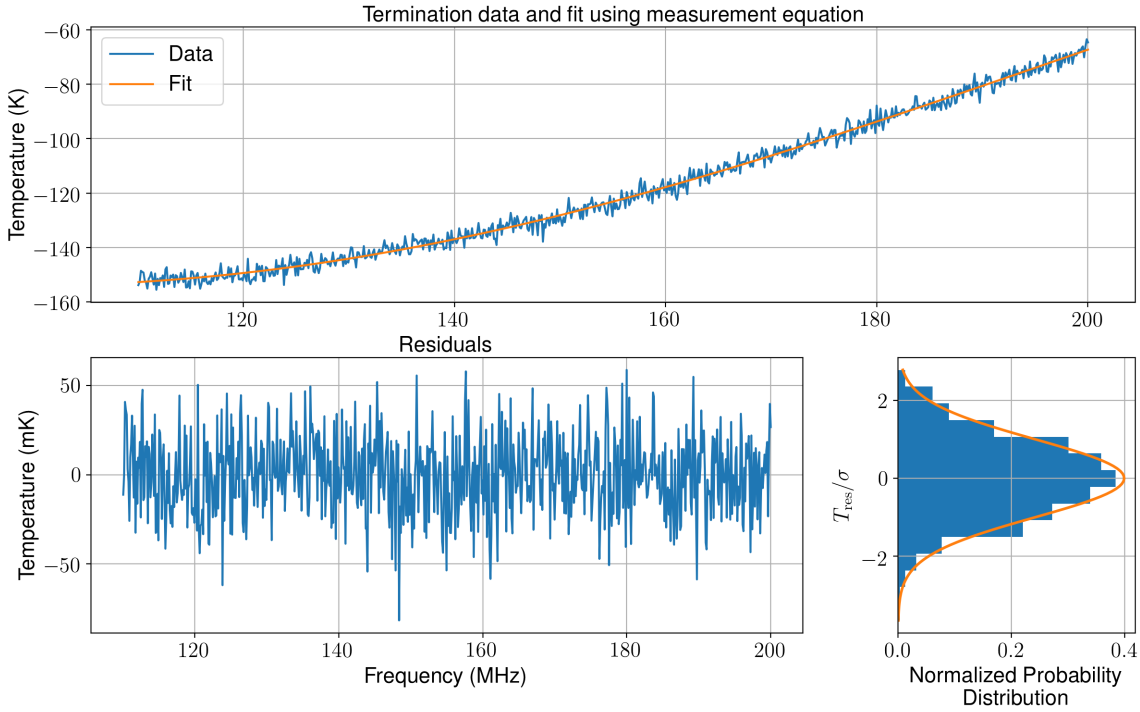

Figure 2.15: The top panel shows the calibrated measurement data in the case of the RLC termination. The residuals, including noise, in the data has been amplified by a factor of 100 for better representation (only for the top panel). The bottom left panel is the residual left after subtracting the best fit model based on the measurement equation for this termination. The bottom right panel shows the histogram of residuals overlaid with a Gaussian with same mean and standard deviation as that of the residuals.

residuals for the data obtained with an RLC termination at the antenna terminal.

We also obtain models for the measurement data for different terminations via best fits of the measurement equation to the data. These data models capture the overall complexity of the spectrum. We have tested their smoothness by fitting these models with maximally smooth functions. The maximally smooth function is found to be able to approximate these models to 2 mK level, which is a smoothness of 1 part in 10^5 considering that the actual spectral shape may be a few hundreds of Kelvin. Thus, the tests suggest that the class of 21-cm signals that have complex variations over the band, and have antenna temperatures more than this confusion limit of 2 mK, can potentially be detected by the system.

2.8 Comparison with other radiometers

We compare below the designs of the radiometers employed in different experiments for detection of global-21-cm signals. Table 2.2 provides a summary.

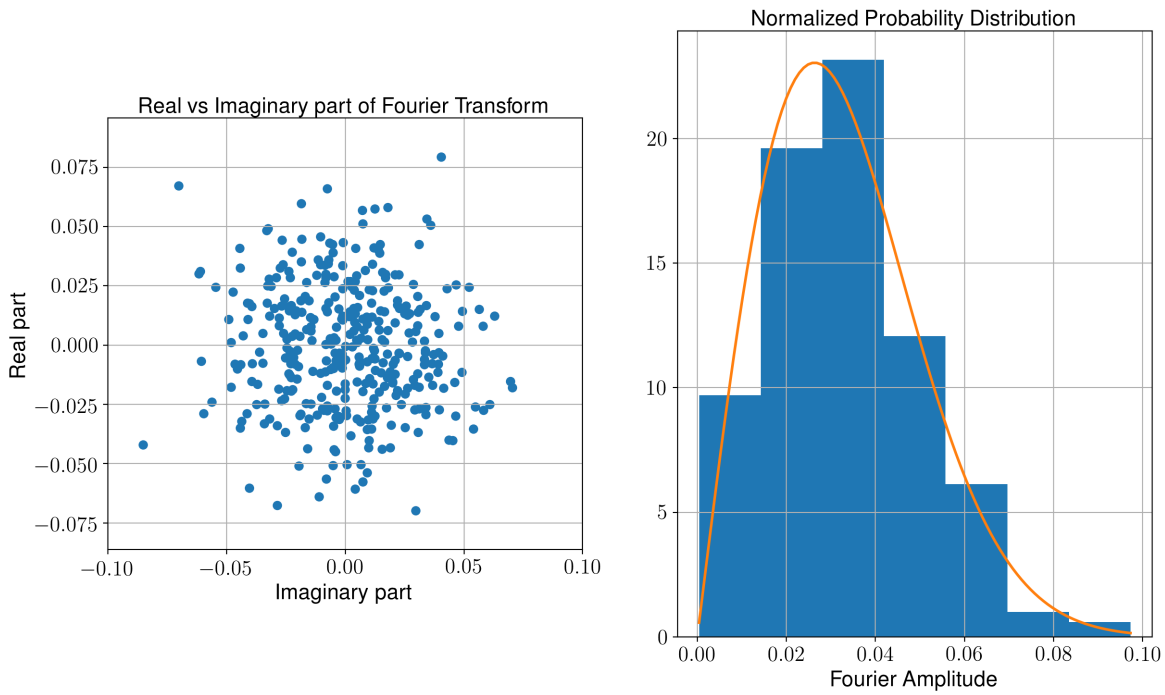

Figure 2.16: The left panel shows 2D plot of the real versus imaginary components of the Fourier transform values for RLC termination residuals. The right panel shows the distribution of amplitudes of the Fourier transform values overlaid with Rayleigh distribution form. The Fourier transform is carried out on normalized residuals; i.e., data residuals are first divided by the corresponding RMS uncertainties and hence the standard deviations of the normalized residuals is unity.

SARAS 2 uses an electrically short spherical monopole antenna, targeting the signal spanning from $40-200$ MHz encompassing CD and EoR. This is in contrast with other experiments which either have different antennas and receiver systems to cover the whole band (EDGES) or target a specific subset of the band (BIGHORNS, SCI-HI and LEDA). The SARAS 2 monopole antenna ensures achromaticity of the beam over its entire wide band; however, suffers from poor efficiency at longer wavelengths. The other experiments, by employing either electrically large antennas or antennas with dimensions matched with operating frequencies, suffer from varying amounts of beam-chromaticity while maintaining good efficiency over their respective bands.

The SARAS 2 antenna design also achieves smoothness of antenna reflection coefficient to 1 part in 10^4, which is desirable in controlling the nature of internal systematics as well as in maintaining a smooth transformation of intrinsic sky signal to the measured spectrum. In other experiments, BIGHORNS antenna has frequency structure at 10^{-1} level [154]. EDGES employs a separate circuitry in the field to measure the reflection coefficient and uses that in the data modeling. LEDA, on the other hand, plans to cross-correlate its radiometer with existing Long Wavelength Array (LWA)

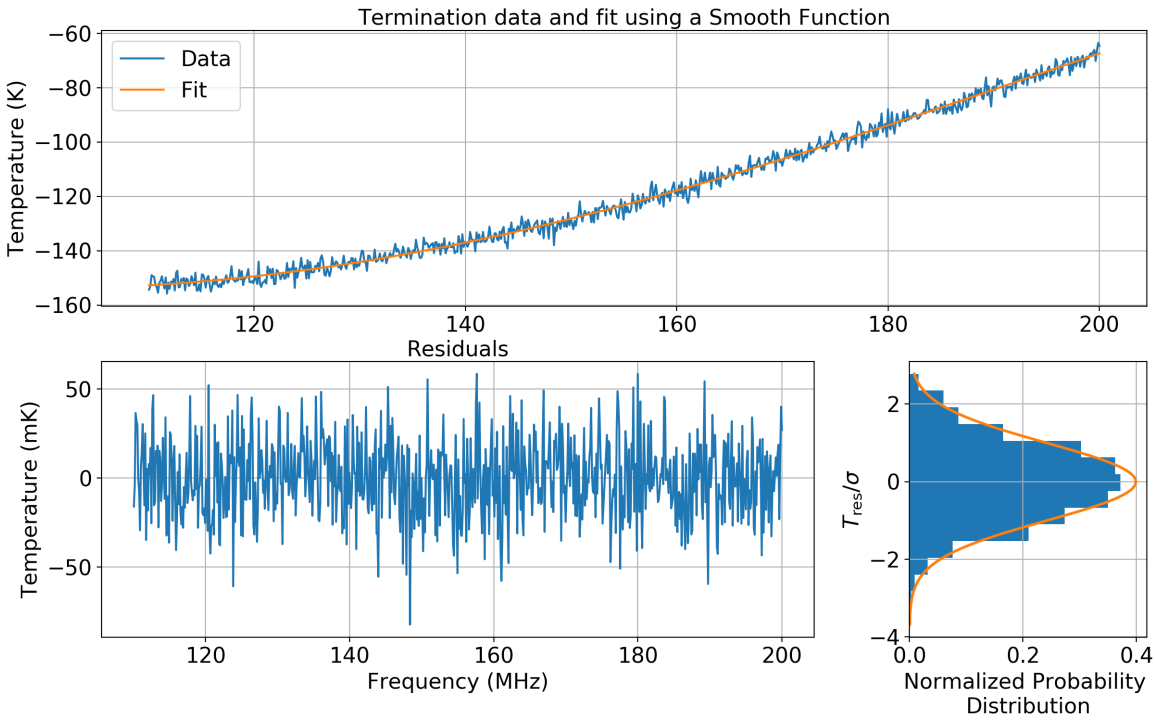

Figure 2.17: The top panel shows the result of a maximally smooth function fit to the RLC termination data. The residuals, including noise, in the data has been amplified by a factor of 100 for better representation (only for the top panel). The bottom left panel shows the corresponding residuals while the bottom right panel shows the distribution of the residuals with an overlaid Gaussian of same mean and standard deviation as that of the residuals. Datasets with comparatively lesser complex shapes; e.g., when the termination is 50 Ω or Open/Short, also reach thermal noise levels on fitting with a maximally smooth function.

antennas and use the interferometer visibilities to solve for the antenna characteristics. Further, the SARAS 2 antenna is the only one that is a monopole and it is the only radiometer that does not have a balun, presence of which can lead to frequency dependent losses that are difficult to calibrate.

Comparing receivers, other experiments essentially measure the autocorrelation of a single RF chain, and the single antenna signal is carried over to their respective digital receivers over RF cables. Further, bandpass calibration is performed by toggling between the antenna and calibration loads or noise source (Dicke switching). SARAS 2 differs from these schemes in that it employs a crosscorrelation spectrometer where the signal is split into two paths immediately after it enters the receiver and the signals in the two RF paths are cross-correlated. Further, instead of toggling between load and antenna, that changes the nature of systematics in each switch position, SARAS 2 utilizes a cross-over switch where the antenna and noise source are connected all the time and hence the nature of systematics remains the same in all switch positions. The combination of crosscorrelation along with the

devised architecture of the receiver results in phase switching which cancels out the spurious additive signals in the process of calibration. For the transmission of RF signal from the receiver output at the antenna to the filters placed 100 m away, SARAS 2 employs optical fibers instead of RF cables. This prevents the undesirable coupling of noise from the filters and amplifiers, which are in the signal processing unit, from one receiver arm to the other via internal reflection at the antenna; such internal reflections can result in the system noise manifesting as additive short period ripples in the measured spectrum.

Table 2.2: Comparison of system designs in different experiments

Experiment	Frequency Range	Antenna	Presence of Balun	Calibration Scheme	Type of Spectrometer
SARAS 2	40 – 200 MHz	Spherical Monopole antenna	No	Noise source coupled into system via power combiner without Dicke switch	Crosscorrelation
EDGES	100 – 200 MHz (High-Band) 50 – 100 MHz (Low-Band)	Blade Antenna	Yes	Switching between antenna and noise source	Autocorrelation
BIGHORNS	70 – 200 MHz	Conical log-spiral antenna	Yes	Switching between antenna and reference load	Autocorrelation
SCI-HI	40 – 130 MHz	HIbiscus antenna	Yes	Switching between antenna, 50 Ω, 100 Ω and short termination	Autocorrelation
LEDA	40 – 85 MHz	Dual-polarized dipole antenna	Yes	Switching between antenna and noise source combined with crosscorrelation from other antennas for antenna gain and beam estimation	Autocorrelation

2.9 Summary

We have developed a wideband precision spectral radiometer, SARAS 2, towards detection of 21-cm global signal from Cosmic Dawn and the Epoch of Reionization in the frequency range 110 – 200 MHz. For each sub-system, as well as for various data processing strategies, we have discussed the favorable features that would aid in the detection. Using these criteria, we have evolved the radiometer design to have characteristics conducive to the experiment.

The electromagnetic sensor is a spherical monopole antenna, with a frequency independent beam along with spectrally smooth reflection and radiation efficiencies. The properties of the antenna have been characterized by simulations and field measurements. As discussed in detail in the next chapter, we have also developed a novel way of measuring the total antenna efficiency using GMOSS and acquired sky data. The analog receiver has been designed such that the system can be calibrated without Dicke switching, along with a mechanism to cancel the spurious additive signals through signal splitting and crosscorrelation. The receiver is connected directly to the antenna thereby minimizing the lengths in the system, which otherwise would result in high order frequency structure. The configuration has been devised to control the nature of internal systematics and keep them spectrally smooth in order to discern between foreground, systematics and the 21-cm signal.

We have outlined the signal path in the system leading to the measurement equation, including multi-order reflections, along with the description and the rationale of the algorithms developed for data pre-processing, calibration and RFI rejection. This is followed by the evaluation of system performance by connecting various terminations replacing the antenna, with increasing complexities of the resulting systematics.

We have analyzed the internal systematics by using the measurement equation to approximate the spectrum as well as by modeling it with a maximally smooth function. Using both these methods, we get data residuals with RMS noise ranging from 15–20 mK for 10 hr of integration for all terminations. The residuals, which are dominated by Gaussian noise, are then tested for the presence of sinusoids and Gaussian shaped structures. Using various tests developed, we place an upper limit of 2 mK for sinusoidal spurious signals and an upper limit of 2–15 mK for Gaussian shaped structures with width in the corresponding range of 20–1 MHz.

Thus the system has been demonstrated to be sensitive to mK levels without being limited by any un-modeled systematic structure, consistent with the requirements of radiometer design for precision measurements of global cosmological redshifted 21-cm from CD/EoR.

Chapter 3

SARAS 2 Observations, Data and Constraints on EoR[†]

"The total amount of energy from outside the solar system ever received by all the radio telescopes on the planet Earth is less than the energy of a single snowflake striking the ground. In detecting the cosmic background radiation, in counting quasars, in searching for intelligent signals from space, radio astronomers are dealing with amounts of energy that are barely there at all." - Carl Sagan

3.1 Introduction

Amongst the primary challenges in the detection of 21-cm from CD/EoR are the accurate modeling of internal systematics and foregrounds. This involves rigorous exercise in modeling the system response, measuring the frequency characteristics of the antenna and developing algorithms to model foregrounds.

Modeling the internal systematics requires a detailed knowledge about the system, signal path and the contributions from different modules of the radiometer. This gains importance since the system response needs to be calibrated or modeled to mK levels. Different aspects of modeling of the internal systematics have been discussed in Chapter 2.

Modeling the foreground from the measurement set needs a detailed insight of the underlying physics of radiative processes that contribute to the observed power. This understanding is enabled

[†]Based on:

1. *Singh, S., Subrahmanyan, R., Shankar, N. U., et al. 2017, The Astrophysical Journal Letters, 845, L12*
2. *Singh, S., Subrahmanyan, R., Shankar, N. U., et al. 2018, The Astrophysical Journal, 858, 54*

by the sky maps available over a range of frequencies and their modeling using a physics-driven approach. These studies have shown the foregrounds to be spectrally smooth without embedded wiggles that can confuse in distinguishing spectral features present in the global 21-cm signal, which is expected to have multiple turning points in its spectrum. Thus foreground removal strategies have tried to exploit the smoothness of foregrounds using constrained parametric and non-parametric approaches [145, 62, 63].

However, equally important to a high precision experiment is an observation site that is radio quiet. Though there are robust routines to detect and flag RFI, they are limited in their abilities to pick up very low lying RFI. This issue is further exacerbated by the different spectral shapes of the RFI, as discussed in Sec. 2.6. Since mitigation routines are mostly sensitive to narrowband RFI, the ones with very broad spectrum, especially with weak amplitudes, can potentially be the showstopper in the detection of the 21-cm signal. We have selected the observation sites through extensive survey of various remote regions in Southern India and trans-Himalayan regions.

In this chapter, we address these challenges, and derive constraints on EoR using the observation data. We begin in Sec. 3.2 with results of a site survey that was undertaken over 2015-16 in remote regions in Southern India and Trans-Himalayan regions in Ladakh, India. We then describe the SARAS 2 observations in Sec. 3.3 and proceed to derive the total efficiency of the antenna using the observations and a global sky model in Sec. 3.4. We perform data quality assessment in Sec. 3.5. This is followed by employing different approaches to modeling the foreground plus systematics leading to constraints on EoR in Sec. 3.6. We conclude in Sec. 3.7.

3.2 Site Survey

For characterization of RFI environment of the sites, we developed a portable radiometer that could be quickly assembled and deployed in remote sites. The electromagnetic sensor was a discone antenna which was connected to the first amplification stage through a 10 m coaxial cable. 100 m coaxial cable from the first amplification stage lead to the shielded enclosure that housed the second amplification and filter stage along with Spectrum Analyzer and a laptop. The Spectrum Analyzer was interfaced with the laptop for data acquisition and recording the measurements. The power to the first amplification stage was supplied through the 100 m coaxial cable through a bias-T. The entire setup was operated on batteries. The setup schematic and the antenna are shown in Fig. 3.2. We present below 30 minute data from different sites surveyed, where we show the median averaged spectrum along with the time-frequency plots from each site. Fig. 3.1 shows the locations of the sites where the RFI environment was characterized.

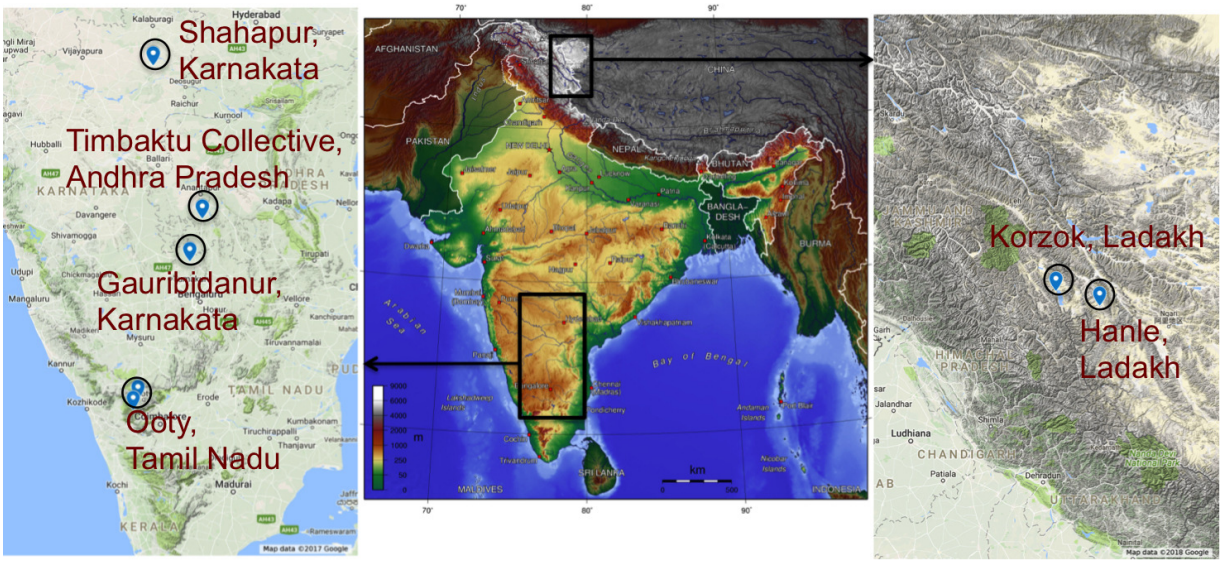

Figure 3.1: Location of different sites where the RFI characterization was carried out.

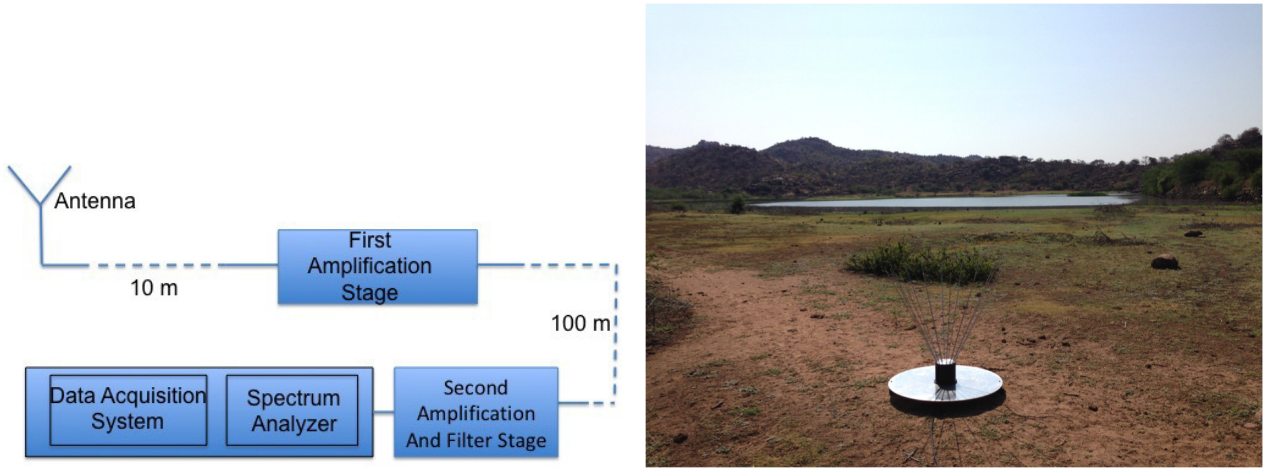

(a) (b)

Figure 3.2: (a) Schematic of the radiometer employed for characterizing the sites and (b) Discone antenna used for the characterization.

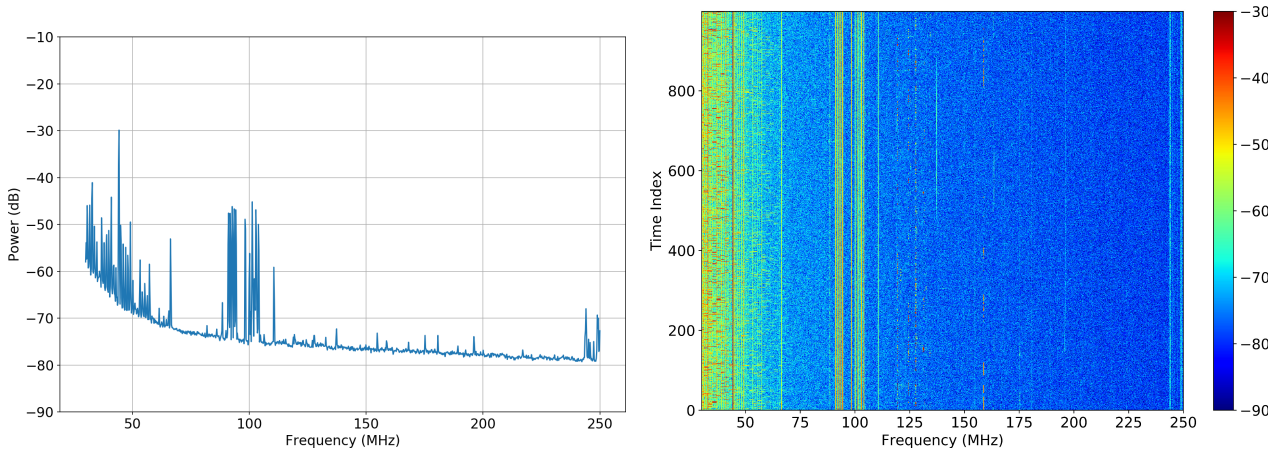

(a) (b)

Figure 3.3: (a) Averaged spectrum and (b) Time-Frequency Plot for Gauribidanur Radio Observatory, Karnataka. Date: 31-01-2015.

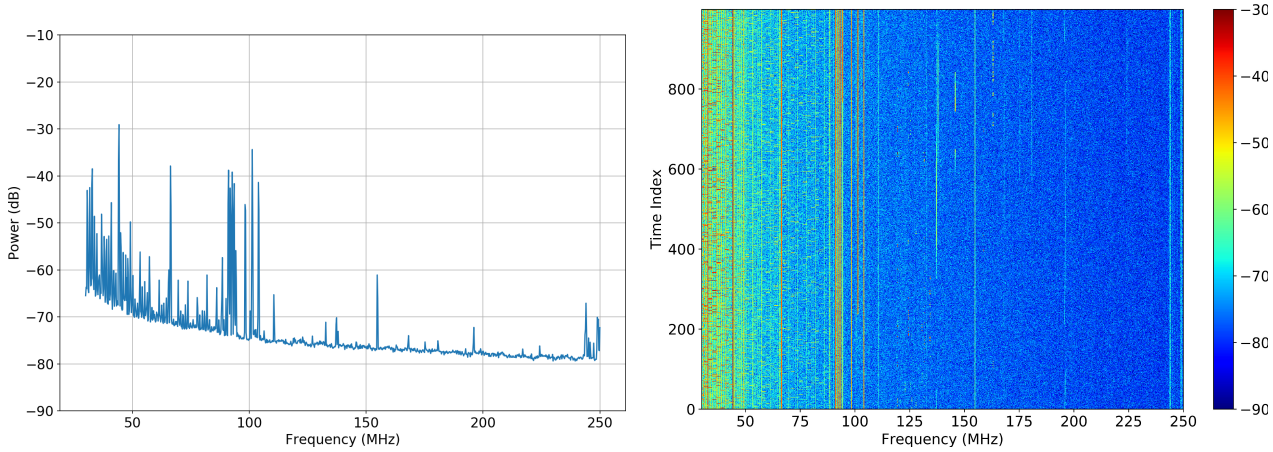

(a) (b)

Figure 3.4: (a) Averaged spectrum and (b) Time-Frequency Plot for Kashapura, Gauribidanur, Karnataka. Though the site is only 6 km from Gauribidanur Radio Observatory (Fig. 3.3), there is a clear deterioration in the radio environment. Date: 31-01-2015.

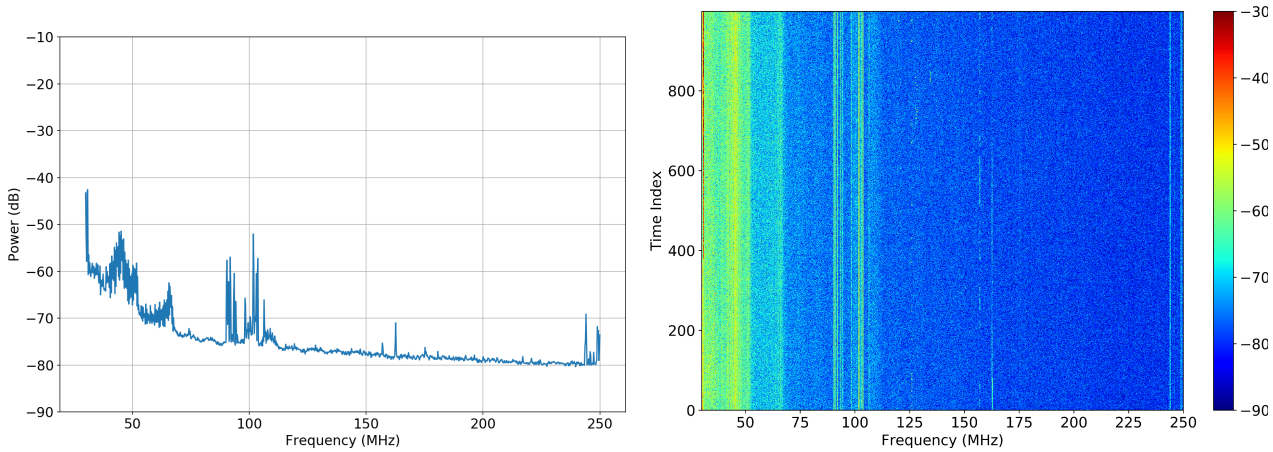

(a) (b)

Figure 3.5: (a) Averaged spectrum and (b) Time-Frequency Plot for Upper Bhawani Region, Ooty, Tamil Nadu. Date: 25-02-2015.

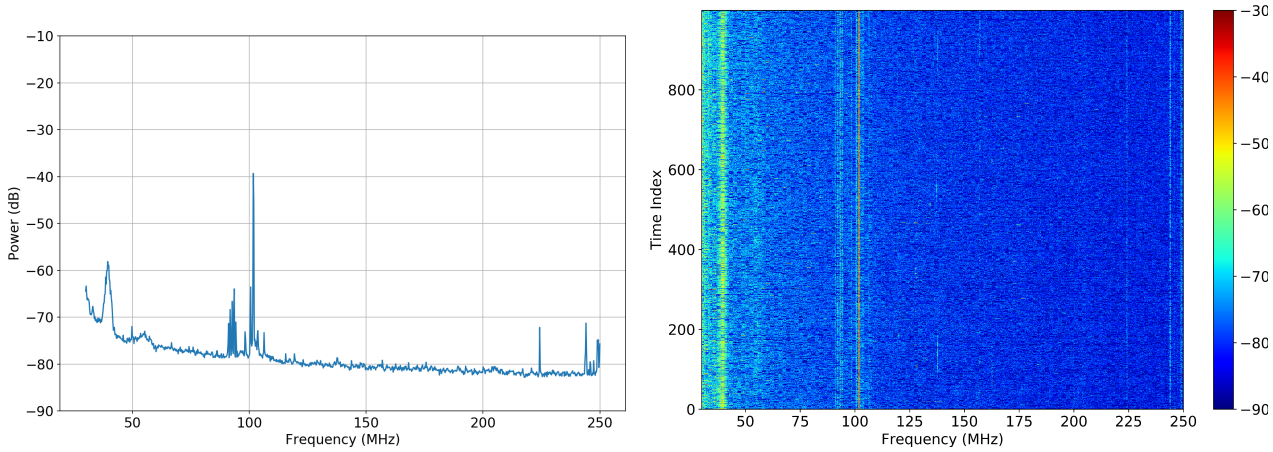

(a) (b)

Figure 3.6: (a) Averaged spectrum and (b) Time-Frequency Plot for Parson's Valley, Ooty, Tamil Nadu. Date: 26-02-2015.

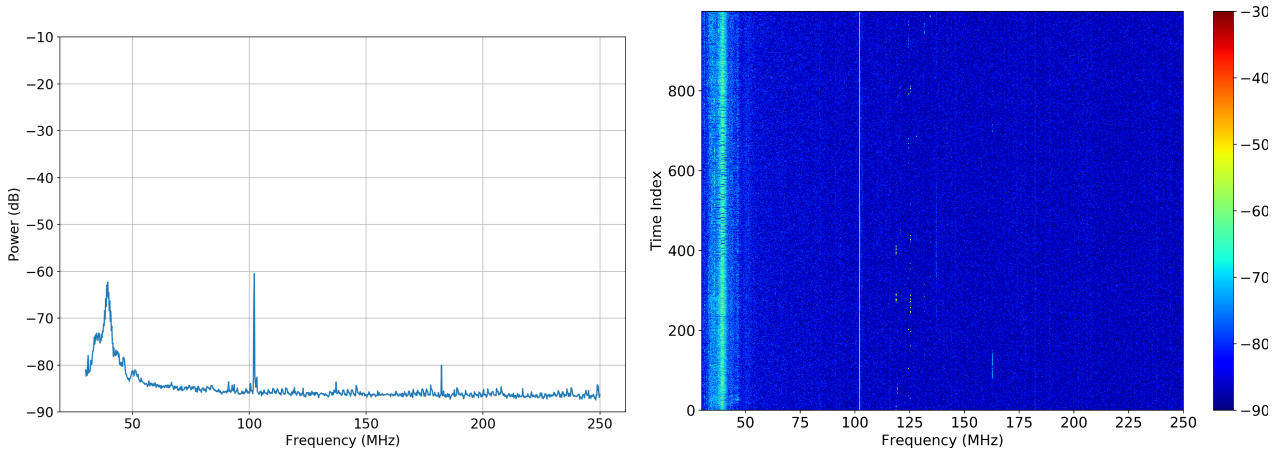

(a) (b)

Figure 3.7: (a) Averaged spectrum and (b) Time-Frequency Plot for Shahapur region, Karnataka. Date: 11-03-2015.

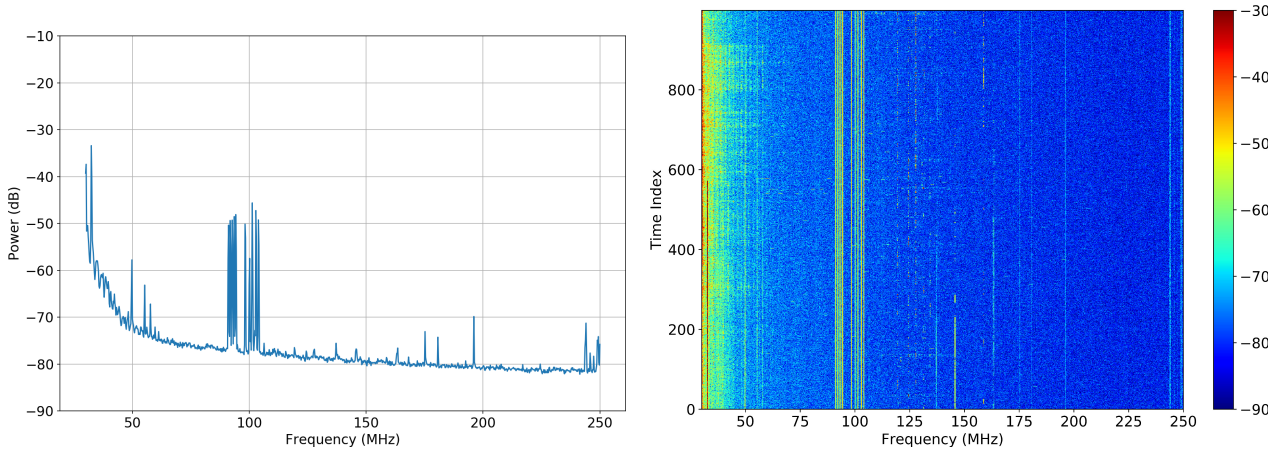

(a) (b)

Figure 3.8: (a) Averaged spectrum and (b) Time-Frequency Plot for Nyamaddala, Andhra Pradesh. Date: 24-03-2015.

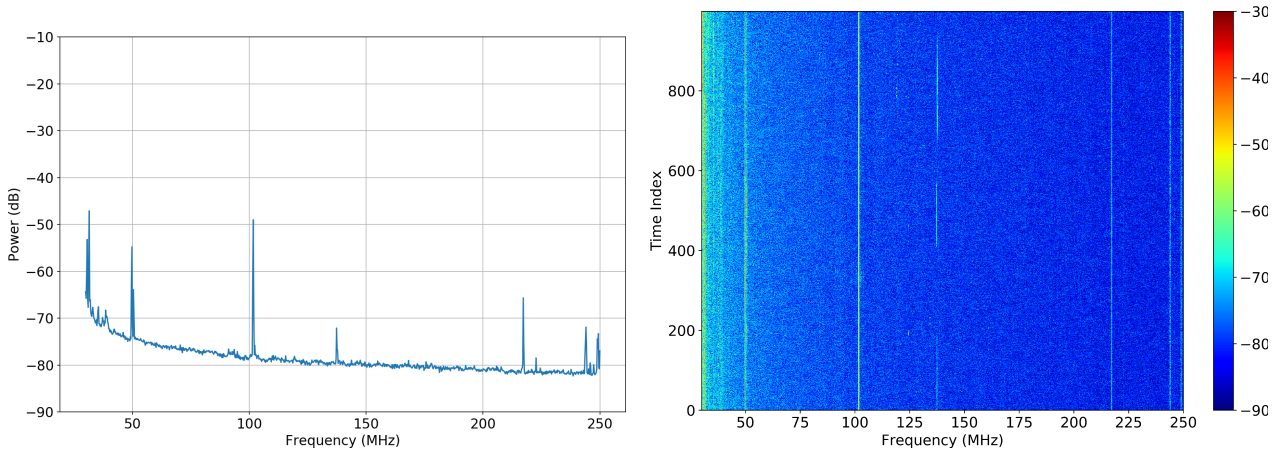

(a) (b)

Figure 3.9: (a) Averaged spectrum and (b) Time-Frequency Plot for Timbaktu Collective, Andhra Pradesh. This again reflects the varying RFI environment in a region. The RFI environment in Fig. 3.8 is only a few kilometers from this site, but the site being a valley surrounded by hills improves the RFI environment considerably. Date: 24-03-2015.

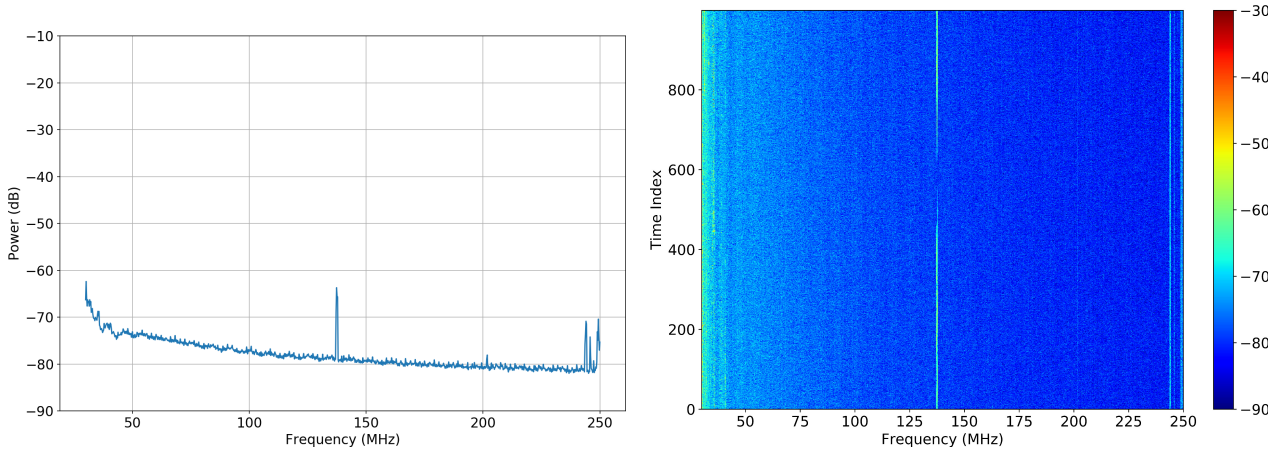

(a) (b)

Figure 3.10: (a) Averaged spectrum and (b) Time-Frequency Plot for Hanle Region, Ladakh, Jammu and Kashmir. Date: 02-04-2016. The comb-like structure in the spectrum is the noise-floor of the Spectrum Analyzer.

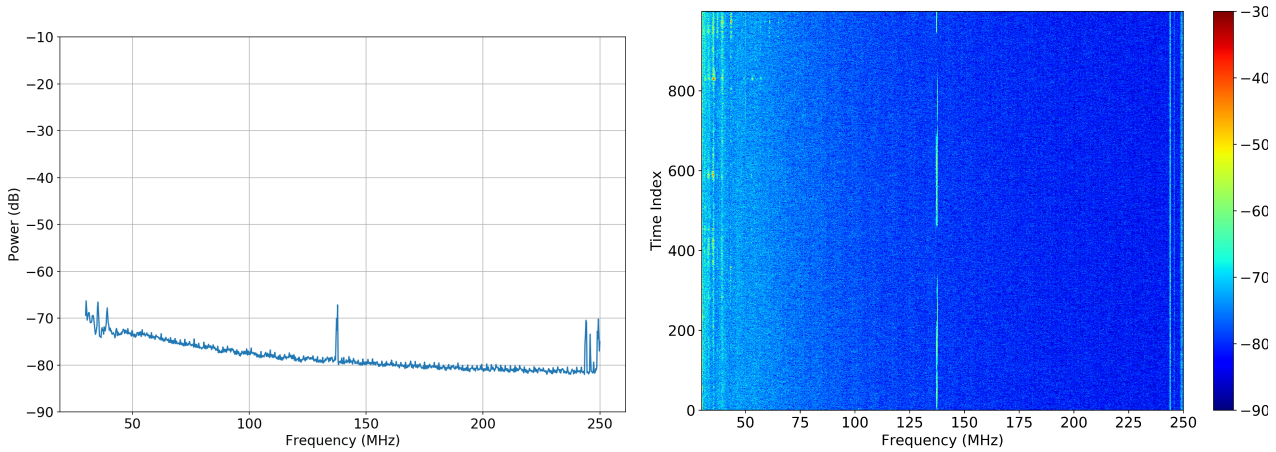

(a) (b)

Figure 3.11: (a) Averaged spectrum and (b) Time-Frequency Plot for Korzok, Ladakh, Jammu and Kashmir. Date: 07-04-2016.

We carried out site survey in six different regions in India, ranging from peninsular to Trans-Himalayan regions. It was interesting to see the variation in the RFI environment within a region. Two clear examples of this were found in Gauribidanur and Timbaktu Collective area. In both the regions, sites separated within 10 km showed different radio environments due to presence of hilly terrain or change in the altitude. The opposite effect was seen in Ladakh region where the sites separated by more than 100 km were very similar in their radio environments.

Based on radio quietness of the sites, ease of performing iterative runs, accessibility and the logistical support, the final set of night sky observations with the current SARAS 2 system were carried out at Timbaktu Collective. From Sec. 3.3 onwards, we present the analysis and results from the data collected at Timbaktu Collective.

3.3 A measurement for the 21-cm EoR global signal

SARAS 2 was deployed at the Timbaktu Collective (Latitude=+14.°242328, Longitude=77.°612606E). Data were acquired over 13 nights from 2016 October to 2017 June. Ionospheric Total Electron Content (TEC) for the entire observing was less than 20 units, corresponding to quiet conditions*. Pre-processing and data calibration was performed within the MIRIAD environment [146] using custom tools.

Data were acquired cycling through each of four states: alternating the cross-over switch and toggling the calibration noise in each switch position. A batch of sixteen 67.1-ms integrated spectra were acquired in each state of the receiver. They were Hampel filtered [61] to reject strong RFI and then

*CODE data archive (ftp://ftp.unibe.ch/aiub/CODE/2016/)

averaged. Common-mode responses of the correlation spectrometer were rejected by differencing spectra corresponding to the two switch states; this was followed by complex bandpass calibration.

The calibrated spectra were processed using algorithms for detection/rejection of data corrupted by lower levels of RFI. Spectra were fit with suitably high-order (10-th order) Legendre polynomials over multiple overlapping bands, in order to fit out plausible models for the EoR spectrum as well as foregrounds and instrumental systematics, and outliers in the residuals were detected using median filters and rejected. This was performed in successive iterations while progressively lowering the detection threshold and repeating the fits. Data were also progressively averaged in frequency and time to detect faint RFI that may be present in contiguous channels and/or times. The algorithm was designed to avoid asymmetric clipping of noise peaks that may result in bias in averaged residuals at levels at which the EoR signal is expected. Details of the calibration process and RFI rejection were discussed in Sec. 2.6.

Long duration laboratory tests of the receiver were done with the antenna replaced by a variety of terminations: open, short and impedance matched terminations and a resistor–inductor–capacitor network with $\Gamma_c(\nu)$ similar to that of the SARAS 2 antenna. All of these, on processing as above and fitted using a single smooth function as defined in Sathyanarayana Rao et al. [143], yielded residuals consistent with expected thermal noise. Different terminations and their corresponding modeling have been presented in Sec. 2.7.

3.4 Measurement of the total efficiency of SARAS 2 antenna using an all-sky model

Using the observation datasets, acquired and processed as described in Sec. 3.3, we developed a method to derive the total efficiency of the SARAS 2 antenna. This is a crucial input to the data modeling and the method is sufficiently generic to be applicable to any antenna. The method uses a global model for the sky brightness distribution. We have used Global MOdel for the radio Sky Spectrum (GMOSS) [144] as the model and the SARAS 2 receiver to measure the total efficiency of the SARAS 2 monopole antenna.

At any frequency, the calibrated measurement data can be decomposed into a sum of contributions from the foreground, ground and receiver systematics. Further, the data is measured with reference to a standard load, whose physical temperature over the observing time is recorded using a logger. The contributions from foreground and the reference load temperature are the only significant time-varying components in the data. Since the instrument bandpass is being calibrated every second, all the temporal variations in receiver gain are calibrated out. Though the ground temperature may vary over the observing time, this is a variation on the surface; the effective temperature of the ground

emission corresponds to the temperature at an effective penetration depth. In the frequencies of interest, the effective penetration depth is ~ 2.5 m [158, Chapter 3]. At this depth, the diurnal temperature variations have been found to be negligible [50]. Thus the contributions from instrument systematics as well as contributions from the ground are essentially time invariant and may be treated as constant additive signals in the spectrum.

The measured temperature, thus, can be represented as :

$$T_A(\nu,t) = \eta_t(\nu)T_{\rm W}(\nu,t) + T_{\rm add}(\nu) - T_{\rm ref}(t), \tag{3.1}$$

where T_A is the measured temperature, $T_{\rm W}$ is the beam-weighted foreground that couples to the system through the total efficiency η_t of the antenna, and $T_{\rm ref}$ is the reference temperature. It is to be noted that we actually measure the physical temperature of the reference load $T_{\rm p}$, which is linearly related to the actual temperature $T_{\rm ref}$. This is because there is a thermal resistance between the actual source of noise and the outer metallic body where the temperature is measured. The time-invariant component of the data consisting of the systematics and ground contributions is represented by $T_{\rm add}$.

Using GMOSS, we decompose the time series data at each frequency into three components:

- a component correlated with temporal variations in the foreground brightness,
- a component correlated with temporal variations in the reference load temperature, and
- a component that is constant over time.

Thus, at any frequency ν we have the following equation:

$$T_A(\nu,t) = \eta_t(\nu)T_{\rm W}(\nu,t) + a_1 T_{\rm p}(t) + a_2(\nu), \tag{3.2}$$

where T_A is the measured equivalent temperature, $T_{\rm W}$ is derived from GMOSS as a weighted average of the model T_B over the sky with a weighting by the antenna beam. $T_{\rm p}$ is taken from the reference load temperature measurements. Using these, we optimize for a_1 using measurement data across time and frequency that includes sufficient LST range so that the antenna temperature varies significantly. η_t and a_2 are optimized for each frequency independently. Constant a_1, along with η_t and $a_2(\nu)$ that are functions of frequency, are globally optimized.

We show the fit for the first term in Eq. 3.2 at four representative frequencies in Fig. 3.12. The curve is a straight line, with slope yielding the total efficiency at the given frequency. This method also provides an estimate of the additive signals in the system $a_2(\nu)$, shown in Fig. 3.13, which may be used as a tool to model the data.

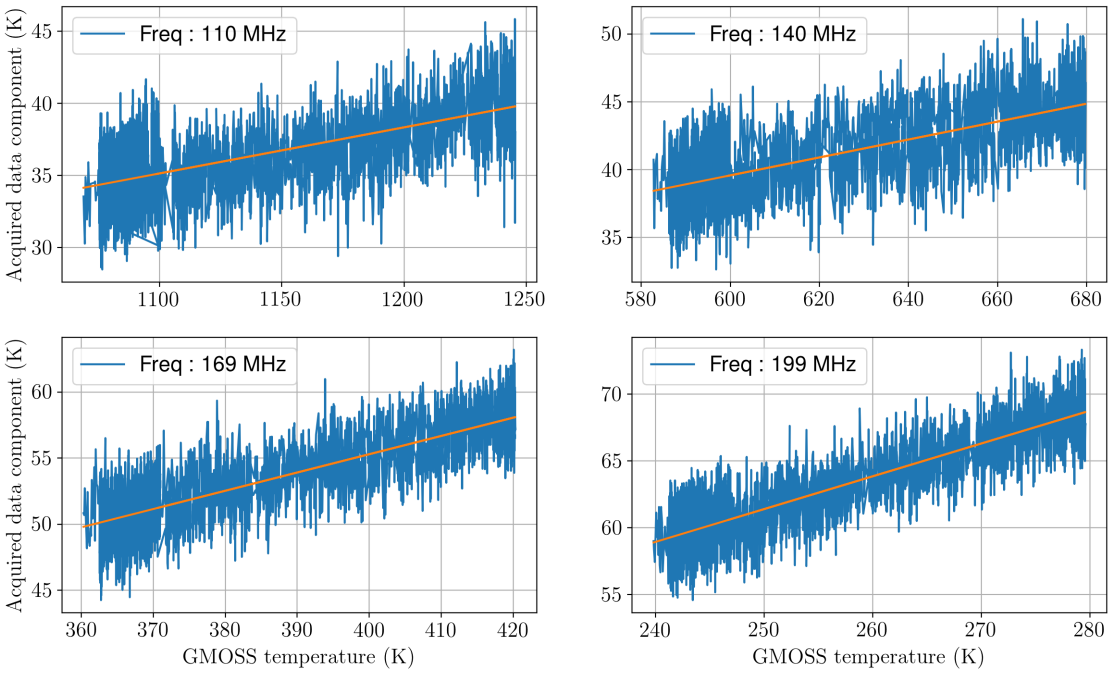

Figure 3.12: The component of data that is correlated with GMOSS foreground predictions shown at four sample frequencies. The slope of the line at each frequency provides an estimate of the total efficiency at that frequency.

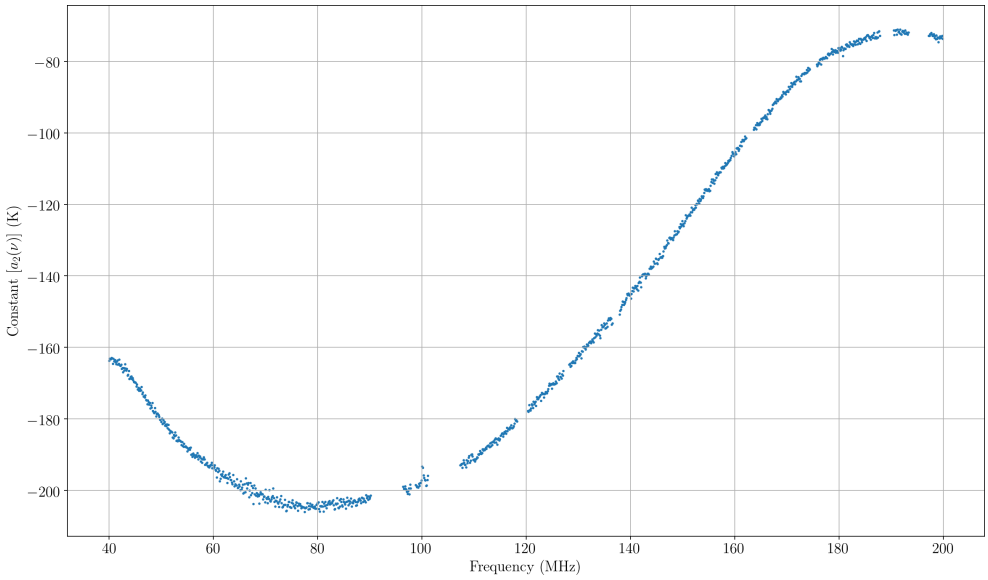

Figure 3.13: The component of data that is time invariant, which includes contribution from foreground, reference temperature, ground and internal systematics.

The resulting total efficiency across the band is shown in Fig. 2.8 and is reproduced in the middle panel of Fig. 3.19 for reference. The total efficiency represents the attenuation with which any EoR signature would be present in observed spectra. It may be noted here that the efficiency is poor and more so at lower frequencies; this was a design compromise made for SARAS 2 in that efficiency was sacrificed for spectral smoothness in the reflection efficiency and frequency independence of the beam. We have discussed this trade-off in Sec. 2.3.1.2.

Poor total efficiency below 100 MHz and rejection of data corrupted by RFI resulted in useful data in the 110–200 MHz band and these calibrated spectra were used for foreground removal and signal detection.

3.5 Data quality assessment

A total of 63 hr of useful night time data were obtained over the frequency band of 110–200 MHz. Data residuals, after modeling for foregrounds and internal systematics, yielded spectra with resolution 122 kHz and root-mean-square (RMS) noise of 11 mK, consistent with expectations from the radiometer system temperature, observing time etc.

The calibrated data, along with the corresponding relative weights across the band, are shown in Fig. 3.14. The weights vary due to different RFI rejections at different frequency channels. We show the representative residuals after 7-th order polynomial fit in Fig. 3.15.

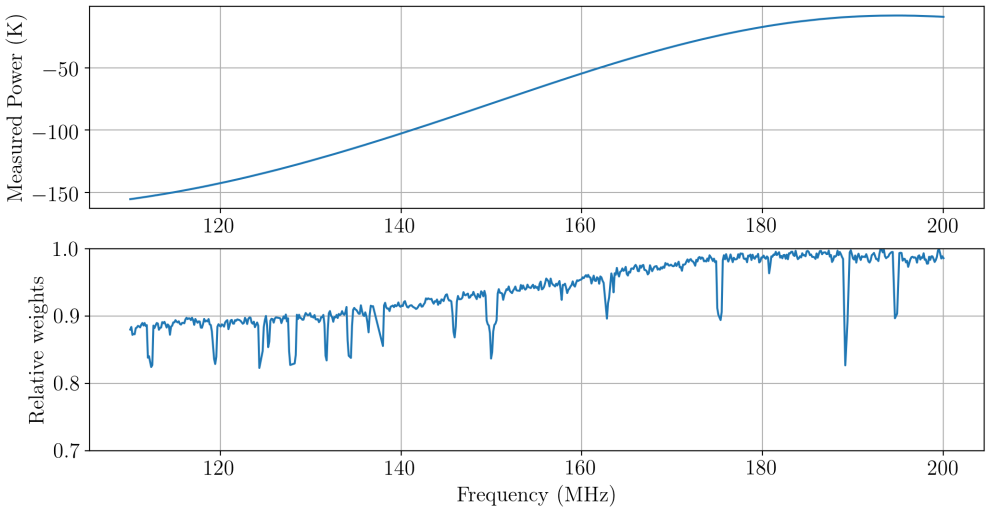

Figure 3.14: The top panel shows the calibrated data. The bottom panel shows the relative weights.

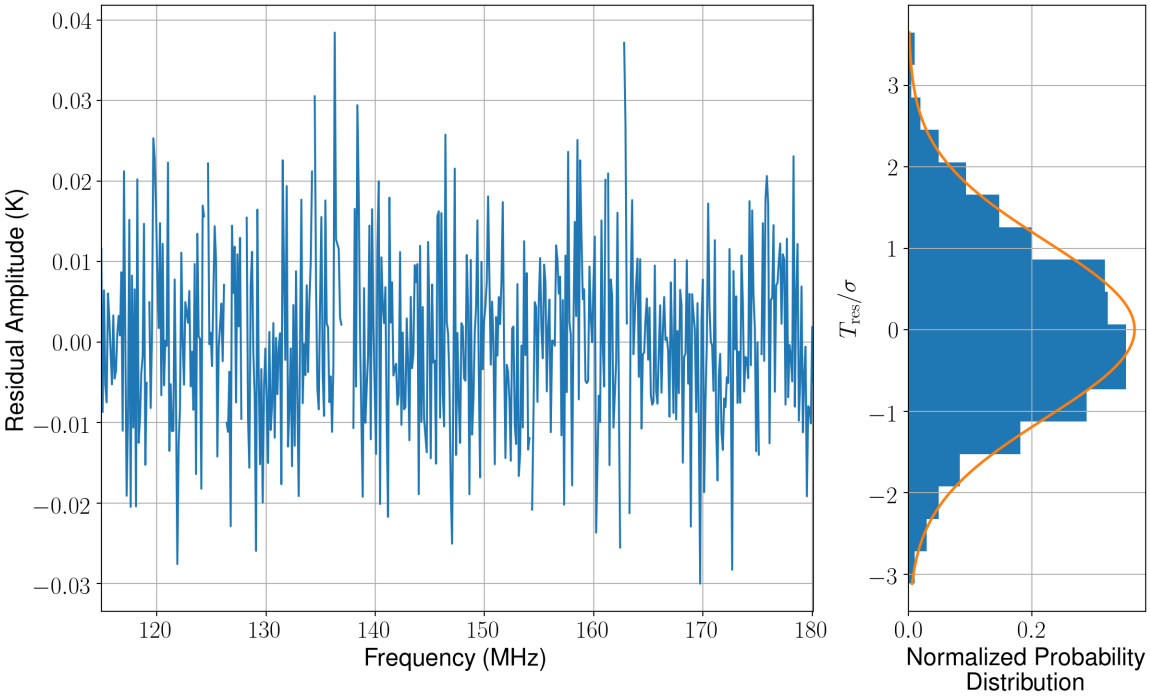

Figure 3.15: Residuals obtained after fitting calibrated sky data, following RFI rejection, with a 7-th order polynomial representing the foreground. On the right is a histogram for the amplitudes along with the best-fit Gaussian. Since data rejection for RFI varies across channels, the channel amplitudes vary in their signal-to-noise ratio and, therefore, amplitudes are normalized by their 1σ errors for the histogram.

We show in Fig. 3.16 the data residuals for 63-hr averaging for polynomial fits with different orders of polynomial. With increasing orders, the residuals are noise-like with no apparent systematic structure present.

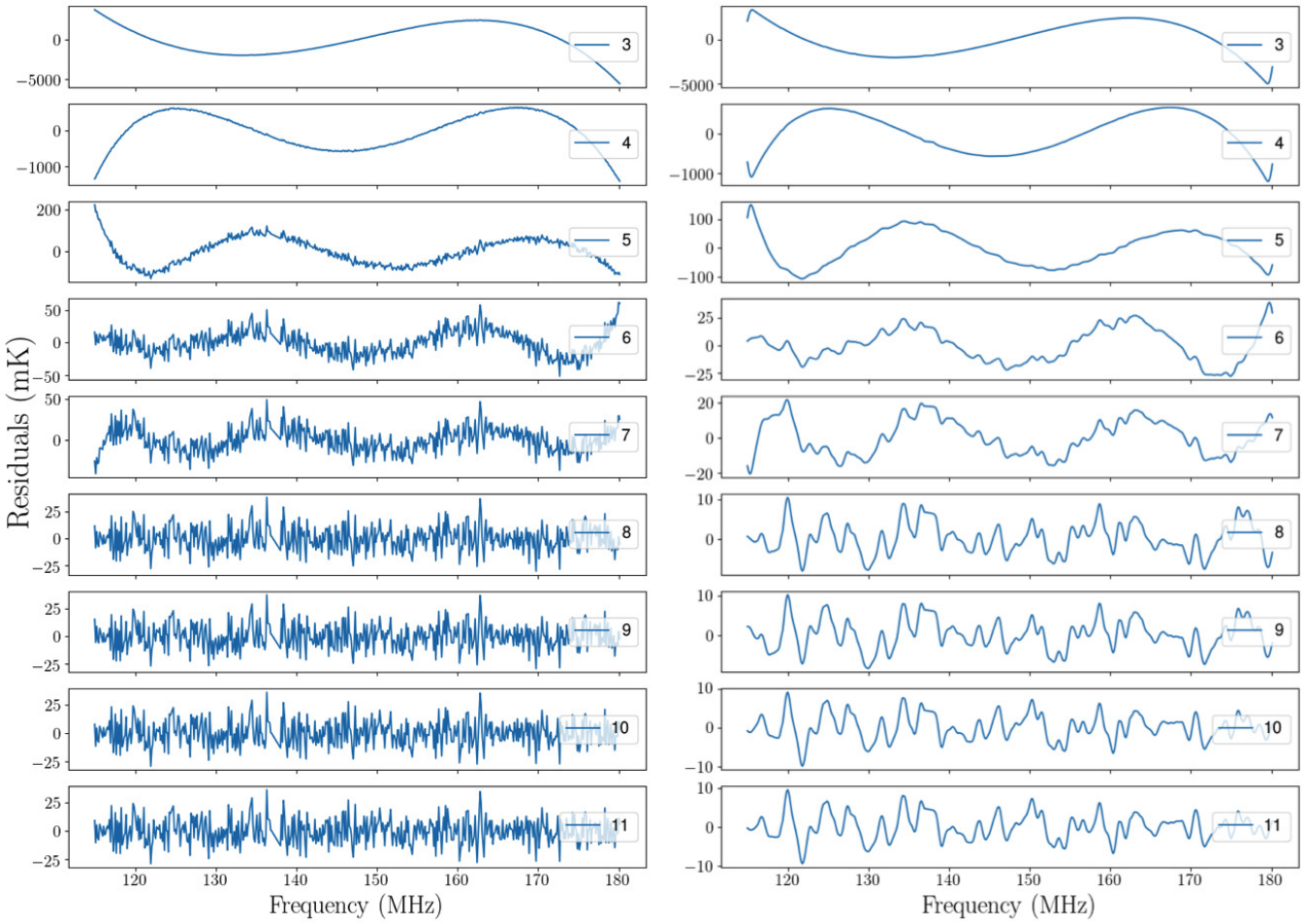

Figure 3.16: The figure shows data residuals obtained after subtracting different orders of polynomials; the numbers in the legends indicate the number of terms in the polynomial fit, order being one less than the number of terms. The panel on the left shows the residuals without any averaging in frequency, while the panel on the right shows the residuals smoothed using Hanning window with width of 1 MHz [114].

We further inspect the data quality across different nights selected for analysis. We show the residuals for different nights in Fig. 3.17 for the 7-th order polynomial fit, which are also consistent with noise with no apparent residual systematics.

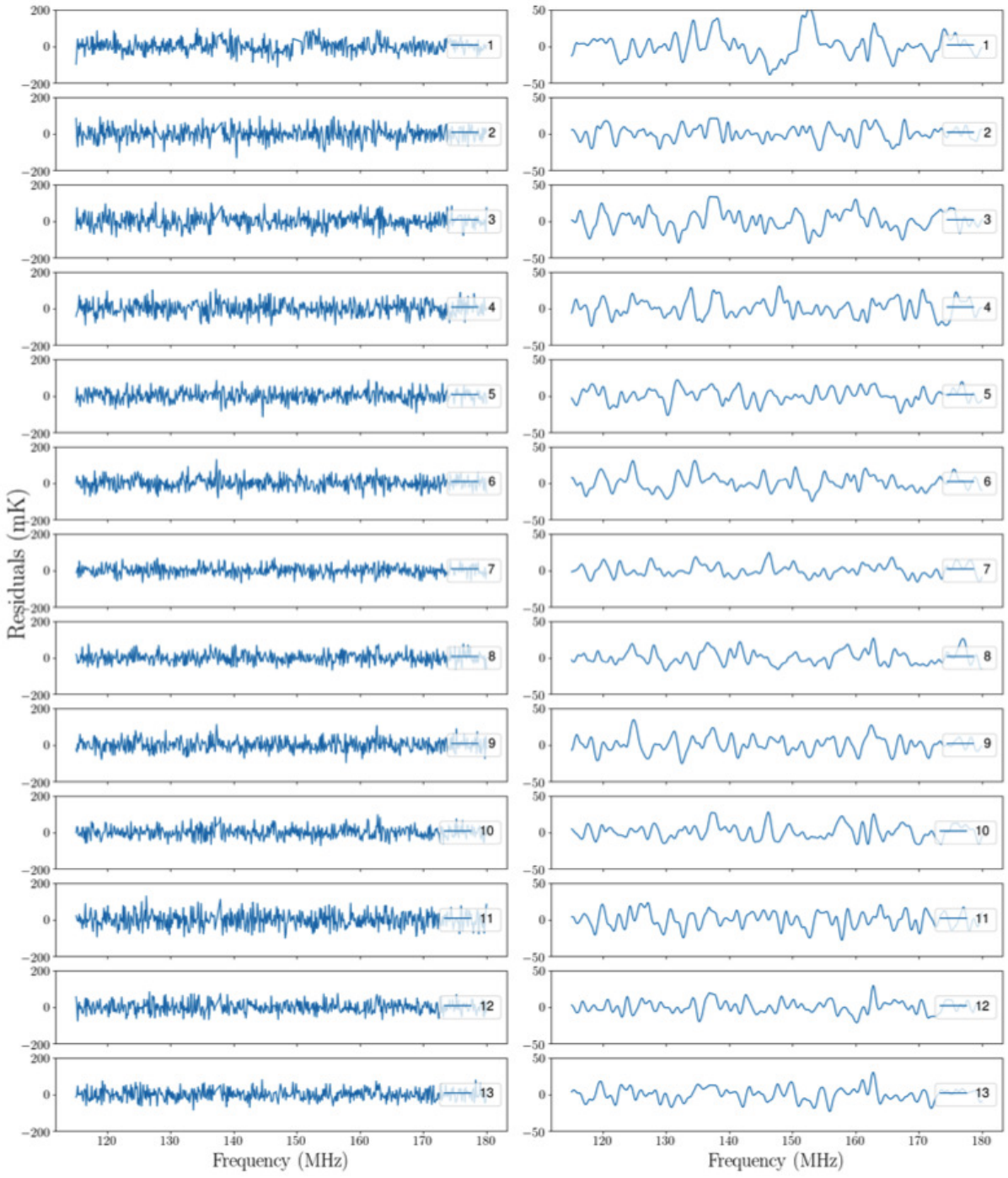

Figure 3.17: The figure shows the residuals from each night selected for analysis, obtained by fitting and subtracting 7-th order polynomial. On an average, the observing time for a single night is ~ 5 hours. The total observing time is 63 hours for 13 nights. The panel on the right shows the residual from each night after averaging in frequency using Hanning window with width of 1 MHz [114]. The numbers in the legend represent indices for different nights.

Finally, since the design philosophy of the radiometer has been to have a spectrally smooth response, we attempt modeling the systematics plus foreground by a single maximally smooth function. As discussed in [143], maximally smooth functions are constrained class of polynomials that do not allow zero-crossings in higher order derivatives. Hence they can fit only to the *smooth* component of the data preserving all the spectral features in the residuals of the fit. Since there are higher order internal reflections of system temperature that contribute above a mK, we allow for a maximum of one inflection point in the band as discussed in Sec. 2.7.3. Using this approach, we obtain the residual spectrum averaged over 63-hr as shown in Fig. 3.18. Employing maximally smooth functions to constrain global 21-cm signals is a work under progress.

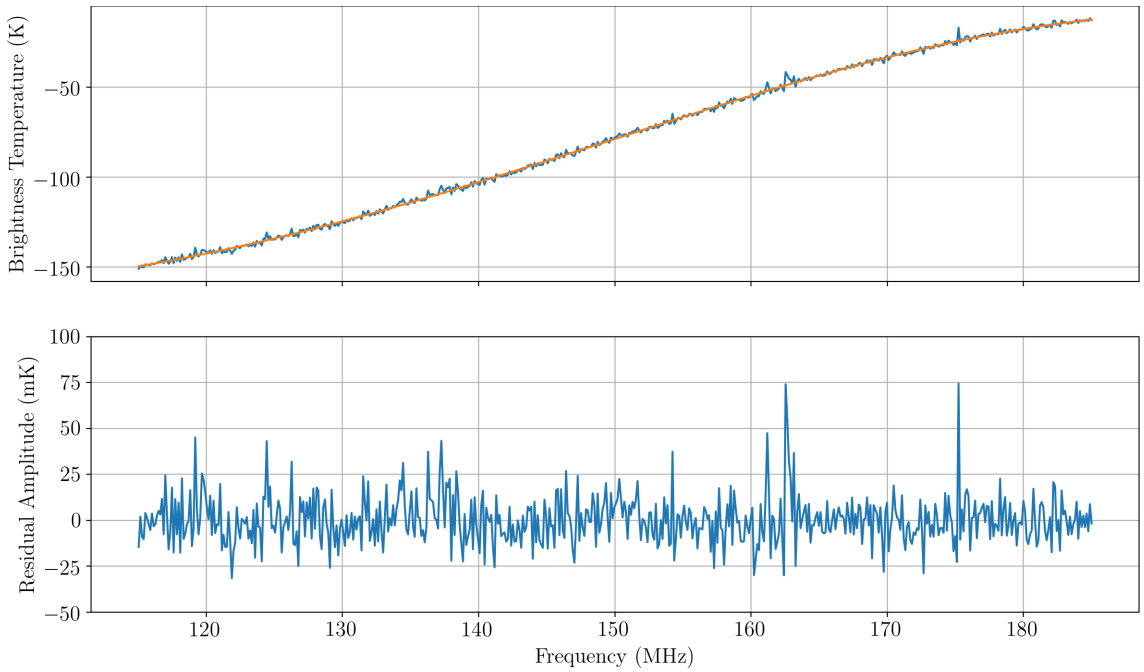

Figure 3.18: The top panel shows the averaged, calibrated spectrum along with the maximally smooth function fit with at most one inflection allowed. The residuals, including noise, in the data have been amplified 100 times for better visualization. The bottom panel shows the residuals of the smooth fit.

3.6 Modeling methods

Modeling the data for internal systematics and foregrounds may be done using several approaches. A physical approach is to use the measurement equation, as described in Sec. 2.4.3.4, along with a physical model for the foregrounds. However, such an approach requires exact functional form to describe the system, foregrounds and other components that are present in the data. In order to

represent foregrounds and systematics, a large number of parameters may become necessary which may have degeneracies between them.

However, since the design philosophy of the radiometer has been motivated towards keeping the system response spectrally smooth, we follow the approach of modeling the data using low-order polynomials to represent internal systematics and foregrounds in a single function. We follow the Bayesian as well as frequentist approach towards constraining the EoR models.

Since the modeling and subtraction of foreground was performed by fitting low-order polynomials, it also inevitably resulted in partial filtering out of the EoR signal. We adopt the global 21-cm templates predicted by the semi-numerical simulations of Cohen et al. [29] as representative of currently allowed signals. The templates are outputs of a self-consistent 4-D (3 spatial dimensions + time) large-scale simulation of the high redshift universe [e.g., 169, 46]. In this simulation X-ray and UV photons emitted by a realistic non-uniform and time-dependent population of sources are propagated accounting for time delay and cosmological redshift. These photons heat and ionize the initially cold and neutral IGM which produces the 21-cm signal.

The cosmological 21-cm signal propagated through the SARAS 2 system, $S(\nu)$, is related to the input cosmological signal, $S_0(\nu)$, by the total efficiency $\eta_t(\nu)$ of the SARAS 2 monopole antenna; *i.e.*, $S(\nu) = \eta_t(\nu) \times S_0(\nu)$. To model the cosmological component in our data analysis we use 264 different theoretical 21-cm spectra presented by Cohen et al. [29]. In Fig. 3.19 (top) we show a representative set of 25 input cosmological spectra in the 40–200 MHz band, from which the contribution of the Planckian form of CMB has been subtracted. To demonstrate the effect of the SARAS 2 system, on the bottom panel of Fig. 3.19 we show the same signals after they have been propagated through the system. The signals are attenuated when propagated through the system due to the total efficiency, with the loss increasing towards lower frequencies. The total efficiency of the SARAS 2 system has been discussed in Sec. 2.3.2.3. We provide the measured total efficiency in middle panel of Fig. 3.19 for reference.

3.6.1 Bayesian Approach

We employ low-order polynomials for modeling the foregrounds and systematics, considering the spectral smoothness of the foregrounds and system response. Since the different EoR templates have different variations with frequency, we separately optimize for different templates the order of polynomial and frequency sub-band for their analysis to maximize the signal-to-noise ratio in the residual. This yields a set of residuals, individually optimized for the detection of different templates, and these are used below for deriving constraints on the EoR.

Any EoR signal appearing in each of the residual spectra obtained after fitting data with appropriate polynomials would be attenuated by the total efficiency η_t, shown in Fig. 3.19, and "high-pass

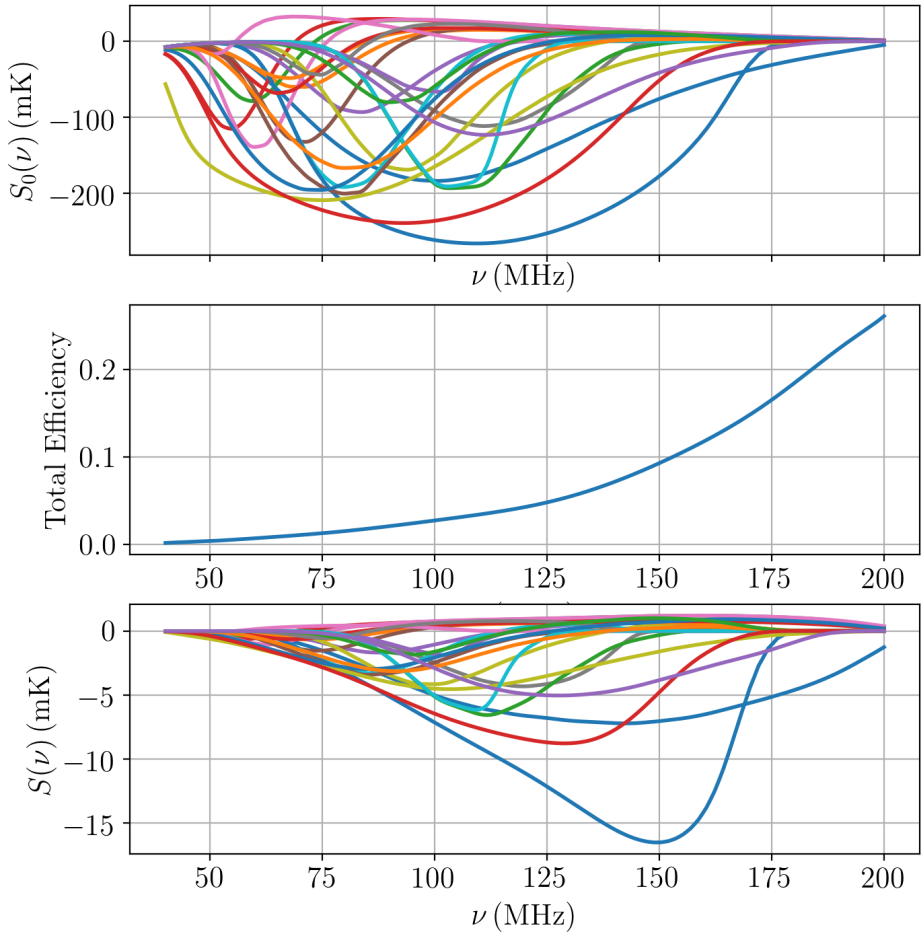

Figure 3.19: Top: A representative set of 25 input global 21-cm spectra $S_0(\nu)$ as a function of frequency [29]. The middle plot shows the total efficiency of the SARAS 2 antenna as computed in Sec. 3.4. Bottom: propagated spectra, $S(\nu)$.

filtered" due to the subtraction of the fitted polynomial from the data.

Corresponding to any plausible EoR signal we may thus construct a "processed" EoR signal that is expected in the residual by fitting out a polynomial of the same order to the attenuated template. We have confirmed via simulations that this polynomial fitting process is linear.

To test for the presence of any plausible EoR signal in the data residual, we compute the ratio of the likelihood of the residual containing the processed signal plus expected Gaussian noise (the alternate hypothesis H_1), and the likelihood of the residual containing just noise (the null hypothesis

H_0). We assume both cases to be equally likely and hence assign uniform priors. The likelihoods are defined to be:

$$P(D|M) = \prod_{i=1}^{N} \frac{1}{\sqrt{(2\pi\sigma_i^2)}} e^{\frac{-(y_i - M_i)^2}{2\sigma_i^2}}, \tag{3.3}$$

where y_i is the data residual in the i^{th} frequency channel, σ_i is the associated error, M_i is the model amplitude at that channel and N is the number of independent frequency channels. We derive the measurement noise σ_i by accounting for all of the data rejection for RFI, measurements of the system temperature, absolute calibration of SARAS 2 and finally from differences between adjacent channel data. The likelihood ratio

$$\mathrm{LR} = \prod_{i=1}^{N} \frac{e^{\frac{-(y_i - M_i)^2}{2\sigma_i^2}}}{e^{\frac{-y_i^2}{2\sigma_i^2}}} \tag{3.4}$$

is the ratio of likelihoods of M being the processed signal to that for M being zero.

To determine the significance of the likelihood ratio corresponding to any particular EoR signal template, we generate mock datasets with the same σ_i distribution as that in the data residual. One dataset D_1 contains the processed EoR template plus noise, while the second dataset D_0 contains only noise. We compute likelihood ratios for D_0 and D_1 for multiple realizations of noise to derive the expected distributions of these likelihood ratios. These distributions are then used to infer the probabilities for false positives and false negatives for the likelihood ratio derived from the data depending on whether the ratio for any EoR template exceeds unity or is below unity [71, Chapter 3].

3.6.2 Constraints from Bayesian Analysis

Given the rms noise in the data and the amplitude of the processed signal, we infer that the data is sensitive to the class of signals corresponding to late heating or poor X-ray efficiency, with $f_X \leq 0.1$ (see Cohen et al. [29] for details), along with peak $\frac{dT_b}{dz} \geq 120$ mK per unit redshift interval corresponding to a rapid rate of reionization. We compute likelihood ratios from the residual data for the 21-cm templates that satisfied these criteria; there were 9 such cases out of the total of 264 in the atlas. In Fig. 3.20 we show these templates as well as their processed residuals.

We show in Fig. 3.21 the likelihood ratios inferred from the data along with the expected distributions of these ratios. For almost all of the signals belonging to this class the distributions of D_1 and D_0 are significantly separated and hence the data has the sensitivity to discriminate between the hypotheses H_1 and H_0 (presence or absence of the signal). Of these allowed signals, six are disfavored in that

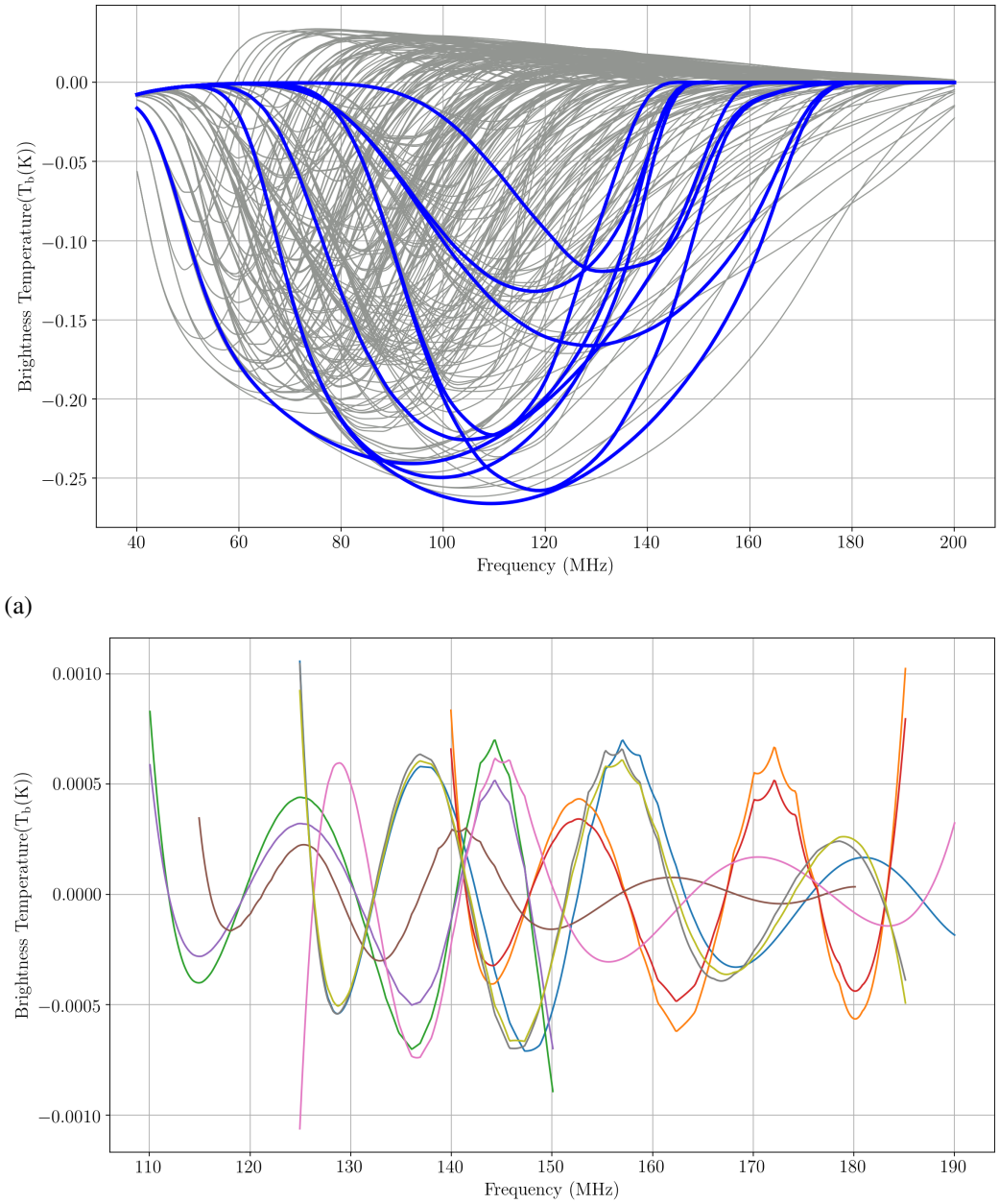

Figure 3.20: Panel (a) shows the atlas of 21-cm templates highlighting those 9 that belong to the selected class of late heating and rapid reionization. The grey curves show models that are not significantly constrained by the data. Panel (b) shows the processed EoR signals, which were obtained from the templates after attenuation by the antenna efficiency followed by high-pass filtering resulting from polynomial fits.

their likelihood ratios place them in the domain of H_0, within its 32^{nd} to 68^{th} percentile band, and the probability of their being false negatives is in the range 14 % to 28%. Two signals have likelihood ratios within the 32^{nd} to 68^{th} percentile band of H_1; however, the probability that these are false alarms is as much as 25 to 30%. In the case of one signal—the one with index number 9 in the Figure—the data analysis leads to a result of relatively poorer significance. The class as a whole, taking into account all 9 signals, has likelihood ratios with an average probability of 31% of being false negatives; therefore, the class of signals is more likely to be from D_0 than D_1. This implies that the data is more consistent with noise-only hypothesis as against the hypothesis in which noise and template are present. We thus disfavor this class of models with $f_X \leq 0.1$ and peak $\frac{dT_b}{dz} \geq 120$ mK per unit redshift interval with 69% confidence.

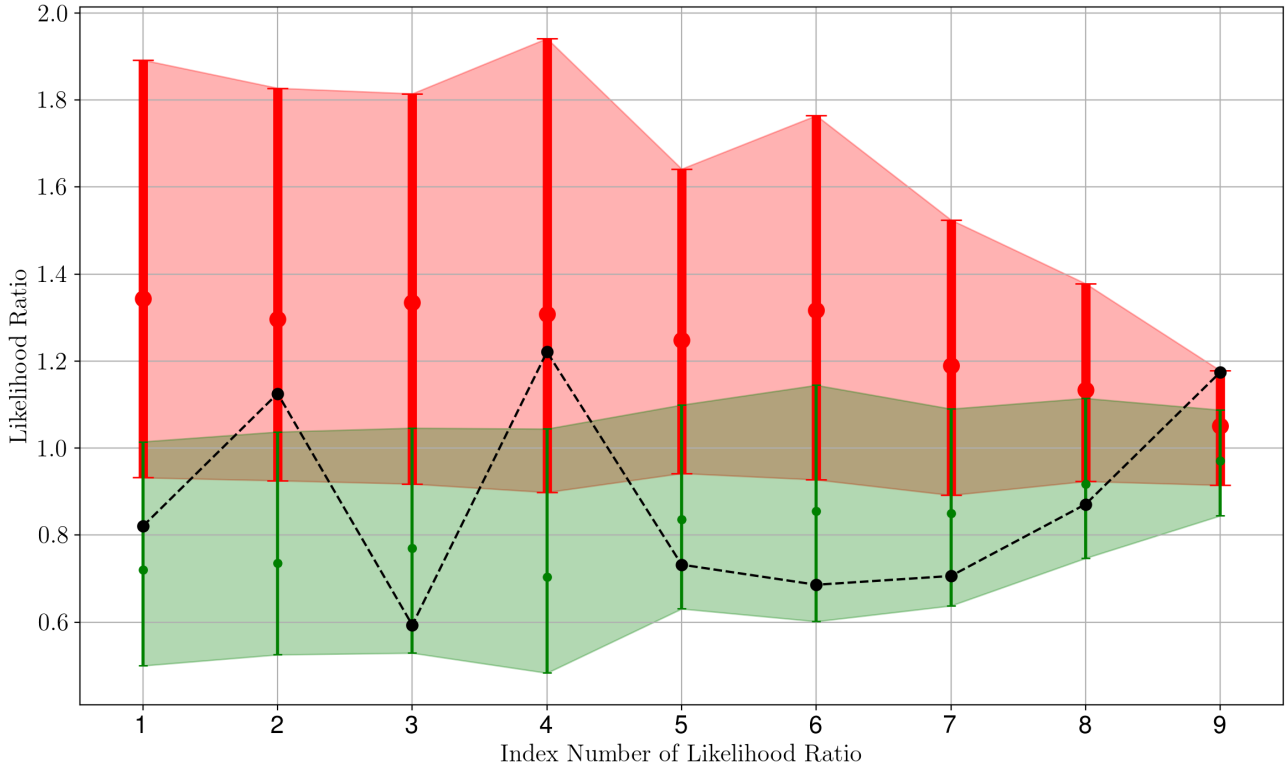

Figure 3.21: Likelihood ratios for the 9 EoR templates that belong to the class defined in the text. For each template, we show the inferred likelihood ratio from the data (marked in black and connected using a dotted line). We also show the extents (from 32^{nd} to 68^{th} percentile) of the distributions of D_1 and D_0 as shaded regions. The regions corresponding to the hypotheses H_1 (upper vertical column) and H_0 (lower vertical column) are shown in red and green respectively; their medians are shown using filled circles.

The models that are disfavored by the Bayesian analysis all lie in the area of parameter space corresponding to late heating [48], actually a regime we might call very late heating, in which cosmic reionization ends without the global 21-cm signal having reached emission. More specifically, the analysis disfavors models that have late (i.e., weak) X-ray heating and a rapid end to reionization (due, for example, to large galaxies dominating star formation and a large mean free path available within the ionized bubbles).

3.6.3 Forward Modeling using Frequentist Approach

We adopt the frequentist approach of Monsalve et al. [98], and forward modeling, and revisit prospects for each one of the cosmological signals examined in Sec. 3.6.1.

3.6.3.1 Foreground Modeling

The observed data consists of the cosmological and foreground signals, propagated through the SARAS 2 system (Fig. 3.19), plus the internal systematics generated by the instrument. Both the foreground and the systematics are modeled using polynomials over an optimal frequency band (as described below). The total contribution of foregrounds and systematics is thus $F(\nu) = \sum_{i=0}^{N} c_i \nu^i$, where c_i are the $(N+1)$ coefficients of the polynomial.

3.6.3.2 Sensitivity Test

In this Subsection our goal is to determine the optimal frequency band $\Delta_{1,2}$, covering frequency range ν_1 to ν_2, and the polynomial order, N, of $F(\nu)$ which provide the best constraint on the particular signal template, $S_0(\nu)$. Using this information we derive confidence with which each theoretically proposed signal is ruled out by the SARAS 2 data.

We first perform a sensitivity test which, for each one of the 264 input templates $S_0(\nu)$ and given $\Delta_{1,2}$ and N, determines whether or not the signal can in principle be extracted from the data considering the RMS thermal noise and the total efficiency of the system $\eta_t(\nu)$. The test delineates the 2D $\Delta_{1,2}$–N parameter space in which the signal can be either detected or rejected with at least 1σ confidence.

For given $\Delta_{1,2}$ & N we first generate 500 independent realizations of mock thermal noise with Gaussian statistics. The RMS thermal noise in any mock spectrum is made same as that in the data within the corresponding frequency band. We then add the propagated signal $S(\nu)$, in the frequency range ν_1 to ν_2, to each realization of the mock thermal noise, creating 500 mock datasets. Each one of these datasets is then jointly fit with a model,

$$M(\nu) = F(\nu) + a \times S(\nu), \tag{3.5}$$

using linear least squares [130], where a is a scale factor for the signal. The procedure returns best-fit values of the scale factor and coefficients of the polynomial, c_i, for each mock dataset separately. For each realization of the thermal noise, the fitting uncertainties in the polynomial coefficients, σ_{c_i}, and in the scale factor, σ_a, are computed as part of the modeling process from the covariance matrix. We next perform joint fitting for all the 500 datasets and derive the mean, $\bar{a}$, and standard deviation, $\sigma_{\bar{a}}$, for the scale factor across the ensemble of the mock datasets.

For a detection, the computed scale factor, $\bar{a}$, should be consistent with unity within the fitting uncertainties $\sigma_{\bar{a}}$. In other words, for each input signal $S_0(\nu)$ to be detected with more than 1σ confidence, and assuming the particular choice of $\Delta_{1,2}$ & N, we require the following condition to be satisfied:

$$0 < (\bar{a} - \sigma_{\bar{a}}) \leq 1 \leq (\bar{a} + \sigma_{\bar{a}}). \tag{3.6}$$

If this condition is not satisfied, we infer that the collected data (given its thermal RMS noise, $\Delta_{1,2}$ & N) is not sufficient to detect the particular $S_0(\nu)$ at 1σ level.

This exercise ignores foregrounds and systematics that may leave residuals thus confusing detection of the 21-cm signal. Therefore, it should be considered only as a feasibility test which helps to determine whether or not the RMS noise is sufficiently low for a detection with significance greater than 1σ. This sensitivity test affirms that if (i) the 21-cm signal is indeed present in the measurement data, and (2) there are no residual foregrounds and systematics limiting the decision, then the best fit results should yield $\bar{a} = 1$ with confidence exceeding 1σ.

Examination of the distribution of $\bar{a}$ for different $\Delta_{1,2}$ & N provides a 2D parameter space ($\Delta_{1,2}$–N) in which the condition above is satisfied. We use the allowed values of $\Delta_{1,2}$ & N in the next Subsection to test each template against real data. If for a particular 21-cm signal the $\Delta_{1,2}$–N parameter space is empty, this template is taken out of the ensemble and is not searched for. Therefore, the sensitivity test may be viewed as a preliminary filter that selects potentially good candidate 21-cm signals which can be detected/rejected using the collected data.

3.6.3.3 Fitting the data

We construct a set of models (Eq. 3.5) for each one of the 21-cm signals that pass the sensitivity test and for every combination of $\Delta_{1,2}$ & N from the allowed part of the parameter space. We fit every model to the real data using linear least squares. The objective function defined as

$$\chi^2 = \sum_{\nu_1}^{\nu_2} w_{\nu_i}^2 (y_{\nu_i} - M(\nu_i))^2 \tag{3.7}$$

is minimized, where y_{ν_i} is the real data in the ith frequency channel and $M(\nu_i)$ is the model (Eq. 3.5). w_{ν_i} are the relative weights for the data in each frequency channel i based on the system temperature and effective integration times, which differ across the band depending on the RFI excision during the processing.

In the fitting procedure to the SARAS 2 data, for each given theoretical 21-cm signal that passes the sensitivity test, the optimal $\Delta_{1,2}$ and N are selected to be the combination for which the fit yields minimum uncertainty in the scale factor. The best fit scale factor is denoted as $\tilde{a}$ with the standard deviation, $\sigma_{\tilde{a}}$, given by the relevant diagonal term in the corresponding covariance matrix. In our analysis of all the plausible theoretical 21-cm signals in the atlas, the median value of the optimal N is 3, and the associated frequency band is 110–180 MHz. This is consistent with the fact that the foregrounds as well as internal systematics of SARAS 2 are indeed spectrally smooth and hence require only low-order polynomials for the modeling. Typically, larger N remove a greater part of the 21-cm signal; and, therefore, return a larger uncertainty $\sigma_{\tilde{a}}$; while smaller N are not sufficient to fit the foreground thus leaving behind larger residuals and increase the uncertainty $\sigma_{\tilde{a}}$.

For each valid theoretical 21-cm signal we compute a standard score, ζ, given by

$$\zeta = \left| \frac{1-\tilde{a}}{\sigma_{\tilde{a}}} \right|. \tag{3.8}$$

The value of ζ yields the confidence of the rejection in units of $\sigma_{\tilde{a}}$. Based on this score we rule out any 21-cm signal with $\zeta > 1$, which ensures that the signal is inconsistent with the data at greater than 1σ confidence level.

For none of the considered theoretical models $\tilde{a}$ was found to be consistent with unity, which would indicate a detection. However, we find that for all the theoretical 21-cm signals which pass the sensitivity test, the condition for rejection is satisfied with confidence above 1σ; 25 templates have greater than 5σ rejection significance. These cases are shown in colors in Fig. 3.22 with each color representing the significance of rejection according to the colorbar. The corresponding residuals are shown in the bottom panel of Fig. 3.23. Both the number of rejected cases and the significance of rejection are an improvement compared to Bayesian approach in Sec. 3.6.1. We note that very high values of rejection significance should be interpreted cautiously since the real data may include significant systematics with substantial non-Gaussianity.

3.6.4 An alternative method of model fitting using non-linear optimization

The method of sensitivity test and fitting the data adopted in Sec. 3.6.3 employs linear least squares where the best fit scale factor, $\tilde{a}$, is unconstrained in the process of modeling. Such an approach may lead to unphysical values of the scale factor.

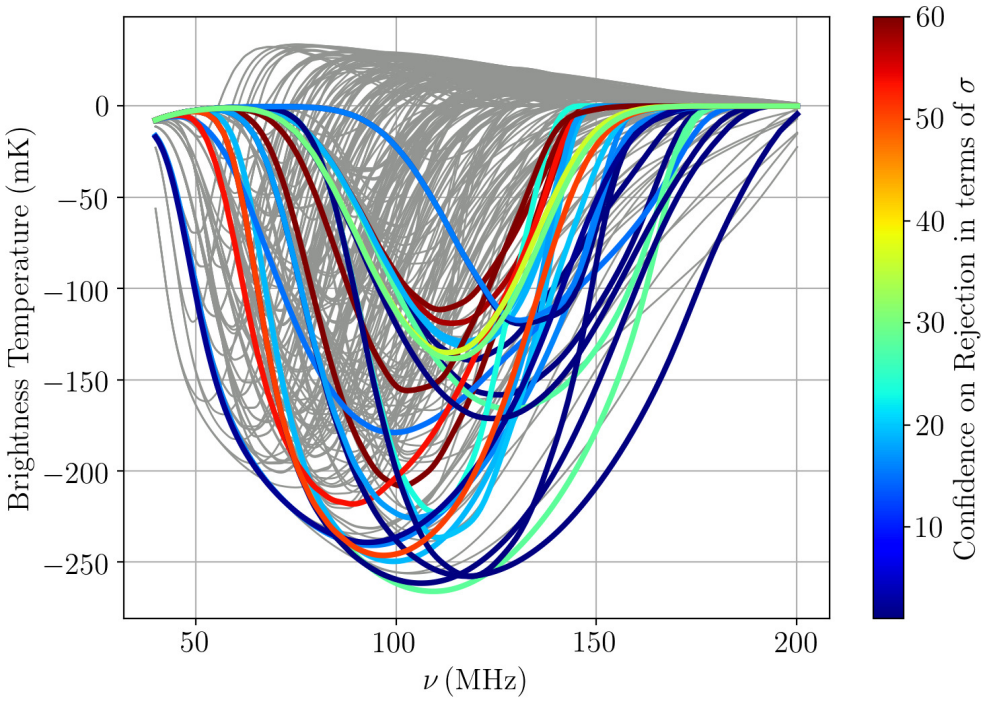

Figure 3.22: The entire set of 264 theoretical models [29]. The rejected signals are shown in color with each color corresponding to the rejection significance as indicated by the colorbar. The data does not have sensitivity for the signals shown in gray. Linear least squares was used to model the foregrounds+systematics.

In order to perform a constrained joint optimization of scale factor with the polynomial terms, we compute the coefficients and their associated uncertainties using Levenberg-Marquardt algorithm [86] for sensitivity test and fitting the data. Except for the method of optimization, the framework for sensitivity test and data fitting remain the same, where the model is described by Eq. 3.5 while the objective function to be minimized is given by Eq. 3.7.

Non-linear optimization routines are often biased by the initial guess on the parameters to be estimated; therefore, in the case of the sensitivity test described in Sec. 3.6.3, since we are testing for a detection, we provide an initial guess of 0 to the parameter $\tilde{a}$. Conversely, in the case of modeling the real data, where we are seeking to identify 21-cm signals that may be ruled out, we provide an initial guess of unity for $\tilde{a}$. Thus, by providing initial guesses that are the opposite of the outcomes being examined for, we conservatively minimize the chances of a false rejection of 21-cm signals in the fitting to the data. Further, for the given signal, we disallow scale factors less than 0, which would then correspond to a different, inverted signal.

The median value of the optimal N and the associated frequency band with this approach continues

to be the same as that obtained via linear least square approach.

Since this is a constrained non-linear approach to compute the scale factor, we take a more conservative approach in rejecting a signal. We rule out any 21-cm signal for which the following condition is met:

$$(\tilde{a} - \sigma_{\tilde{a}}) \leq 0 \leq (\tilde{a} + \sigma_{\tilde{a}}) < 1. \tag{3.9}$$

While $(\tilde{a} + \sigma_{\tilde{a}}) < 1$ ensures that the signal is inconsistent with the data with greater than 1σ confidence, the condition $(\tilde{a} - \sigma_{\tilde{a}}) \leq 0 \leq (\tilde{a} + \sigma_{\tilde{a}})$ ensures that the best fit scale factor is consistent with 0 within $\pm 1\sigma$. The value of ζ, as defined in Eq. 3.8, yields the confidence of the rejection in units of σ.

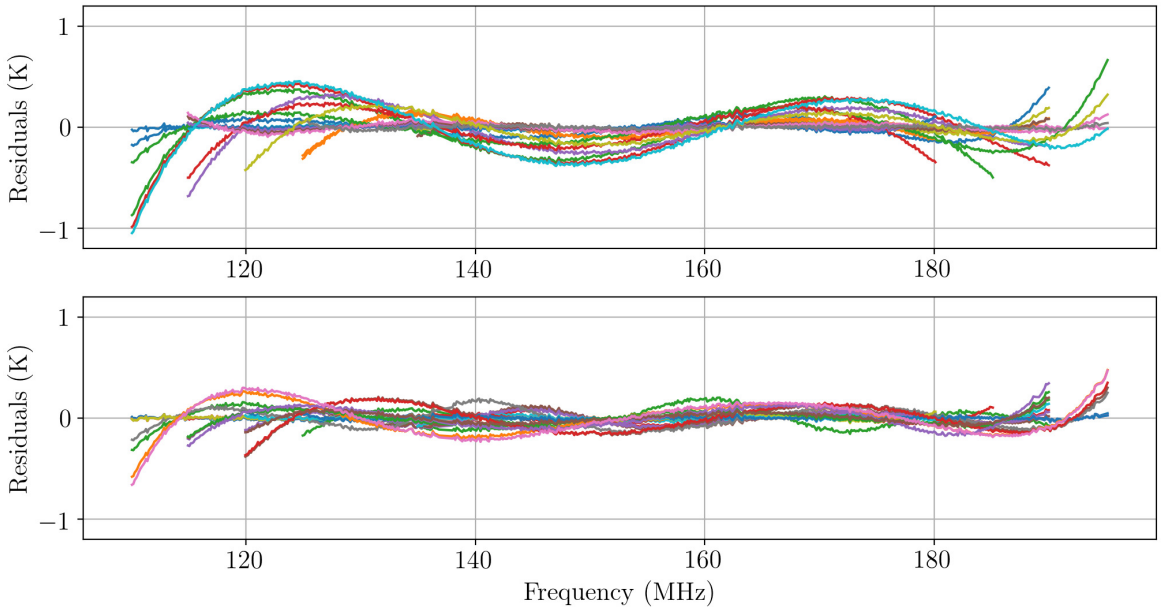

Figure 3.23: The figure shows the residual obtained after subtracting the fit model from data, with band and number of polynomial terms chosen based on the minimum error on scale factor. Different colors represent residuals for different rejected 21-cm templates. The fitting was performed using non-linear least squares for computing the residuals for top panel while the residuals in bottom panel were obtained using linear least squares.

Using the method of non-linear optimization and same set of theoretical models of global 21-cm signals, we reject 20 templates with significance of rejection exceeding 1σ. The rejected templates form a subset of models ruled out using linear least squares. We highlight the rejected models in Fig. 3.24 where the color denotes the significance of rejection in units of σ. The corresponding data residuals are shown in top panel of Fig. 3.23. We next proceed to investigate the parameter space spanned by the 20 rejected templates.

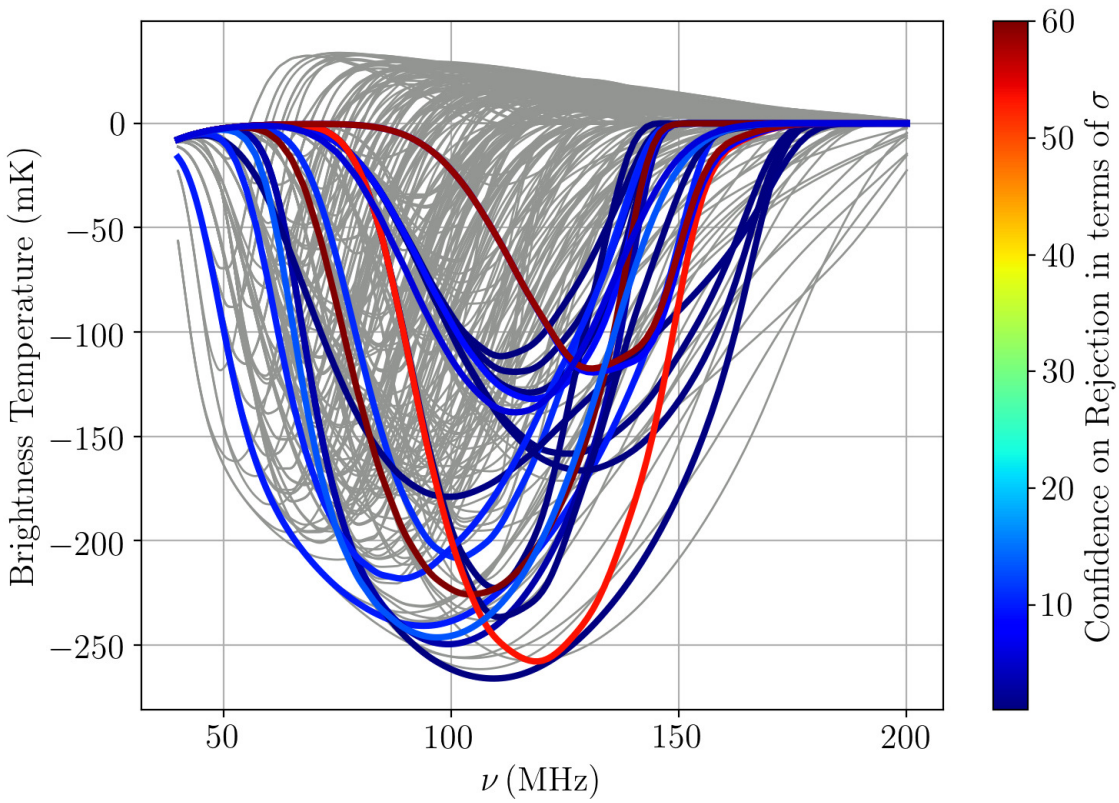

Figure 3.24: The entire set of 264 theoretical models [29]. The rejected signals are shown in color with each color corresponding to the rejection significance as indicated by the colorbar. The data does not have sensitivity for the signals shown in gray. Non-linear optimization was used to model the foregrounds+systematics.

3.6.5 Constraints from forward modeling approach

In the parameter study conducted by Cohen et al. [29] the entire astrophysical parameter space, allowed by current observational and theoretical constraints, was sampled, and the 21-cm signals were derived for different combinations of the astrophysical parameters. In this study, key astrophysical parameters were varied including the minimal circular velocity of star forming halos (starting from the minimal velocity of 4.2 km s^{-1} characteristic for star formation via molecular cooling and up to 76.5 km s^{-1}), star formation efficiency (SFE) between 0.5% and 50%, spectral energy distribution (SED) of X-ray sources including hard and soft spectra [48], X-ray efficiency compared to the low-redshift counterparts, mean free path (mfp) of ionizing radiation (cases with 5, 20 and 70 Mpc were considered), and the total optical depth, τ. The data collected by SARAS 2 is sufficient to rule out 8% of the considered theoretical models using forward modeling approach.

The rejected models all share similar astrophysical properties: rapid reionization in tandem with

either late X-ray heating due to very inefficient sources (10 cases) or no heating at all (10 cases). In all these models the gas does not have enough time to heat up to the temperature of the CMB, and the 21-cm signal is seen in absorption throughout the EoR (colored lines in Fig. 3.24).

All the models ruled out by the forward modeling approach share rapid reionization. We quantify this by the maximum rate of change of the brightness temperature of the 21-cm signal with respect to redshift, $(\frac{dS_0}{dz})_{\rm max}$. The rejected signals have high values of $(\frac{dS_0}{dz})_{\rm max}$ with the median value of the rejected set being 114 mK over $z \sim 10-6$ redshift interval. This is in contrast to the set of non-rejected signals where the median value of $(\frac{dS_0}{dz})_{\rm max}$ is 9 mK over the same redshift range. Rapid reionization scenarios typically require one or more of the following: large mean free path of the ionizing photons, high star formation and ionizing efficiencies of the sources. All but 2 rejected cases have mfp of 70 Mpc; however, the values of SFE and τ are unconstrained. The other 2 cases have mfp of 20 Mpc and high values of τ. None of the rejected cases has mfp of 5 Mpc.

Considering "inefficient heating" models (sources with X-ray bolometric luminosity per star formation rate of up to 10% of their low redshift counterparts) all the rejected cases share late star formation which only happens in massive halos with circular velocities above 35 km s^{-1}. In these cases the absorption trough is shifted into the SARAS 2 band, owing to the delayed build up of the Lyα background, making either detection or rejection easier. Majority of these cases have hard X-ray SED, while the value of SFE varies from model to model.

The rejected astrophysical models with "no heating" have all possible values of circular velocities (from 4.2 to 76.5 km s^{-1}), SFE (from 0.5% to 50%) and values of τ. Out of the 264 tested models, the only cases with "no heating" that were not ruled out have either very efficient star formation in light halos, and thus the absorption peak is shifted out of the SARAS 2 band, or have short mfp (5 Mpc) which implies more gradual reionization.

A summary of astrophysical parameters for the rejected signals using non-linear optimization along with the optimal band, polynomial order and significance of rejection is listed in Table 3.1.

3.6.6 Caveats

Experiments aiming to detect the global 21-cm from CD/EoR are difficult long-wavelength radiometer measurements, requiring a substantially wider dynamic range than what is typically necessary in most engineering applications at these frequencies. Limitations may arise from unknowns in the internal systematics, antenna characteristics, ground emission, low level distributed RFI, and mode coupling of sky spatial structure into spectral measurement data owing to frequency dependent beams.

If the measurement equation describes the data to mK levels, including foregrounds and internal systematics, then a forward modeling approach is expected to be unbiased. This would apply even in the case of an excessive modeling of foreground + systematics with a higher than necessary order

polynomial (which, however, would degrade the confidence in the derived results). In an extreme case, if the model adopted for the foreground+systematics is also capable of fitting out the 21-cm template, the result would be completely ambiguous, with equal likelihoods for the presence and absence of the template.

Problems potentially arise when the measurement equation or the adopted model is inadequate to describe the foreground + systematics, given the large dynamic range required for 21-cm signal detection. In this case, residual systematics can bias the results of the decision tests. The adoption of an inadequate model may be inadvertent, particularly in the case where 21-cm signals are extracted via statistical analysis that aims to detect the signals in measurement data wherein the signal-to-noise ratio in individual channels are substantially below unity.

Adopting an inadequate model would result in systematic residuals to the fit to foregrounds + systematics. The least squares fit would attempt to maximize the correlation (or anti-correlation) of these residuals to the 21-cm template under consideration so that including a scale factor times the 21-cm template, the overall residuals would be a minimum. Consequently, the un-modeled foreground + systematics might partially or wholly mimic the 21-cm signal—thus yielding a false positive—or partially or wholly cancel a true 21-cm signal in the data, thus yielding a false negative. In these circumstances small fit residuals might suggest excellent fits with low formal statistical errors in the fitted scale factor a; however, the errors are obviously underestimates since the un-modeled systematics are not considered in the error computation.

It is also necessary to consider cases where the true cosmological signal in the measurement data is substantially different from the template used in modeling. If the true cosmological signal is uncorrelated with the template, then the fit value of the scale factor a will not be biased. However, if there is partial correlation (or anti-correlation), then the fit would bias the a parameter to be positive or negative depending on the correlation or anti-correlation respectively.

The work presented herein has adopted polynomial models for the foreground+systematics. Higher N would obviously fit this term better; however, it would also increasingly subsume the cosmological signal and, hence, reduce the confidence in either detection or rejection. Future effort is directed towards improving the modeling of foregrounds+systematics and avoiding fitting out of a significant fraction of 21-cm signals. The design of SARAS 2, which aims to constrain the systematics to be maximally smooth [153] is along the lines of this approach.

3.7 Conclusion

In this work we have analyzed the first light data from SARAS 2 using Bayesian and frequentist approaches. The analysis has led to the rejection of 9 signals using Bayesian approach. The Bayesian approach disfavors, with 69% confidence, the class of global 21-cm models that represent late heating

or poor X-ray efficiency, with $f_X \leq 0.1$, and with peak $\frac{dT_b}{dz} \geq 120$ mK per unit redshift interval corresponding to a rapid rate of reionization. Using the frequentist approach and constrained non-linear optimization, we reject 20 plausible 21-cm signals out of 264 tested models. In 15 out of 20 cases the confidence on rejection is above 5σ. All the rejected signals lie in the regime of either late or non-existent heating by the first population of X-ray sources, which creates a deep absorption trough in the 21-cm signal observed against the CMB. In addition, in all the rejected models reionization happens fast owing to the assumed long mean free path of the ionizing photons as well as efficient star formation and ionization. We leave robust estimation of the rejected parameter space to future work.

Table 3.1: Parameters of the 21-cm signals rejected by the SARAS 2 data.

f_*	V_c (km/s)	f_X	SED	τ	$R_{\rm mfp}$	$(\frac{dS_0}{dz})_{\rm max}$	Band (MHz)	Order of polynomial (N)	Significance of rejection
0.005	35.50	0	Hard	0.082	20	67.40	110 – 195	3	1.26
0.005	35.50	1	Hard	0.082	70	69.71	110 – 190	3	1.40
0.050	16.50	0	Hard	0.096	70	94.92	115 – 180	3	1.89
0.005	35.50	0.1	Soft	0.082	70	88.33	110 – 185	3	3.23
0.500	35.50	0	Hard	0.082	20	94.45	120 – 195	3	4.88
0.500	76.50	0.1	Hard	0.066	70	97.17	125 – 190	3	5.63
0.005	4.20	0	Hard	0.082	70	74.32	135 – 190	3	8.01
0.500	76.50	0.1	Hard	0.082	70	128.98	110 – 195	4	8.27
0.050	35.50	0.1	Hard	0.082	70	94.26	115 – 190	3	8.90
0.005	35.50	0.1	Hard	0.082	70	110.48	125 – 180	3	9.84
0.500	4.20	0	Hard	0.082	70	164.83	135 – 180	3	10.06
0.005	35.50	0.1	Hard	0.066	70	104.18	110 – 190	4	10.83
0.015	76.50	0.1	MQ	0.066	70	146.62	125 – 195	5	12.41
0.005	35.50	0	Hard	0.082	70	118.34	110 – 180	4	13.31
0.015	76.50	0.1	Soft	0.066	70	159.21	115 – 195	5	16.40
0.050	35.50	0	Hard	0.083	70	164.71	115 – 180	5	18.56
0.500	76.50	0.1	MQ	0.066	70	169.85	115 – 190	5	31.24
0.500	35.50	0	Hard	0.082	70	172.80	115 – 175	5	53.42
0.005	35.50	0	Hard	0.066	70	131.70	115 – 180	4	58.94
0.500	35.50	0	Hard	0.066	70	172.59	115 – 195	7	89.20

f_* denotes the star formation efficiency, V_c represents minimum virial circular velocity for star formation, f_X is the efficiency of the X-ray sources, SED refers to spectral energy distribution of X-ray sources. The SEDs considered are of hard and soft X-ray sources along with that of mini-quasars (MQ). τ is CMB optical depth, $R_{\rm mfp}$ denotes the mean free path of ionizing photons, $(\frac{dS_0}{dz})_{\rm max}$ is the maximum rate of change of brightness temperature of the signal with respect to redshift. Significance of rejection is computed as given in Eq. 3.8. A detailed description of most of these parameters is given in [29].

Chapter 4

On the detection of Global 21-cm signal from Reionization using interferometers[†]

"*Eventually, we reach... the utmost limits of our telescopes. There, we measure shadows, and we search among ghostly errors of measurement for landmarks that are scarcely more substantial.*"
-Edwin Hubble

4.1 Introduction

Radiometers are limited by their ability to distinguish between constant internal systematics and the global 21-cm signal. The internal systematics may arise because of the multi-path propagation of components that constitute the system temperature, as discussed in Sec. 2.4.3. There has been work on interferometer based detection of the global signal [166, 84, 129] motivated by the formidable challenge of discriminating against instrument related internal systematics in single-element radiometers. Compared to single-element radiometers, interferometers are relatively insensitive to receiver noise and noise originating internally in ohmic losses and passive components in the paths corresponding to the arms of the interferometer. The work presented herein develops the theory of the response of interferometers to the global 21-cm signal and explores a variety of configurations that may usefully make interferometer measurements of the global spectrum. The configurations include measurements of the spatial coherence in the electromagnetic field owing to the global signal as well as methods that enhance this coherence so as to improve the detection sensitivity.

Recent studies have also shown that ionospheric refraction and absorption may add excess power which could be 2–3 orders of magnitude greater than the signal of interest [166, 31]. This consideration is a compelling argument for observations to be made from above the atmosphere and from space

[†]Based on *Singh, S., Subrahmanyan, R., Shankar, N. U., & Raghunathan, A. 2015, The Astrophysical Journal, 815, 88*

where the response is free of ionospheric distortions; therefore, the configurations we consider here are assumed to be in space. Nevertheless, the conclusions arrived at here following the analyses and comparisons apply equally well for ground based interferometers.

4.2 Notations and preliminaries

We begin by clarifying the notations. We consider interferometer measurements of the global 21-cm and hence the interferometers and methods considered herein operate at radio frequencies. In all cases, we consider here the response of *two-element interferometers*; therefore, any reference to interferometers refers to two-element interferometers only. Any two-element interferometer measures the spatial and temporal coherence between the fields at two spatially separated locations at which sensors are positioned. The pair of sensors in a two-element interferometer are called the *elements of the interferometer*; the interferometer elements are *antennas*. The term *baseline* refers to the relative spacing and orientation of the interferometer elements; baseline is a vector.

The antenna, which is the interferometer element, may in practice be a single sensing unit such as a dipole antenna or resonant loop: we refer to such antennas as *unit* antennas. The antenna may be a 1-D phased array of such units. The antenna may be 2-D phased array of units, or a 2-D aperture made of reflectors along with sensors at the focus that act together as concentrators of the electromagnetic (EM) field.

The antennas essentially sense the EM field at their location and provide a weighted summation of the EM field over the antenna area or *aperture*; a voltage waveform corresponding to the net field is provided at the antenna terminals and the two-element interferometer measures the coherence between such voltage waveforms sensed by a pair of elements. We use the term *response* to refer to the response of an interferometer to the global signal unless stated otherwise. It may be noted here that the effective aperture of an antenna might be larger than the physical aperture.

Finally, although the detection method discussed here is relevant to the monopole component of any astronomical signal, our signal of interest is specifically the all-sky or uniform component of the redshifted 21 cm from HI in the Epoch of Reionization, which is referred to as the 21-cm monopole or the global 21-cm signal.

While considering this uniform component, we assume a sky across which the emission is uniform but spatially incoherent. For such a sky, the square of the voltage at the antenna terminals represents the average brightness temperature over the beam power pattern or radiation pattern of the antenna, which represents the relative sensitivity of the antenna over sky temperature. As an illustrative example, we may consider an antenna whose planar aperture is a collection of unit dipoles that are combined in an impedance matched network to yield the net voltage at the antenna terminals. In this case, all the dipoles would sense the same rms voltage at their spatial locations owing to the uniform

sky, and the output would have the same rms voltage as the rms voltages sensed by the individual dipoles. This is required by thermodynamics considerations. The output power has fractional contributions from all parts of the aperture; the output power is a weighted average of the aperture powers, where the weighting is by the aperture illumination. In summary, for a sky across which the emission is uniform and incoherent, the antenna has an aperture that defines an area over which the antenna does a weighted averaging of the field strength to provide a voltage at its terminals.

For a uniform sky that is incoherent across angle on the sky plane, we may define the spatial coherence function in the visibility domain to be the mutual coherence in fields sensed or sampled by antennas with isotropic beam patterns. The response of an interferometer made of such isotropic antennas is what we define to be a "true" coherence. This "true" coherence function has a value at the origin of the visibility plane that is the brightness of the uniform sky. Assuming identical antenna elements, the interferometer response is an integral of the coherence function over a visibility-plane footprint of a shape that is the auto-correlation of the element aperture. This footprint is centered at the location of the baseline vector on the visibility plane.

If the baseline length is less than the effective diameters of the apertures, then the footprint will cover the origin and hence the integral response would include a substantial response to the brightness of the uniform sky. Otherwise, the integral will always be less than the sky brightness, and might be expected to be smaller for longer baselines and larger aperture sizes if not zero.

4.3 Response of a two element interferometer to a global signal

Interferometers measure the spatial coherence function [27] of the electromagnetic field. It is commonly believed that interferometers are sensitive only to brightness temperature variations on the sky and do not respond to the uniform or monopole component. Therefore, interferometers and Fourier synthesis telescope arrays are usually used in astronomy to measure the spatial coherence owing to discrete sources of radiation on the sky, and thereby indirectly image the source structures and brightness variations.

In contrast, here we focus on the spatial coherence that is due to the monopole component of the sky brightness distribution. We present a study of the expected variation in the coherence with changing baseline as well as with observing frequency. While it is indeed true that by and large interferometers are "blind" to the uniform sky, we show below that there are special circumstances in which interferometers might usefully respond to the monopole component of the sky brightness distribution.

The response $V(\vec{b},\nu)$ of an interferometer to sky brightness distribution $T_{sky}(\vec{r},\nu)$ is a function of

the baseline vector $\vec{b}$ and frequency ν (or equivalently the wavelength λ) [164]:

$$V(\vec{b},\nu) = \frac{1}{4\pi}\int_{\Omega} A(\vec{r},\nu)T_{sky}(\vec{r},\nu)e^{-i2\pi\frac{\vec{b}\cdot\vec{r}}{\lambda}}d\Omega. \tag{4.1}$$

The integral here is over the entire sky, with $\vec{r}$ representing position unit vector towards solid angle element $d\Omega$ on the sky. $A(\vec{r},\nu)$ represents the beam power pattern of the interferometer elements. It is assumed that the interferometer elements constituting the 2-element interferometer are identical.

For a signal that is global in nature and uniform over the sky, $T_{sky}(\vec{r},\nu)$ may be written as just $T_{sky}(\nu)$ and taken out of the above integral, which may then be written as

$$V(\vec{b},\nu) = \frac{1}{4\pi}T_{sky}(\nu)\int_{\Omega} A(\vec{r},\nu)e^{-i2\pi\frac{\vec{b}\cdot\vec{r}}{\lambda}}d\Omega. \tag{4.2}$$

If $T_{sky}(\nu)$ is in units of Kelvin, then the response $V(\vec{b},\nu)$ is also in Kelvin units. As shown below, this integral is nonzero. Indeed, for short-spacing interferometers the integral may be a substantial part of the mean brightness temperature of the sky, which indicates that interferometers may be configured to have a substantial and useful response to the global redshifted 21-cm signal. We compute this integral below for different types of interferometer elements.

4.3.1 Interferometers made of unit antennas

In this subsection, we compute Equation 4.2 for four cases in which the interferometer elements are unit antennas.

In the first two cases, the interferometer elements are assumed to be identical short dipoles at the observing frequency, with lengths much less than $\lambda/2$, where λ is the wavelength of the observation. The radiation pattern of a short dipole is of toroidal form with nulls along the axis of the dipole, with response of the form $\sin^2(\theta)$, where θ is the angle measured from the axis. In the first case, the axes of the pair of antennas are oriented to be parallel to each other and perpendicular to the baseline vector, as depicted in the figure in Panel (a) of Fig. 4.1. In the second case the interferometer elements are once again assumed to be identical short dipoles but with their axes oriented along the baseline vector; this configuration is depicted in Panel (b) of Fig. 4.1. We call these first and second cases as "parallel" and "in-line" configurations respectively.

In the third case the elements are assumed to be circularly-polarized resonant loop antennas tuned to the observing frequency, with the loop axes orthogonal to the baseline vector. The circumferences of the loops are equal to the observing wavelength and the antenna patterns for the resonant loops are of $\cos^2(\theta)$ form, where θ in this case is the angle from the axis of the loop antenna.

For reference, we also compute Equation 4.2 for the case where the interferometer elements are

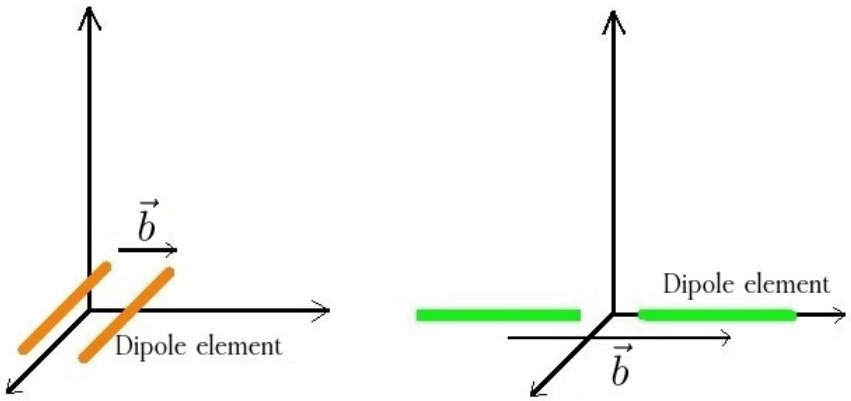

(a) Parallel configuration (b) In-line configuration

Figure 4.1: Configuration for two element interferometers.

isotropic antennas.

We show in Fig. 4.2 the response of the interferometer versus baseline length for these four cases. All plots are normalized to the value at a baseline length of zero, which is the value that a conventional total-power measurement using a single antenna element would yield for a uniform sky. Isotropic antennas or antennas with isotropic radiation patterns are not realizable in practice, they notionally correspond to point sensors of the field. As discussed earlier, the trace in Fig. 4.2 corresponding to isotropic antennas represents a "true" spatial coherence in the field arising from a uniform sky brightness.

First, there is substantial response of the interferometers to uniform sky - interferometers can indeed measure a global signal. At zero length baseline, this coherence represents the autocorrelation or power in the field from the uniform sky. With increasing baseline length the spatial coherence in the field falls off substantially; in fact, the spatial coherence is a sizable fraction of the total power only for separations less than a wavelength. This is consistent with what is known in optics of the coherence properties of the radiation field in a cavity filled with blackbody radiation [88].

The response in the case of dipoles in parallel configuration is greater than that for the isotropic case, and the response for in-line dipoles is smaller than for isotropic; the response in the case of resonant loop antennas is same as that for dipoles in in-line configuration. As seen in Fig. 4.2, for baselines of a few wavelengths, the peak response in the case of parallel dipoles is about a factor of five greater than that for in-line dipoles. However, the response amplitude is strongly dependent on the baseline length, fluctuating about zero and reducing with increasing baseline length as in a damped sinusoid, and the amplitude and the amount of damping of the amplitude with increasing baseline length are both strongly dependent on the nature of the interferometer elements.

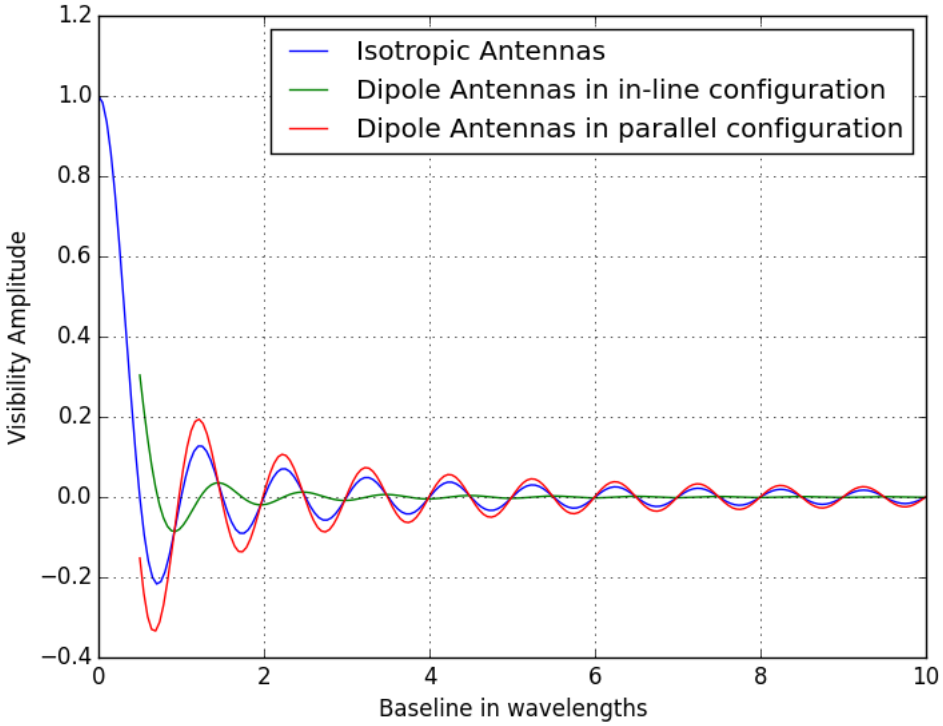

Figure 4.2: Response to uniform sky of a 2-element interferometer made of identical unit antennas. The response of a resonant loop antenna is identical to the case of short dipoles in in-line configuration and their traces overlap. In-line and parallel configuration responses have been traced from 0.5λ avoiding the near field regions of the antennas.

Since the coherence in the field varies fairly rapidly with the baseline, varying by close to a period for a change in baseline length of a wavelength, integrating over visibility domains comparable to or greater than a wavelength would substantially diminish the net interferometer response. This decrease in the response would be more pronounced if the aperture has a greater extent along the baseline vector, since it is in this direction that the coherence in the field varies. Dipoles in in-line configuration have a greater effective extent along the baseline vector compared to dipoles in parallel configuration; it is for this reason that the interferometer response of two-element interferometers with dipoles in in-line configuration have relatively lower response.

Response to uniform sky is a maximum when the baseline length is zero. An alternate physical understanding for the cause of the interferometer response to uniform sky may be arrived at by examining the effective area afforded in directions where the projected baseline is zero. Dipoles in parallel configuration have maxima along this zero-baseline direction and nulls in the orthogonal direction towards which the projected baseline is a maximum. Short-dipole interferometers in in-line configuration, as well as interferometers with elements that are resonant loops, have nulls in their beam

patterns along the baseline vector in the direction where the projected baseline is zero; therefore it is unsurprising that these configurations have a smaller response to uniform sky compared to the case of the parallel configuration.

It may be noted here that we have assumed that the interferometers are in space, with no ground. If the interferometer is placed above ground, and the ground below the antennas are covered with ideal absorbers, the sky response of the interferometer and that of the total-power of a single antenna would both be halved, without any change in the normalized visibility functions.

4.3.2 Interferometers made of 1-D antenna arrays

We next extend the analysis to interferometers whose elements are 1-D linear arrays consisting of short dipoles. The short dipoles that form the units of the 1-D antenna are assumed to be arrayed along the length of the antenna; i.e., their linear polarizations are aligned to be along the length of the 1-D antenna. We also assume that the signals from the units of the 1-D antennas are combined with zero phase difference and equal weights to provide the voltage signal at the terminals of the antennas. Because the dipole units are collinear and arrayed along the length of the antenna, and because antennas with such a configuration have isotropic radiation patterns in the plane perpendicular to the axis along which the units are arrayed, we refer to such interferometer elements as 1-D antennas.

We consider a linear array of N identical dipole units spaced $d = (\lambda/2)$ apart. As stated above, in the plane perpendicular to the antenna axis, the 1-D antennas have omnidirectional radiation patterns. In any plane containing the axis, the net far-field radiation pattern is obtained by multiplying the radiation pattern of a single unit with an Array Factor:

$$AF = \frac{1}{N}\left[\frac{\sin(\frac{N\psi}{2})}{\sin(\frac{\psi}{2})}\right]. \tag{4.3}$$

Here $\psi = (2\pi/\lambda)\, d\, \cos(\theta)$, where θ in this case is the angle from the long axis of the 1-D array [5]. The Array Factor is maximum along directions perpendicular to the 1-D array.

We consider two cases in this category: one in which the 1-D antennas are perpendicular to the baseline vector, a parallel configuration, and a second case in which the 1-D antennas are along the baseline vector, which is an in-line configuration. The geometries for both cases are shown in Fig. 4.3.

In each of these two cases we compute the response to uniform sky as a function of baseline length and for different numbers of short dipole units within the 1-D antennas. Fig. 4.4 shows the response of the parallel configuration versus baseline length, in this figure the response to isotropic antennas is also shown for reference. The corresponding plot for the in-line configuration of 1-D antennas is in Fig. 4.5.

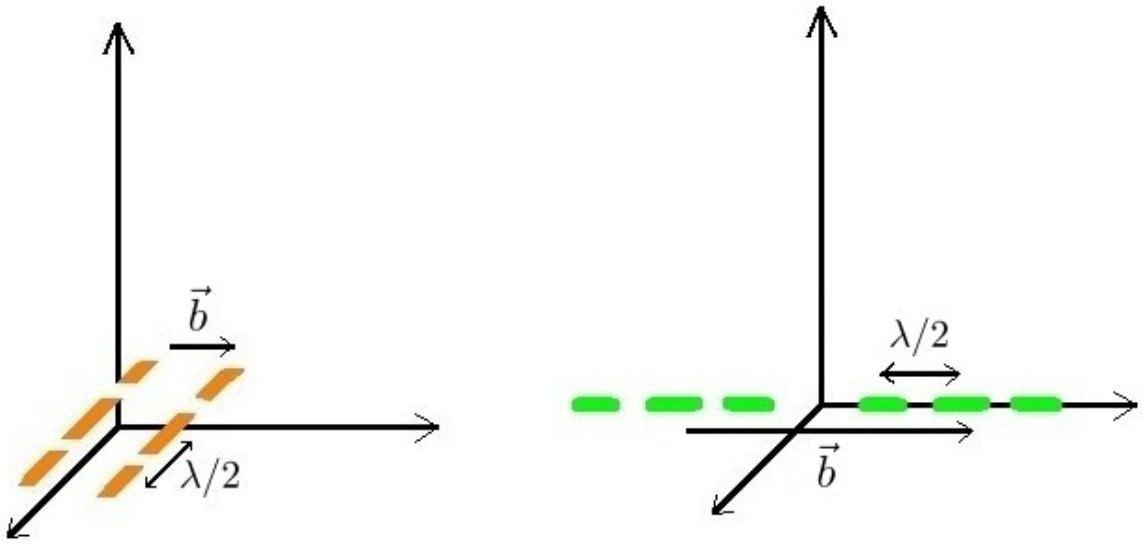

(a) Parallel configuration

(b) In-line configuration

Figure 4.3: Configurations for two-element interferometers consisting of 1-D arrays as interferometer elements.

First, the in-line configuration does not admit close packing and small baselines because of overlap and shadowing. Therefore, the shortest baseline in the case of the in-line configuration of 1-D antennas is equal to the length of the 1-D antenna elements, which is larger when the antennas are made of greater numbers of units. When the shortest baseline is larger, the maximum response, which occurs when the baseline is smallest, is diminished. For this reason, in-line configurations are inherently poorer in sensitivity compared to parallel configurations.

The limiting baseline is either set by geometry, as discussed above, or the size of reactive zones of the interferometer elements. If a pair of antennas were placed close to each other and within their respective reactive zones, they would suffer significant mutual coupling. For any antenna of dimension D, operating at wavelength λ, the reactive zone is considered to be within a radial distance of $\frac{D^2}{\lambda}$, and baselines are best maintained to well exceed this size if the individual antenna performances are to be unperturbed by proximity to their neighbor. In the case of the parallel configuration the system performance is better defined when the interferometer elements are separated by more than their reactive zones, which sets the minimum baseline.

The visibility amplitude in the case of the parallel configuration is greater than that for the case of isotropic antenna elements, where as the response of the interferometer with in-line configuration is relatively small and also diminishes more rapidly with increasing baseline length. As in the case for unit dipole antennas as elements of the interferometer, this is consistent with the expectation

that averaging of the baseline-dependent complex coherence over longer baseline lengths results in diminishing of the response.

The response falls rapidly with increasing number of units in the case of 1-D interferometer elements in an in-line configuration. The result may be understood by arguments similar to those presented in Sec. 4.3.1. Adding more units in an in-line configuration directly increases the extent of the aperture in the radial direction in the visibility plane along which the complex coherence varies most rapidly. Additionally, the domain of the integration is over a one-sided radial segment of the complex coherence function that does not include the origin. Therefore, any increase in the extents of the 1-D antennas beyond about half a wavelength results in a substantial diminishing of the integral response. In the alternate perspective discussed above, increasing the numbers of units in the in-line antennas increases the gains of the interferometer elements, narrows the beam pattern to be more directed in the plane perpendicular to the axis, which results in reduced response towards the direction in which the projected baseline is zero.

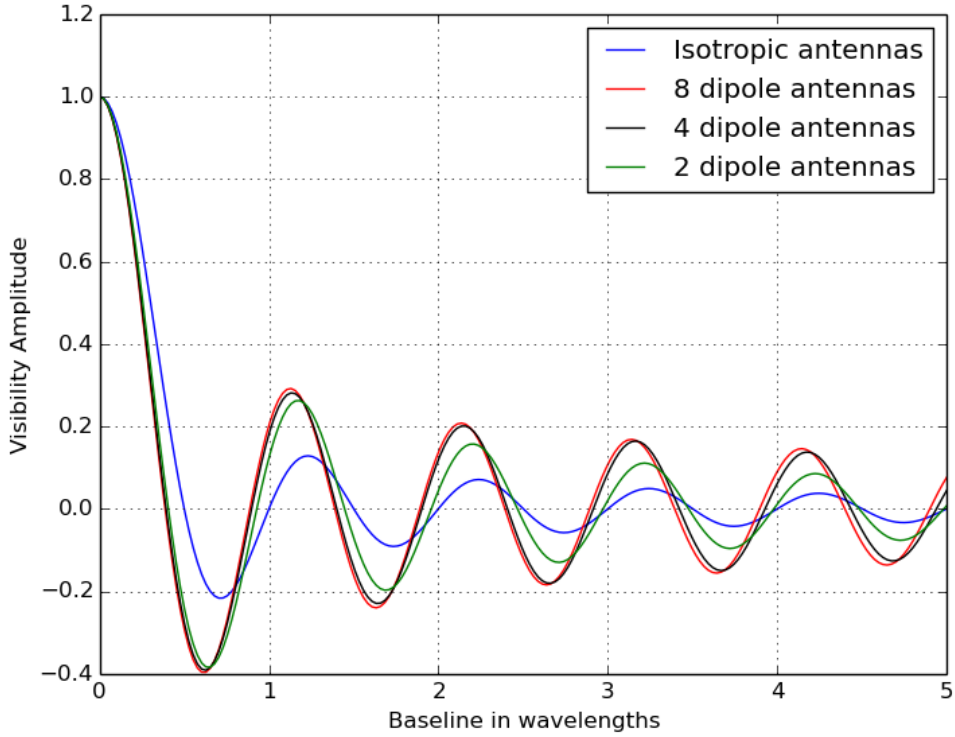

Figure 4.4: Interferometer response in the case of 1-D antennas in parallel configuration, for antennas with different numbers of dipoles.

On the other hand, increasing the number of short dipole units within the 1-D antennas in the parallel configuration tends to increase the sensitivity of the array to the global signal. Increasing

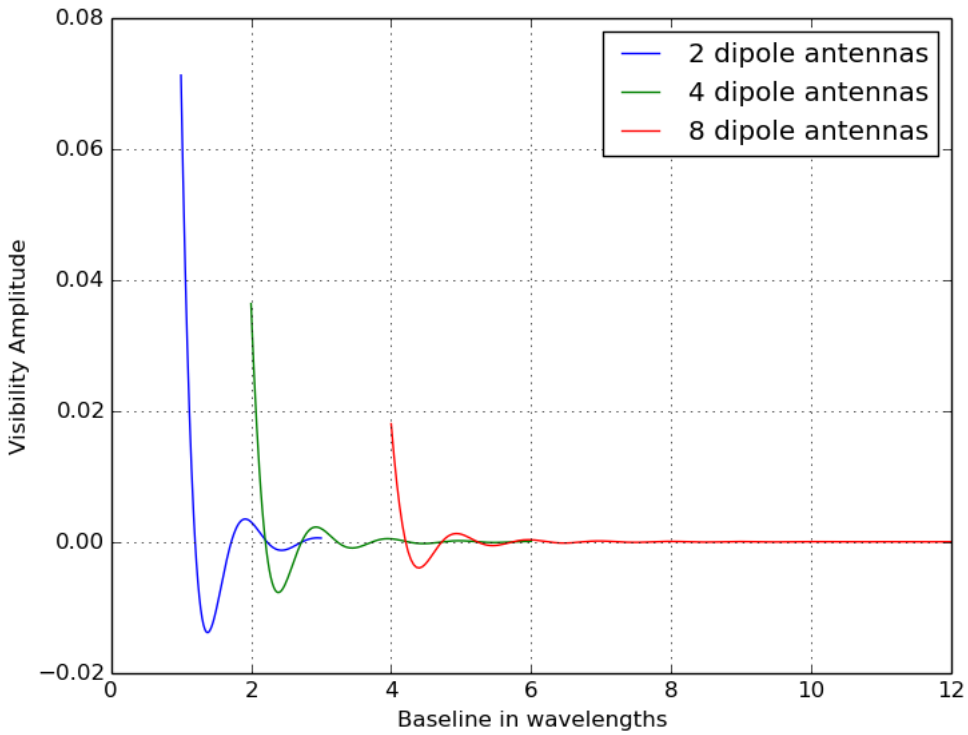

Figure 4.5: Interferometer visibility amplitude versus baseline length for antennas with in-line arrays in in-line configuration (for antennas with different numbers of dipoles). The visibilities are normalized to give the fractional response to the global sky brightness temperature.

the number of units in this case extends the 1-D array, and hence the integration over the coherence function, in a direction tangential to the baseline vector. Most importantly this integral is over a domain that is two sided in which the coherence function is symmetric. Therefore, for small increases in numbers of units the response is enhanced; however, as the numbers of units grows and the length of the 1-D antennas is substantially greater than the baseline length the integral yields diminishing returns in terms of increased response. In the alternate perspective, increasing the numbers of units in the 1-D antennas oriented perpendicular to the baseline increases the gain towards the direction where the projected baseline is zero, reducing the response in orthogonal directions, and this may be viewed as causing the enhanced response to uniform sky.

4.3.3 The case of aperture antennas

We next consider interferometers between antennas with circular apertures. This case has been discussed previously by Presley et al. [129] and we comment on their analysis below at the end of this section. In this case study the antennas may be 2-D aperture arrays or reflectors with focal feeds.

We describe the aperture antennas using a function $g(u)$ that describes the field distribution on the aperture plane. We assume circular symmetry in this field distribution and that the field $g(u)$ may be expressed as a function of the distance u from the center point only. Therefore, the far field radiation pattern of the aperture antenna may be computed as a Radial Fourier Transform, also known as Hankel Transform, of the aperture field distribution:

$$F(\theta) = 2\pi \int_0^{u_{max}} u J_0(2\pi u \sin\theta) g(u) du. \tag{4.4}$$

Here u is expressed in wavelengths and u_{max} is the radius of the circular aperture in wavelengths. $F(\theta)$ is the far-field voltage radiation pattern; θ here is the offset angle in radians from the axis of the aperture. J_0 is the Bessel function of zeroth order.

We consider aperture antennas of two descriptions: one in which the sensor of the field provides a uniformly weighted summation over the aperture plane and a second in which the field in the aperture is added with an amplitude weighting corresponding to a Gaussian taper. Since the aperture is of finite size, even for the case where the aperture field is averaged with a Gaussian taper the far-field radiation pattern cannot be of Gaussian form; instead, the pattern would be the Fourier Transform of a truncated Gaussian.

Using $F(\theta)$ from Equation 4.4 as the response function of the antenna elements, we may now use Equation 4.2 to compute the response to a global sky brightness for an interferometer made from a pair of circular apertures. In Fig. 4.6 we show this response for the case of uniform weighting of the field over the antenna aperture. We show the responses for the cases where the aperture diameters D are 6λ and 12λ. The response is only shown where the baseline exceeds the aperture diameter since smaller baselines are impossible without overlap and hence shadowing. The magnitude of response to global sky is at most about 10^{-3} of the global sky brightness; additionally, the visibility amplitude diminishes with increasing dish size and increasing baseline length.

For antenna apertures of diameter D as the elements of an interferometer, the integration of the coherence function is over regions of diameter $2D$ in the visibility plane. As discussed earlier, any integration over a region of the visibility plane that exceeds half a wavelength in size would substantially diminish the response of such an interferometer to the global 21-cm signal because (a) the coherence of the signal varies substantially with baseline length and (b) the footprint on the interferometer response on the visibility plane does not include the origin. Aperture antennas with diameters exceeding a few wavelengths would have little response to the global mean brightness of the sky because they provide such spatially integrated measures of the coherence function. This averaging over the varying complex coherence function, over domains that are substantially offset from the origin, is the cause for the substantial reduction in response in the case of aperture antennas.

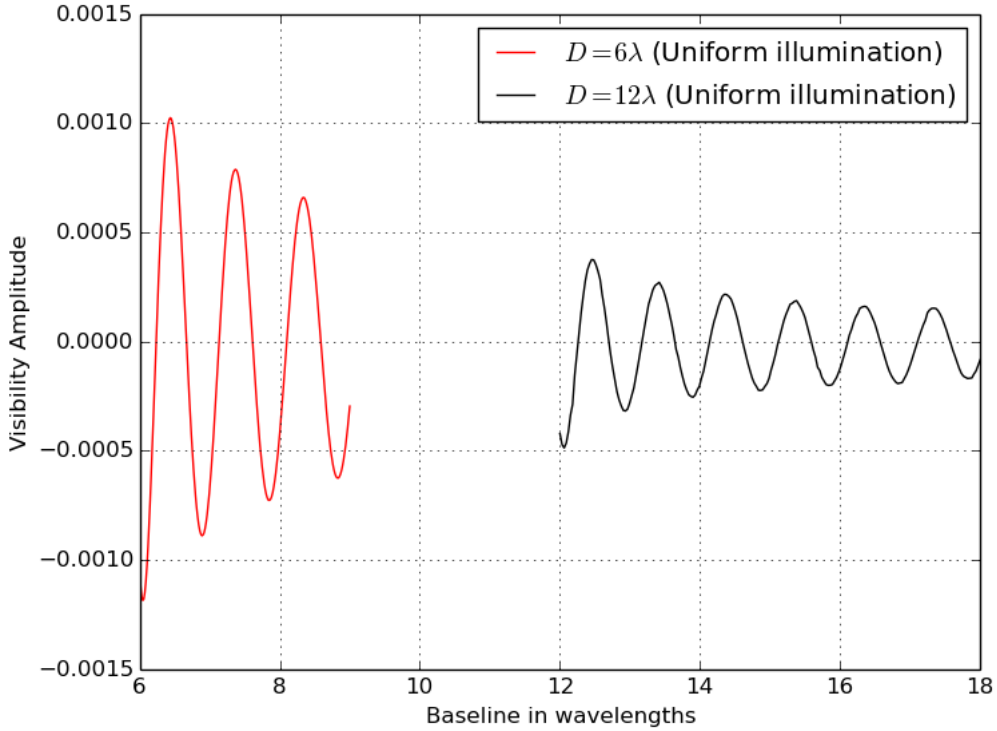

Figure 4.6: Interferometer visibility amplitude versus baseline length for circular aperture antennas that have a uniform sampling of their aperture fields.

Most often a tapering is used to down-weight the fields at the edges of the aperture while averaging to provide the voltages at the terminals of conventional aperture antennas. This is done so that the antenna beam patterns have lower sidelobes and hence unwanted off-axis response is reduced. In our second case study of two-element interferometers with aperture antennas we assume Gaussian form tapers of the aperture fields, in which the field at the aperture edges are down weighted to 10% of the central value. We find that the interferometer response to global mean sky is furthermore reduced in this case relative to the uniform weighting case. For apertures of diameter 6λ, the visibility amplitude is below 10^{-7} at about the closest baseline length of 6λ, and diminishes further with increasing aperture size and baseline length.

In any short spacing interferometer formed between aperture antennas, the mutual coherence is a maximum between the fields at the edge portions of the two apertures that are closest to each other. When the aperture fields are tapered and the fields at the edges are down-weighted by the feeds of the aperture antennas, the mutual coherence between the signals from the pair of closely spaced antennas is reduced. This explains why the interferometer response to a global signal is furthermore reduced in aperture antennas with tapers compared to aperture antennas with uniform illumination. In summary,

interferometers made using 2-D aperture antennas are clearly substantially less sensitive to the global EoR signal compared to interferometers using 1-D antennas or unit antennas.

It has been pointed out earlier in Presley et al. [129] that the EoR monopole signal resides at the origin of the visibility plane of interferometers, and what is required is for an interferometer response to be sensitive to the origin. It is also suggested therein that a primary beam of aperture elements could cause the response to sample this origin and, therefore, make an interferometer sensitive to the monopole. As discussed above, the visibility-plane footprint of an interferometer has the size and shape of the autocorrelation of the antenna aperture; therefore, to get the origin into the visibility-plane footprint of an interferometer would require an antenna diameter d exceeding the baseline length. To achieve this with aperture antennas, the two antennas forming the interferometer would have to overlap or shadow. No interferometer made of finite aperture antennas, which do not overlap or shadow, could possibly sample the origin of the visibility plane. The primary beam profile assumed in Presley et al. [129] has been argued to be realistic and the response function in the visibility plane, as computed from the adopted beam pattern, has been shown to sample the origin. This is only possible if the effective apertures of the antennas are larger than the physical apertures and the sampling of the origin of the visibility plane arises from overlap of the effective apertures. Our view is that interferometers with finite aperture antennas do respond to the uniform sky, not because they sample the origin of the visibility plane, but because the coherence function corresponding to a uniform sky does extend away from the origin and may be sampled by aperture antenna interferometers.

4.4 Enhancement of the spatial coherence corresponding to a uniform sky

Vedantham et al. [167] suggested using lunar occultation of the uniform sky to generate and enhance the spatial coherence corresponding to a global sky signal, which may then be detected using interferometers. In so far as the global redshifted 21-cm signal is concerned, blocking the sky with the Moon creates a disk shaped source, with diameter equal to the lunar disk, with a relative brightness temperature equal to the difference between the brightness of the lunar disc and the brightness of the global redshifted 21-cm signal. The spatial coherence in the field corresponding to this differential disk source is what is proposed by Vedantham et al. [167] to be detected using interferometers. In this section, we discuss another technique to enhance the spatial coherence and hence the response of interferometers to any global signal.

Any beam splitter that partially reflects and partially transmits incident electromagnetic radiation results in fields on the two sides that have a mutual coherence, which may be measured using an interferometer whose elements are placed on the two sides of the beam splitter. We show in Fig. 4.7 a

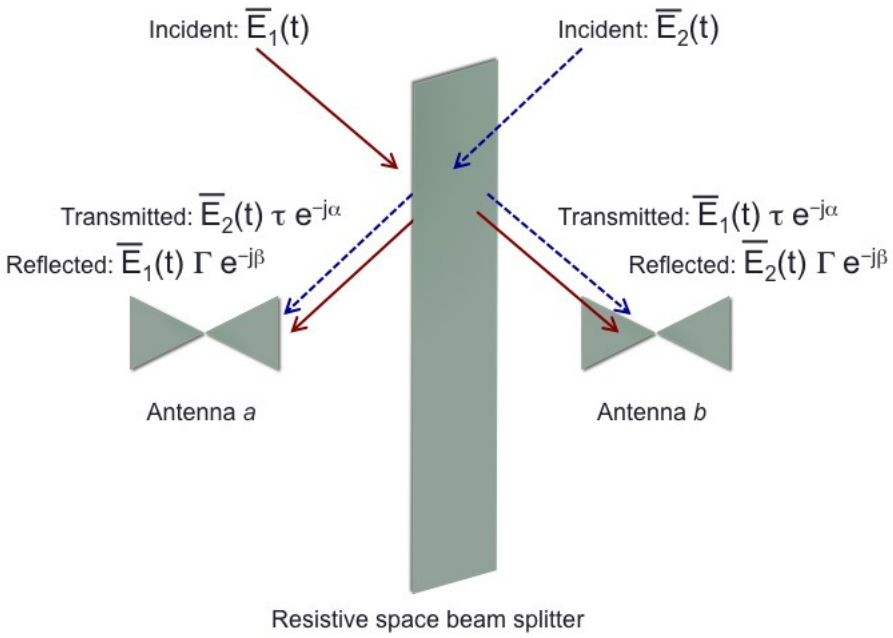

Figure 4.7: Schematic of a configuration with a beam splitter sheet in between the interferometer elements [84].

configuration in which a space beam splitter is placed in between antenna elements of a two-element interferometer: the pair of antennas receives sky radiation that is partially transmitted through the sheet from the far side and partially reflected off the sheet from the near side. Sky radiation is incident on the two sides from any uniform component of the sky and the reflected and transmitted fields that are sensed by the antenna elements now have a substantial mutual coherence. This coherence would be well above that without a beam splitter in between. The performance of space beam splitters was analyzed in Mahesh et al. [84] where it was shown that the sheet impedance was required to be resistive and of value half the impedance of free space (377/2 Ω) for maximum coherence and hence interferometer response. Mahesh et al. [84] also proposed a method for the construction of such a screen as a resistor grid, and demonstrated consistency between measurements of its performance with expectations based on electromagnetic modeling.

In a space beam splitter, the enhancement of spatial coherence in the fields corresponding to global signals may be alternately understood as follows. As viewed from any sky direction the antenna element on the far side is seen through the screen and a reflected image of the antenna on the near side is seen to be coincident with the former. In effect, the interferometer elements appear from all directions on the sky to present a zero length baseline. This sampling of the origin of the visibility

space may be considered, in this case where a beam splitter sheet is placed between the antenna elements, to be the cause of the enhanced response to global components of sky brightness.

4.5 The sensitivity of small interferometer arrays to wideband global signals

We consider below the spectral sensitivity of interferometers, based on useful configurations emerging from the above discussions, to measure the global EoR signal over the 40–200 MHz frequency range. The signal is assumed to be of 10 mK amplitude and the telescope system temperature is assumed to be dominated by the antenna temperature T_a, which is the sky brightness temperature modeled as a function of frequency f as:

$$T_a = 400 \left(\frac{f}{150 \text{ MHz}} \right)^{-2.5} \text{ K}. \tag{4.5}$$

The antenna temperature has been assumed to be 400 K at 150 MHz and varying with frequency with a temperature spectral index of -2.5; the reference value of 400 K was obtained by computing the average brightness temperature over the whole sky in the 150 MHz map of Landecker and Wielebinski [75].

In the above discussions we have considered responses as function of baseline length; however, here we use those results to infer the response as function of frequency for interferometers that have fixed baselines. A single baseline would have a frequency response— the telescope response or "*telescope filter function*"—that would have substantial variation over the 1:5 band, including null response at some frequencies. Adding baselines of different lengths would avoid nulls in the net response. We have chosen, as an undemanding illustration, to consider a very small array of three interferometer elements, indeed the smallest possible. The first two are assumed to be spaced λ_{max} apart and the third is at a distance of $1.5\lambda_{max}$ from the second, where λ_{max} is the longest wavelength of interest, corresponding to 40 MHz. This configuration gives three baselines of length λ_{max}, $1.5\lambda_{max}$ and $2.5\lambda_{max}$. This distribution of spacings ensures that visibilities are sampled at $(b/\lambda) > 1$, where b is the baseline length, at all frequencies. Thus mutual coupling, which is most severe when adjacent interferometer elements are within the reactive near fields of neighboring elements, is reduced. The spacings between the interferometer elements is a trade off between deleterious mutual coupling and desirable signal power, both of which are greater at shorter baselines.

The analysis in Sec. 4.4 suggests that amongst the different antennas that might be elements of an interferometer, a 1-D antenna oriented perpendicular to the baseline vector, i.e. an in-line array in parallel configuration, has a better response to global sky signals. Hence we first consider 1-D antennas made as an array of short wideband dipoles in parallel configuration (as shown in Fig. 4.3(a)),

then consider 1-D antennas that are designed and constructed to be wideband 1-D apertures fully filled over the operating frequency range. Finally we consider the broadband response of a two-element interferometer with a space beam splitter in between two dipoles (as discussed in Sec. 4.4); we consider only the case of an in-line interferometer (as shown in Fig. 4.1(b)) since this configuration would have minimum mutual coupling and cross talk, which result in spurious unwanted responses. We refer to this last configuration as a zero-spacing interferometer.

4.5.1 Very small interferometer array of 1-D antennas made of short dipoles in parallel configuration

The antennas in this interferometer configuration are assumed to be linear arrays of collinear short dipoles spaced half wavelength apart at 40 MHz, so that the spacing in wavelengths would only be greater at all other frequencies in the band of interest. As discussed in Sec. 4.3.2, since the improvement in gain diminishes substantially with increasing number of short dipoles in the 1-D antenna, we fix the number of dipoles to be four in each antenna of the interferometers.

We now estimate the effective signal-to-noise ratio (SNR) as a function of frequency. Let m_i denote the measurement set recorded in the i^{th} interferometer baseline and r_i denote the telescope filter function or interferometer response for that baseline. An estimate of the global sky signal is given by (m_i/r_i). We then compute a weighted average of the estimates made in different baselines, optimally weighting the estimates by the inverse of the noise variance, which is proportional to r_i^2. This weighted average estimate of the signal X_{eor} is given by:

$$X_{\text{eor}} = \sum_{i=1}^{3} \left(\frac{m_i}{r_i} \right) \frac{r_i^2}{\sum_{i=1}^{3} r_i^2}, \tag{4.6}$$

which can be simplified as:

$$X_{\text{eor}} = \frac{\sum_{i=1}^{3} m_i r_i}{\sum_{i=1}^{3} r_i^2}, \tag{4.7}$$

where the summations are over corresponding frequency data in the three baselines.

Equation 4.7 can be re-written as:

$$X_{\text{eor}} = \sum_{i=1}^{3} m_i W_i, \tag{4.8}$$

where W_i is defined as:

$$W_i = \frac{r_i}{\sum_{i=1}^{3} r_i^2}, \tag{4.9}$$

and is the weighting factor for different baseline responses.

In any frequency channel, the rms noise uncertainty in the weighted mean estimate $X_{\rm eor}$ of the global EoR signal is then given by:

$$\sigma_{\rm eff} = \sqrt{\sum_{i=1}^{3} \sigma_{\rm noise}^2 W_i^2}, \tag{4.10}$$

where $\sigma_{\rm noise}$ is the rms noise in that channel. We assume here that $\sigma_{\rm noise}$ is the same in all baselines and is dominated by the antenna temperature T_a corresponding to the foreground brightness temperature (Equation 4.5). $\sigma_{\rm noise}$ is given by [173] $\sigma_{\rm noise}^2 = \frac{T_{\rm b}^2}{2\beta\tau}$. We have assumed a channel bandwidth β of 1 MHz and integration time τ of 200 hr.

Thus we can re-express $\sigma_{\rm eff}$ as:

$$\sigma_{\rm eff} = \frac{\sigma_{\rm noise}}{\sqrt{\sum_{i=1}^{3} r_i^2}}. \tag{4.11}$$

The ratio of weighted mean estimate $X_{\rm eor}$ of the global EoR signal (Equation 4.8) and the effective rms noise $\sigma_{\rm eff}$ (Equation 4.11) yields the effective SNR for the telescope.

4.5.2 Very small interferometer array made of 1-D aperture antennas

The 1-D antennas in Sec. 4.5.1 were linear arrays of short dipoles, spaced half wavelength apart at 40 MHz. At this frequency the linear antenna is a fully filled 1-D aperture; however, at higher frequencies in the 40-200 MHz band the filling is increasingly sparse. In this section we consider, as the interferometer elements, 1-D aperture antennas that are fully filled at all frequencies in the band. This is indeed practically realizable by arraying small and wideband sensor elements all along the 1-D aperture so that the fields may be coherently combined with uniform weighting. The 1-D aperture antennas are assumed to form interferometers in parallel configuration.

The effective SNR versus frequency is shown in Fig. 4.8 for the 3-element interferometer telescope. Separate lines show the SNR for the case where the 1-D antenna is an array of dipoles spaced half wavelength apart at 40 MHz and the case where the antenna is a 1-D aperture. Unsurprisingly, the 1-D aperture antenna improves upon the sensitivity at the higher frequencies (see Fig. 4.8).

4.5.3 Zero Spacing Interferometer

We finally consider the wideband response of a zero spacing interferometer. The interferometer elements in this case consists of short wideband dipoles and the interferometer is of in-line configuration. A resistive sheet is in between the in-line dipoles and serves as a space beam splitter. As discussed in Mahesh et al. [84], for a resistive sheet with sheet impedance equal to half the impedance of free space, the reflected and transmitted powers received by an interferometer element are equal and each is one-fourth of the incident power. Further, half the incident power is absorbed in the resistive sheet. Assuming that the resistive sheet is sufficiently large in extent and the antennas are wideband, the interferometer response is frequency independent and the telescope filter function is a constant at 0.25. The SNR for such a zero-spacing interferometer is also shown in Fig. 4.8.

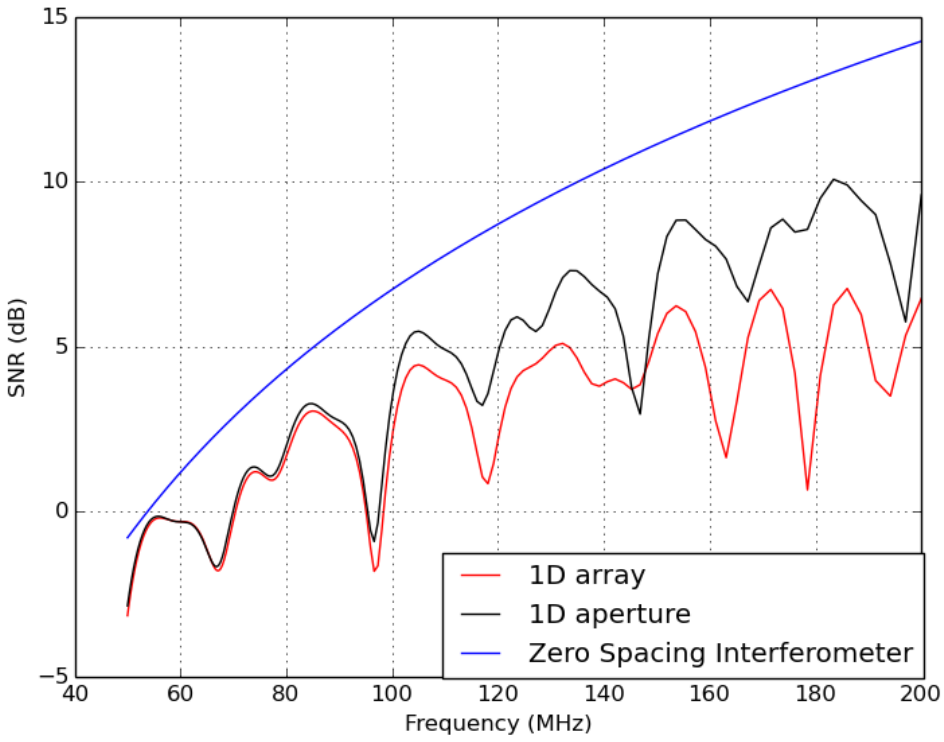

Figure 4.8: Effective signal-to-noise ratio for the detection of a global signal of amplitude 10 mK. The interferometer array is assumed to consist of three interferometer elements with three baselines formed between the elements; the configuration of the in-line interferometers and 1-D elements are as described in the text. Also shown is the signal-to-noise ratio for a zero-spacing interferometer: a 2-element in-line interferometer of unit dipoles with a resistive sheet in between. 200 hr integration time and 1 MHz spectral bandwidth are assumed.

4.6 Discussion and Summary

First, it is clear that all-sky spectral signals that are uniform across the sky, like the global EoR signal that is otherwise known as the EoR monopole, is detectable using interferometer methods, which have their inherent advantages over single element total power spectral radiometers. 2-element interferometers made of unit dipole elements or 1-D antennas that are composed of an array of short wideband dipoles do capture up to about 20% of the global signal on baselines of a few wavelengths.

Second, owing to the extremely small response to the global EoR signal of interferometers made using aperture antennas, any attempt at interferometer detection of global EoR ought to be done with elemental or 1-D antennas. The response of interferometers made of small aperture antennas, with diameters 6–12 λ, and with uniform weighting in their sensing of the aperture fields, have a response that is less than 10^{-3} of the global EoR. If the element apertures have a realistic Gaussian taper in their sensing over their apertures, then this response drops to lower than 10^{-7}. Since the system noise in interferometers at the frequencies at which the global EoR signal appears is dominated by the sky foreground brightness, interferometers made using aperture antennas would require at least 10^4 times greater observing time making them unattractive in comparison.

The spatial coherence in the field arising from the global EoR signal may be enhanced using a semi-transparent screen. The response of any two-element interferometer to global EoR may be enhanced by placing a resistive screen in between, with sheet resistance equal to half the impedance of free space (377/2 Ω). The interferometer then senses the altered fields on the two sides of the screen, whose coherence has been enhanced by the screen. The elements of the interferometer may now be a pair of short wideband dipoles oriented in in-line configuration, so that their mutual coupling and hence cross talk is minimized. A critical advantage of global EoR measurements using such a zero-spacing interferometer is that its telescope filter function is relatively smooth compared to the net function derived from a small array of unit or 1-D antennas.

It may be noted here that interferometers also respond to angular structure in sky brightness distribution and this response depends on the spatial frequency mode corresponding to the baseline length. Since this is frequency dependent, interferometers mode-couple angular structure in brightness distribution to frequency structure in the spectral domain. This results in confusion to the global EoR signal. Placing interferometers EW, and averaging the response over time, removes the spectral structure arising from this mode coupling.

Antenna elements that have frequency dependent radiation patterns also mode couple angular structure in brightness distribution to the spectral domain. Therefore, it is advantageous to use only frequency independent antennas as interferometer elements. This is yet another argument against using 2-D aperture antennas. This is also an argument against using 1-D aperture antennas, and hence

the antennas may simply be electrically-short wideband dipoles.

The work presented here advances the understanding of the usefulness of interferometers in measurements of global EoR. The work motivates in depth study of issues related to mutual coupling in short spacing interferometers and the consequent systematics and limitations to sensitivity. Additionally, careful modeling of the response of interferometers with finite-size resistive sheets in between is suggested as future work, including the response to emission from the resistive screen itself.

Chapter 5

Conclusion

> "*In this modern era of cosmology, each new observation, each morsel of data wields a two-edged sword: it enables cosmology to thrive on the kind of foundation that so much of the rest of science enjoys, but it also constrains theories that people thought up when there wasn't enough data to say whether they were wrong or not. No science achieves maturity without it.*
> *Let there be cosmology.*" - Neil deGrasse Tyson

The discovery of the cosmic microwave background (CMB) and understanding its origin, strongly favored the Hot Big Bang model. The CMB represents observational evidence that the expanding and cooling Universe transitioned from completely ionized to almost neutral around $z \sim 1100$. In the same year CMB discovery was reported (1965), Gunn and Peterson pointed out that the non-detection of an absorption trough in the spectrum of a quasar at redshift $z \sim 2$, shortward of Lyα, implied that the intergalactic medium was predominantly ionized. This was the first evidence that somewhere in the recent past, subsequent to the recombination of the primordial gas at $z \sim 1100$, the Universe made a transition from being almost neutral to ionized and we currently live in an ionized Universe.

36 years later, the first Gunn-Peterson absorption trough was detected in a quasar at $z = 6.28$. Examination of the spectra of quasars at redshifts 5.82, 5.99 and 6.28 provided strong evidence of a rapid decline in the mean ionizing background between $z \sim 5$ and 6, indicating the completion of reionization around $z \sim 6$ [12] .

This led to studying different observables through which high-redshift Universe could be probed. Constraints from CMB, Lyα emitters and quasars assisted in placing constraints on the ionization history of EoR. We have discussed the constraints derived from these observables in Chapter 1. However, these observables are indirect or integrated measurements, and are limited by instrument sensitivities. As a result, various aspects of CD/EoR, from the nature of the first sources to the mechanism of reionization, are poorly constrained.

In parallel, it was established that 21-cm radiation from neutral hydrogen depends non-trivially on the background radiation, including Lyα, and atomic collisions [49]. This led to suggestions that detection of gas during CD/EoR in redshifted 21-cm from the neutral hydrogen fraction could be used as a probe of reionization [162, 148, 150, 8], which triggered a host of experiments aiming to detect both the mean and the fluctuating components of the 21-cm signal from EoR [100, 56, 132].

As discussed in Sec. 1.5.1, in order to get a complete information of the 21-cm brightness temperature field, we require the measurements of the 21-cm fluctuations as well as the mean component. Together, the measurements can be employed to place a joint constraint on astrophysical parameters ranging from properties of IGM to the first sources of radiation. Since the advent of a new generation of 21-cm experiments over the last decade targeting the power spectrum as well as the global signal, there has been impressive advancements in system design, calibration schemes and data modeling. While interferometers are progressively improving their sensitivities towards detecting the power spectrum, constraints on cosmic dawn and reionization have already starting to emerge from single dish experiments. In the following sections, we briefly review the limits and astrophysical constraints obtained from power spectrum and global signal measurements respectively.

5.1 Status of 21-cm power spectrum measurements

The 21-cm power spectrum, $P_{21}(k)$, is a statistical description of the spatial fluctuations of the 21-cm brightness temperature. It can be computed for different redshifts and over a range of spatial scales, k. Mathematically, k is inversely related to the physical mode wavelength λ, and is defined as $k = 2\pi/\lambda$.

Aiming to detect this fluctuating 21-cm, of maximum strength a few tens of mK, embedded in the foreground that is 5-6 orders of magnitude brighter, is extremely challenging. High dynamic range imaging with long wavelength interferometers is required to go beyond current imaging capabilities in pursuit of the detection. With this motivation, there has been steady progress in developing algorithms to push the sensitivity further down. However, the residual levels, left after calibration and foreground modeling, are still significantly higher than the amplitudes of the theoretically predicted 21-cm power spectrum [28]. Consequently, using the best available calibration techniques and foreground modeling, the residuals have resulted in upper limits on the 21-cm power spectrum. These upper bounds are limited by calibration techniques, cross-talk, ionosphere-induced gain errors and inadequate modeling of the foreground and internal systematics.

The upper limits are placed in terms of Δ^2, which represents the integration of 21-cm power spectrum over a range of spatial scales. Mathematically, it is related to $P_{21}(k)$ as $\Delta^2 \equiv k^3 P_{21}(k)/2\pi^2$. Δ^2 effectively denotes the residual variance in the image which can be assumed to be an upper limit to the integrated power spectrum over the range of k over which the image has responsiveness.

The first limits came from GMRT which reported an upper limit of $\Delta^2 < (248\ \mathrm{mK})^2$ for $k =$

$0.5h\,\mathrm{Mpc}^{-1}$ at $z = 8.6$ [115]. PAPER placed a limit of $\Delta^2(k) < (22.4\ \mathrm{mK})^2$ in the range of $0.15 < k < 0.5h\,\mathrm{Mpc}^{-1}$ at $z = 8.4$ [1]. MWA probed to deeper redshifts and placed a limit on $\Delta^2 < (10^4\ \mathrm{mK})^2$ for $k \lesssim 0.5h\,\mathrm{Mpc}^{-1}$ at redshifts $12 \lesssim z \lesssim 18$ [40]. MWA observations at $z = 7.1$ placed an upper limit of $\Delta^2(k) < (164\ \mathrm{mK})^2$ at $k = 0.27\,h\,\mathrm{cMpc}^{-1}$ [11]. LOFAR placed an upper limit of $\Delta^2 < (79.6\ \mathrm{mK})^2$ at $k = 0.053h\,c\mathrm{Mpc}^{-1}$ in the range $z = 9.6 - 10.6$ [119].

5.2 Status of global 21-cm measurements

Ongoing experiments that target detection of the global 21-cm signal from CD and EoR also need to contend with orders of magnitude stronger Galactic and extragalactic foregrounds [150, 145]. These foregrounds couple to the radiometer system through its frequency dependent transfer function and can potentially confuse a detection of the relatively faint cosmological 21-cm signal. Additional challenges include modeling the internal additives from within the receiver system, which are often difficult to calibrate, and excision of terrestrial Radio Frequency Interference (RFI). All these demand stringent requirements on the antenna and receiver design, clever calibration strategies and innovative data analysis methods [153].

Despite these challenges, pioneering experiments have attained sensitivity levels at which plausible scenarios of reionization are being ruled out. The first constraint on EoR from global 21-cm experiments came from the Experiment to Detect the Global EoR Signature (EDGES) high band antenna covering 90–190 MHz frequency range, which ruled out rapid reionization with $\Delta z < 0.06$ at the 95% confidence level [16]. Bernardi et al. [15] used an outrigger Large Aperture Experiment to Detect the Dark Ages (LEDA) antenna to measure the spectrum at lower frequencies, 50–100 MHz. This measurement constrained the amplitude of the absorption trough to be less than 890 mK for a Gaussian-shaped absorption with width greater than 6.5 MHz at the 95% confidence level. Constraints on the redshift interval, Δz, over which reionization occurred have significantly improved with the recent high-band data from EDGES [98]. The constraint depends on the assumptions for the thermal state of the IGM during the EoR: for heated IGM models, $\Delta z \leq 1$ with EoR happening at $z \approx 8.5$ is rejected with 95% confidence; whereas for cold IGM scenarios, $\Delta z \lesssim 2$ is rejected over most of the plausible redshift range for the EoR. All the analyses mentioned above were carried out adopting simple functions to mimic the cosmological signal: a *tanh* form was used to imitate the variation in ionization fraction with frequency, and the absorption trough was modeled as a Gaussian. SARAS 2 significantly added to the constraints by ruling out, for the first time, theoretically plausible models of global 21-cm signals which shared the scenario of late heating in tandem with rapid reionization. As discussed in Chapter 3, it also became the first experiment to constrain the astrophysical properties of the sources through global 21-cm observations [151, 152]. We summarize these results in Fig. 5.1.

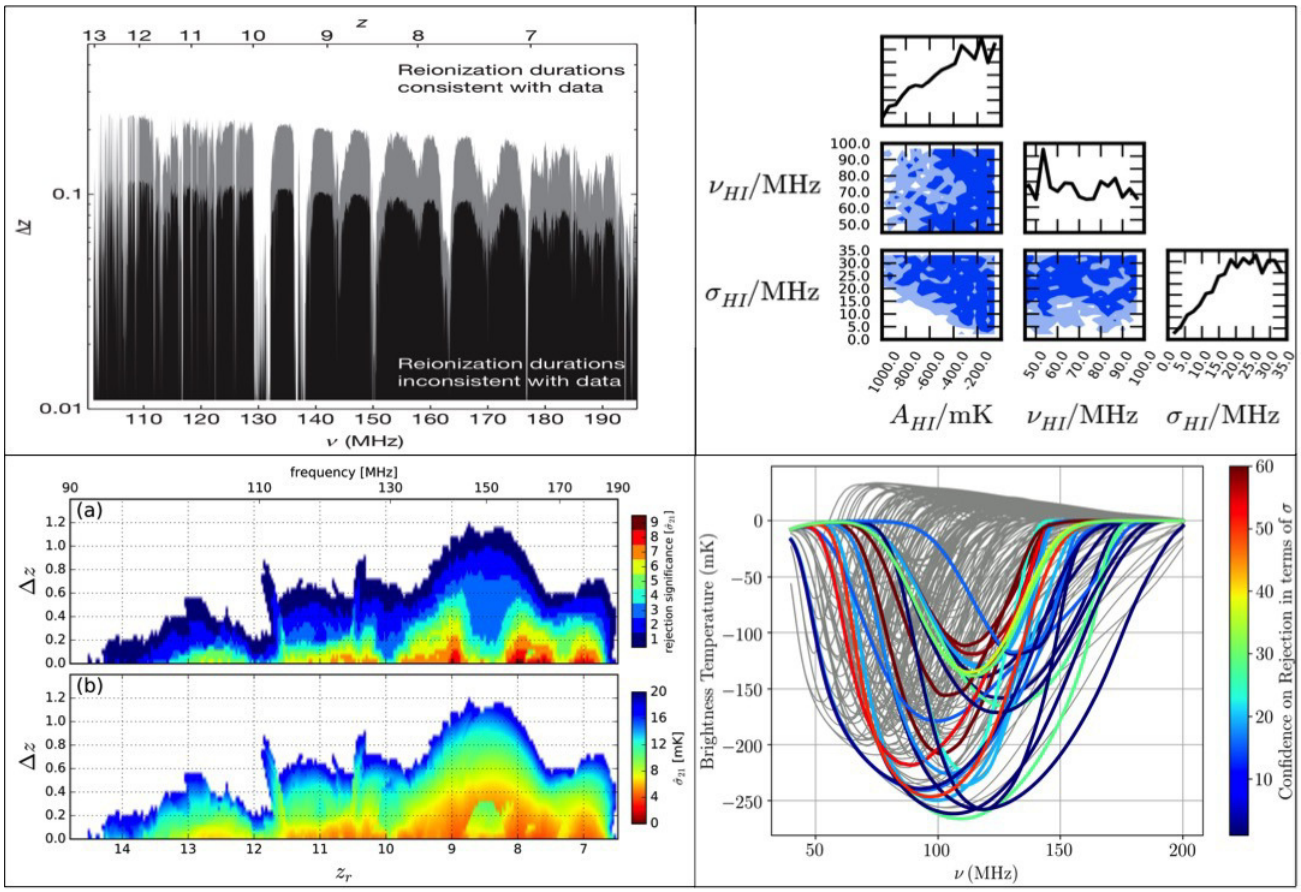

Figure 5.1: The top left panel shows the constraints from EDGES [16], where the duration of reionization, Δz, is constrained to be less than 0.06. Bottom left panel shows the revised constraints from EDGES high band [98] where $\Delta z \leq 1$ is ruled-out for the case of a hot IGM. The top right panel shows the constraints from LEDA (adapted from [15]) on Gaussian-shaped absorption feature in the 21-cm signal, constraining its amplitude, width and location. One and two dimensional probability distributions of all the three parameters are shown. The bottom right panel shows the theoretically plausible global 21-cm signals from Cohen et al. [29], where the colored subset is ruled out by SARAS 2 [152].

5.2.1 On the EDGES detection of a signature from Cosmic Dawn

Recently, EDGES reported detection of an absorption trough at 78 MHz [18]. The signature is characterized by four parameters, amplitude (A), centre frequency (ν_0), width (w) and flattening factor (τ). The best fit values of the parameters are listed below:

1. $A = 0.5^{+0.5}_{-0.2}$ mK

2. $\nu_0 = 78 \pm 1$ MHz

3. $w = 19^{+4}_{-2}$ MHz

4. $\tau = 7^{+5}_{-3}$,

where the errors show 99% confidence limits. The detected signal is shown in Fig. 5.2 (d).

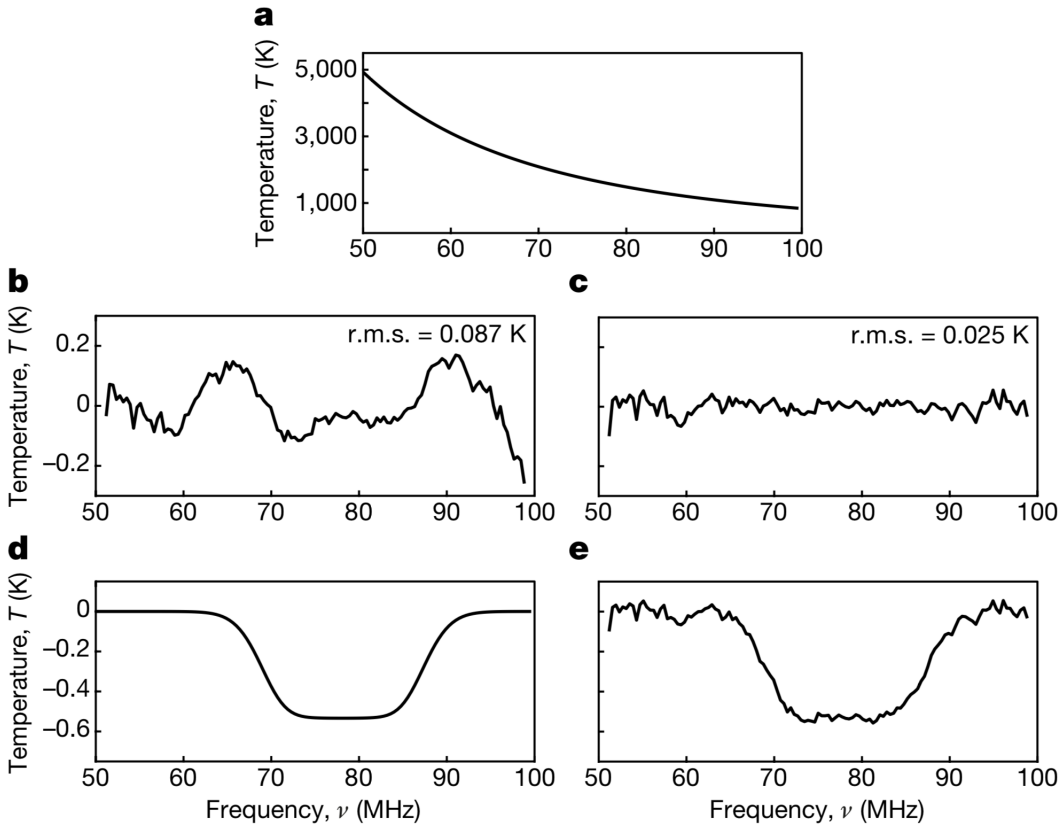

Figure 5.2: (a) The measured sky spectrum, (b) residuals after only foreground is modeled and subtracted from the measured sky spectrum, (c) residuals after the foreground and the signal are jointly modeled and subtracted from the measured sky spectrum, (d) the modeled signal with best fit parameters, and (e) the best fit signal added to residuals of case (c).

However, at least two parameters of the signal do not fall within *standard* predictions, namely the amplitude and flattening. As shown by the suite of theoretically plausible 21-cm signals from Cohen et al. [29], the maximum amplitude of the signal can be at most ~ 250 mK at the centre frequency, as shown in Fig. 5.3. The detected amplitude of the signal turns out to be at least a factor of two

larger than the maximum allowed value under ΛCDM framework [174]. At the same time, none of the models predict a flattening as observed in the detected signature.

There have been several works attempting to explain the peculiar absorption profile by proposing dark matter-baryon interactions that may lead to excessive cooling of gas, more than what could have been achieved by adiabatic cooling [9]. However, cooling of the baryonic matter by scattering with dark matter is extremely unlikely in the light of current experimental constraints. There is a possibility of energy exchange between dark matter and electrons and protons leading to cooling of gas, but it requires the presence of millicharged dark matter [10]. There are also attempts at explaining the amplitude by invoking excess radio background [41, 44]; however, this requires a large excess at very early times ($z \sim 17$) which is difficult to produce theoretically [149].

Given that exotic explanations are required to explain the signal, the detection needs a confirmation.

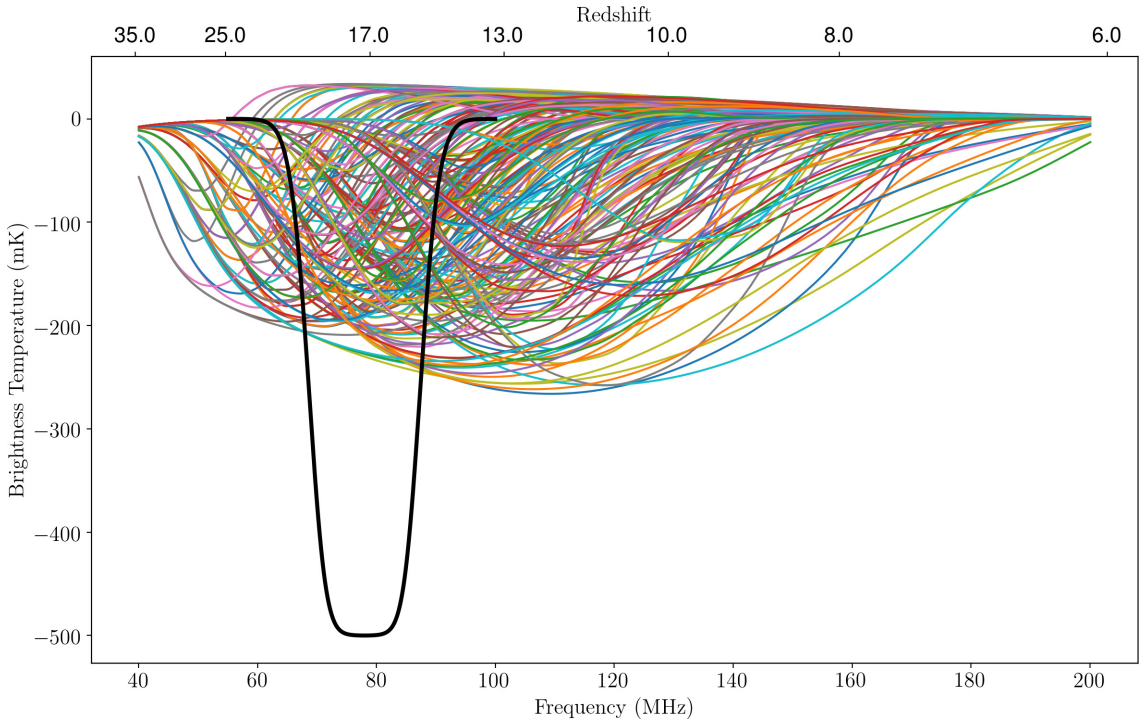

Figure 5.3: For perspective, the figure shows the EDGES detection along with the atlas of theoretically predicted signals [29].

5.3 SARAS: The present and way forward

SARAS 2 has resulted in useful constraints on EoR by rejecting a class from the atlas of theoretically allowed models generated by Cohen et al. [29], which are representative of the signal space. Having rejected roughly 10% of the theoretically plausible 21-cm signals, it has ruled out scenarios of late X-ray heating and rapid reionization. Consequently, SARAS 2 has been able to place limits on astrophysical properties, namely, X-ray efficiency ($f_X \geq 0.1$) and rate of reionization (peak $\frac{dT_b}{dz} \leq 120$ mK per unit redshift interval).

These constraints from SARAS 2 have been enabled by the design of the radiometer, which has emphasized spectrally smooth transfer functions, both for the multiplicative and additive components.

Such a system response is a result of the following key considerations:

1. Carefully designed antenna with smooth reflection and total efficiencies, with smoothness confirmed via measurements all the way to 1 part in 10^4.

2. A frequency independent antenna power pattern, which avoids coupling of spatial structures in the foreground into spectral domain.

3. Avoiding any resistive elements in the antenna design. The antenna is designed not to have a balun, which may have frequency dependent resistive losses.

4. The antenna plus receiver was designed to be compact, thus ensuring that any internal multipath propagation of the system temperature would not compromise the spectral smoothness of the system response.

5. Designing the receiver architecture such that the nature of systematics do not change while switching the calibrator. This is realized by employing a cross-over switch where both the calibrator and antenna continue to be connected to the receiver throughout the observing.

6. Phase switching, implemented using signal splitting and crosscorrelation, to cancel out the additives that may arise due to cross-talk between the two arms of the receiver.

7. Optical isolation of the antenna plus analog receiver from the rest of the system.

All of these system design features have been complemented by developing data processing algorithms that guarantee to preserve the smoothness of the spectrum during the process of data reduction, calibration and RFI rejection. The analysis strategy has exploited smoothness designed into the system response. All these along with the smoothness of the foregrounds enables placing high confidence constraints on the plausible 21-cm signals.

SARAS 2 demonstrates how the receiver architecture sets the foundations for the analysis strategy. The design criteria for each subsection of the instrument has been to avoid any unwanted spurious feature in the spectrum. SARAS 2 development also emphasized the need for carrying out extensive simulations coupled with laboratory and field measurements to ensure the conformity of the radiometer properties with the design criteria. At the same time, the calibration strategy dispenses with using any pre-measured characteristics of the receiver in the analysis (Measurements performed in the lab stay in the lab!). The focus is towards performing *in-situ* measurements, and ensuring that the system response follows a behavior which can be modeled, to mK levels, using either some specific class of functions or through measurement equation.

Extensive site surveys for locating radio quiet zones have reduced the data corruption due to RFI. Further, having a range of characterized sites at different distances from the laboratory has facilitated in the iterative development of the radiometer. However, a significant downside is that the strong emphasis on smoothness of antenna response led to poor total efficiency below 100 MHz.

The next natural step is to extend the observing band to lower frequencies to probe signals that we are currently not sensitive to. An extended band would also minimize the loss of signal due to foreground modeling since the complete CD/EoR signal, ranging from $40 - 200$ MHz, would have more number of turning points. Further, in light of the current claim of detection by EDGES, SARAS observations at low frequencies would help either verify or refute the claim.

5.4 Concluding remarks

Cosmology has quickly grown into an experimental science. Theories have made testable predictions triggering the design of dedicated instruments to verify them. Over the years, high quality data delivered by precision, purpose-built instruments have greatly helped in confirming and disfavoring different theories regarding the origin and evolution of the Universe. This development is evident when one sees a range of ground and space based experiments probing inflation, nature of dark matter and dark energy, neutrinos, dark ages and reionization, to name a few. We are at a stage where we are pushing limits, both in theory and instruments, to understand the details of different processes that resulted in the Universe we see today.

SARAS 2 has been an effort of this nature, probing a crucial phase of the cosmos when the first generation of stars and galaxies emerged and changed its ionization state. With further improvements planned, efforts are on to evolve the instrument to the next version, develop more robust analysis schemes and continue the quest to understand the high-redshift Universe better.

Bibliography

[1] Zaki S. Ali, Aaron R. Parsons, Haoxuan Zheng, Jonathan C. Pober, Adrian Liu, James E. Aguirre, Richard F. Bradley, Gianni Bernardi, Chris L. Carilli, Carina Cheng, David R. DeBoer, Matthew R. Dexter, Jasper Grobbelaar, Jasper Horrell, Daniel C. Jacobs, Pat Klima, David H. E. MacMahon, Matthys Maree, David F. Moore, Nima Razavi, Irina I. Stefan, William P. Walbrugh, and Andre Walker. PAPER-64 Constraints on Reionization: The 21 cm Power Spectrum at z = 8.4. ApJ, 809, August 2015. doi: 10.1088/0004-637X/809/1/61. 123

[2] C. Azeredo-Leme. Clock jitter effects on sampling: A tutorial. *IEEE Circuits and Systems Magazine*, 11(3):26–37, thirdquarter 2011. ISSN 1531-636X. doi: 10.1109/MCAS.2011.942067. 49

[3] J. W. M. Baars, R. Genzel, I. I. K. Pauliny-Toth, and A. Witzel. The absolute spectrum of CAS A - an accurate flux density scale and a set of secondary calibrators. *Astronomy and Astrophysics*, 61:99–106, October 1977. 39

[4] D. K. Bailey. On a new method for exploring the upper ionosphere. *Terrestrial Magnetism and Atmospheric Electricity (Journal of Geophysical Research)*, 53:41, 1948. doi: 10.1029/TE053i001p00041. 20, 29

[5] Constantine A. Balanis. *Antenna Theory: Analysis and Design*. Wiley-Interscience, 2005. ISBN 0471714623. 29, 30, 33, 107

[6] R. Barkana. Did the universe reionize at redshift six? New A, 7:85–100, March 2002. doi: 10.1016/S1384-1076(01)00091-4. 6

[7] R. Barkana. The rise of the first stars: Supersonic streaming, radiative feedback, and 21-cm cosmology. Phys. Rep., 645:1–59, July 2016. doi: 10.1016/j.physrep.2016.06.006. 9

[8] R. Barkana and A. Loeb. In the beginning: the first sources of light and the reionization of the universe. Phys. Rep., 349:125–238, July 2001. doi: 10.1016/S0370-1573(01)00019-9. 2, 122

[9] Rennan Barkana. Possible interaction between baryons and dark-matter particles revealed by the first stars. Nature, 555:71–74, March 2018. doi: 10.1038/nature25791. 126

[10] Rennan Barkana, Nadav Joseph Outmezguine, Diego Redigolo, and Tomer Volansky. Signs of Dark Matter at 21-cm? *ArXiv e-prints*, March 2018. 126

[11] A. P. Beardsley, B. J. Hazelton, I. S. Sullivan, P. Carroll, N. Barry, M. Rahimi, B. Pindor, C. M. Trott, J. Line, D. C. Jacobs, M. F. Morales, J. C. Pober, G. Bernardi, J. D. Bowman, M. P. Busch, F. Briggs, R. J. Cappallo, B. E. Corey, A. de Oliveira-Costa, J. S. Dillon, D. Emrich, A. Ewall-Wice, L. Feng, B. M. Gaensler, R. Goeke, L. J. Greenhill, J. N. Hewitt, N. Hurley-Walker, M. Johnston-Hollitt, D. L. Kaplan, J. C. Kasper, H. S. Kim, E. Kratzenberg, E. Lenc, A. Loeb, C. J. Lonsdale, M. J. Lynch, B. McKinley, S. R. McWhirter, D. A. Mitchell, E. Morgan, A. R. Neben, N. Thyagarajan, D. Oberoi, A. R. Offringa, S. M. Ord, S. Paul, T. Prabu, P. Procopio, J. Riding, A. E. E. Rogers, A. Roshi, N. Udaya Shankar, S. K. Sethi, K. S. Srivani, R. Subrahmanyan, M. Tegmark, S. J. Tingay, M. Waterson, R. B. Wayth, R. L. Webster, A. R. Whitney, A. Williams, C. L. Williams, C. Wu, and J. S. B. Wyithe. First Season MWA EoR Power spectrum Results at Redshift 7. ApJ, 833:102, December 2016. doi: 10.3847/1538-4357/833/1/102. 123

[12] R. H. Becker, X. Fan, R. L. White, M. A. Strauss, V. K. Narayanan, R. H. Lupton, J. E. Gunn, J. Annis, N. A. Bahcall, J. Brinkmann, A. J. Connolly, I. Csabai, P. C. Czarapata, M. Doi, T. M. Heckman, G. S. Hennessy, Ž. Ivezić, G. R. Knapp, D. Q. Lamb, T. A. McKay, J. A. Munn, T. Nash, R. Nichol, J. R. Pier, G. T. Richards, D. P. Schneider, C. Stoughton, A. S. Szalay, A. R. Thakar, and D. G. York. Evidence for Reionization at z˜6: Detection of a Gunn-Peterson Trough in a z=6.28 Quasar. AJ, 122:2850–2857, December 2001. doi: 10.1086/324231. 6, 121

[13] A. J. Benson, N. Sugiyama, A. Nusser, and C. G. Lacey. The epoch of reionization. MNRAS, 369:1055–1080, July 2006. doi: 10.1111/j.1365-2966.2006.10426.x. 5

[14] G. Bernardi, M. McQuinn, and L. J. Greenhill. Foreground Model and Antenna Calibration Errors in the Measurement of the Sky-averaged λ21 cm Signal at z˜ 20. ApJ, 799:90, January 2015. doi: 10.1088/0004-637X/799/1/90. 21

[15] G. Bernardi, J. T. L. Zwart, D. Price, L. J. Greenhill, A. Mesinger, J. Dowell, T. Eftekhari, S. W. Ellingson, J. Kocz, and F. Schinzel. Bayesian constraints on the global 21-cm signal from the Cosmic Dawn. MNRAS, 461:2847–2855, September 2016. doi: 10.1093/mnras/stw1499. 123, 124

[16] J. D. Bowman and A. E. E. Rogers. A lower limit of $\Delta z > 0.06$ for the duration of the reionization epoch. Nature, 468:796–798, December 2010. doi: 10.1038/nature09601. 123, 124

[17] J. D. Bowman, M. F. Morales, and J. N. Hewitt. The Sensitivity of First-Generation Epoch of Reionization Observatories and Their Potential for Differentiating Theoretical Power Spectra. ApJ, 638:20–26, February 2006. doi: 10.1086/498703. 16

[18] J. D. Bowman, A. E. E. Rogers, R. A. Monsalve, T. J. Mozdzen, and N. Mahesh. An absorption profile centred at 78 megahertz in the sky-averaged spectrum. Nature, 555:67–70, March 2018. doi: 10.1038/nature25792. 19, 124

[19] V. Bromm, N. Yoshida, L. Hernquist, and C. F. McKee. The formation of the first stars and galaxies. Nature, 459:49–54, May 2009. doi: 10.1038/nature07990. 1

[20] Philip Bull, Pedro G. Ferreira, Prina Patel, and Mário G. Santos. Late-time cosmology with 21 cm intensity mapping experiments. *The Astrophysical Journal*, 803(1):21, 2015. URL http://stacks.iop.org/0004-637X/803/i=1/a=21. 1

[21] J. O. Burns, R. Bradley, K. Tauscher, S. Furlanetto, J. Mirocha, R. Monsalve, D. Rapetti, W. Purcell, D. Newell, D. Draper, R. MacDowall, J. Bowman, B. Nhan, E. J. Wollack, A. Fialkov, D. Jones, J. C. Kasper, A. Loeb, A. Datta, J. Pritchard, E. Switzer, and M. Bicay. A Space-based Observational Strategy for Characterizing the First Stars and Galaxies Using the Redshifted 21 cm Global Spectrum. ApJ, 844:33, July 2017. doi: 10.3847/1538-4357/aa77f4. 19

[22] J. E. Carlstrom, G. P. Holder, and E. D. Reese. Cosmology with the Sunyaev-Zel'dovich Effect. ARA&A, 40:643–680, 2002. doi: 10.1146/annurev.astro.40.060401.093803. 6

[23] Renyue Cen. The universe was reionized twice. *The Astrophysical Journal*, 591(1):12, 2003. URL http://stacks.iop.org/0004-637X/591/i=1/a=12. 5

[24] E. Chapman, A. Bonaldi, G. Harker, V. Jelic, F. B. Abdalla, G. Bernardi, J. Bobin, F. Dulwich, B. Mort, M. Santos, and J. L. Starck. Cosmic Dawn and Epoch of Reionization Foreground Removal with the SKA. *Advancing Astrophysics with the Square Kilometre Array (AASKA14)*, art. 5, April 2015. 20

[25] John S. Chipman. *Gauss-Markov Theorem*, pages 577–582. Springer Berlin Heidelberg, Berlin, Heidelberg, 2011. ISBN 978-3-642-04898-2. doi: 10.1007/978-3-642-04898-2_270. 53

[26] T. R. Choudhury, E. Puchwein, M. G. Haehnelt, and J. S. Bolton. Lyman α emitters gone missing: evidence for late reionization? MNRAS, 452:261–277, September 2015. doi: 10.1093/mnras/stv1250. 5

[27] B. G. Clark. Coherence in Radio Astronomy. In G. B. Taylor, C. L. Carilli, and R. A. Perley, editors, *Synthesis Imaging in Radio Astronomy II*, volume 180 of *Astronomical Society of the Pacific Conference Series*, page 1, 1999. 103

[28] A. Cohen, A. Fialkov, and R. Barkana. Charting the Parameter Space of the 21-cm Power Spectrum. *ArXiv e-prints*, September 2017. 16, 122

[29] A. Cohen, A. Fialkov, R. Barkana, and M. Lotem. Charting the parameter space of the global 21-cm signal. *Monthly Notices of the Royal Astronomical Society*, 472:1915–1931, December 2017. doi: 10.1093/mnras/stx2065. 4, 15, 18, 53, 85, 86, 87, 93, 95, 99, 124, 125, 126, 127

[30] James J. Condon and Scott M. Ransom. *Essential Radio Astronomy (Princeton Series in Modern Observational Astronomy)*. Princeton University Press, 2016. 10, 39

[31] Abhirup Datta, Richard Bradley, Jack O. Burns, Geraint Harker, Attila Komjathy, and T. Joseph W. Lazio. The Effects of the Ionosphere on Ground-based Detection of the Global 21 cm Signal from the Cosmic Dawn and the Dark Ages. ApJ, 831, November 2016. doi: 10.3847/0004-637X/831/1/6. 21, 101

[32] G. De Zotti. Prospects for next generation Cosmic Microwave Background experiments. *ArXiv e-prints*, February 2018. 1

[33] R. H. Dicke. *The Measurement of Thermal Radiation at Microwave Frequencies*, pages 106–113. Springer Netherlands, Dordrecht, 1982. ISBN 978-94-009-7752-5. doi: 10.1007/978-94-009-7752-5_11. 40

[34] R. H. Dicke, P. J. E. Peebles, P. G. Roll, and D. T. Wilkinson. Cosmic Black-Body Radiation. ApJ, 142:414–419, July 1965. doi: 10.1086/148306. 1

[35] M. Dijkstra. Constraining Reionization with Lyα; Emitting Galaxies. In A. Mesinger, editor, *Understanding the Epoch of Cosmic Reionization: Challenges and Progress*, volume 423 of *Astrophysics and Space Science Library*, page 145, 2016. doi: 10.1007/978-3-319-21957-8_5. 8, 9

[36] M. Dijkstra, M. Gilfanov, A. Loeb, and R. Sunyaev. Constraints on the redshift evolution of the L_X-SFR relation from the cosmic X-ray backgrounds. MNRAS, 421:213–223, March 2012. doi: 10.1111/j.1365-2966.2011.20292.x. 4

[37] M. Dijkstra, S. Wyithe, Z. Haiman, A. Mesinger, and L. Pentericci. Evolution in the escape fraction of ionizing photons and the decline in strong Lyα emission from $z > 6$ galaxies. MNRAS, 440:3309–3316, June 2014. doi: 10.1093/mnras/stu531. 8

[38] S. G. Djorgovski, S. Castro, D. Stern, and A. A. Mahabal. On the threshold of the reionization epoch. *The Astrophysical Journal Letters*, 560(1):L5, 2001. URL http://stacks.iop.org/1538-4357/560/i=1/a=L5. 5

[39] Olivier Doré, Gil Holder, Marcelo Alvarez, Ilian T. Iliev, Garrelt Mellema, Ue-Li Pen, and Paul R. Shapiro. Signature of patchy reionization in the polarization anisotropy of the cmb. *Phys. Rev. D*, 76:043002, Aug 2007. doi: 10.1103/PhysRevD.76.043002. URL https://link.aps.org/doi/10.1103/PhysRevD.76.043002. 5

[40] A. Ewall-Wice, Joshua S. Dillon, J. N. Hewitt, A. Loeb, A. Mesinger, A. R. Neben, A. R. Offringa, M. Tegmark, N. Barry, A. P. Beardsley, G. Bernardi, Judd D. Bowman, F. Briggs, R. J. Cappallo, P. Carroll, B. E. Corey, A. de Oliveira-Costa, D. Emrich, L. Feng, B. M. Gaensler, R. Goeke, L. J. Greenhill, B. J. Hazelton, N. Hurley-Walker, M. Johnston- Hollitt, Daniel C. Jacobs, D. L. Kaplan, J. C. Kasper, HS Kim, E. Kratzenberg, E. Lenc, J. Line, C. J. Lonsdale, M. J. Lynch, B. McKinley, S. R. McWhirter, D. A. Mitchell, M. F. Morales, E. Morgan, Nithyanandan Thyagarajan, D. Oberoi, S. M. Ord, S. Paul, B. Pindor, J. C. Pober, T. Prabu, P. Procopio, J. Riding, A. E. E. Rogers, A. Roshi, N. Udaya Shankar, Shiv K. Sethi, K. S. Srivani, R. Subrahmanyan, I. S. Sullivan, S. J. Tingay, C. M. Trott, M. Waterson, R. B. Wayth, R. L. Webster, A. R. Whitney, A. Williams, C. L. Williams, C. Wu, and J. S. B. Wyithe. First limits on the 21 cm power spectrum during the Epoch of X-ray heating. MNRAS, 460:4320–4347, August 2016. doi: 10.1093/mnras/stw1022. 123

[41] A. Ewall-Wice, T. C. Chang, J. Lazio, O. Doré, M. Seiffert, and R. A. Monsalve. Modeling the Radio Background from the First Black Holes at Cosmic Dawn: Implications for the 21 cm Absorption Amplitude. *ArXiv e-prints*, March 2018. 126

[42] X. Fan, C. L. Carilli, and B. Keating. Observational Constraints on Cosmic Reionization. ARA&A, 44:415–462, September 2006. doi: 10.1146/annurev.astro.44.051905.092514. 5, 6

[43] X. Fan, M. A. Strauss, R. H. Becker, R. L. White, J. E. Gunn, G. R. Knapp, G. T. Richards, D. P. Schneider, J. Brinkmann, and M. Fukugita. Constraining the Evolution of the Ionizing

Background and the Epoch of Reionization with z˜6 Quasars. II. A Sample of 19 Quasars. AJ, 132:117–136, July 2006. doi: 10.1086/504836. 6, 7

[44] Chang Feng and Gilbert Holder. Enhanced global signal of neutral hydrogen due to excess radiation at cosmic dawn. *ArXiv e-prints*, February 2018. 126

[45] A. Ferrara. Feedback Processes at Cosmic Dawn. In *EAS Publications Series, Volume 24, 2007, pp.229-243*, volume 24, pages 229–243, January 2007. doi: 10.1051/eas:2007032. 4

[46] A. Fialkov and R. Barkana. The rich complexity of 21-cm fluctuations produced by the first stars. MNRAS, 445:213–224, November 2014. doi: 10.1093/mnras/stu1744. 85

[47] A. Fialkov, R. Barkana, A. Pinhas, and E. Visbal. Complete history of the observable 21 cm signal from the first stars during the pre-reionization era. MNRAS, 437:L36–L40, January 2014. doi: 10.1093/mnrasl/slt135. 15

[48] A. Fialkov, R. Barkana, and E. Visbal. The observable signature of late heating of the Universe during cosmic reionization. Nature, 506:197–199, February 2014. doi: 10.1038/nature12999. 90, 95

[49] G. B. Field. Excitation of the Hydrogen 21-CM Line. *Proceedings of the IRE*, 46:240–250, January 1958. doi: 10.1109/JRPROC.1958.286741. 12, 13, 122

[50] Georgios Florides and Soteris Kalogirou. 1 annual ground temperature measurements at various depths. 78

[51] S. R. Furlanetto. The global 21-centimeter background from high redshifts. MNRAS, 371: 867–878, September 2006. doi: 10.1111/j.1365-2966.2006.10725.x. 13

[52] S. R. Furlanetto, S. P. Oh, and F. H. Briggs. Cosmology at low frequencies: The 21 cm transition and the high-redshift Universe. Phys. Rep., 433:181–301, October 2006. doi: 10.1016/j.physrep.2006.08.002. 3, 10, 12

[53] S. R. Furlanetto, A. Lidz, A. Loeb, M. McQuinn, J. R. Pritchard, M. A. Alvarez, D. C. Backer, J. D. Bowman, J. O. Burns, C. L. Carilli, R. Cen, A. Cooray, N. Gnedin, L. J. Greenhill, Z. Haiman, J. N. Hewitt, C. M. Hirata, J. Lazio, A. Mesinger, P. Madau, M. F. Morales, S. P. Oh, J. B. Peterson, Y. M. Pihlström, P. R. Shapiro, M. Tegmark, H. Trac, O. Zahn, and M. Zaldarriaga. Astrophysics from the Highly-Redshifted 21 cm Line. In *astro2010: The Astronomy and Astrophysics Decadal Survey*, volume 2010 of *Astronomy*, 2009. 15

[54] S. R. Furlanetto, A. Lidz, A. Loeb, M. McQuinn, J. R. Pritchard, P. R. Shapiro, M. A. Alvarez, D. C. Backer, J. D. Bowman, J. O. Burns, C. L. Carilli, R. Cen, A. Cooray, N. Gnedin, L. J. Greenhill, Z. Haiman, J. N. Hewitt, C. M. Hirata, J. Lazio, A. Mesinger, P. Madau, M. F. Morales, S. P. Oh, J. B. Peterson, Y. M. Pihlström, M. Tegmark, H. Trac, O. Zahn, and M. Zaldarriaga. Cosmology from the Highly-Redshifted 21 cm Line. In *astro2010: The Astronomy and Astrophysics Decadal Survey*, volume 2010 of *ArXiv Astrophysics e-prints*, 2009. 15

[55] E. M. George, C. L. Reichardt, K. A. Aird, B. A. Benson, L. E. Bleem, J. E. Carlstrom, C. L. Chang, H.-M. Cho, T. M. Crawford, A. T. Crites, T. de Haan, M. A. Dobbs, J. Dudley, N. W. Halverson, N. L. Harrington, G. P. Holder, W. L. Holzapfel, Z. Hou, J. D. Hrubes, R. Keisler, L. Knox, A. T. Lee, E. M. Leitch, M. Lueker, D. Luong-Van, J. J. McMahon, J. Mehl, S. S. Meyer, M. Millea, L. M. Mocanu, J. J. Mohr, T. E. Montroy, S. Padin, T. Plagge, C. Pryke, J. E. Ruhl, K. K. Schaffer, L. Shaw, E. Shirokoff, H. G. Spieler, Z. Staniszewski, A. A. Stark, K. T. Story, A. van Engelen, K. Vanderlinde, J. D. Vieira, R. Williamson, and O. Zahn. A Measurement of Secondary Cosmic Microwave Background Anisotropies from the 2500 Square-degree SPT-SZ Survey. ApJ, 799:177, February 2015. doi: 10.1088/0004-637X/799/2/177. 6

[56] N. Y. Gnedin and P. A. Shaver. Redshifted 21 Centimeter Emission from the Pre-Reionization Era. I. Mean Signal and Linear Fluctuations. ApJ, 608:611–621, June 2004. doi: 10.1086/420735. 122

[57] Nickolay Y. Gnedin. Cosmological reionization by stellar sources. *The Astrophysical Journal*, 535(2):530, 2000. URL http://stacks.iop.org/0004-637X/535/i=2/a=530. 3

[58] Priscilla E. Greenwood and Michael S. Nikulin. *A Guide to Chi-Squared Testing (Wiley Series in Probability and Statistics)*. Wiley-Interscience, 1996. ISBN 047155779X. 57

[59] J. E. Gunn and B. A. Peterson. On the Density of Neutral Hydrogen in Intergalactic Space. ApJ, 142:1633–1641, November 1965. doi: 10.1086/148444. 5

[60] Z. Haiman. Formation of the first stars and quasars. *Advances in Space Research*, 23:915–924, 1999. doi: 10.1016/S0273-1177(99)00216-1. 4

[61] Frank R. Hampel. The influence curve and its role in robust estimation. *Journal of the American Statistical Association*, 69(346):383–393, 1974. ISSN 01621459. URL http://www.jstor.org/stable/2285666. 52, 76

[62] G. Harker, S. Zaroubi, G. Bernardi, M. A. Brentjens, A. G. de Bruyn, B. Ciardi, V. Jelić, L. V. E. Koopmans, P. Labropoulos, G. Mellema, A. Offringa, V. N. Pandey, J. Schaye, R. M. Thomas,

and S. Yatawatta. Non-parametric foreground subtraction for 21-cm epoch of reionization experiments. MNRAS, 397:1138–1152, August 2009. doi: 10.1111/j.1365-2966.2009.15081.x. 20, 70

[63] G. J. A. Harker. Selection between foreground models for global 21-cm experiments. MNRAS, 449:L21–L25, April 2015. doi: 10.1093/mnrasl/slv011. 70

[64] J. F. Helmboldt and N. E. Kassim. The Evolution of Cassiopeia A at Low Radio Frequencies. *The Astronomical Journal*, 138:838–844, September 2009. doi: 10.1088/0004-6256/138/3/838. 39

[65] G. Hinshaw, D. Larson, E. Komatsu, D. N. Spergel, C. L. Bennett, J. Dunkley, M. R. Nolta, M. Halpern, R. S. Hill, N. Odegard, L. Page, K. M. Smith, J. L. Weiland, B. Gold, N. Jarosik, A. Kogut, M. Limon, S. S. Meyer, G. S. Tucker, E. Wollack, and E. L. Wright. Nine-year wilkinson microwave anisotropy probe (wmap) observations: Cosmological parameter results. *The Astrophysical Journal Supplement Series*, 208(2):19, 2013. URL http://stacks.iop.org/0067-0049/208/i=2/a=19. 1

[66] W. Hu and M. White. A CMB polarization primer. New A, 2:323–344, October 1997. doi: 10.1016/S1384-1076(97)00022-5. 6

[67] Yi Huang. *Radiation Efficiency Measurements of Small Antennas*, pages 1–21. Springer Singapore, Singapore, 2014. ISBN 978-981-4560-75-7. doi: 10.1007/978-981-4560-75-7_71-1. 36

[68] A. Hutter, P. Dayal, A. M. Partl, and V. Müller. The visibility of Lyman α emitters: constraining reionization, ionizing photon escape fractions and dust. MNRAS, 441:2861–2877, July 2014. doi: 10.1093/mnras/stu791. 8

[69] H. Jensen, P. Laursen, G. Mellema, I. T. Iliev, J. Sommer-Larsen, and P. R. Shapiro. On the use of Lyα emitters as probes of reionization. MNRAS, 428:1366–1381, January 2013. doi: 10.1093/mnras/sts116. 8

[70] N. Kashikawa, K. Shimasaku, Y. Matsuda, E. Egami, L. Jiang, T. Nagao, M. Ouchi, M. A. Malkan, T. Hattori, K. Ota, Y. Taniguchi, S. Okamura, C. Ly, M. Iye, H. Furusawa, Y. Shioya, T. Shibuya, Y. Ishizaki, and J. Toshikawa. Completing the Census of Lyα Emitters at the Reionization Epoch. ApJ, 734:119, June 2011. doi: 10.1088/0004-637X/734/2/119. 8

[71] Steven M. Kay. *Fundamentals of Statistical Signal Processing, Volume II: Detection Theory*. Prentice Hall, 1998. ISBN 013504135X. 87

[72] Walt Kester. Understand SINAD, ENOB, SNR, THD, THD+ N, and SFDR so you don't get lost in the noise floor. *MT-003 Tutorial*, 2009. URL www.Analog.com/static/importedfiles/tutorials/MT-003.pdf. 49

[73] V. Khaire, R. Srianand, T. R. Choudhury, and P. Gaikwad. The redshift evolution of escape fraction of hydrogen ionizing photons from galaxies. MNRAS, 457:4051–4062, April 2016. doi: 10.1093/mnras/stw192. 4

[74] S. S. Kirby, L. V. Berkner, and D. M. Stuart. Studies of the ionosphere and their application to radio transmission. *Proceedings of the Institute of Radio Engineers*, 22(4):481–521, April 1934. ISSN 0731-5996. doi: 10.1109/JRPROC.1934.225867. 20

[75] T. L. Landecker and R. Wielebinski. The Galactic Metre Wave Radiation: A two-frequency survey between declinations +25^o and -25^o and the preparation of a map of the whole sky. *Australian Journal of Physics Astrophysical Supplement*, 16:1, 1970. 115

[76] R. S. Lawrence, C. G. Little, and H. J. A. Chivers. A survey of ionospheric effects upon earth-space radio propagation. *Proceedings of the IEEE*, 52(1):4–27, Jan 1964. ISSN 0018-9219. doi: 10.1109/PROC.1964.2737. 20

[77] A. Liu and A. R. Parsons. Constraining cosmology and ionization history with combined 21 cm power spectrum and global signal measurements. MNRAS, 457:1864–1877, April 2016. doi: 10.1093/mnras/stw071. 18

[78] A. Liu and M. Tegmark. How well can we measure and understand foregrounds with 21-cm experiments? MNRAS, 419:3491–3504, February 2012. doi: 10.1111/j.1365-2966.2011.19989.x. 20

[79] A. Liu, J. R. Pritchard, M. Tegmark, and A. Loeb. Global 21 cm signal experiments: A designer's guide. Phys. Rev. D, 87(4):043002, February 2013. doi: 10.1103/PhysRevD.87.043002. 21

[80] A. Liu, J. R. Pritchard, R. Allison, A. R. Parsons, U. Seljak, and B. D. Sherwin. Eliminating the optical depth nuisance from the CMB with 21 cm cosmology. Phys. Rev. D, 93(4):043013, February 2016. doi: 10.1103/PhysRevD.93.043013. 18

[81] Abraham Loeb. *How Did the First Stars and Galaxies Form?* Princeton University Press, 2010. ISBN 9781400834068. 3

[82] P. Madau and T. Fragos. Radiation Backgrounds at Cosmic Dawn: X-Rays from Compact Binaries. ApJ, 840:39, May 2017. doi: 10.3847/1538-4357/aa6af9. 3

[83] Piero Madau and Francesco Haardt. Cosmic reionization after planck: Could quasars do it all? *The Astrophysical Journal Letters*, 813(1):L8, 2015. URL http://stacks.iop.org/2041-8205/813/i=1/a=L8. 5

[84] N. Mahesh, R. Subrahmanyan, N. Udaya Shankar, and A. Raghunathan. A wideband resistive beam-splitter screen. *Antennas and Propagation, IEEE Transactions on*, 63(11):4835–4847, Nov 2015. ISSN 0018-926X. doi: 10.1109/TAP.2015.2478443. 101, 114, 118

[85] S. Malhotra and J. E. Rhoads. Luminosity Functions of Lyα Emitters at Redshifts z=6.5 and z=5.7: Evidence against Reionization at $z \leq 6.5$. ApJ, 617:L5–L8, December 2004. doi: 10.1086/427182. 8

[86] Donald W. Marquardt. An algorithm for least-squares estimation of nonlinear parameters. *SIAM Journal on Applied Mathematics*, 11(2):431–441, 1963. doi: 10.1137/0111030. URL http://dx.doi.org/10.1137/0111030. 93

[87] J. C. Mather, E. S. Cheng, R. E. Eplee, Jr., R. B. Isaacman, S. S. Meyer, R. A. Shafer, R. Weiss, E. L. Wright, C. L. Bennett, N. W. Boggess, E. Dwek, S. Gulkis, M. G. Hauser, M. Janssen, T. Kelsall, P. M. Lubin, S. H. Moseley, Jr., T. L. Murdock, R. F. Silverberg, G. F. Smoot, and D. T. Wilkinson. A preliminary measurement of the cosmic microwave background spectrum by the Cosmic Background Explorer (COBE) satellite. ApJ, 354:L37–L40, May 1990. doi: 10.1086/185717. 1

[88] C. L. Mehta and E. Wolf. Coherence Properties of Blackbody Radiation. I. Correlation Tensors of the Classical Field. *Physical Review*, 134:1143–1149, June 1964. doi: 10.1103/PhysRev.134.A1143. 105

[89] G. Mellema, L. V. E. Koopmans, F. A. Abdalla, G. Bernardi, B. Ciardi, S. Daiboo, A. G. de Bruyn, K. K. Datta, H. Falcke, A. Ferrara, I. T. Iliev, F. Iocco, V. Jelić, H. Jensen, R. Joseph, P. Labroupoulos, A. Meiksin, A. Mesinger, A. R. Offringa, V. N. Pandey, J. R. Pritchard, M. G. Santos, D. J. Schwarz, B. Semelin, H. Vedantham, S. Yatawatta, and S. Zaroubi. Reionization and the Cosmic Dawn with the Square Kilometre Array. *Experimental Astronomy*, 36:235–318, August 2013. doi: 10.1007/s10686-013-9334-5. 11, 16

[90] A. Mesinger. Reionization and Cosmic Dawn: theory and simulations. *ArXiv e-prints*, January 2018. 11

[91] Andrei Mesinger, Steven Furlanetto, and Renyue Cen. 21cmfast: a fast, seminumerical simulation of the high-redshift 21-cm signal. *Monthly Notices of the Royal Astronomical Society*, 411(2):955–972, 2011. doi: 10.1111/j.1365-2966.2010.17731.x. URL http://dx.doi.org/10.1111/j.1365-2966.2010.17731.x. 16

[92] RP Meys. A wave approach to the noise properties of linear microwave devices. *IEEE Transactions on Microwave Theory and Techniques*, 26(1):34–37, 1978. 40

[93] J. Miralda-Escudé. The Dark Age of the Universe. *Science*, 300:1904–1909, June 2003. doi: 10.1126/science.1085325. 3

[94] Jordi Miralda-Escudé, Martin Haehnelt, and Martin J. Rees. Reionization of the inhomogeneous universe. *The Astrophysical Journal*, 530(1):1, 2000. URL http://stacks.iop.org/0004-637X/530/i=1/a=1. 5

[95] J. Mirocha, G. J. A. Harker, and J. O. Burns. Interpreting the Global 21 cm Signal from High Redshifts. I. Model-independent constraints. ApJ, 777:118, November 2013. doi: 10.1088/0004-637X/777/2/118. 15

[96] J. Mirocha, G. J. A. Harker, and J. O. Burns. Interpreting the Global 21-cm Signal from High Redshifts. II. Parameter Estimation for Models of Galaxy Formation. *The Astrophysical Journal*, 813:11, November 2015. doi: 10.1088/0004-637X/813/1/11. 15, 18

[97] R. A. Monsalve, A. E. E. Rogers, J. D. Bowman, and T. J. Mozdzen. Calibration of the EDGES High-band Receiver to Observe the Global 21 cm Signature from the Epoch of Reionization. *The Astrophysical Journal*, 835:49, January 2017. doi: 10.3847/1538-4357/835/1/49. 21, 23, 27

[98] R. A. Monsalve, A. E. E. Rogers, J. D. Bowman, and T. J. Mozdzen. Results from EDGES High-band. I. Constraints on Phenomenological Models for the Global 21 cm Signal. ApJ, 847:64, September 2017. doi: 10.3847/1538-4357/aa88d1. 90, 123, 124

[99] M. F. Morales and J. S. B. Wyithe. Reionization and Cosmology with 21-cm Fluctuations. ARA&A, 48:127–171, September 2010. doi: 10.1146/annurev-astro-081309-130936. 11, 16, 21

[100] Miguel F. Morales and Jacqueline Hewitt. Toward Epoch of Reionization Measurements with Wide-Field Radio Observations. ApJ, 615:7–18, November 2004. doi: 10.1086/424437. 122

[101] D. Mortlock. Quasars as Probes of Cosmological Reionization. In A. Mesinger, editor, *Understanding the Epoch of Cosmic Reionization: Challenges and Progress*, volume 423 of *Astrophysics and Space Science Library*, page 187, 2016. doi: 10.1007/978-3-319-21957-8_7. 6

[102] T. J. Mozdzen, J. D. Bowman, R. A. Monsalve, and A. E. E. Rogers. Limits on foreground subtraction from chromatic beam effects in global redshifted 21 cm measurements. *Monthly Notices of the Royal Astronomical Society*, 455(4):3890–3900, 2016. doi: 10.1093/mnras/stv2601. URL +http://dx.doi.org/10.1093/mnras/stv2601. 21

[103] Subhash C. Narula and Pekka J. Korhonen. Multivariate multiple linear regression based on the minimum sum of absolute errors criterion. *European Journal of Operational Research*, 73 (1):70–75, February 1994. 53

[104] J. A. Nelder and R. Mead. A simplex method for function minimization. *The Computer Journal*, 7(4):308–313, 1965. doi: 10.1093/comjnl/7.4.308. 58

[105] Thomas Neu. Clock jitter analyzed in the time domain, part 1. *Analog Applications*, 2010. 49

[106] K. K. Nilsson. *The Lyman-alpha Emission Line as a Cosmological Tool*. PhD thesis, Dark Cosmology Centre, Niels Bohr Institute Faculty of Science, University of Copenhagen, November 2007. 8

[107] Adi Nusser, Andrew J. Benson, Naoshi Sugiyama, and Cedric Lacey. Statistics of neutral regions during hydrogen reionization. *The Astrophysical Journal Letters*, 580(2):L93, 2002. URL http://stacks.iop.org/1538-4357/580/i=2/a=L93. 5

[108] A. H. Nuttall. Some Windows with Very Good Sidelobe Behavior. *IEEE Transactions on Acoustics Speech and Signal Processing*, 29:84–91, 1981. 48, 49

[109] A. R. Offringa. *Algorithms for radio interference detection and removal*. PhD thesis, University of Groningen, June 2012. 53

[110] A. R. Offringa, A. G. de Bruyn, M. Biehl, S. Zaroubi, G. Bernardi, and V. N. Pandey. Post-correlation radio frequency interference classification methods. MNRAS, 405:155–167, June 2010. doi: 10.1111/j.1365-2966.2010.16471.x. 21

[111] A. R. Offringa, A. G. de Bruyn, S. Zaroubi, G. van Diepen, O. Martinez-Ruby, P. Labropoulos, M. A. Brentjens, B. Ciardi, S. Daiboo, G. Harker, V. Jelić, S. Kazemi, L. V. E. Koopmans, G. Mellema, V. N. Pandey, R. F. Pizzo, J. Schaye, H. Vedantham, V. Veligatla, S. J. Wijnholds,

S. Yatawatta, P. Zarka, A. Alexov, J. Anderson, A. Asgekar, M. Avruch, R. Beck, M. Bell, M. R. Bell, M. Bentum, G. Bernardi, P. Best, L. Birzan, A. Bonafede, F. Breitling, J. W. Broderick, M. Brüggen, H. Butcher, J. Conway, M. de Vos, R. J. Dettmar, J. Eisloeffel, H. Falcke, R. Fender, W. Frieswijk, M. Gerbers, J. M. Griessmeier, A. W. Gunst, T. E. Hassall, G. Heald, J. Hessels, M. Hoeft, A. Horneffer, A. Karastergiou, V. Kondratiev, Y. Koopman, M. Kuniyoshi, G. Kuper, P. Maat, G. Mann, J. McKean, H. Meulman, M. Mevius, J. D. Mol, R. Nijboer, J. Noordam, M. Norden, H. Paas, M. Pandey, R. Pizzo, A. Polatidis, D. Rafferty, S. Rawlings, W. Reich, H. J. A. Röttgering, A. P. Schoenmakers, J. Sluman, O. Smirnov, C. Sobey, B. Stappers, M. Steinmetz, J. Swinbank, M. Tagger, Y. Tang, C. Tasse, A. van Ardenne, W. van Cappellen, A. P. van Duin, M. van Haarlem, J. van Leeuwen, R. J. van Weeren, R. Vermeulen, C. Vocks, R. A. M. J. Wijers, M. Wise, and O. Wucknitz. The LOFAR radio environment. A&A, 549:A11, January 2013. doi: 10.1051/0004-6361/201220293. 21

[112] A. R. Offringa, R. B. Wayth, N. Hurley-Walker, D. L. Kaplan, N. Barry, A. P. Beardsley, M. E. Bell, G. Bernardi, J. D. Bowman, F. Briggs, J. R. Callingham, R. J. Cappallo, P. Carroll, A. A. Deshpande, J. S. Dillon, K. S. Dwarakanath, A. Ewall-Wice, L. Feng, B.-Q. For, B. M. Gaensler, L. J. Greenhill, P. Hancock, B. J. Hazelton, J. N. Hewitt, L. Hindson, D. C. Jacobs, M. Johnston-Hollitt, A. D. Kapińska, H.-S. Kim, P. Kittiwisit, E. Lenc, J. Line, A. Loeb, C. J. Lonsdale, B. McKinley, S. R. McWhirter, D. A. Mitchell, M. F. Morales, E. Morgan, J. Morgan, A. R. Neben, D. Oberoi, S. M. Ord, S. Paul, B. Pindor, J. C. Pober, T. Prabu, P. Procopio, J. Riding, N. Udaya Shankar, S. Sethi, K. S. Srivani, L. Staveley-Smith, R. Subrahmanyan, I. S. Sullivan, M. Tegmark, N. Thyagarajan, S. J. Tingay, C. M. Trott, R. L. Webster, A. Williams, C. L. Williams, C. Wu, J. S. Wyithe, and Q. Zheng. The Low-Frequency Environment of the Murchison Widefield Array: Radio-Frequency Interference Analysis and Mitigation. PASA, 32:e008, March 2015. doi: 10.1017/pasa.2015.7. 21

[113] Y. Ono, M. Ouchi, B. Mobasher, M. Dickinson, K. Penner, K. Shimasaku, B. J. Weiner, J. S. Kartaltepe, K. Nakajima, H. Nayyeri, D. Stern, N. Kashikawa, and H. Spinrad. Spectroscopic Confirmation of Three z-dropout Galaxies at z = 6.844-7.213: Demographics of Lyα Emission in z ˜ 7 Galaxies. ApJ, 744:83, January 2012. doi: 10.1088/0004-637X/744/2/83. 8

[114] A.V. Oppenheim. *Discrete-Time Signal Processing*. Pearson education signal processing series. Pearson Education, 1999. ISBN 9788131704929. URL https://books.google.co.in/books?id=geTn5W47KEsC. 82, 83

[115] Gregory Paciga, Joshua G. Albert, Kevin Bandura, Tzu-Ching Chang, Yashwant Gupta, Christopher Hirata, Julia Odegova, Ue-Li Pen, Jeffrey B. Peterson, Jayanta Roy, J. Richard

Shaw, Kris Sigurdson, and Tabitha Voytek. A simulation-calibrated limit on the H I power spectrum from the GMRT Epoch of Reionization experiment. MNRAS, 433:639–647, July 2013. doi: 10.1093/mnras/stt753. 123

[116] Athanasios Papoulis. *Probability, random variables, and stochastic processes*. McGraw-Hill Kogakush, 1981. ISBN 9780070486584. 57

[117] S. Parsa, J. S. Dunlop, and R. J. McLure. No evidence for a significant AGN contribution to cosmic hydrogen reionization. MNRAS, 474:2904–2923, March 2018. doi: 10.1093/mnras/stx2887. 5

[118] P. Paschos and M. L. Norman. A Statistical Analysis of Intergalactic Medium Transmission Approaching Reionization. ApJ, 631:59–84, September 2005. doi: 10.1086/431787. 6

[119] A. H. Patil, S. Yatawatta, L. V. E. Koopmans, A. G. de Bruyn, M. A. Brentjens, S. Zaroubi, K. M. B. Asad, M. Hatef, V. Jelić, M. Mevius, A. R. Offringa, V. N. Pandey, H. Vedantham, F. B. Abdalla, W. N. Brouw, E. Chapman, B. Ciardi, B. K. Gehlot, A. Ghosh, G. Harker, I. T. Iliev, K. Kakiichi, S. Majumdar, G. Mellema, M. B. Silva, J. Schaye, D. Vrbanec, and S. J. Wijnholds. Upper limits on the 21 cm epoch of reionization power spectrum from one night with lofar. ApJ, 838, March 2017. doi: 10.3847/1538-4357/aa63e7. 123

[120] N. Patra, R. Subrahmanyan, A. Raghunathan, and N. Udaya Shankar. SARAS: a precision system for measurement of the cosmic radio background and signatures from the epoch of reionization. *Experimental Astronomy*, 36:319–370, August 2013. doi: 10.1007/s10686-013-9336-3. 24, 47, 48

[121] N. Patra, J. D. Bray, P. Roberts, and R. D. Ekers. Bandpass calibration of a wideband spectrometer using coherent pulse injection. *Experimental Astronomy*, 43:119–129, April 2017. doi: 10.1007/s10686-017-9523-8. 39

[122] Nipanjana Patra, Ravi Subrahmanyan, Shiv Sethi, N. Udaya Shankar, and A. Raghunathan. Saras measurement of the radio background at long wavelengths. *The Astrophysical Journal*, 801(2):138, 2015. URL http://stacks.iop.org/0004-637X/801/i=2/a=138. 24

[123] P. J. E. Peebles. Recombination of the Primeval Plasma. ApJ, 153:1, July 1968. doi: 10.1086/149628. 2

[124] A. A. Penzias and R. W. Wilson. A Measurement of Excess Antenna Temperature at 4080 Mc/s. ApJ, 142:419–421, July 1965. doi: 10.1086/148307. 1

[125] R.A. Perley, F.R. Schwab, and A.H. Bridle. *Synthesis imaging in radio astronomy*. San Francisco, CA (US); Astronomical Society of the Pacific, Jan 1989. 39

[126] Planck Collaboration, R. Adam, P. A. R. Ade, N. Aghanim, Y. Akrami, M. I. R. Alves, F. Argüeso, M. Arnaud, F. Arroja, M. Ashdown, and et al. Planck 2015 results. I. Overview of products and scientific results. A&A, 594:A1, September 2016. doi: 10.1051/0004-6361/201527101. 1

[127] Planck Collaboration, R. Adam, N. Aghanim, M. Ashdown, J. Aumont, C. Baccigalupi, M. Ballardini, A. J. Banday, R. B. Barreiro, N. Bartolo, S. Basak, R. Battye, K. Benabed, J.-P. Bernard, M. Bersanelli, P. Bielewicz, J. J. Bock, A. Bonaldi, L. Bonavera, J. R. Bond, J. Borrill, F. R. Bouchet, F. Boulanger, M. Bucher, C. Burigana, E. Calabrese, J.-F. Cardoso, J. Carron, H. C. Chiang, L. P. L. Colombo, C. Combet, B. Comis, F. Couchot, A. Coulais, B. P. Crill, A. Curto, F. Cuttaia, R. J. Davis, P. de Bernardis, A. de Rosa, G. de Zotti, J. Delabrouille, E. Di Valentino, C. Dickinson, J. M. Diego, O. Doré, M. Douspis, A. Ducout, X. Dupac, F. Elsner, T. A. Enßlin, H. K. Eriksen, E. Falgarone, Y. Fantaye, F. Finelli, F. Forastieri, M. Frailis, A. A. Fraisse, E. Franceschi, A. Frolov, S. Galeotta, S. Galli, K. Ganga, R. T. Génova-Santos, M. Gerbino, T. Ghosh, J. González-Nuevo, K. M. Górski, A. Gruppuso, J. E. Gudmundsson, F. K. Hansen, G. Helou, S. Henrot-Versillé, D. Herranz, E. Hivon, Z. Huang, S. Ilić, A. H. Jaffe, W. C. Jones, E. Keihänen, R. Keskitalo, T. S. Kisner, L. Knox, N. Krachmalnicoff, M. Kunz, H. Kurki-Suonio, G. Lagache, A. Lähteenmäki, J.-M. Lamarre, M. Langer, A. Lasenby, M. Lattanzi, C. R. Lawrence, M. Le Jeune, F. Levrier, A. Lewis, M. Liguori, P. B. Lilje, M. López-Caniego, Y.-Z. Ma, J. F. Macías-Pérez, G. Maggio, A. Mangilli, M. Maris, P. G. Martin, E. Martínez-González, S. Matarrese, N. Mauri, J. D. McEwen, P. R. Meinhold, A. Melchiorri, A. Mennella, M. Migliaccio, M.-A. Miville-Deschênes, D. Molinari, A. Moneti, L. Montier, G. Morgante, A. Moss, P. Naselsky, P. Natoli, C. A. Oxborrow, L. Pagano, D. Paoletti, B. Partridge, G. Patanchon, L. Patrizii, O. Perdereau, L. Perotto, V. Pettorino, F. Piacentini, S. Plaszczynski, L. Polastri, G. Polenta, J.-L. Puget, J. P. Rachen, B. Racine, M. Reinecke, M. Remazeilles, A. Renzi, G. Rocha, M. Rossetti, G. Roudier, J. A. Rubiño-Martín, B. Ruiz-Granados, L. Salvati, M. Sandri, M. Savelainen, D. Scott, G. Sirri, R. Sunyaev, A.-S. Suur-Uski, J. A. Tauber, M. Tenti, L. Toffolatti, M. Tomasi, M. Tristram, T. Trombetti, J. Valiviita, F. Van Tent, P. Vielva, F. Villa, N. Vittorio, B. D. Wandelt, I. K. Wehus, M. White, A. Zacchei, and A. Zonca. Planck intermediate results. XLVII. Planck constraints on reionization history. A&A, 596:A108, December 2016. doi: 10.1051/0004-6361/201628897. 6

[128] D. M. Pozar and B. Kaufman. Comparison of three methods for the measurement of printed an-

tenna efficiency. *IEEE Transactions on Antennas and Propagation*, 36(1):136–139, Jan 1988. ISSN 0018-926X. doi: 10.1109/8.1084. 36

[129] Morgan E. Presley, Adrian Liu, and Aaron R. Parsons. Measuring the cosmological 21 cm monopole with an interferometer. ApJ, 809, August 2015. doi: 10.1088/0004-637X/809/1/18. 101, 110, 113

[130] William H. Press, Saul A. Teukolsky, William T. Vetterling, and Brian P. Flannery. Numerical recipes in c: The art of scientific computing. second edition, 1992. 91

[131] D. C. Price, L. J. Greenhill, A. Fialkov, and et al. Design and characterization of the Large-Aperture Experiment to Detect the Dark Age (LEDA) radiometer systems. *ArXiv e-prints*, September 2017. 19, 23, 27

[132] J. R. Pritchard and A. Loeb. Evolution of the 21cm signal throughout cosmic history. Phys. Rev. D, 78(10):103511, November 2008. doi: 10.1103/PhysRevD.78.103511. 9, 122

[133] J. R. Pritchard and A. Loeb. Constraining the unexplored period between the dark ages and reionization with observations of the global 21 cm signal. Phys. Rev. D, 82(2):023006, July 2010. doi: 10.1103/PhysRevD.82.023006. 11, 13

[134] J. R. Pritchard and A. Loeb. 21 cm cosmology in the 21st century. *Reports on Progress in Physics*, 75(8):086901, August 2012. doi: 10.1088/0034-4885/75/8/086901. 5, 12, 13

[135] M. J. Rees. Polarization and Spectrum of the Primeval Radiation in an Anisotropic Universe. ApJ, 153:L1, July 1968. doi: 10.1086/180208. 6

[136] Martin J Rees. 'first light' in the universe: what ended the 'dark age'? *Physics Reports*, 333-334:203 – 214, 2000. ISSN 0370-1573. doi: https://doi.org/10.1016/S0370-1573(00)00023-5. URL http://www.sciencedirect.com/science/article/pii/S0370157300000235. 3

[137] C. L. Reichardt. Observing the Epoch of Reionization with the Cosmic Microwave Background. In A. Mesinger, editor, *Understanding the Epoch of Cosmic Reionization: Challenges and Progress*, volume 423 of *Astrophysics and Space Science Library*, page 227, 2016. doi: 10.1007/978-3-319-21957-8_8. 8

[138] B. E. Robertson, R. S. Ellis, J. S. Dunlop, R. J. McLure, and D. P. Stark. Early star-forming galaxies and the reionization of the Universe. Nature, 468:49–55, November 2010. doi: 10.1038/nature09527. 4

[139] A. E. E. Rogers and J. D. Bowman. Absolute calibration of a wideband antenna and spectrometer for accurate sky noise temperature measurements. *Radio Science*, 47:RS0K06, August 2012. doi: 10.1029/2011RS004962. 29, 40

[140] V. Rumsey. Frequency independent antennas. In *1958 IRE International Convention Record*, volume 5, pages 114–118, March 1957. doi: 10.1109/IRECON.1957.1150565. 30

[141] G. B. Rybicki and A. P. Lightman. *Radiative Processes in Astrophysics*. June 1986. 10

[142] M. G. Santos, A. Amblard, J. Pritchard, H. Trac, R. Cen, and A. Cooray. Cosmic Reionization and the 21 cm Signal: Comparison between an Analytical Model and a Simulation. ApJ, 689: 1-16, December 2008. doi: 10.1086/592487. 11

[143] M. Sathyanarayana Rao, R. Subrahmanyan, N. Udaya Shankar, and J. Chluba. On the Detection of Spectral Ripples from the Recombination Epoch. *The Astrophysical Journal*, 810:3, September 2015. doi: 10.1088/0004-637X/810/1/3. 28, 62, 77, 84

[144] M. Sathyanarayana Rao, R. Subrahmanyan, N. Udaya Shankar, and J. Chluba. GMOSS: All-sky Model of Spectral Radio Brightness Based on Physical Components and Associated Radiative Processes. *Astronomical Journal*, 153:26, January 2017. doi: 10.3847/1538-3881/153/1/26. 20, 37, 77

[145] M. Sathyanarayana Rao, R. Subrahmanyan, N. Udaya Shankar, and J. Chluba. Modeling the Radio Foreground for Detection of CMB Spectral Distortions from the Cosmic Dawn and the Epoch of Reionization. *The Astrophysical Journal*, 840:33, May 2017. doi: 10.3847/1538-4357/aa69bd. 20, 21, 28, 62, 70, 123

[146] R. J. Sault, P. J. Teuben, and M. C. H. Wright. A Retrospective View of MIRIAD. In R. A. Shaw, H. E. Payne, and J. J. E. Hayes, editors, *Astronomical Data Analysis Software and Systems IV*, volume 77 of *Astronomical Society of the Pacific Conference Series*, page 433, 1995. 49, 76

[147] R. B. Schulz, V. C. Plantz, and D. R. Brush. Shielding theory and practice. *IEEE Transactions on Electromagnetic Compatibility*, 30(3):187–201, Aug 1988. ISSN 0018-9375. doi: 10.1109/15.3297. 21

[148] D. Scott and M. J. Rees. The 21-cm line at high redshift: a diagnostic for the origin of large scale structure. MNRAS, 247:510, December 1990. 122

[149] Prateek Sharma. Astrophysical radio background cannot explain the EDGES signal: constraints from cooling of non-thermal electrons. *ArXiv e-prints*, April 2018. 126

[150] P. A. Shaver, R. A. Windhorst, P. Madau, and A. G. de Bruyn. Can the reionization epoch be detected as a global signature in the cosmic background? *Astronomy and Astrophysics*, 345: 380–390, May 1999. 21, 28, 39, 122, 123

[151] S. Singh, R. Subrahmanyan, N. Udaya Shankar, and et al. First Results on the Epoch of Reionization from First Light with SARAS 2. *The Astrophysical Journal Letters*, 845:L12, aug 2017. doi: 10.3847/2041-8213/aa831b. 19, 27, 123

[152] Saurabh Singh, Ravi Subrahmanyan, N. Udaya Shankar, Mayuri Sathyanarayana Rao, Anastasia Fialkov, Aviad Cohen, Rennan Barkana, B. S. Girish, A. Raghunathan, R. Somashekar, and K. S. Srivani. Saras 2 constraints on global 21 cm signals from the epoch of reionization. *The Astrophysical Journal*, 858(1):54, 2018. URL http://stacks.iop.org/0004-637X/858/i=1/a=54. 27, 123, 124

[153] Saurabh Singh, Ravi Subrahmanyan, N. Udaya Shankar, Mayuri Sathyanarayana Rao, B. S. Girish, A. Raghunathan, R. Somashekar, and K. S. Srivani. SARAS 2: a spectral radiometer for probing cosmic dawn and the epoch of reionization through detection of the global 21-cm signal. *Experimental Astronomy*, page 30, April 2018. doi: 10.1007/s10686-018-9584-3. 97, 123

[154] M. Sokolowski, S. E. Tremblay, R. B. Wayth, S. J. Tingay, N. Clarke, P. Roberts, M. Waterson, R. D. Ekers, P. Hall, M. Lewis, M. Mossammaparast, S. Padhi, F. Schlagenhaufer, A. Sutinjo, and J. Tickner. BIGHORNS - Broadband Instrument for Global HydrOgen ReioNisation Signal. PASA, 32:e004, February 2015. doi: 10.1017/pasa.2015.3. 19, 23, 27, 64

[155] M. Sokolowski, R. B. Wayth, S. E. Tremblay, S. J. Tingay, M. Waterson, J. Tickner, D. Emrich, F. Schlagenhaufer, D. Kenney, and S. Padhi. The Impact of the Ionosphere on Ground-based Detection of the Global Epoch of Reionization Signal. ApJ, 813:18, November 2015. doi: 10.1088/0004-637X/813/1/18. 20

[156] K. S. Srivani, B. S. Girish, N. U. Shankar, and R. Subrahmanyan. A precision spectrometer for measuring signals from the epoch of cosmological recombination. In *2014 XXXIth URSI General Assembly and Scientific Symposium (URSI GASS)*, pages 1–4, Aug 2014. doi: 10.1109/URSIGASS.2014.6930031. 49

[157] S. Staggs, J. Dunkley, and L. Page. Recent discoveries from the cosmic microwave background: a review of recent progress. *Reports on Progress in Physics*, 81(4):044901, April 2018. doi: 10.1088/1361-6633/aa94d5. 1

[158] R.D. Straw, American Radio Relay League, L.B. Cebik, D. Hallidy, and D. Jansson, editors. *The ARRL Antenna Book*. ARRL Antenna Book. ARRL, 2007. ISBN 9780872599871. 78

[159] Warren Stutzman. *Antenna theory and design*. Wiley, Hoboken, NJ, 2013. ISBN 978-0470576649. 32

[160] R. Subrahmanyan, U. N. Shankar, J. Pritchard, and H. K. Vedantham. All-sky signals from recombination to reionization with the SKA. *Advancing Astrophysics with the Square Kilometre Array (AASKA14)*, art. 14, April 2015. 16

[161] R. A. Sunyaev and Y. B. Zeldovich. The Observations of Relic Radiation as a Test of the Nature of X-Ray Radiation from the Clusters of Galaxies. *Comments on Astrophysics and Space Physics*, 4:173, November 1972. 6

[162] R. A. Sunyaev and Ya. B. Zeldovich. Formation of Clusters of Galaxies; Protocluster Fragmentation and Intergalactic Gas Heating. A&A, 20:189, August 1972. 122

[163] E. R. Switzer and A. Liu. Erasing the Variable: Empirical Foreground Discovery for Global 21 cm Spectrum Experiments. ApJ, 793:102, October 2014. doi: 10.1088/0004-637X/793/2/102. 20

[164] A Richard Thompson, James M Moran, and George W Swenson Jr. *Interferometry and synthesis in radio astronomy*. John Wiley & Sons, 2008. 104

[165] H. C. van de Hulst. *1945, The Origin of Radio Waves from Space*, page 302. 1982. 9

[166] H. K. Vedantham, L. V. E. Koopmans, A. G. de Bruyn, S. J. Wijnholds, B. Ciardi, and M. A. Brentjens. Chromatic effects in the 21 cm global signal from the cosmic dawn. MNRAS, 437: 1056–1069, January 2014. doi: 10.1093/mnras/stt1878. 20, 29, 101

[167] H. K. Vedantham, L. V. E. Koopmans, A. G. de Bruyn, S. J. Wijnholds, M. Brentjens, F. B. Abdalla, K. M. B. Asad, G. Bernardi, S. Bus, E. Chapman, B. Ciardi, S. Daiboo, E. R. Fernandez, A. Ghosh, G. Harker, V. Jelic, H. Jensen, S. Kazemi, P. Lambropoulos, O. Martinez-Rubi, G. Mellema, M. Mevius, A. R. Offringa, V. N. Pandey, A. H. Patil, R. M. Thomas, V. Veligatla, S. Yatawatta, S. Zaroubi, J. Anderson, A. Asgekar, M. E. Bell, M. J. Bentum, P. Best, A. Bonafede, F. Breitling, J. Broderick, M. Brüggen, H. R. Butcher, A. Corstanje, F. de

Gasperin, E. de Geus, A. Deller, S. Duscha, J. Eislöffel, D. Engels, H. Falcke, R. A. Fallows, R. Fender, C. Ferrari, W. Frieswijk, M. A. Garrett, J. Grießmeier, A. W. Gunst, T. E. Hassall, G. Heald, M. Hoeft, J. Hörandel, M. Iacobelli, E. Juette, V. I. Kondratiev, M. Kuniyoshi, G. Kuper, G. Mann, S. Markoff, R. McFadden, D. McKay-Bukowski, J. P. McKean, D. D. Mulcahy, H. Munk, A. Nelles, M. J. Norden, E. Orru, M. Pandey-Pommier, R. Pizzo, A. G. Polatidis, W. Reich, A. Renting, H. Röttgering, D. Schwarz, A. Shulevski, O. Smirnov, B. W. Stappers, M. Steinmetz, J. Swinbank, M. Tagger, Y. Tang, C. Tasse, S. ter Veen, S. Thoudam, C. Toribio, C. Vocks, M. W. Wise, O. Wucknitz, and P. Zarka. Lunar occultation of the diffuse radio sky: LOFAR measurements between 35 and 80 MHz. MNRAS, 450:2291–2305, July 2015. doi: 10.1093/mnras/stv746. 39, 113

[168] Pablo Villanueva-Domingo, Stefano Gariazzo, Nickolay Y. Gnedin, and Olga Mena. Was there an early reionization component in our universe? *Journal of Cosmology and Astro-Particle Physics*, 2018, April 2018. doi: 10.1088/1475-7516/2018/04/024. 5

[169] E. Visbal, R. Barkana, A. Fialkov, D. Tseliakhovich, and C. M. Hirata. The signature of the first stars in atomic hydrogen at redshift 20. Nature, 487:70–73, July 2012. doi: 10.1038/nature11177. 85

[170] T. C. Voytek, A. Natarajan, J. M. Jáuregui García, J. B. Peterson, and O. López-Cruz. Probing the Dark Ages at z ˜ 20: The SCI-HI 21 cm All-sky Spectrum Experiment. ApJ, 782:L9, February 2014. doi: 10.1088/2041-8205/782/1/L9. 19, 23, 27

[171] David J. Wales and Jonathan P. K. Doye. Global optimization by basin-hopping and the lowest energy structures of lennard-jones clusters containing up to 110 atoms. *The Journal of Physical Chemistry A*, 101(28):5111–5116, 1997. doi: 10.1021/jp970984n. 58

[172] Melwin M. Weiner. *Monopole Antennas*. Dekker, 2009. 39

[173] Thomas L. Wilson, Kristen. Rohlfs, and Susanne. Hüttemeister. *Tools of Radio Astronomy*. Springer Berlin Heidelberg,, Berlin, Heidelberg :, 2009. 117

[174] Samuel Witte, Pablo Villanueva-Domingo, Stefano Gariazzo, Olga Mena, and Sergio Palomares-Ruiz. EDGES result versus CMB and low-redshift constraints on ionization histories. *ArXiv e-prints*, April 2018. 126

[175] S. Zaroubi. The Epoch of Reionization. In T. Wiklind, B. Mobasher, and V. Bromm, editors, *The First Galaxies*, volume 396 of *Astrophysics and Space Science Library*, page 45, 2013. doi: 10.1007/978-3-642-32362-1_2. 4